UNIVERSITÉ DE GENÈVE
Département de physique
nucléaire et corpusculaire
CERN

FACULTÉ DE SCIENCES
Professeur Alain Blondel

Docteur Simone Giani

Hadron production cross section measurement with the HARP large angle detectors

THÈSE

présentée à la Faculté des sciences de l'Université de Genève
pour obtenir le grade de Docteur ès sciences, mention physique

par

Silvia Borghi

d'Italie

Thèse N° 3781

GENÈVE

2006

UNIVERSITÉ DE GENÈVE

FACULTÉ DES SCIENCES

Doctorat ès sciences
mention physique

Thèse de Madame Silvia BORGHI

intitulée :

" Hadron Production Cross Section Measurement with the HARP Large Angle Detectors "

La Faculté des sciences, sur le préavis de Messieurs A. BLONDEL, professeur ordinaire (Département de physique nucléaire & corpusculaire), directeur de thèse et S. GIANI, docteur (CERN - Conseil Européen pour la Recherche Nucléaire, Département de physique, Genève, Suisse), codirecteur de thèse, A. CLARK, professeur ordinaire (Département de physique nucléaire et corpusculaire), L. ROLANDI, docteur (CERN - Conseil Européen pour la Recherche Nucléaire, Département de physique, Genève, Suisse) et V. GRICHINE, Professeur (Russian Academy of Sciences, P.N. Lebedev Institute of Physics – FIAN - Fizicheskii Institut Akademiya Nauk – Moscow, Russia), autorise l'impression de la présente thèse, sans exprimer d'opinion sur les propositions qui y sont énoncées.

Genève, le 19 septembre 2006

Thèse - 3781 -

P. Spierer

Le Doyen, Pierre SPIERER

To Simone

Contents

Acknowledgements

I would like to thank my supervisor, Prof. Alain Blondel, for giving me the opportunity to participate in the HARP collaboration and to accomplish this PhD thesis; it taught me a lot on particle physics and not only.

Thanks to Prof. Allan Clark and to all colleagues of Geneva's University.

A special thank to Prof. Maria Kienzle it was a real pleasure to discuss with her issues related to the life of PhD student and to be part of her group of assistants for her physics lectures.

Thanks to all my students to who I have tried to teach the basic physics and who tried to improve my French (unfortunately with little success!). Teaching reminded me that research is not complete if knowledge is not shared.

Thanks to Dr. Simone Giani for his guidance, for his constant support, for many fruitful discussions, for his capacity to restart from scratch every time that something was not understood, and in a special way for having found always time for me also for long discussions about life.

Thanks to Prof. Vladimir Grichine for accepting to participate in the thesis jury and for his remarks about the analysis and the thesis and for his teaching about particles-matter interactions.

Thank to Prof. Luigi Rolandi for accepting to participate in the jury of my thesis and for his astute remarks. I would like to have had other possibilities to collaborate with you.

Merci à Catherine et à Peggy, qui m'ont constamment aidée avec mes problèmes burocratiques.

A special thank to Jaap Panman, HARP spokesperson, that collaborated during the development of the two parallel analyses, I am grateful to him because he showed how to do science in a very professional way.

This analysis would not have been possible without the support of the HARP TPC group whose efforts allowed to understand the TPC:
thanks to Ugo and Gabriella for their suggestions, for the stimulating discussion and their remarks that taught me so much;
thanks to Marco and Pietro for your contribution during the boring and pre-

cious period of calibration and understanding of the detector;
thanks to Emilio and Piotr for their advice, for having a different point of view and for having very good ideas!

I would like to thank all members of HARP collaboration: Malcolm (during the first years he helped me with my rudimentary c++), Vladimir (for discussions and help with Geant4), Helge (without him my computer would not be still alive), Simon and Charles (I was really alone when you left our office at CERN), Dimitar (one pleasant company during the summer Sundays), Gersende (we have shared not only the experiment), Rob (for the availability and all the precious knowledge on the TPC), Jean Sebastien (without you the French summary would be not readable!), Valerie, JJ, Stefan, Giovanni, Pavel, Evgueni, Serguei, Ioannis, Ilya, Vittorio, Roumen, Misha, Alex, Lara, Mariyan, Anselmo, Alessandra.

Vorrei ringraziare tutti i miei amici di sempre, quelli che mi hanno supportato in questi anni, sorbendosi per ore i racconti di questa strana avventura, quelli che hanno sopportato per mesi di non ricevere risposte alle email e che stanno ancora aspettando di festeggiare questo dottorato con una bella rimpatriata... é stato fondamentale sapere che voi ci siete sempre. Grazie a tutti: Caterina, Lorenzo, Tito, Marcella, Giulia, Samantha, Michele, Daniela, Michele, Alessandra, Giovanni, Sara, Barbara, Chiara, Allegra, Davide, Romano, Simona, Massimo, Mauro, Chiara, Sonia, Luca e tutti quelli che ora non mi vengono in mente ma vi assicuro che é solo colpa della vecchiaia!

Un particolare grazie va a tutta la mia grande famiglia che mi ha sempre supportato, che mi ha aiutato a trovare la grinta per superare le difficoltà e che ha sempre creduto in me. Un particolare grazie va a Stefania di poche parole ma un supporto indispensabile e a te mamma che mi hai permesso di diventare la donna che sono!

Per te Simo non ci sono parole: mi hai aiutato a non perdere la determinazione nel volere capire le cose, mi sei stato accanto aiutandomi a risolvere i problemi di paw (e non solo), mi hai supportato nei momenti di crisi, hai gioito con me nell'ottenere i risultati, mi hai fatto sorridere anche quando non c'erano più motivi, hai sempre creduto in me e nei miei sogni e mi hai sempre fatto trovare un motivo per apprezzare la vita anche quando la vita era solo lavoro, senza di te non sarei mai arrivata a finire questa tesi!

Finally I would like to thank my CAST colleagues (Martyn, Konstantin, Jaime, Julia, Annika, Thomas, Berkol, Nuno, Asun, Tasos) who helped me to find out the time to finish this thesis and for reminding me that the work for this thesis was made only for the love of science!

Résumé

Chapitre 1 : La physique des neutrinos

Ce chapitre résume les propriétés des neutrinos, discute les questions et les intrigantes possibilités ouvertes par la découverte que les neutrinos ont une masse non nulle. Ensuite, on décrit l'importance qu'a la connaissance de la production des hadrons dans le contexte de la physique des neutrinos pour l'analyse des résultats des expériences sur les oscillations de neutrinos actuelles et futures, et en particulier pour le cas d'une usine à neutrinos.

Le calcul du flux de neutrinos et sa composition relative en différentes saveurs demande une mesure précise des sections efficaces d'interaction entre les protons primaires et les différents matériaux qui composent la cible. Dans le cas des expériences MiniBoone et K2K, la fraction la plus importante des neutrinos est produite par la désintégration des pions positifs. Ces derniers sont générés par l'interaction de protons sur la cible. Pour évaluer le flux des neutrinos d'une façon assez précise, il faut une paramétrisation de la section efficace différentielle sur tout l'angle solide qui doit elle-même dériver d'une mesure précise et fiable sur tout l'angle solide.

La conception et l'optimisation d'une usine à neutrinos demande quant à elle la connaissance des sections efficaces différentielles de production des pions en fonction de l'énergie des protons primaires. L'expérience HARP couvre une large région angulaire et un intervalle d'impulsion des protons primaires compris entre 1.5 GeV/c et 15 GeV/c pour différentes cibles de numéros atomiques fort différents. Ces mesures des sections efficaces doublement différentielles pour des pions positifs et négatifs permettront de choisir la meilleure cible, l'énergie du faisceau des protons primaires et le système de focalisation des pions d'une future usine à neutrinos.

Chapitre 2 : L'expérience HARP

L'expérience PS214, plus connue sous le nom de HARP, a comme but la mesure des sections efficaces de production de hadrons à partir d'un faisceau de protons ou de pions à différentes énergies (1.5 - 15 GeV/c) qui interagissent dans différents matériaux. En particulier, l'expérience a été conçue pour déterminer avec la meilleure précision possible le taux de production de pions à partir d'un faisceau de protons pour différentes énergies et matériaux en vue du choix du type d'accélérateur primaire d'une usine à neutrinos. Pour cette raison, HARP a été construite pour couvrir la fraction la plus large de l'angle solide, en utilisant différents détecteurs pour différents intervalles angulaires. Les grands angles sont couverts par une TPC, (Time Projection Chambre ou Chambre à Projection Temporelle), dans laquelle est disposée la cible. La zone d'angle vers l'avant, en revanche, est couverte, grâce à un aimant dipolaire, par un spectromètre.

L’expérience a étudié sept cibles de matériau solide (Be, C, Al, Cu, Sn, Ta, Pb) pour couvrir l’intervalle des nombres atomiques entre 4 et 82. Les cibles sélectionnées ont une épaisseur comprise entre 2% ou 5% d’une longueur d’interaction nucléaire pour minimiser l’effet de possibles re-interactions dans la cible ou de distorsions des traces dues aux diffusions multiples. Parmi les cibles solides, HARP a également étudié la copie des cibles employées dans l’expérience K2K et Miniboone, avec l’idée de réduire les incertitudes dans le calcul de flux de neutrinos pour ces deux expériences. De plus, HARP a aussi étudié des cibles d’Hydrogène, de Deutérium, d’Oxygène et d’Azote à températures cryogéniques, et donc dans l’état liquide.

Le dispositif expérimental peut être séparé en quatre parties, selon les fonctionnalités assurées par chacune : les détecteurs de la ligne de transfert du faisceau, les détecteurs utilisés pour le déclenchement de l’acquisition (« trigger »), le spectromètre à grand angle et le spectromètre vers l’avant (Figure 1).

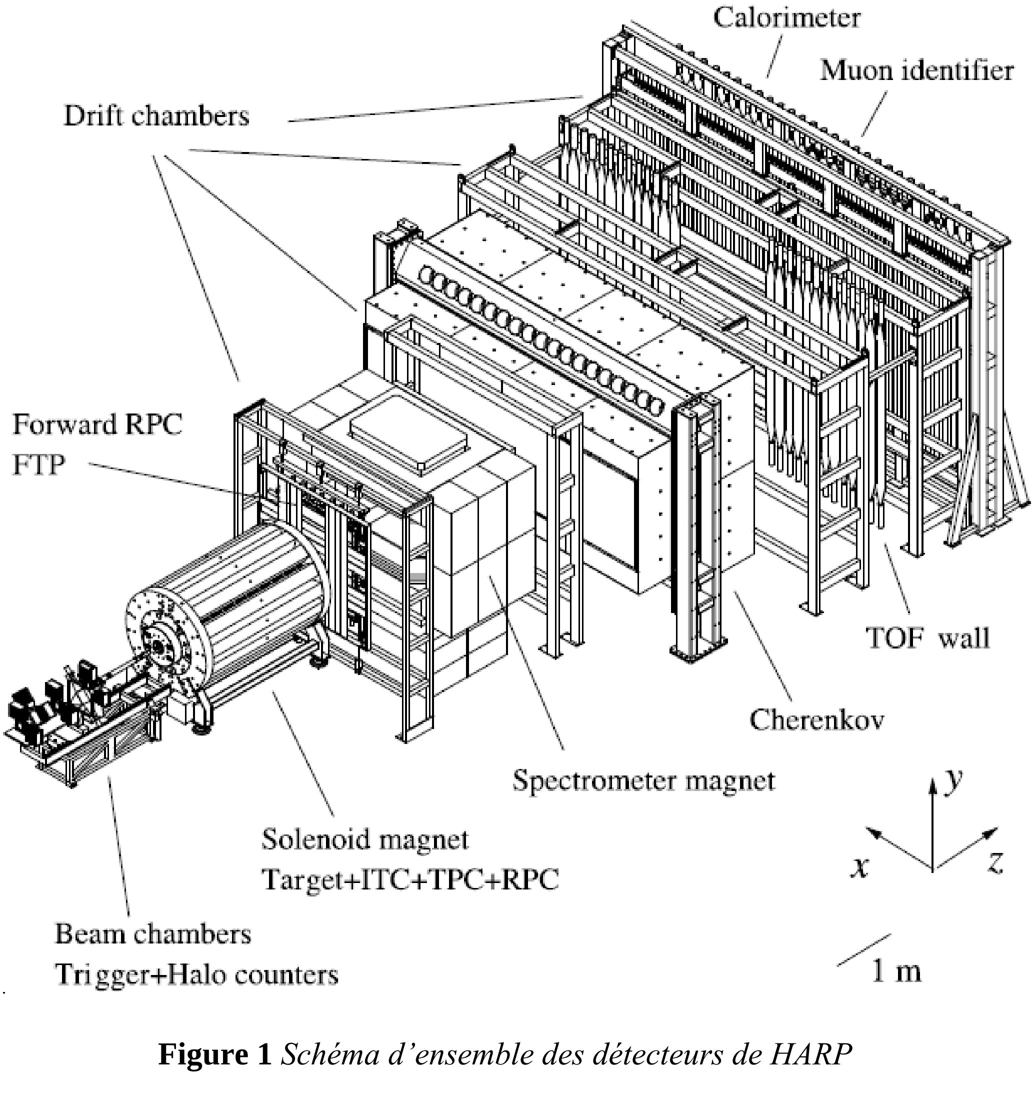

Figure 1 *Schéma d’ensemble des détecteurs de HARP*

L'instrumentation située en amont de la cible est formée d'une paire de détecteurs Cherenkov à gaz, deux compteurs pour les particules qui forment le halo du faisceau, un système de mesure du temps de vol, un ensemble de quatre chambres multi fils et deux compteurs à scintillations. Le but de ce groupe de détecteurs est double : d'abord ils fournissent la détection, l'identification et la mesure de la trajectoire des particules primaires, ensuite ils donnent le premier signal de la chaîne de déclenchement.

L'expérience s'étend sur une longueur totale de 13.5 m dans la direction parallèle au faisceau. Le spectromètre à grand angle est formé par la TPC et un ensemble de chambres à multicouches résistives (RPC), le deux système sont placés à l'intérieur d'un solénoïde pour assurer la mesure de l'impulsion des particules (Figure 2). La TPC est utilisée pour reconstruire les trajectoires des particules et pour leur identification. Cette dernière tache est complétée par les RPC grâce à la mesure du temps de vol des particules. Les détecteurs doivent mesurer et identifier les particules dans une région angulaire comprise entre 0.35 et 2.15 rad par rapport à la direction du faisceau primaire. L'identification du type de particule est possible grâce au pouvoir d'arrêt (dE/dx) déterminé dans la TPC, sauf pour la région en impulsion entre 150-300 MeV/c, à cause de la superposition de la courbe de dE/dx des pions et des électrons.

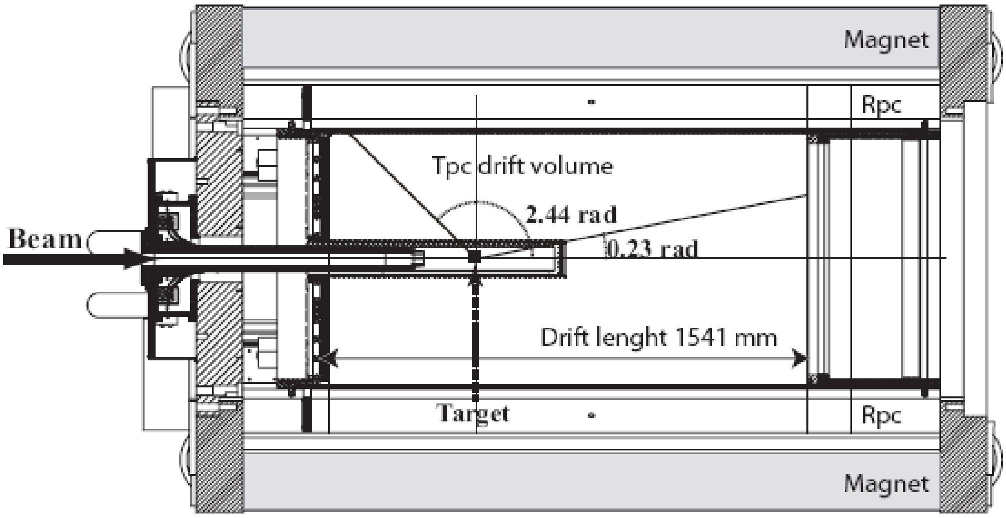

Figure 2 *Schéma de la TPC de HARP*

Le spectromètre vers l'avant mesure les particules secondaires produites à des angles inférieurs à 14.3°. Autour d'un dipôle qui assure la déviation nécessaire à la mesure de l'impulsion, un certain nombre de chambres à dérive (NDC) sont placées pour la reconstruction des trajectoires. L'identification du type de particule est rendue possible par la combinaison des mesures faites par un détecteur Cherenkov à seuil (pour les grandes impulsions), un détecteur du temps de vol (TOFW pour les petites impulsions) et un calorimètre hadronique. Le dipôle qui sert à mesurer l'impulsion pour des petits angles présente un champ non-homogène : le champ vertical a une valeur de 0.5 T dans la région centrale et décroît rapidement vers zéro en dehors de son ouverture nominale.

Chapitre 3 : Reconstruction des traces dans la TPC

Le logiciel de simulation et d'analyse (« software ») de l'expérience est basé sur la programmation orientée objet et les programmes ont été implémentéss dans le langage C++. Dans cet environnement, le software est organisé en « packages », chacun avec un but défini dans un document des requêtes de l'utilisateur.

L'algorithme de reconstruction des traces dans la TPC peut être résumé en une série d'opérations :

1) les signaux de la TPC sont calibrés pour chaque pad de lecture, en fonction du temps et du gain du pad spécifique. Les canaux avec un seuil de bruit trop bas ou hors-service sont éliminés des données;
2) un algorithme de regroupement cherche les points contigus dans la TPC en trois dimensions;
3) un algorithme de correction corrige les erreurs de positions causées par les distorsions statiques;
4) un algorithme de reconnaissance de forme regroupe les points pour former une trace ;
5) un algorithme d'ajustement calcule les paramètres de l'hélice qui représente le mieux la trace pour déduire l'impulsion de la particule;
6) un algorithme d'ajustement calcule une seconde hélice en prenant en compte le vertex de production de la trace;
7) un algorithme de reconnaissance identifie le type de particule en utilisant le dE/dx ;
8) un algorithme de correction évalue la perte d'énergie de la particule lorsqu'elle traverse différents matériaux avant d'entrer dans le volume actif de la TPC.

Un programme de simulation de la TPC cherche à reproduire tous les phénomènes de physique liés à la génération des signaux dans la TPC pour comprendre les performances du détecteur. La simulation inclut la chaîne d'électronique, avec la numérisation, l'échantillonnage et la compression des données. La simulation est conçue pour produire des données sous le même format que les données brutes.

Chapitre 4 : La calibration de la TPC

La calibration de la TPC est nécessaire pour améliorer les performances du détecteur et pour corriger certains défauts. Ces derniers peuvent changer la trajectoire des électrons produits par ionisation et donc induire une mauvaise reconstruction des paramètres cinématiques des particules.

Les deux premières étapes da la calibration sont l'évaluation de la vitesse de dérive des électrons dans le gaz de la TPC et la calibration en temps des signaux. L'évaluation de la vitesse de dérive et la calibration en temps sont fondamentales pour déterminer la position longitudinale des particules qui traversent la chambre. Une calibration supplémentaire du temps pour chaque pad est nécessaire pour corriger une imprécision de la chaîne d'électronique qui cause une déplacement en temps des signaux de 100 ns pour 30% des pads.

La réponse des pads et de leur chaîne d'électronique ne s'est révélée constante ni dans le temps ni d'un pad à l'autre. C'est pourquoi des méthodes ont été développées pour caractériser le comportement de l'électronique, pour suivre les variations de la réponse dans le temps et pour égaliser la réponse des différents pad.

Pendant la prise de données, on a découvert qu'environ 50% des canaux de la chaîne de preamplification de l'électronique étaient mal isolés entre eux. Ceci était la cause de faux signaux (« cross-talk ») qui détériorent la résolution de la reconstruction des traces et donc la mesure de l'impulsion et de l'énergie des particules.

Les trajectoires reconstruites sont distordues par deux effets produits par une variation accidentelle du champ électrique de la TPC. Le premier, appelé distorsion statique, est constant dans le temps et a été reconnu comme étant lié à un décalage de 150 kV entre la tension de la cage électrique autour de la cible et la cage sur la surface interne de la chambre. L'étude de ce décalage a permis de déterminer une correction pour la trajectoire des traces. Le deuxième effet, appelé distorsion dynamique, varie avec le temps. Il montre une dépendance en fonction de la longueur du paquet de particules du faisceau (« spill ») et est sensible au réglage et aux caractéristiques du faisceau (par exemple, l'intensité ou l'alignement par rapport à la cible) et aux conditions de la prise de données. Cette distorsion est la cause des variations du comportement de la TPC au sein de chaque spill.

La chambre semble se charger pendant le spill, probablement à cause de la création d'ions positifs produits par le faisceau primaire. L'accumulation des ions dans la chambre augmente la composante perpendiculaire du champ électrique de dérive d'une façon non homogène et induit une distorsion dépendant de l'angle azimutal ϕ. Cet effet n'est pas présent en début de spill, et il est donc possible de sélectionner certains événements qui ne sont pas affectées par ces distorsions. Le rejet des événements sur la base de leur temps d'arrivée à l'intérieur du spill n'affecte pas l'efficacité générale du détecteur et n'a comme seule conséquence la diminution du nombre total d'événements disponibles pour l'analyse finale. L'augmentation de l'erreur statistique finale qui en résulte est largement compensée par la diminution de l'erreur systématique liée à l'incertitude introduite par les distorsions dynamiques.

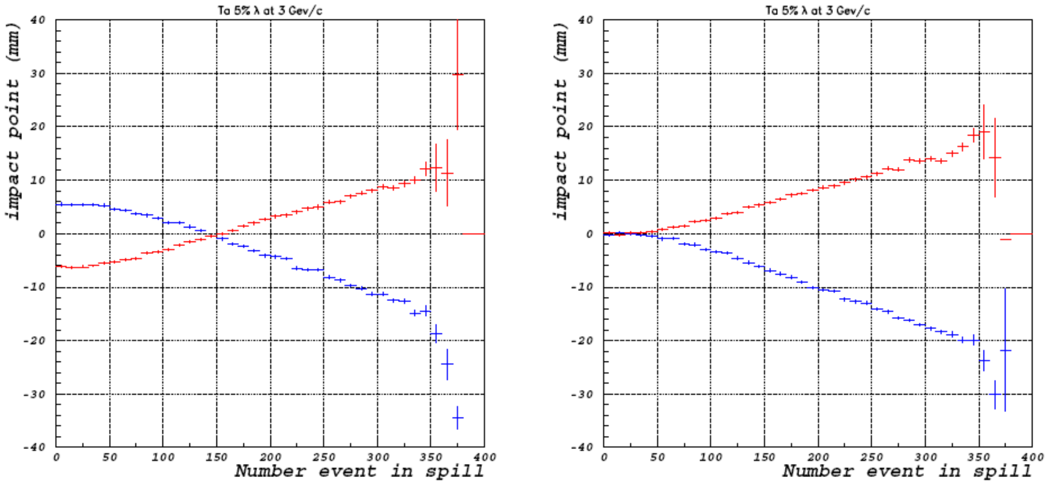

Figure 3 *La position moyenne du point d'impact pour les traces positives et négatives en fonction du nombre d'événements pendant le spill, sans correction des distorsions statiques (à gauche) et après la correction des distorsions statiques (à droite).*

Chapitre 5 : Les performances de la TPC

Les performances de la TPC peuvent être évaluées en analysant deux types de données: les données prises avec des rayons cosmiques et les données prises avec les cibles de production. L'évaluation des performances ouvre la possibilité de régler la simulation MonteCarlo du détecteur pour reproduire au mieux les données réelles.

Pour évaluer la résolution sur l'impulsion transverse on a utilisé les données des rayons cosmiques et on a comparé l'impulsion reconstruite des deux segments qui composent une trace. En revanche, la résolution sur l'impulsion totale est déterminée à partir des spectre de dE/dx obtenus avec une cible de Tantale: le dE/dx change d'une façon assez importante pour des petites variations de l'énergie pour des particules non ultra-relativistes. En sélectionnant différents intervalles de dE/dx on peut contrôler la qualité de la résolution sur l'impulsion. Pour comparaison, la résolution sur l'impulsion transverse peut aussi être déterminée à partir de la formule de Gluckstern en utilisant les informations relatives à la trace (le nombre de points, la longueur de la trace, la résolution des points), et la valeur du champ magnétique de la TPC.

L'étude des performances du détecteur est réalisée grâce à une simulation MonteCarlo. Les événements simulés sont sélectionnés si ils présentent seulement un pion positif dans la TPC (on rejette les événements dès que le pion se désintègre ou interagit avec la matière autourant la cible). L'efficacité est calculée comme le rapport entre le nombre de particules correctement reconstruites et le nombre de particules générées. L'efficacité est de 30% pour les particules de faible impulsion (< 100 MeV/c) à cause de l'importante perte d'énergie qu'elles subissent. Elle augmente rapidement jusque à atteindre un plateau à 85% au-delà de 250 MeV/c. Lorsqu'on exige également que le vertex soit correctement reconstruit, l'efficacité sature à 75% (Figure 4).

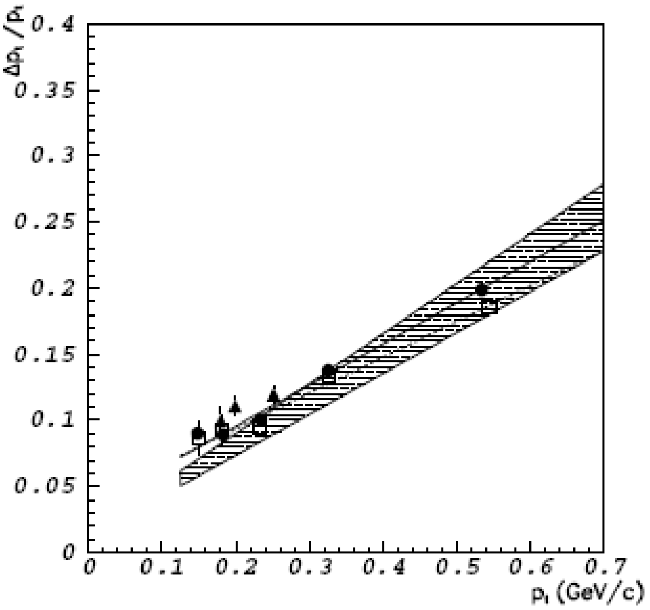

Figure 3 *La résolution sur l'impulsion transverse pour les données des rayons cosmiques (points noirs), sélectionnant des intervalles de dE/dx (triangle) et évaluée par la simulation MonteCarlo (bande gris).*

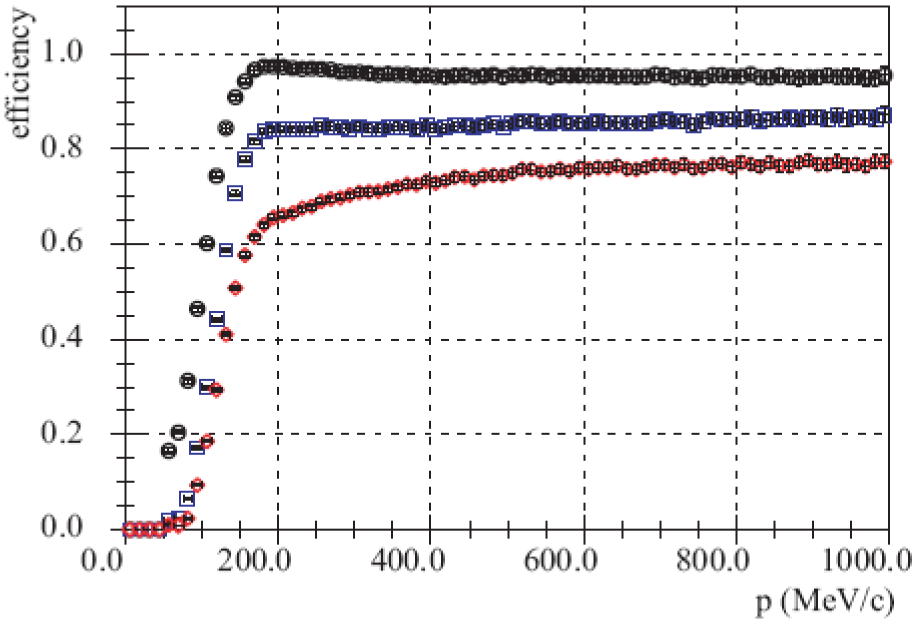

Figure 4 *Efficacité de reconstruction des pions en fonction de l'impulsion: exigeant une trace reconstruite (en noire), exigeant au moins 11 points et un bon ajustement (en bleu), exigeant également un bon ajustement du vertex (en rouge).*

L’identification des particules chargées (PID) dans la TPC est possible grâce à la mesure de la densité d’ionisation dans le gaz combinée à l’information sur l’impulsion totale de la particule.

Pour évaluer la perte d’énergie moyenne d’une particule qui traverse la TPC on détermine pour chaque point la perte d’énergie par unité de longueur (dE/dx) ou:

- dE est la perte d’énergie moyenne de la particule sur une distance dx ou le signal total détecté sur la surface des pads pour un ensemble des signaux sur une rangée de pads.
- dx est le segment de la trajectoire hélicoïdale d’une particule dans une rangée.

Le dE/dx est calculé comme une moyenne tronquée, en éliminant les 20% des valeurs les plus élevées, mais sans coupures pour éliminer les valeurs les plus faibles. La résolution sur le dE/dx est évaluée en sélectionnant des pions (ou des muons dans le cas des rayons cosmiques) avec une impulsion comprise entre 300 et 400 MeV/c. La résolution obtenue est de 19.8% pour les données du Tantale, 20.2% pour les données MonteCarlo et 13% pour les rayons cosmiques. Cette dernière valeur est compatible avec une amélioration de la résolution d’un facteur √2 dû au fait que les traces comptent deux fois plus de points dans le cas des rayons cosmiques.

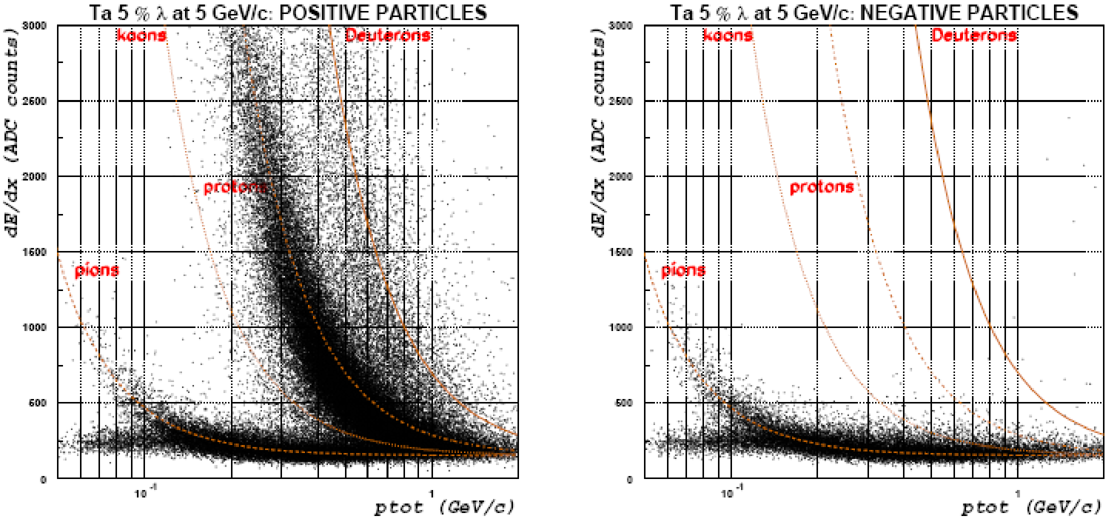

Figure 5 *Le spectre de dE/dx pour les particules positives (à gauche) et négatives (à droite) dans le cas de protons de 5 GeV/c frappant une cible de Ta 5%* λ_I.

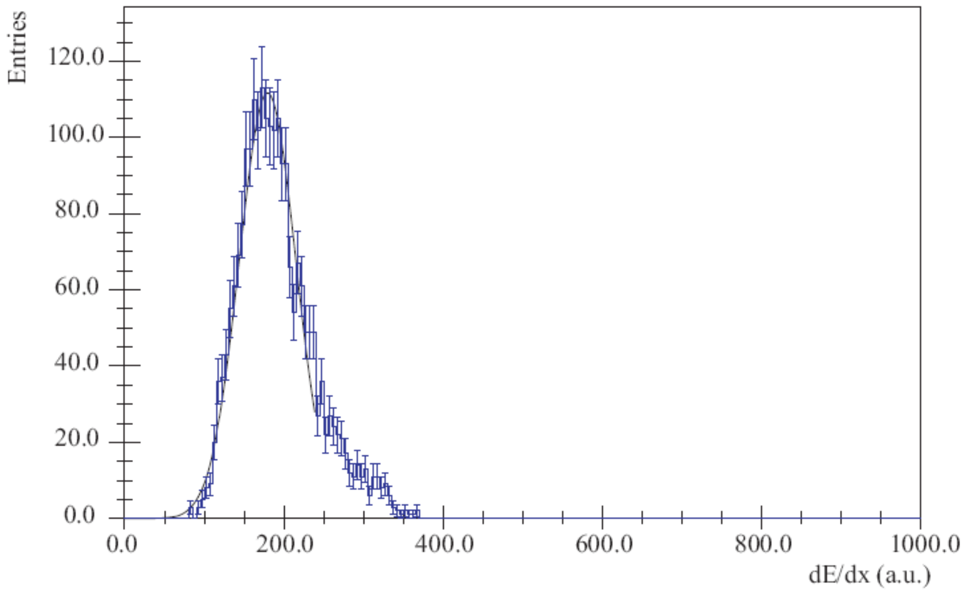

Figure 6 *La résolution sur le dE/dx pour les pions d'impulsion comprise entre 300 et 400 MeV/c dans le cas de protons de 5 GeV/c frappant une cible de Ta 5%* λ_I.

Chapitre 6 : Les réactions élastiques

Les réactions élastiques constituent un outil fondamental pour la calibration et la détermination des performances de la TPC. D'abord grâce au fait que les résultats sont déjà connus (parce que mesurés par d'autres expériences), mais aussi parce qu'elles présentent des contraintes cinématiques additionnelles et un état final bien défini.

La section efficace élastique représente entre10 % et 30% de la section efficace totale selon l'énergie du faisceau primaire et elle est bien connue. De plus, au moins la moitié de l'angle solide couvert par les produits est compris dans l'acceptance de HARP. Les données pertinentes ont été enregistrées avec des cibles d'hydrogène liquide et des faisceaux primaires de protons et des pions d'impulsion comprise entre 3 GeV/c et 14.5 GeV/c.

Les réactions élastiques

$$p + p \rightarrow p + p$$
$$\pi^{\pm} + p \rightarrow \pi^{\pm} + p$$

ont des propriétés cinématiques bien définies et la présence de seulement deux particules dans l'état final les rend particulièrement bien indiquées pour la calibration du détecteur. La particule primaire est identifiée à partir des détecteurs de temps de vol de la ligne de transfert. Une des deux particules produites par la réaction n'est pas mesurée dans la TPC à cause de son petit angle de production, par contre l'autre est bien détectée par la chambre. En utilisant seulement le spectromètre à grand angle il est possible d'évaluer la masse de la particule du faisceau déviée dans le spectromètre à petit angle, définie comme la masse manquante.

La cinématique des collisions élastiques des protons ou des pions sur l'hydrogène est totalement déterminée par la direction de la particule à petit angle. On peut évaluer la résolution sur l'impulsion, l'écart de l'impulsion mesurée par rapport à la valeur réelle et l'efficacité de la TPC en utilisant des événements avec une seule particule détectée dans le spectromètre à petit angle pour prédire l'impulsion et l'angle de la particule dans la TPC.

D'abord nous avons calculé la masse manquante (de la particule à petit angle) en utilisant la trace à grand angle en supposant qu'il s'agissait d'un proton. La distribution de la masse manquante (m_x^2) peut être obtenue à partir de la relation :

$$M_x^2 = (p_{\text{beam}} + p_{\text{target}} - p_{\text{TPC}})^2$$

où le p_{beam}, le p_{target} et le p_{TPC} sont les impulsions (4D) de la particule du faisceau, de la particule cible et de la particule diffusée au grand angle et mesurée dans le TPC, respectivement.

Les sections efficaces mesurées sont (Figure 7) :

$$\sigma_{pp \to pp} = 6.8 \pm 4\%\ mb (6.1 \pm 4\%\ mb)$$

$$\sigma_{\pi p \to \pi p} = 2.9\ mb \pm 4\%$$

où 4% est l'erreur statistique et les deux valeurs correspondent aux deux approches différentes utilisées pour l'ajustement de la masse manquante. Cette mesure est en accord avec la mesure précédente au niveau de l'erreur systématique de ±6%.

La mesure de la section efficace confirme la bonne compréhension de tous les ingrédients requis pour l'analyse: l'identification des particules, le calcul des différentes efficacités, l'identification des particules du faisceau primaire, la normalisation absolue en utilisant des événements avec un minimum de biais. En plus, cette mesure permet la détermination de l'écart de l'impulsion mesuré par rapport à la valeur réelle, en particulier en fonction des événements à l'intérieur du spill.

L'efficacité peut être comparée à celle déterminée par la simulation MonteCarlo. A partir des données à 5 GeV/c, l'efficacité de reconstruction des traces obtenue est de 91% ± 1%. L'efficacité estimée à partir de la simulation est de 93%. L'efficacité à 8 GeV/c est sensiblement la même qu'à 5 GeV/c. Dans ces données une différence d'environ 1% peut être attribué aux canaux affectés par un problème intermittent de connexion, un effet non simulé à Monte Carlo. L'inefficacité est dominée par l'effet des « spokes », comme l'indique la Figure 8.

En résumé, l'efficacité de reconstruction des traces a été déterminée par la simulation comme dans les données avec moins de 2% de différence: ceci justifie l'utilisation de la simulation de déterminer l'efficacité de détection des pions.

L'étude des collisions élastiques a également permis d'évaluer que l'erreur sur la mesure de l'impulsion est inférieure à 5%. Nous avons établi que les distorsions dynamiques produisent une polarisation dépendant du nombre d'événement dans le spill qui peut être déterminée par une étude de la distribution du d_0 . L'effet de ces distorsions est rendu négligeable en appliquant une coupure appropriée sur le numéro de l'événement dans le spill.

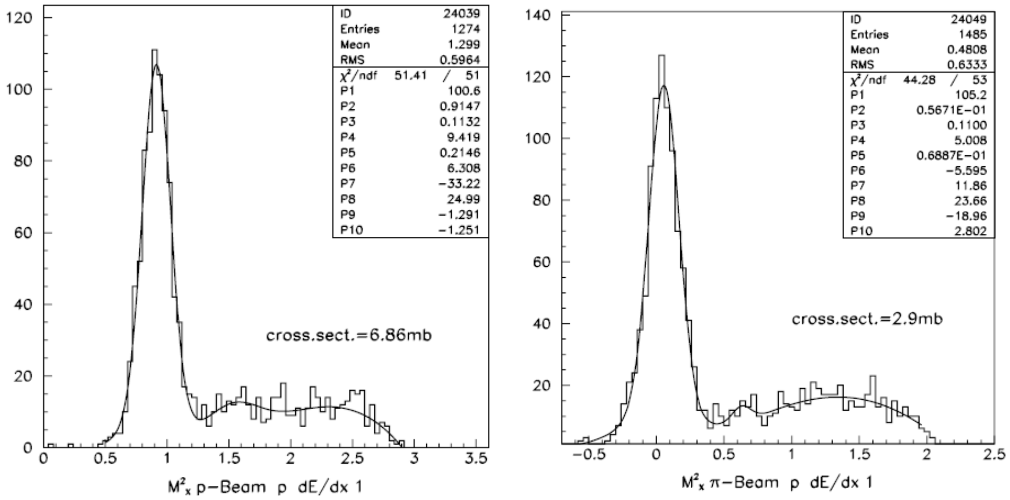

Figure 7 *La masse manquante de la particule à petit angle pour un faisceau de protons (à gauche) et un faisceau de pions (à droite).*

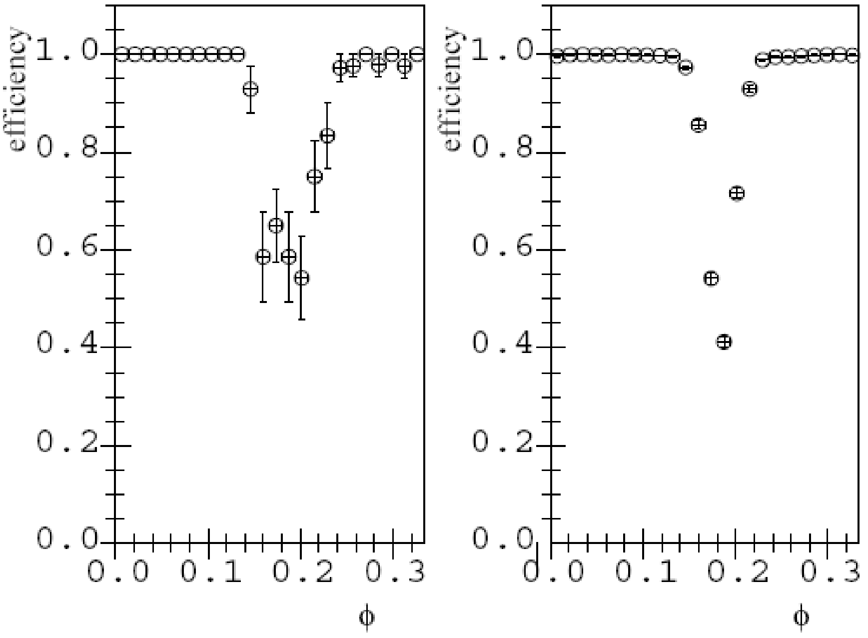

Figure 8 *L'efficacité en fonction de l'angle azimuthal φ dans les « spokes » entre les secteurs du plan de pads de la TPC pour les données de 5 GeV/c p-H, mesurée à partir des événements élastiques. Le panneau gauche montre l'efficacité pour les données, le panneau droit pour la simulation.*

Chapitre 7: La mesure de la section efficace doublement différentielle pour la production de pions chargés par de protons d'impulsion égale à 5 GeV/c qui interagissent dans une cible de Ta.

Ce chapitre décrit la mesure de la section efficace doublement différentielle pour la production de pions chargés par de protons avec une impulsion de 5 GeV/c qui interagissent dans une cible de Ta. Les intervalles d'impulsion et d'angle couverts par l'expérience sont fondamentaux pour la conception d'une usine à neutrinos. Un système élaboré de détecteurs dans la ligne du faisceau primaire détermine le type de particule primaire. Les particules produites par l'interaction avec des cibles différentes sont possible grâce à la TPC pour la reconstruction des traces, la détermination du type des particules secondaires et la mesure de l'impulsion.

Cette analyse représente la motivation la plus importante pour l'expérience HARP: la mesure des taux de production de pions positifs et négatifs pour la conception d'une usine à neutrinos. Les variables qui contrôlent la production des pions sont: l'énergie du faisceau primaire des protons et le matériau et la géométrie de la cible (longueur et rayon). Pour optimiser le flux des pions qui pourraient être acceptés par une usine à neutrinos il faut mesurer le taux de production des pions dans différentes conditions.

La Figure 9 montre l'acceptance de l'expérience couverte par les spectromètres à petit et grand angle. Si le spectromètre à petit angle est nécessaire pour les expériences courantes qui utilisent des neutrinos produits d'une façon classique, c'est le détecteur à grand angle qui couvre la partie cinématique pertinente pour une usine à neutrinos.

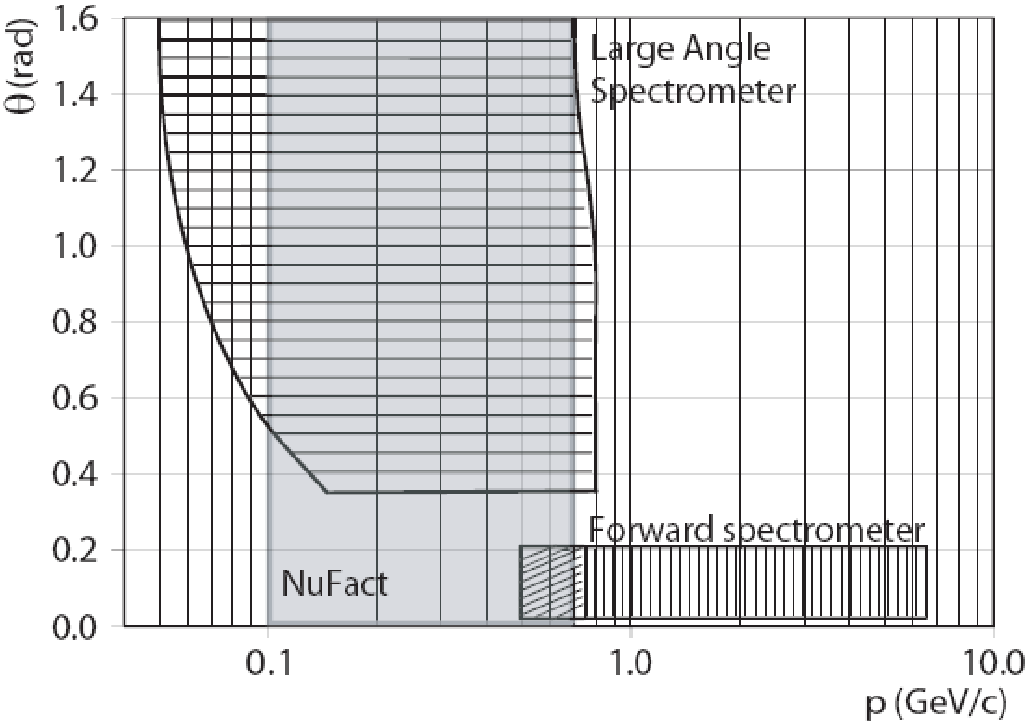

Figure 9 *L'acceptance de l'expérience HARP couverte par les spectromètres à petit et grand angle.*

Cette analyse décrit la section efficace doublement différentielle pour la production de pions positifs et négatifs à grand angle (0.35 rad < θ < 2.15 rad) par rapport à la direction des protons primaires à 5 GeV/c interagissant sur une cible de Ta mince (5% d'une longueur d'interaction nucléaire).

La section efficace doublement différentielle est :

$$\frac{d^2\sigma_\alpha}{dp_i d\theta_j} = \frac{1}{N_{\text{pot}}} \frac{A}{N_A \rho\, t} M^{-1}_{ij\alpha i'j'\alpha'} \cdot \left(N^{\alpha'}_{i'j'}(T) - N^{\alpha'}_{i'j'}(E) \right)$$

- $N^{\alpha'}_{i'j'}$ est le nombre de particules d'observées autour des valeurs $p_{i'}$ et $\theta_{j'}$; le terme T se refère aux données prises avec la cible de Tantale et le terme E se rapporte aux données prises sans la cible.
- $M^{-1}_{ij\alpha i'j'\alpha'}$ corrige pour l'efficacité et la résolution du détecteur.
- le facteur $\frac{A}{N_A \rho\, t}$ est l'inverse du nombre de noyaux cibles par unité de surface.
- le résultat est normalisé au nombre de protons incidents sur la cible N_{pot}.

La Figure 10 résume les résultats obtenus.

En conclusion, nous avons montré que la TPC de HARP permet de mesurer les sections efficaces doublement différentielles avec la précision nécessaire pour la conception d'une usine à neutrinos.

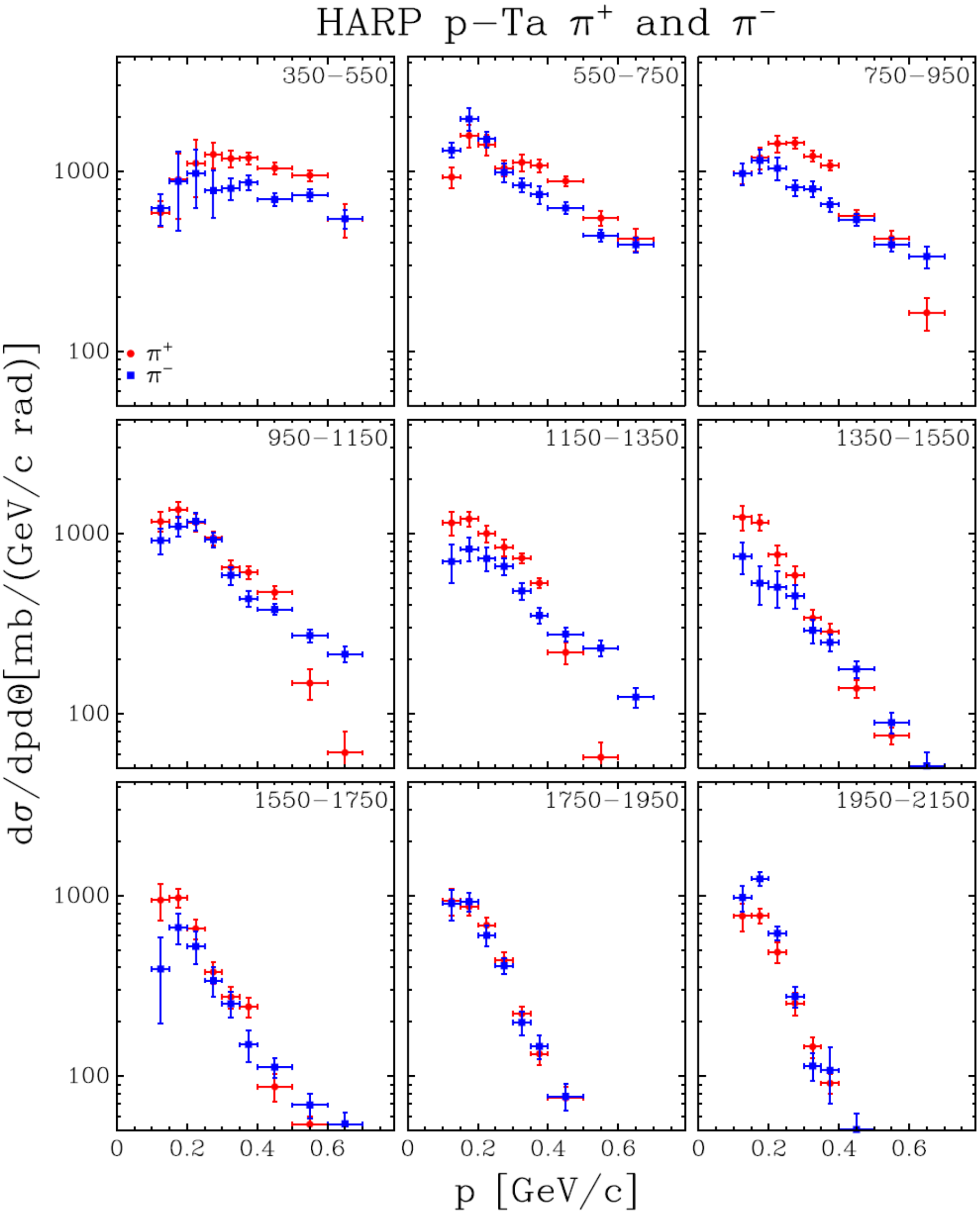

Figure 10 *La section efficace doublement différentielle pour la production de pions positifs et négatifs à grand angle (0.35 rad<θ<2.15 rad) par rapport à la direction des protons primaires à 5 GeV/c interagissant sur une cible de Ta mince (5% d'une longueur d'interaction nucléaire).*

Chapter 1

Neutrino physics

This chapter recalls the properties of neutrinos, and discusses the open questions and fascinating possibilities opened by the discovery that neutrinos have mass. Then it describes the relevance of the hadron production measurements in the context of the neutrino physics, in particular for the analysis of neutrino oscillation experiments of the present generation and for the optimization of future projects.

1.1 Introduction

Neutrinos were invented by Pauli to solve the problem of the electron spectrum emitted in beta decay, but his regret was the invention of a particle that could not be experimentally observed. At that time only alpha decay had been explained, since every element participating in the reaction was detected. Being a two-body decay, the energy of the alpha emitted is almost fixed. Instead in the beta decay the energy of the particle emitted and detected, the electron, has a continuous spectrum. This is impossible without admitting the presence of a third particle, which escapes detection: the 'neutron' invented by Pauli [1]. Today the neutron is the particle discovered by Chadwick [2] in 1932 and it is the partner of the proton as a constituent of the nucleus, while E. Fermi introduced the name of neutrino for Pauli's particle. The first (anti)neutrino was detected by F. Reines and C.L. Cowan in 1956 using as source the Savannah River nuclear reactor [3]. The exciting history of this particular particle had started, and even today reserves surprises. Nowadays, after 50 years of experimental neutrino physics an in spite of the Pauli's worries, the discovery of neutrino oscillations has opened a new era for physics beyond the Standard Model.

A number of intriguing questions are still waiting for an answer. Why are neutrino masses so small compared to those of other leptons? Why are the mixing angles so large compared to those of quarks? Is the fermion number conservation violated in the neutrino sector? Is there CP violation in the leptonic sector?

1.2 A 40 years long revolution in neutrino physics

In the last 40 years the neutrino physics has become one of the most active areas of research in particle physics. The most relevant revolution began in 1968 when Davis and his collaborators [4] reported their discovery of solar neutrinos: the first direct evidence for the nuclear reactions that power the sun (using a liquid tetrachlor ethene target deep underground). The solar neutrino flux measured was several times lower than the first calculations by John Bahcall [5] predicted–a discrepancy dubbed the "solar neutrino puzzle." The solutions proposed to solve this puzzle indicate two possible errors: the solar standard model (SSM) calculation could be wrong or the experimental results could be wrong, but both doubts have presently been ruled out. The SSM predicts perfectly the power emitted from the sun in form of visible light, which is produced by the same fusion processes generating neutrinos. The same SSM predicts also the vibration modes of the solar surface, again in agreement with the observations. The experiments described in the following ruled out the second possibility.

Then in 1998 Super-Kamiokande's atmospheric neutrino data [6] gave the first clear evidence for neutrino oscillation. The data exhibit a deficit of muon neutrinos and they are consistent with two-flavour $\nu_\mu \rightarrow \nu_\tau$ oscillations. Neutrino oscillation implies that neutrinos do have a mass and the finding that the mixing angle is large was completely unexpected. In analogy to the quark sector, the common belief was that if neutrinos mixed at all then the mixing angles should be small. The Super-Kamiokande result constitutes the first evidence for physics beyond the Standard Model. Also the evidence for oscillation in atmospheric neutrinos has been confirmed independently by K2K [7, 8], which is the first long baseline experiment.

In 2002 the solar neutrino puzzle was proven to be due to the neutrino properties and not by a lack of knowledge of the fusion processes in the Sun following the new results by SNO [9] and Kamland [10]. The fact that all the previous experiments measured only about a half of the predicted neutrino flux from the Sun is explained by their sensitivity only to ν_e and not to all neutrinos flavours. The neutral current data of SNO, a heavy water detector, yielded an independent determination of the total flux of active neutrinos from the Sun and in combination with other solar neutrino data proved that solar neutrinos undergo a flavour transition. Kamland, a scintillator oil detector, provided an independent check of the oscillation hypothesis by using reactor neutrinos and constrained the mixing parameters. The most natural explanations for these results are the neutrino oscillations [11].

All the existing data for neutrino oscillations with exception of LSND [12] can separately be analyzed in an effective two neutrino framework, *i.e.* the data do not indicate any genuine three flavour effects, in particular all data can be accommodated without any complex entries in the mixing matrix. The LSND experiment searched for muon anti-neutrino to electron anti-neutrino oscillations by the Liquid Scintillator Neutrino Detector at the Los Alamos Neutron Science Center using muon anti-neutrinos from positive muon decay at rest. However the LSND experiment observes evidence for neutrino oscillations. Its results indicate that there is a third mass splitting $\Delta m^2_{\rm LSND}$ in the range $0.2 - 10\,{\rm eV}^2$ [12]. On the other hand, the Karmen experiment [13] at the spallation neutron source ISIS [14], used $\bar{\nu}_\mu$ from μ^+–decay at rest in a search for neutrino oscillations $\bar{\nu}_\mu \bar{\nu}_e$ in the appearance mode. Its detection reaction of $\bar{\nu}_e$, p($\bar{\nu}_e$, e^+) excludes a large part of the parameter region claimed by LSND. In a combined analysis of both data sets there remains a combined allowed region [15]. The MiniBooNE experiment [16] will thoroughly test the results of LSND.

1.3 Neutrino physics

Neutrinos have always been considered as elusive particles. They have no electric charge and they interact only via weak currents, either charged or neutral, making their detection difficult. From existing experimental evidence, neutrinos are left handed particles while antineutrinos are right handed particles.

In the Standard Model there are three light neutrino eigenflavours (ν_e, ν_μ, ν_τ), as proven by the measurements at LEP by the Z peak shape fitting [17]. They form with the electron, the muon and the tau three leptonic $SU(2)_L$ weak doublets. The only way to identify the neutrino flavour is via a charged current weak interaction, in which the lepton partner can be identified. Somehow, neutrinos have no other identity than that transmitted by the lepton which appears when they are created or detected. Moreover this identity seems to be a quantity which is not conserved at different points in space or at different time. This can be considered the first clear experimental evidence that the Standard Model (SM), which is extremely successful in describing elementary particles and their interactions, is incomplete. It seems to be the correct description of the physics which can be observed at low energies but it is obvious from its structure that it cannot be correct up to the highest energies of the Plank scale, or even at energies accessible to the LHC. This has inspired many attempts to provide a convincing model for the physics beyond the Standard Model. These attempts strongly suffered from the fact that no deviation from the Standard Model had been found before the discovery of neutrino flavour transitions.

In the Standard Model, neutrinos are strictly massless, and thus can be described in a two-dimensional Hilbert space: left handed neutrino and its antiparticle. Massive neutrinos must be described by a four-dimension space, thus require the existence of two new particles, corresponding to the right handed neutrino and its antiparticle. Two terms appear in the Lagrangian that correspond to these massive particles. The first one

$$\mathcal{L}_\nu = m_D \left(\overline{\nu_L} N_R + \overline{N_R} \nu_L \right) \tag{1.1}$$

is similar to that for charged fermions and corresponds to the helicity-flip required by Lorentz Invariance for a massive particle. As for other fermions, this term can be generated by the Higgs vacuum expectation value, as $m_D = \lambda_\nu < v >$, with a surprising and unnatural value of the coupling λ_ν between 10^{-6} and 10^{-13} times smaller for neutrinos than for all other fermions.

Another term arises naturally for neutrinos, which corresponds to a neutrino-antineutrino transition. This term, called "Majorana mass term",

$$\mathcal{L}_\nu = m_D \overline{\nu_L} N_R + \frac{1}{2} m_R \overline{N_L^c} N_R + h.c.. \tag{1.2}$$

is forbidden for charged fermions, by virtue of electric charge conservation, but is perfectly possible for neutrinos which carry no electric charge. It cannot be generated by the Higgs mechanism, and requires a new physical mechanism. At this point one faces the following choice:

- Accept the unnaturally small value of the coupling and introduce a new conservation law, (e.g. fermion number conservation) for which there is no experimental proof, and accept the existence of light, right handed neutrinos which can neither be produced nor observed in any known interaction. This is the "Dirac neutrino hypothesis".

- Accept the possibility that there can be a transition between the neutrino and its anti-particle. In this case, the Yukawa coupling m_D need not be any different than that of other fermions, provided the right-handed neutrino is very massive, which explains its lack of observation. Such a scheme is provided naturally by the "seesaw" mechanism [18], in which the light neutrino mass is obtained by the overall diagonalization of the neutrino mass matrix (including the Majorana and Dirac mass terms) and obeys the relation:

$$m_\nu \simeq \frac{m_D^2}{m_R} \tag{1.3}$$

which gives a right handed neutrino mass of the order of 10^{10} to 10^{15} GeV, suggestingly close to the mass scale required by coupling unification in Grand Unified Theories.

Putting a typical fermion mass of $m_D = 100\,\mathrm{GeV}$ and $m_R = 10^{15}\,\mathrm{GeV}$ at the GUT scale yields a neutrino mass of order 0.01 eV. This value is close to the order of magnitude indicated by oscillations. In this scheme the smallness of neutrino masses apeears as a natural consequence of the heaviness of the right handed neutrino and neutrino masses become a probe of very high energy scales which may otherwise be not accessible. However, it turns out that it is far from trivial to construct a theory which can account for the observed mixing pattern, *i.e.* predict two large mixing angles. The seesaw mechanism is just one example and there are a plethora of other possibilities, but the introduction of heavy right handed neutrinos opens an appealing way to generate the baryogenesis asymmetry via leptogenesis [19]. Moreover it would be mandatory to understand the real nature of neutrinos, if they are Majorana or Dirac particles. The only process in which the real identity of the neutrino can be revealed is the neutrino-less double beta decay, a special beta decay in which two electrons are emitted but no neutrinos [20], [21]. This process occurs only if the transition between neutrinos and antineutrinos is possible, namely if neutrinos are Majorana particles.

1.3.1 Baryogenesis through leptogenesis

The observable Universe only contains matter and no anti-matter. This is a very surprising experimental fact since the initial conditions are thought to be symmetric with respect to matter and anti-matter. Baryogenesis aims at finding an explanation for the observed matter anti-matter asymmetry. Within the SM model it is in principle possible to create some asymmetry but the numerical value is far too small, as result of the small CP violation measured in the hadronic sector. For that reason this asymmetry points to physics beyond the SM. More surprisingly, the same new physics which is invoked to explain neutrino masses may be at the heart of baryogenesis. Assuming that the Universe was hot enough at some point in its history to keep N_R in thermal equilibrium there would have been a vast abundance of N_R. The N_R would have fallen out of equilibrium during the evolution and finally decay. This decay can be CP-violating and therefore produce a net lepton number

$$\Gamma(N_R \to LH) - \Gamma(N_R \to \overline{L}H^*) \neq 0. \tag{1.4}$$

where Γ is the branching ratio for the reaction. This lepton number later on can be converted to baryon number by processes that are naturally present in GUT, as the sphaleron [22].

1.3.2 Neutrino oscillations

The flavour changing process of neutrino oscillations is possible if the neutrino mass eigenstates, which describe the propagation in space, are different from the weak flavour eigenstates, which describe the weak interaction of neutrinos in the Standard Model.

At the time $t_0 = 0$, when a neutrino is created by weak interactions such as $W^\pm \to l^\pm_\alpha + \nu_\alpha(\bar{\nu}_\alpha)$ in a weak decay, it is produced in one of the possible flavour states ν_α $(\alpha = e, \mu, \tau)$, namely in a given mix of mass states ν_i $(i = 1, 2, 3)$, together with its lepton partner $l_\alpha(l_\alpha = e, \mu, \tau)$. A neutrino flavour state ν_α is hence expressed in terms of mass states in quantum mechanics as:

$$|\nu_\alpha\rangle = \sum_i U_{\alpha i}|\nu_i\rangle \tag{1.5}$$

where $|\nu_\alpha\rangle$ and $|\nu_i\rangle$ are quantum mechanical states and U is the mixing matrix, that is similar to what happens for quarks. Once the neutrino propagates, the mass states m_i $(i = 1, 2, 3)$ will evolve differently according to the Schrödinger equation since the masses are different, and will acquire different phases. At a distance L, where the detector is placed, or at the time $t > t_0$, the probability to observe a given flavour changes with time. Then the experiment identifies the neutrino flavour via the lepton of the same flavour of the neutrino produced by a weak interaction (see fig. 1.1 for a sketch of the oscillation process). The process of flavour transformation can be described

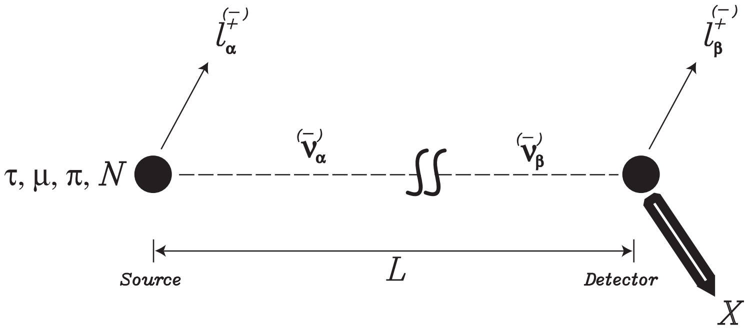

Figure 1.1: *Sketch of the neutrino production, propagation and detection.*

by neutrino oscillations as invented by Pontecorvo in 1969 [23].

The minimum number of mass states required to explain the observed oscillation pattern is three (m_1, m_2, m_3). In the standard scenario with 3 weak lepton doublets, the mass eigenstates ν_i and the flavour eigenstates ν_α are related via a 3×3 unitary mixing matrix U:

$$U = \begin{pmatrix} c_{12}c_{13} & s_{12}c_{13} & s_{13}e^{-i\delta} \\ -s_{12}c_{23} - c_{12}s_{23}s_{13}e^{i\delta} & c_{12}c_{23} - s_{12}s_{23}s_{13}e^{i\delta} & s_{23}c_{13} \\ s_{12}s_{23} - c_{12}c_{23}s_{13}e^{i\delta} & -c_{12}s_{23} - s_{12}c_{23}s_{13}e^{i\delta} & c_{23}c_{13} \end{pmatrix} \tag{1.6}$$

with $c_{ij} = \cos\theta_{ij}, s_{ij} = \sin\theta_{ij}$, θ_{ij} defined as the mixing angles, and δ a CP violating phase. Every weak neutrino eigenstate is hence a linear combination of the mass eigenstates according to:

$$|\nu_\alpha\rangle = \sum_i U_{\alpha i}|\nu_i\rangle \tag{1.7}$$

When the neutrino is created by a weak interaction at the point in space $\vec{x}_0$ its flavour state can be written as:

$$|\nu_\alpha\rangle = |\nu(\vec{x}_0, 0)\rangle \; = \; \sum_i U_{\alpha i}|\nu_i(\vec{x}_0, 0)\rangle \; = \; \sum_i U_{\alpha i}e^{i\vec{p}_i\cdot\vec{x}_0}|\nu_i\rangle \tag{1.8}$$

where p_i is the momentum associated to $|\nu_i\rangle$ in the laboratory frame.

The neutrino flavour state is defined by the lepton flavour produced in the weak interaction. In particular $|\nu_e\rangle$ is a neutrino generated either by a β decay such as

$$p \rightarrow n \; + \; \nu_e \; + \; e^+$$

or, in general for a nucleus A(Z,N), by:

$$A(Z, N) \rightarrow \; A(Z-1, N+1) \; + \; e^+ \; + \nu_e$$

A muon neutrino state $|\nu_\mu\rangle$ is produced by pion or muon decay:

$$\begin{aligned} \pi^+ \;\; &\rightarrow \;\; \mu^+ \; + \; \nu_\mu \\ \mu^+ \;\; &\rightarrow \;\; e^+ \; + \; \bar{\nu}_\mu \; + \; \nu_e \end{aligned}$$

Finally, a tau neutrino state $|\nu_\tau\rangle$ is produced by τ decays:

$$\begin{aligned} \tau^- \;\; &\rightarrow \;\; \nu_\tau \; + \; W^- \\ &\rightarrow \;\; \nu_\tau \; + \; e^- \; + \; \bar{\nu}_e \\ &\rightarrow \;\; \nu_\tau \; + \; \mu^- \; + \; \bar{\nu}_\mu \\ &\rightarrow \;\; \nu_\tau \; + \; hadrons \end{aligned}$$

The production of antineutrinos is obtained reversing the charges and transforming particles into their antiparticles in those processes.

After generation, the neutrino propagates to the new $\vec{x}$ position according to the Schrödinger equation*, and the previous state is multiplied by the time-evolution propagator:

$$|\nu(\vec{x},t)\rangle = \sum_i U_{\alpha i} e^{i\vec{p}_i\cdot\vec{x}} e^{-iE_i t}|\nu_i\rangle \tag{1.9}$$

with E_i the energy of the ν_i mass state.

As the neutrino masses do not exceed few eV, neutrinos can be always considered as ultrarelativistic particles, and the approximation $m_i \ll p_i$ for which:

$$E_i = \sqrt{m_i^2 + p_i^2} \approx\ p_i + \frac{m_i^2}{2p_i} \tag{1.10}$$

can be applied together with $t \approx x$. Due to Heisenberg uncertainty relation it is impossible to distinguish production of different neutrinos in neutrino production processes [24]. Let us consider as a further approximation that ν_α has been produced with a defined momentum p, and that all the mass eigenstates are supposed to have all the same momentum p but different energies.

Then the neutrino propagation state can be rewritten as:

$$|\nu(x)\rangle = \sum_i U_{\alpha i} e^{-i\frac{m_i^2}{2p}x}|\nu_i\rangle \tag{1.11}$$

Expressing a mass state in terms of flavour eigenstates β, one gets:

$$|\nu_i\rangle = \sum_\beta U^*_{\beta i}|\nu_\beta\rangle \tag{1.12}$$

and the propagated state $|\nu(x)\rangle$ becomes:

$$|\nu(x)\rangle = \sum_\beta \left[\sum_i U^*_{\beta i} U_{\alpha i} e^{-i\frac{m_i^2}{2p_i}x}\right]|\nu_\beta\rangle \tag{1.13}$$

The neutrino flavour ν_α, propagating to $\vec{x}$ as $|\nu(x)\rangle$, has become a combination of different neutrino flavour eigenstates $|\nu_\beta\rangle$. Considering a detector located at a distance $x = L$ from the neutrino source, the probability to find the neutrino of original flavour α to have the flavour β is:

$$P(\nu_\alpha \to \nu_\beta) = \left|A_{(\alpha\to\beta)}(L)\right|^2 \tag{1.14}$$

---

[*] Here and in the following $\hbar = c = 1$ and hence $t \approx x$.

where the amplitude $A_{(\alpha\to\beta)}(L)$ is:

$$A_{(\alpha\to\beta)}(L) = \langle\nu_\beta|\nu(x)\rangle \tag{1.15}$$

which is the usual collapse of a quantum-mechanics state into one of the eigenstates. Then the probability can be expressed as:

$$\begin{aligned} P(\nu_\alpha \to \nu_\beta) = {} & \delta_{\alpha\beta} \\ & - 4\sum_{i>j} Re\left(U_{\alpha i}U^*_{\beta i}U^*_{\alpha j}U_{\beta j}\sin^2\left(\frac{\Delta m^2_{ij}\,L}{4\,E}\right)\right) \\ & + 2\sum_{i>j} Im\left(U_{\alpha i}U^*_{\beta i}U^*_{\alpha j}U_{\beta j}\sin^2\left(\frac{\Delta m^2_{ij}\,L}{2\,E}\right)\right) \end{aligned} \tag{1.16}$$

where $\Delta m^2_{ij} = m_i^2 - m_j^2$ is the mass splitting between two mass eigenstates i and j and can be either positive or negative, E is the energy of the neutrino flavour α computed as the weighted average energy of the mass states [24]. From this formulation it is clear that neutrino oscillations exist only if

- all the masses are different and at least two of them are non-vanishing;
- the neutrino mixing matrix U has non diagonal elements different from zero.

In case of two-neutrino oscillation, the mixing matrix U can be rewritten in blocks of 2×2 matrices, obtaining:

$$U = \begin{pmatrix} 1 & 0 & 0 \\ 0 & c_{23} & s_{23} \\ 0 & -s_{23} & c_{23} \end{pmatrix} \begin{pmatrix} c_{13} & 0 & s_{13}e^{-i\delta} \\ 0 & 1 & 0 \\ -s_{13}e^{-i\delta} & 0 & c_{13} \end{pmatrix} \begin{pmatrix} c_{12} & s_{12} & 0 \\ -s_{12} & c_{12} & 0 \\ 0 & 0 & 1 \end{pmatrix} \tag{1.17}$$

The central submatrix contains the angle θ_{13}, which has been experimentally shown to be small, and it can be considered diagonal as first approximation. In this case the matrix U describes two rotations in two orthogonal planes (1,2) and (1,3) and the oscillation probabilities have a simplified expression. The oscillation probability $P(\nu_\mu \to \nu_e)$ is reduced to:

$$P(\nu_\mu \to \nu_e) = \sin^2(2\theta)\sin^2\left(\frac{\Delta m^2_{12}\,L}{4E}\right) \tag{1.18}$$

where $\Delta m^2_{12} = m_1^2 - m_2^2$. The oscillation formula can be rewritten in different units as:

$$P(\nu_\mu \to \nu_e) = \sin^2(2\theta)\sin^2\left(\frac{1.27\Delta m^2_{12}\,L}{E}\right) \tag{1.19}$$

with Δm^2_{12} expressed in eV^2, the distance L in km and the energy in GeV. The factor 1.27 comes from the re-introduction of $\hbar$ and c in the formulas, and $1/(4\hbar c) = 1.27\, GeV/(km\, eV^2)$. The experimental results are usually presented as plots on the plane Δm^2 versus $\sin^2(2\theta)$. The collection of pairs of those parameters, compatible with the observed data, describes the allowed regions of neutrino oscillation on this plane.

1.3.3 Experimental study of oscillations and of CP violation

The parameters Δm^2 and θ responsible for oscillations are fundamental constants like the electron mass or the Cabibbo angle. However, the baseline (L) and neutrino energy (E) can in principle be chosen by the experimental setup, according to the set of the oscillation parameter phase space to be investigated. The signature for the value of the mixing angle in an appearance experiment, *i.e.* an experiment which observes $P(\nu_\alpha \to \nu_\beta)$, is given by the height of the oscillation peak, which is also indicated by the vertical arrow in the left hand panel of Figure 1.2. The value of Δm^2 is given by the position of the oscillation peak as a function of the energy, which is shown as a horizontal arrow. For a disappearance experiment the oscillation peak becomes an oscillation dip as shown in the right hand panel of Figure 1.2.

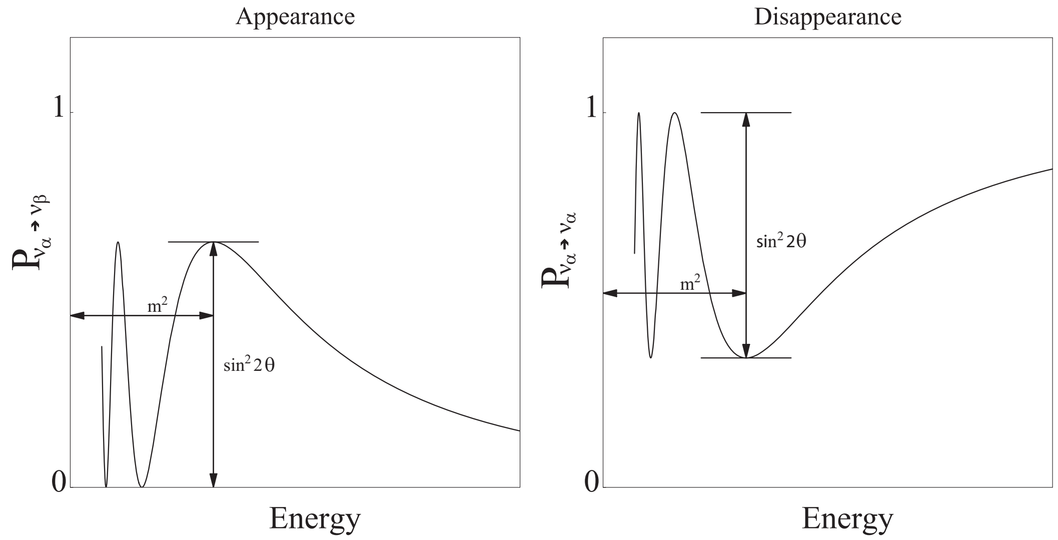

Figure 1.2: *The oscillation probability as a function of the energy in arbitrary units. The left hand panel shows the signature of the mixing angle θ (vertical arrow) and the one of the mass splitting Δm^2 (horizontal arrow) in the case of an appearance experiment, whereas the right hand panel shows the signatures in the case of a disappearance experiment.*

The depth of the dip is now the signature for the mixing angle as indicated by the vertical arrow. The position of the dip yields the value of the mass splitting and is indicated by the horizontal arrow.

For both kinds of experiments, appearance and disappearance, there can be a correlation between the measured values of Δm^2 and θ, *i.e.* an error on the determination of one parameter introduces an additional uncertainty on the other parameter. Furthermore an experiment needs to have enough energy resolution to clearly determine the position of the peak, otherwise the experiment sees an energy independent signal proportional to $\frac{1}{2}\sin^2 2\theta$. Another important factor for the determination of the mass splitting is the energy calibration of the detector – any error on the absolute energy scale directly translates into an error in the position of the oscillation peak or dip. The major difference between the two possible experiments is that an appearance experiment is much more sensitive to small values of θ, because the measurement is performed relative to zero, whereas a disappearance experiment measures relative to unity. This implies a different behaviour of the two types of experiments with respect to certain systematic errors. On the one hand, the level of background is crucial for an appearance experiment, since a large background reduces the sensitivity to small values of θ. On the other hand, the total normalization is vital for a disappearance measurement, because a large normalization error makes it impossible to detect deviations from unity.

A part from the oscillation parameters, future experiments could observe eventually CP violation in the oscillation process, namely:

$$P(\nu_\alpha \to \nu_\beta) - P(\bar{\nu}_\alpha \to \bar{\nu}_\beta) \neq 0 \tag{1.20}$$

In the full three flavour case, like in the quark sector, the size of this effect is proportional to the Jarlskog determinant matrices [25]:

$$J_{CP} = \frac{1}{8}\cos\theta_{13}\sin 2\theta_{13}\sin 2\theta_{23}\sin 2\theta_{12}\sin\delta \tag{1.21}$$

which implies that all non diagonal angles in the mixing matrix U have to be different from zero, all the flavours mix with the others.

The experimentally most suitable transition to study CP violation is $\nu_e \to \nu_\mu$ and $\nu_\mu \to \nu_e$, basically because there are techniques to produce beams of ν_μ or ν_e as well as detectors for them. In any case energies above the muon threshold are needed, which are only available in accelerator based experiments. A common tool to gain some insight into how CP effects are measured is the use of the so called CP asymmetry A_{CP}:

$$A_{CP} = \frac{P(\nu_\mu \to \nu_e) - P(\overline{\nu}_\mu \to \overline{\nu}_e)}{P(\nu_\mu \to \nu_e) + P(\overline{\nu}_\mu \to \overline{\nu}_e)} \tag{1.22}$$

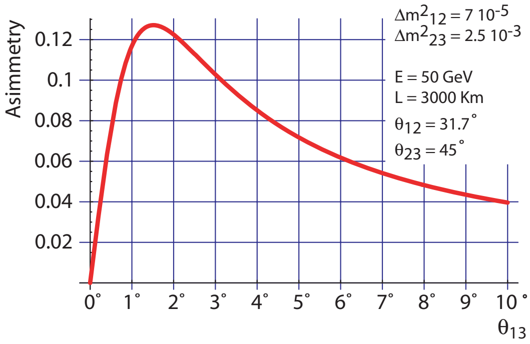

Figure 1.3: *The maximum value of the asymmetry as function of the angle* θ_{13} *for the Neutrino Factory. The oscillation parameters used are mentioned in the inset, for* $|\sin\delta| = 1$.

displayed in fig. 1.3, or the equivalent time reversal asymmetry A_T, supposing that CPT is conserved.

The asymmetry can be large and its value increases for decreasing values of θ_{13} up to the value when the two oscillations (solar and atmospheric) are of the same magnitude. This might pose a challenging issue on the experiment systematics and in any case it requires very large intensity beam.

1.3.4 Matter Effects

In many cases the propagation of neutrinos does not take place in vacuum but in matter. The influence of the passage through matter on the probability oscillation is known as matter effect or MSW effect (Mikheyev, Smirnov, Wolfenstein) [26]. Although the interaction of neutrinos with matter is tiny, matter can have a substantial impact on the oscillation probabilities. The weak interaction couples the neutrinos to matter and besides hard scattering events there is also coherent forward scattering in the same fashion as for visible light travelling through glass. The point is that the coherent forward scattering amplitudes are not the same for all neutrino flavours, since ordinary matter is made of particles of the first family and specifically does not contain muons or tau-leptons. All flavours have the same amplitude for neutral current reactions but the electron neutrinos have an additional contribution due to charged current reactions (see fig. 1.4). The electron (anti-)neutrino is the only one which can scatter coherently with the electrons in the matter via the charged current and this yields an additional contribution to the potential A for electron (anti-)neutrinos of

$$A = (-)2\sqrt{2}\, G_F\, N_e\, E\,, \tag{1.23}$$

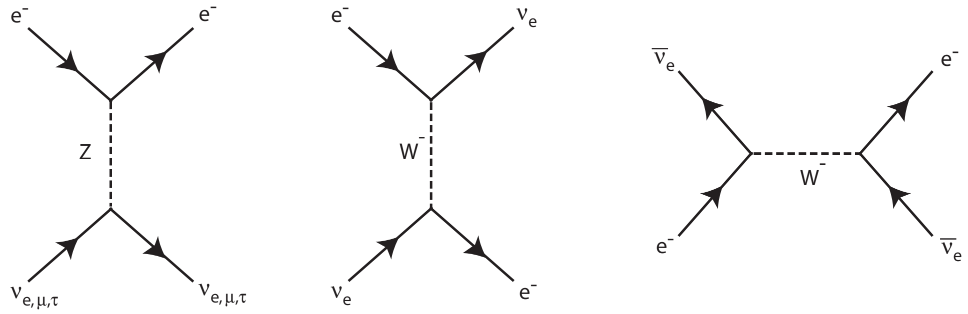

Figure 1.4: *Neutral current neutrino scattering (left) and charged current neutrino scattering (center) together with antielectron neutrino charged current interaction.*

where G_F is the Fermi coupling constant, N_e is the electron density and E is the neutrino energy. The minus sign is for anti-neutrinos.

For reasons of simplicity let consider only the 2 generation case, and take $|\nu_e >$ and $|\nu_\mu >$ as flavour states. The Schrödinger equation for neutrino propagation takes the matrix form of:

$$i\frac{d}{dt}\begin{pmatrix} \nu_e \\ \nu_\mu \end{pmatrix} = \begin{pmatrix} -\frac{\Delta m^2}{4E}\cos 2\theta + \sqrt{2}G_F N_e & \frac{\Delta m^2}{4E}\sin 2\theta \\ \frac{\Delta m^2}{4E}\sin 2\theta & \frac{\Delta m^2}{4E}\cos 2\theta \end{pmatrix}\begin{pmatrix} \nu_e \\ \nu_\mu \end{pmatrix} \tag{1.24}$$

after neglecting all the common phases and the phases coming from the neutral current which do not introduce a relative phase shift in the oscillation probabilities. The new mass eigenstates of the above propagation matrix can be expressed as a function of the flavour eigenstates as:

$$\begin{aligned} |\nu_1^{MSW} >= {} & \cos\theta_{MSW}|\nu_e > + \sin\theta_{MSW}|\nu_\mu > \\ |\nu_2^{MSW} >= {} & -\sin\theta_{MSW}|\nu_e > + \cos\theta_{MSW}|\nu_\mu > \end{aligned} \tag{1.25}$$

considering that the mixing angle θ_{MSW} is different from the vacuum mixing angle θ, and given by the equation, obtained diagonalizing the matrix of equation (1.24):

$$\sin^2 2\theta_{MSW} = \frac{\left(\frac{\Delta m^2}{4E}\right)^2 \sin^2 2\theta}{\left(\frac{\Delta m^2}{4E}\cos 2\theta - \sqrt{2}G_F N_e\right)^2 + \left(\frac{\Delta m^2}{4E}\right)^2 \sin^2 2\theta} \tag{1.26}$$

The oscillation probability takes the same form as the probability in vacuum:

$$P\left(\nu_e \to \nu_\mu\right) = \sin^2 2\theta_{MSW} \sin^2\left(\pi\frac{L}{\lambda_{MSW}}\right) \tag{1.27}$$

The mixing of neutrinos traversing the matter can be large even if it would be very small in vacuum, in particular, the maximum mixing can be reached when the condition:

$$\sqrt{2}G_F N_e = \frac{\Delta m^2}{4E}\cos\theta \tag{1.28}$$

is fulfilled. Since N_e is greater than zero, this condition can be realized only if $\Delta m^2 \cos\theta > 0$. This implies that, for a given mixing angle in vacuum, there is only one sign of Δm^2 which enhances the oscillation probabilities. Moreover, for antineutrinos, the matter induced potential changes sign. This is due to the fact that the antineutrino charged current interaction with electron occurs in the s channel and not in the t channel. Thus the condition to obtain the enhancement of the oscillation probability is opposite comparing the neutrino and antineutrino cases: the same Δm^2 cannot increase the oscillation probabilities for neutrino and antineutrinos at the same time. This has two consequences:

$$A_{CP} \neq 0 \tag{1.29}$$

even if $\delta = 0$, since the potential distinguishes neutrinos from anti-neutrinos. This has to be taken into account in the design of future long base line experiments whose aim would be to measure the CP violating phase of the mixing matrix.

The second consequence of the matter potential is that there can be a resonant conversion – the MSW effect. The condition for the resonance is

$$\Delta m^2 \simeq A \tag{1.30}$$

Obviously the occurrence of this resonance depends on the signs of both sides in this equation. Thus oscillation becomes sensitive to the mass ordering

	ν	$\bar{\nu}$
$\Delta m^2 > 0$	MSW	-
$\Delta m^2 < 0$	-	MSW

and the effect can be used to state the mentioned mass hierarchy.

The analysis of the MSW effect is, in fact, how the sign of the small mass difference Δm^2_{12} was determined, by comparison of the magnitude (and energy dependence) of solar neutrino disappearance, in which electron neutrinos from undergo important matter oscillations in the sun itself, with the disappearance observed in the KAMLAND experiment for which the effect is negligible.

1.4 Short summary of experimental results

1.4.1 Direct measurement of the neutrino mass

Direct laboratory limits on neutrino masses are obtained from kinematical studies. The most stringent current upper limit is that on the $\bar{\nu}_e$ mass, coming from the Mainz experiment measuring the end-point of the electron energy spectrum in Tritium beta decay [27]:

$$m_{\overline{\nu}_e} \leq 2.2 \text{ eV } (95\%\text{CL})$$

The Troitsk group has also published a similar limit [28]:

$$m_{\overline{\nu}_e} \leq 2.1 \text{ eV } (95\%\text{CL})$$

The proposed KATRIN experiment aims to improve the sensitivity to $m_{\bar{\nu}_e} \sim 0.3$ eV [29]. Similar sensitivities are the goal of the longer term MARE experiment [30] based on an array of several thousand of microbolometers.

Limits to neutrino masses come also from cosmology [31]: combining results from cosmic microwave an isotropies, supernovae surveys, galaxy clustering and Lyman α cloud absorption power, limits on the sum of the neutrino masses of the order of 1 eV can be derived.

1.4.2 Oscillation experiment results

The current experimental status for neutrino oscillation can be summarized in the following points [32]:

- the atmospheric neutrino anomaly (the lack of solar neutrinos ν_e) has been clarified by Super-Kamiokande. ν_μ oscillates into ν_τ and not into ν_e. The mixing angles θ_{23} is large $\approx 45°$ and $\Delta m^2_{23} \approx 2.7\, 10^{-3} eV^2$;

- the solar neutrinos puzzle has been solved by SNO and Super-Kamiokande. ν_e oscillate into $\nu_x (x = \mu$ or $\tau)$, the angle θ_{12} is large $\approx 32°$ (LMA, Large Mixing Angle, solution with MSW is preferred) and $\Delta m^2_{12} \sim 710^{-5} eV^2$;

- the angle θ_{13} is not larger than 10° as measured by CHOOZ [33]. However this value is only an upper limit, and the lower limit could be zero.

The measurements of two oscillation parameters, θ_{13} and the CP violating phase δ, require a new powerful neutrino source: as a Neutrino Factory.

1.5 Present and future generation of long baseline experiment

Over[†] the next five years new results are expected from the present generation of oscillation experiments at accelerators with long-baseline ν_μ beams (table 1.1), K2K at KEK [35], MINOS [36] at the NuMI beam from FNAL [37] and OPERA [38] at the CNGS beam from CERN [39]. These experiments are expected to confirm the atmospheric evidence of oscillations and measure $\sin^2 2\theta_{23}$ and $|\Delta m^2_{23}|$ within $10-15$ % of accuracy if $|\Delta m^2_{23}| > 10^{-3}$ eV^2. The K2K and MINOS experiments are looking for neutrino disappearance, by measuring the ν_μ survival probability as a function of neutrino energy while OPERA will search for evidence of ν_τ interactions in a ν_μ beam, the final proof of $\nu_\mu \rightarrow \nu_\tau$ oscillations. The K2K experiment completed data taking at the end of 2004 and MINOS started data taking at the beginning of 2005. CNGS is expected to start operations in the second half of 2006.

Table 1.1: *Main parameters for present long-baseline neutrino beams*

Neutrino facility	Proton momentum (GeV/c)	L (km)	E_ν (GeV)	pot/yr (10^{19})
KEK PS	12	250	1.5	2
FNAL NuMI	120	735	3	20÷ 34
CERN CNGS	400	732	17.4	4.5÷ 7.6

In all these facilities conventional muon neutrino beams are produced through the decay of π and K mesons generated by a high energy proton (few kW power) beam hitting light needle-shaped targets. Positive (negative) mesons are sign-selected and focused (defocused) by large acceptance magnetic lenses into a long evacuated decay tunnel where ν_μ's ($\overline{\nu}_\mu$'s) are generated. In case of positive charge selection, the ν_μ beam has typically a contamination of $\overline{\nu}_\mu$ at a few percent level (from the decay of the residual π^-, K^- and K^0) and $\sim 1\%$ of ν_e and $\overline{\nu}_e$ coming from three-body $K^\pm$, K^0 decays and μ decays. The precision on the evaluation of the intrinsic ν_e to ν_μ contamination is limited by the knowledge of the π and K production in the primary proton beam target. Hadron production measurements at 400 GeV/c and 450 GeV/c performed with the NA20 [40] and SPY [41] experiments at the CERN SPS provided results with $5-7\%$ intrinsic systematic uncertainties.

[†] Material for this Section is mainly taken from ref. [34].

The K2K experiment is designed to measure neutrino oscillations using a man-made beam with well controlled systematics, with the proposal of complementing and confirming the measurement made with atmospheric neutrinos. The KEK to Kamioka long-baseline neutrino oscillation experiment (K2K) [35] uses an accelerator-produced beam of nearly pure ν_μ with a neutrino flight distance of 250 km to probe the same Δm^2 region as the one explored with atmospheric neutrinos. The neutrinos are measured first by a series of detectors located approximately 300 meters from the proton target and then by the SuperKamiokande (SK) detector 250 km away. Neutrino oscillation, mostly $\nu_\mu \to \nu_\tau$, causes both a suppression in the total number of ν_μ events observed at SK and a distortion of the measured energy spectrum compared to that measured at the production point. Therefore, all of the beam-induced neutrino events observed within the fiducial volume of SK are used to measure the overall suppression of flux. If the neutrino interaction which takes place at SK is a charged-current quasi-elastic ($\nu_\mu + n \to \mu + p$), the incoming neutrino energy can be reconstructed using two-body kinematics, and the spectral distortion studied. At the energy of the K2K experiment, typically only the muon in this reaction is energetic enough to produce Cherenkov light and be detected at SK, but kinematics of the muon alone is enough to reconstruct the energy for these events. The effects of neutrino oscillation appear as a reduction in the number of neutrino events and a distortion of the neutrino energy spectrum in SK. The observations for these quantities are compared to their expectations in SK as measured by a near detector or predicted by a Monte Carlo. The near detector (ND) measures the neutrino flux and spectrum before neutrinos oscillate. Those measurements are then extrapolated at the far detector using the far-to-near (F/N) flux ratio, to predict the number of neutrino events and energy spectrum in SK. The neutrino flux can be predicted at any distance from its source when the geometry of the decay volume and the momenta and directions of the pion parents of neutrinos are provided. Due to the finite size of the decay volume and the detectors, the neutrino flux does not simply obey an L^{-2} rule (where L is distance from the neutrino source); rather the flux ratio between far and near detectors has some dependence on neutrino energy. Therefore, we define the F/N flux ratio, $R^{F/N}$, as

$$R^{F/N} = \frac{\Phi^{SK}(E_\nu)}{\Phi_{ND}(E_\nu)}$$

where $\Phi^{SK(ND)}(E_\nu)$ is the neutrino energy spectrum at SK (ND).

The final K2K results show allowed regions in the neutrino oscillation parameter space, corresponding to the 68%, 90% and 99% confidence levels (CL) (see fig. 1.5). The probability that the observations are explained by no

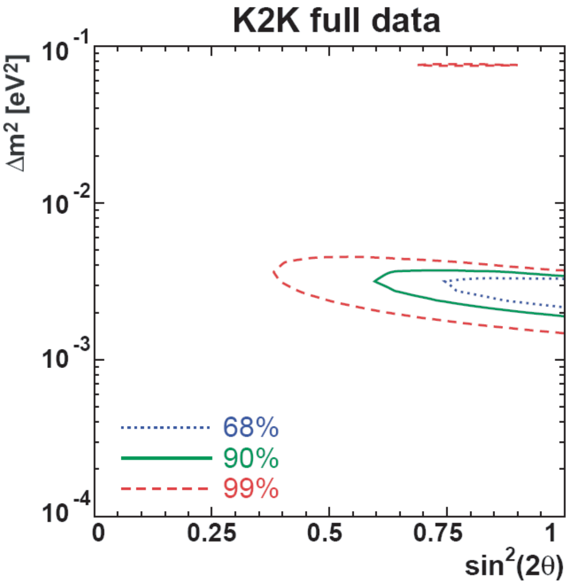

Figure 1.5: *Allowed regions of oscillation parameters. Three contours correspond to the 68% (dotted line), 90% (solid line) and 99% (dashed line) CL. allowed regions, respectively [42].*

neutrino oscillation is 0.0015% (4.3 σ). In a two flavour oscillation scenario (only $\nu_\mu \rightarrow \nu_\tau$, considered neglecting the $\nu_\mu \rightarrow \nu_e$), allowed Δm^2 region at $\sin^2 2\theta = 1$ is between 1.9 and $3.5 \times 10^{-3} eV^2$ at the 90 % C.L. with a best-fit value of $2.8 \times 10^{-3} eV^2$ [42].

The main goal of the MiniBooNE experiment is to unambiguously confirm or refute the evidence for $\bar{\nu}_\mu \rightarrow \bar{\nu}_e$ oscillations reported by the LSND experiment. The outcome of this crosscheck is important since the LSND result is incompatible with the simplest three-neutrino mixing paradigm based upon the robust evidence for solar and atmospheric oscillations, and its confirmation by MiniBooNE would have a profound impact on the understanding of neutrinos. The MiniBooNE neutrino beam is a high-intensity, conventional neutrino beam produced via the decay of mesons and muons in a 50 m long decay region following the target hall, where meson production and focusing occurs. Mesons are produced in the interactions of 8 GeV protons from the Fermilab Booster accelerator in a thick beryllium target, and then focused by a magnetic horn surrounding the target. The decay region is instrumented with a spectrometer and range stack detector (little muon counter, LMC) to measure muons from kaon decays. It is estimated that the large sample of neutrino interactions detected at MiniBooNE will allow the coverage of the full LSND 90% C.L. allowed region at 4σ significance. In the case of a confirmation of the LSND signal, MiniBooNE will also provide a rough determination of the mass and mixing parameters responsible for neutrino oscillations.

Other experiments are starting to test oscillations, in particular $\nu_\mu \rightarrow \nu_\tau$, at even longer distances.

The NuMI [37] project uses neutrinos from the decay of pions and kaons produced by the Fermilab Main Injector (MI), a 120 GeV proton synchrotron. The expected number of protons on target is $3.6\ 10^{20}$/y. The detector of this experiment is located in the Soudan mine at a distance of 730 km from the proton target.

The MINOS [36] experiment (Main Injector Neutrino Oscillations Search) uses two detectors, a near one at Fermilab and another built at the Soudan site. Both detectors are iron-scintillator sandwich calorimeters with a magnetic field in the iron plates. A comparison of the fluxes measured by the two detectors will be sensitive to neutrino oscillations.

The CNGS project consists in a neutrino beam from the CERN 450 GeV SPS to the LNGS (Laboratori Nazionali del Gran Sasso, Italy) at a distance of 732 km [39].

The Double-Chooz experiment [43] aims at improving the current knowledge on θ_{13} by observing the disappearance of $\bar{\nu}_e$ from nuclear reactors. The disappearing probability is

$$P(\bar{\nu}_e \rightarrow \bar{\nu}_e) \simeq 1 - \sin^2 2\theta_{13} \sin^2 \left(\frac{\Delta m^2_{31} L}{4E} \right) + \ldots \tag{1.31}$$

which does not depend on θ_{23} and the CP-phase δ_{CP} and Δm^2_{21} and θ_{12} give a second order contribution for the short baseline chosen of 1.05 km. Therefore this approach allows a unambiguous detection of θ_{13} free of correlations and degeneracies. Double-Chooz will employ a near, at ~200 m, and far, at 1.05 km, detectors to control at best the absolute flux, which limited in the past the sensitivity of this kind of experiments. Both detectors will be based on a Gadolinium loaded liquid scintillator and use inverse β-decay and the delayed neutron capture signal. Both detectors will have a fiducial mass of each 10.16 t. The sensitivity after 5 years of data taking will be $\sin^2 2\theta_{13} = 0.02$ at 90% CL [43], which could be achieved as early as 2012 (see fig. 1.6). Use a larger, second cavern to place a 200 t detector is conceivable, to reduce bound to $\sin^2 2\theta_{13} < 0.01$ [44].

The T2K (Tokai to Kamioka) experiment [45] will aim neutrinos from the Tokai site to the Super-Kamiokande detector 295 km away. The neutrino beam is produced by pion decay from a horn focused beam, with a system of three horns and reflectors. The decay tunnel length (130 m long) is optimized for the decay of 2-8 GeV pions and short enough to minimize the occurrence

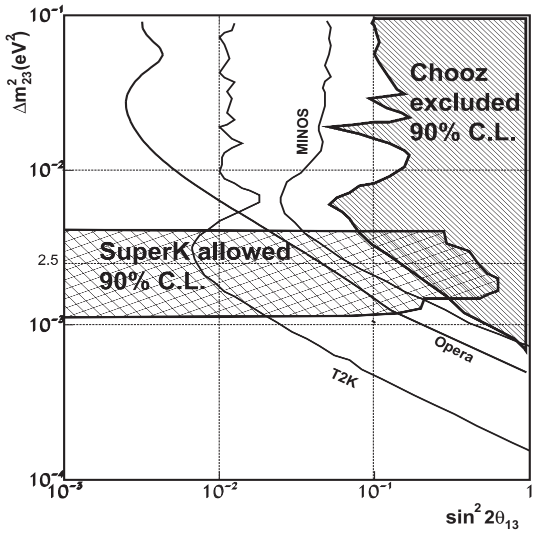

Figure 1.6: *Expected sensitivity on θ_{13} mixing angle (matter effects and CP violation effects not included) for MINOS, OPERA and for the next T2K experiment [45], compared to the CHOOZ exclusion plot [34]*

of muon decays. The neutrino beam is situated at an angle of 2-3 degrees from the direction of the Super-Kamiokande detector, assuring a pion decay peak energy of 0.6 GeV. The beam line is equipped with a set of dedicated on-axis and off-axis detectors at the distance of 280 meters. The main goals of the experiment are as follows:

1. The highest priority is the search for ν_e appearance to detect subleading $\nu_\mu \rightarrow \nu_e$ oscillations. It is expected that the sensitivity of the experiment in a 5 years ν_μ run, will be of the order of $\sin^2 2\theta_{13} \leq 0.006$ [45].

2. Disappearance measurements of ν_μ. This will improve measurement of Δm^2_{23} down to a precision of a 0.0001 eV^2 or so. The exact measurement of the maximum disappearance is a precise measurement of $\sin^2 2\theta_{23}$. These precision measurements of already known quantities require good knowledge of flux shape, absolute energy scale, experimental energy resolution and of the cross-section as a function of energy. They will be crucial to measure the tiny $\nu_\mu \rightarrow \nu_e$ oscillations [46, 47].

3. Neutral current disappearance (in events tagged by π^0 production) will allow for a sensitive search of sterile neutrino production.

The T2K experiment is planned to start in 2009 with a beam intensity reaching 1 MW beam power on target after a couple years, see fig. 1.7. It

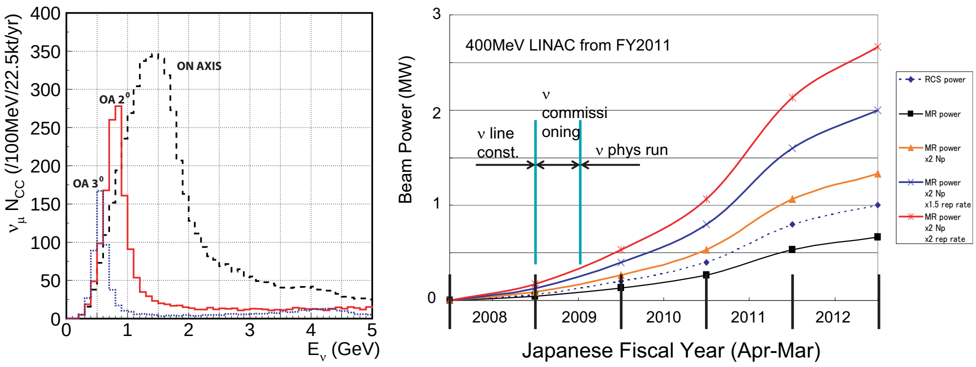

Figure 1.7: *Left: T2K neutrino beam energy spectrum for different off-axis angle θ. Right: expected evolution of T2K beam power as function of time. Baseline option is the second lowest solid curve.*

has an upgrade path which involves: a 2 km near detector station featuring a water Čerenkov detector, a muon monitor and a fine grain detector (possibly liquid argon). The phase II of the experiment, often called T2HK, foresees an increase of beam power up to the maximum feasible with the accelerator and target (4 MW beam power), antineutrino runs, and a very large water Čerenkov (HyperKamiokande) with a rich physics programme in proton decay, atmospheric and supernova neutrinos and, perhaps, leptonic CP violation, that could be built around in about 15-20 years from now.

The NOνA experiment with an upgraded NuMI Off-Axis neutrino beam [48] ($E_\nu \sim 2$ GeV and a ν_e contamination lower than 0.5%) and with a baseline of 810 km (12 km Off-Axis), has been recently proposed at FNAL with the aim to explore the $\nu_\mu \to \nu_e$ oscillations with a sensitivity 10 times better than MINOS. If approved in 2006 the experiment could start data taking in 2011. The NuMI target will receive a 120 GeV/c proton flux with an expected intensity of $6.5{\cdot}10^{20}$ pot/year ($2{\cdot}10^7$ s/year are considered available to NuMI operations while the other beams are normalized to 10^7 s/year). The experiment will use a near and a far detector, both using liquid scintillator (TASD detector). In a 5 years ν_μ run, with 30 kton active mass far detector, a sensitivity on $\sin^2 2\theta_{13}$ slightly better than T2K, as well as a precise measurement of $|\Delta m^2_{23}|$ and $\sin^2 2\theta_{23}$, can be achieved. NOνA can also allow to solve the mass hierarchy problem for a limited range of the $\delta_{\rm CP}$ and sign(Δm^2_{23}) parameters [48].

As a second phase, the new proton driver of 8 GeV/c and 2 MW, could increase the NuMI beam intensity to $17.2 \div 25.2 \cdot 10^{20}$ pot/year, allowing to improve the experimental sensitivity by a factor two and to initiate the experimental search for the CP violation.

1.6 SuperBeam

According to the present experimental situation, conventional neutrino beams can be improved and optimized for the $\nu_\mu \to \nu_e$ searches. The design of a such new SuperBeam facility for a very high intensity and low energy ν_μ flux will demand:

- a new higher power proton driver, exceeding the megawatt, to deliver more intense proton beams on target;
- a tuneable L/E_ν in order to explore the Δm^2_{23} parameter region as indicated by the previous experiments with neutrino beams and atmospheric neutrinos;
- narrow band beams with $E_\nu \sim 1 \div 2$ GeV;
- a lower intrinsic ν_e beam contamination which can be obtained suppressing the K^+ and K^0 production by the primary proton beam in the target.

The actual configuration in study at CERN, described in this session, uses the SPL (Superconducting Proton Linac) to produce a conventional neutrino beam by a 4 MW proton beam.

The SuperBeam is a conventional neutrino beam generated by the first part of the NuFact complex, composing a proton driver (SPL), an accumulator ring, a target, and a horn. The pion focused by the horn decay is a 100 m long tunnel where a ν_μ neutrino beam of a few hundred MeV is generated (see fig. 1.8 for the spectrum). The neutrino helicity can be chosen by selecting the charge of the pions focused by the horn. In this way, a first attempt to test CP violation can be attempted by measuring the probabilities $P(\nu_\mu \to \nu_e)$ and $P(\bar{\nu}_\mu \to \bar{\nu}_e)$. The detector would be located at the place where the maximum of the oscillation occurs, between 100 km and 130 km for the neutrino Superbeam spectrum shown in fig. 1.8. The parameters of a possible Superbeam are summarized in Table 1.2.

The experiment is assumed to run for 10 years (two for neutrinos and eight for antineutrinos) and the number of events are computed assuming an optimistic value of θ_{13}, namely 10°. The asymmetry in the running period is due to the fact that the beam of antineutrinos is produced by negative pions, which are produced less effectively compared to positive pions in the condition chosen for the experiment. Moreover the antineutrino interactions, which at this energy are dominated by quasi elastic scattering, are at least a factor 2 lower compared to neutrinos.

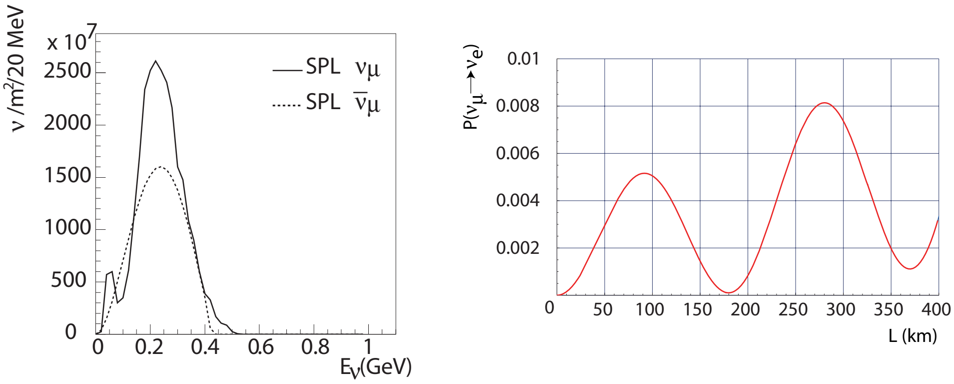

Figure 1.8: *Superbeam neutrino and antineutrino flux computed at 130 km from the SPL (left) and oscillation probability (right). The oscillation probability is calculated with the same values used in section 1.4 but with* $\theta_{13} = 10^\circ$ *and for 270 MeV neutrinos.*

	ν_μ	$\bar{\nu}_\mu$
Neutrino flux (ν/m^2/yr)	4.78 10^{11}	3.33 10^{11}
Neutrino average Energy	0.27 GeV	0.25 GeV
CC events	36698 (2 yrs)	23320 (8 yrs)
Oscillated	1279	774

Table 1.2: *Summary of the Superbeam parameters taken from [49]. The event rate assumes a 4400 kt·y exposure. The oscillating events are calculated with the same values used in section 1.3.2 but with* $\theta_{13} = 10^\circ$.

In the design described, most of the ν_e contamination coming from K_{e3} decays present in high energy neutrinos beams is suppressed by the production threshold effects because of the low energy of the proton driver. The remaining ν_e contamination comes from the μ decay and it will be known within 2% error. The use of a near and far detector will allow for both ν_μ disappearance and $\nu_\mu \to \nu_e$ appearance studies. The physics potential of the 2.2 GeV SPL SuperBeam with a water Čerenkov far detector with a fiducial mass of 440 kton, has been extensively studied [50]. New developments show that the potential of the SPL could be improved by rising the SPL energy to 3.5 GeV [51], to produce more copious secondary mesons at higher energy and to focus them more efficiently.

The focusing system (magnetic horns), originally optimized in the context of a Neutrino Factory, has been redesigned considering the specific requirements of a Super Beam [52, 53]. The most important points are that the phase space covered by the two types of horns are different and that for a Super Beam the pions to be focused should have an energy of the order of

$p_\pi(\mathrm{MeV})/3 \approx E_\nu \geq 2L$ (km) to obtain a maximum oscillation probability. In practice, this means that one should collect 800 MeV/c pions to get a mean neutrino energy of 300 MeV. However at higher beam energy, the expected kaon rates grow rapidly compared to the pion rates; a goal of the HARP experiment [54] is an experimental measurement of these rates.

In this upgraded configuration the neutrino flux could be increased by a factor ~ 3 with respect to the 2.2 GeV configuration and the number of expected ν_μ charged current is calculated to be 95 per kton $\cdot$ yr.

A sensitivity $\sin^2 2\theta_{13} < 0.8 \cdot 10^{-3}$ would be obtained in a 5 years ν_μ plus 5 year $\overline{\nu}_\mu$ run ($\delta = 0$ intrinsic degeneracy accounted for, sign and octant degeneracies not accounted for), allowing to discovery CP violation (at 3 σ level) if $\delta_{\mathrm{CP}} \geq 25°$ and $\theta_{13} \geq 1.4°$ [55, 56]. The expected performance is shown in fig. 1.9 and 1.10 along with those of other setups.

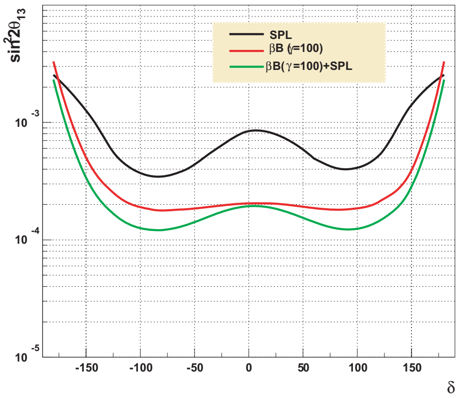

Figure 1.9: *θ_{13} 90% C.L. sensitivity as function of δ_{CP} for $\Delta m^2_{23} = 2.5{\cdot}10^{-3} eV^2$, $\mathrm{sign}(\Delta m^2_{23}) = 1$, 2% systematic errors. SPL-SB sensitivities have been computed for a 10 years ν_μ run, βB and $\beta B_{100,100}$ for a 10 years $\nu_e + \overline{\nu}_e$ run. The SPL-SB 3.5 GeV, BetaBeam with $\gamma = 100, 100$ and their combination are shown.*

1.7 The Neutrino Factory

Most of the long baseline experiments described so far use neutrino from the decay of parents produced directly from the interaction of protons with a target. However, this method limits the maximum energy of the neutrino beam produced to a fraction of the primary proton energy. Moreover, conventional neutrino beams are polluted by the presence of other neutrino flavours, in such a fraction that usually limits the experimental sensitivity. A new accelerator development is the Neutrino Factory (NuFact), whose aim is the

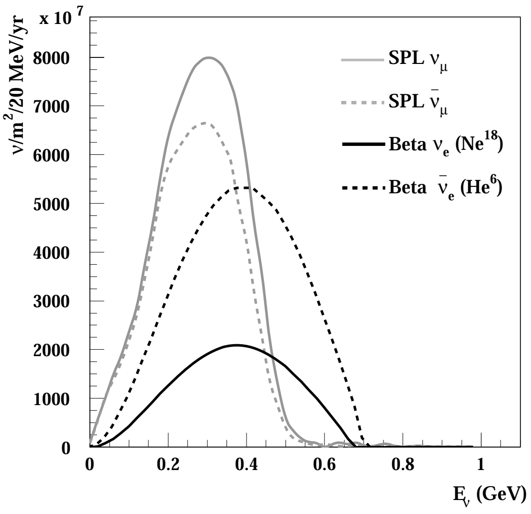

Figure 1.10: *Neutrino flux of β-Beam ($\gamma = 100$) and CERN-SPL SuperBeam, 3.5 GeV, at 130 Km of distance.*

production of high energy, highly collimated (anti)electron and (anti)muon neutrino beams from muon decay:

$$\mu^- \rightarrow e^- + \bar{\nu}_e + \nu_\mu \tag{1.32}$$

or

$$\mu^+ \rightarrow e^+ + \nu_e + \bar{\nu}_\mu \tag{1.33}$$

The advantage of such approach is that muons can be accelerated to large energy and the neutrino beams are free from other flavour of a given helicity. The objective of most of the proposed designs is to achieve a neutrino flux of the order of several times 10^{20} neutrinos per year (1 year is assumed to be 10^7 seconds). Between the several neutrino sources the Neutrino Factory gives the best performance over the neutrino physics parameters. Using such a powerful neutrino source should allow the precise measurement of missing parameters of neutrino physics which include:

- the angle θ_{13} by the oscillation probability $P(\nu_e \rightarrow \nu_\mu)$ with a precision of 10^{-3} (or setting a limit to 10^{-6} degrees);
- the sign of Δm^2_{23} via the MSW effect;
- leptonic CP violation (if any).

The typical neutrino spectrum that could be produced by the European NuFact is shown in fig. 1.11.

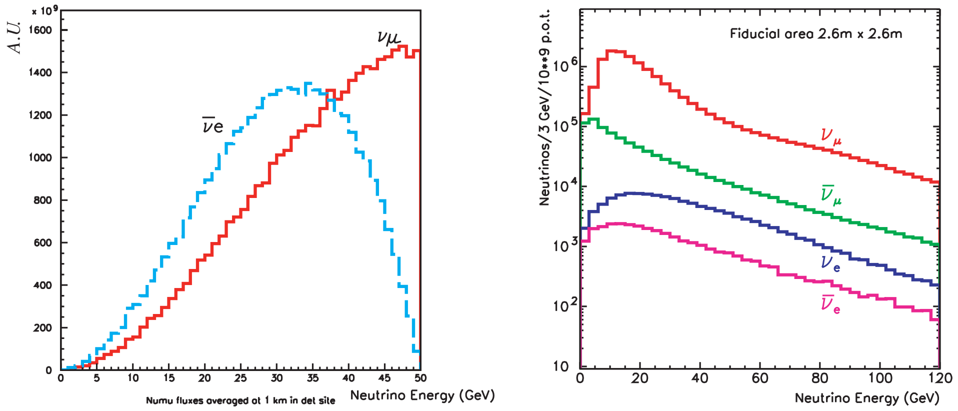

Figure 1.11: *NuFact flux (right) compared to the WANF neutrino beam[53] (plots in different scales).*

1.7.1 Oscillation signature: wrong sign muons

If the NuFact accelerates and stores μ^-, their decays via $\mu^- \rightarrow e^- + \bar{\nu}_e + \nu_\mu$ produced a $\bar{\nu}_e$ and ν_μ beam. If $\bar{\nu}_e$ oscillates into $\bar{\nu}_\mu$, the charged current interaction of $\bar{\nu}_\mu$ in the detector will create a μ^+, while the interaction of ν_μ from the NuFact beam will generate a μ^-. The $\bar{\nu}_e$ oscillation signature is the detection of a wrong sign muon, a muon of charge opposite to that of the muons stored in the decay ring.
The charge separation between wrong sign muons is possible using a large magnetized detector [57]. This signature is much more difficult in traditional neutrino beams produced by pion and kaon decay because those beams contain a large fraction of the neutrinos and antineutrinos of each flavour simultaneously (see fig. 1.11) and the fraction of $\bar{\nu}_e$ is small compared to the other flavours in the beam.

Considering a Neutrino Factory with simultaneous beams of positive and negative muons, which can be distinguished by the time stamp of the accelerator, 12 oscillation processes can in principle be studied, see table 1.3.

$\mu^+ \rightarrow e^+\nu_e\overline{\nu}_\mu$	$\mu^- \rightarrow e^-\overline{\nu}_e$	
$\overline{\nu}_\mu \rightarrow \overline{\nu}_\mu$	$\nu_\mu \rightarrow \nu_\mu$	disappearance
$\overline{\nu}_\mu \rightarrow \overline{\nu}_e$	$\nu_\mu \rightarrow \nu_e$	appearance (challenging)
$\overline{\nu}_\mu \rightarrow \overline{\nu}_\tau$	$\nu_\mu \rightarrow \nu_\tau$	appearance (atm. oscillation)
$\nu_e \rightarrow \nu_e$	$\overline{\nu}_e \rightarrow \overline{\nu}_e$	disappearance
$\nu_e \rightarrow \nu_\mu$	$\overline{\nu}_e \rightarrow \overline{\nu}_\mu$	appearance: “golden” channel
$\nu_e \rightarrow \nu_\tau$	$\overline{\nu}_e \rightarrow \overline{\nu}_\tau$	appearance: “silver” channel

Table 1.3: *Oscillation processes in a Neutrino Factory*

The Neutrino Factory therefore lends itself to the exploration of neutrino oscillations between ν flavours with high sensitivity. Any associated detector should be able to perform both appearance and disappearance experiments, providing lepton identification and charge discrimination which is a tag for the initial flavour and for the oscillation. In particular the search for $\nu_e \rightarrow \nu_\mu$ transitions (golden channel) [58] appears to be very attractive at the Neutrino Factory, because this transition can be studied in appearance mode looking for μ^- (appearance of wrong-sign μ) in neutrino beams where the neutrino type that is searched for is totally absent (μ^+ beam in NuFact).

The emphasis has been placed so far on small mixing angles and small mass differences. With two 40 kton magnetic detectors (MINOS like) at 700 (or 7000) and 3000 km, with a conservative high energy muon detection threshold of 5 GeV and exposed to both polarity beams and 10^{21} muon decays, it will be possible to explore the θ_{13} angle down to $0.1°$ opening the possibility to measure the δ_{CP} phase [58, 59, 60], as it is shown by the plots of fig.1.12.

1.7.2 International scoping study of machine [62]

An international scoping study is evaluating a possible design for the Neutrino Factory. CERN Neutrino Factory accelerator complex layout is shown in fig. 1.13. A possible baseline scheme is the following:

Proton Driver

The proton driver provides 1-4 MW of protons on a pion production target. For the Neutrino Factory application the energy of the beam in the range 4-30 GeV is not critical, since it has been shown that the production of pions is roughly proportional to beam power. The time structure of the proton beam has to be matched with the time spread induced by pion decay (1-2 ns); for a Linac driver such as the SPL, this requires an additional accumulator and compressor ring.

Target, Capture and Decay

A high-power target sits within a 20 T superconducting solenoid, which captures the pions. The high magnetic field smoothly decreases to 1.75 T downstream of the target, matching into a long solenoid decay channel. A design with horn collection (see fig. 1.14) has been proposed at CERN for the Neutrino Factory, with the benefit that it could be also used for a SuperBeam design.

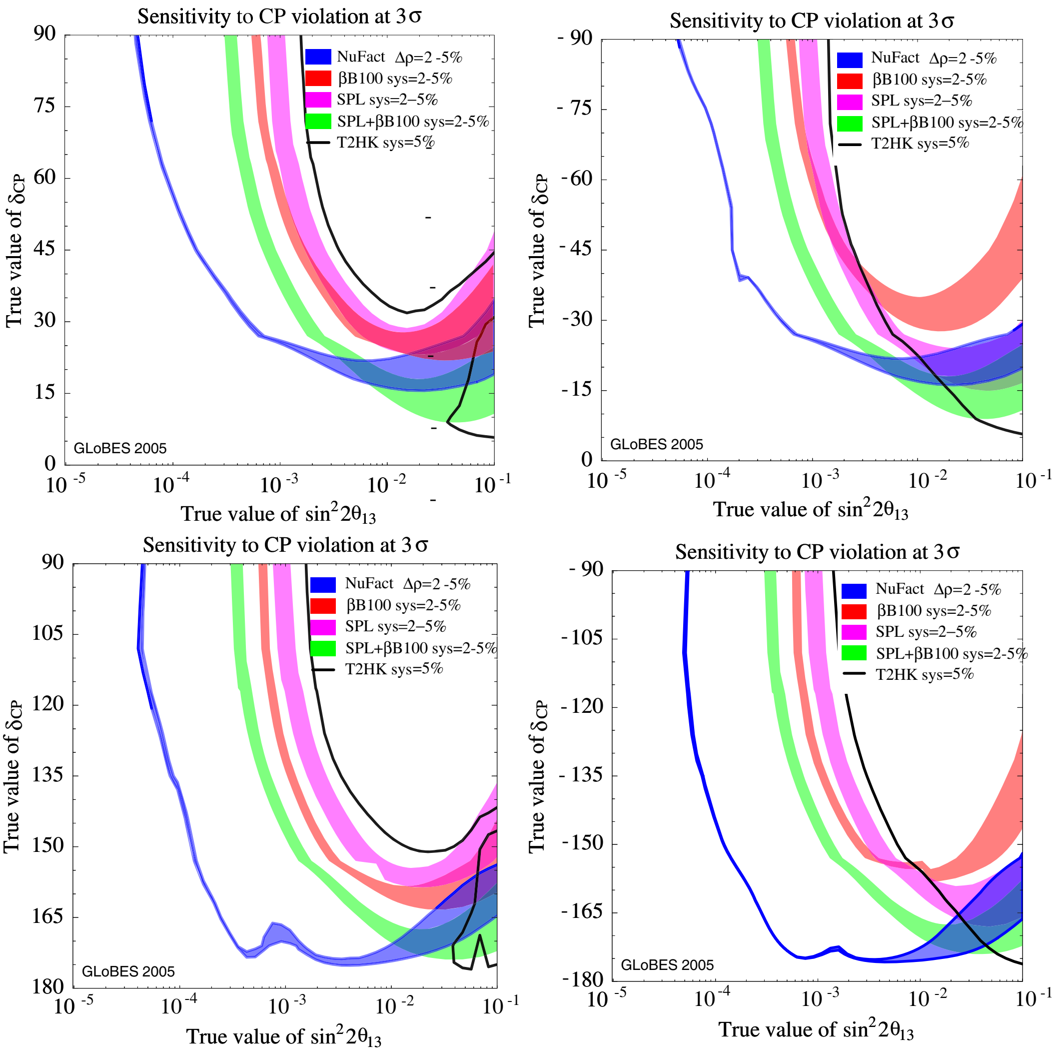

Figure 1.12: *$\delta_{\rm CP}$ discovery potential at 3σ (see text) computed for 10 years running time. For explanation of the proposed facilities see the text [61]. The four plots represent the four possible quadrants of $\delta_{\rm CP}$ values, performances of the different facilities are not at all the same in the different quadrants. The width of the curves reflects the range of systematic errors: 2% and 5% on signal and background errors for SPL-SB and Beta Beam, 2% and 5% for the matter density. Other systematic errors are 5% on signal and background of T2HK, 0.1% for NuFact signal, 20% for NuFact backgrounds. A description of the facilities can be found in [62].*

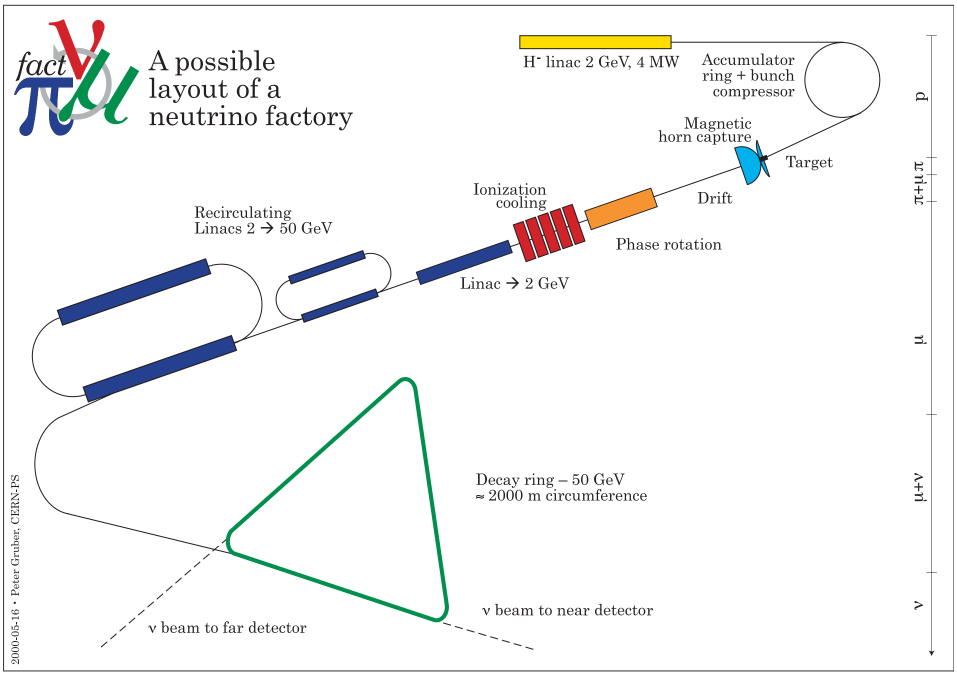

Figure 1.13: *CERN Neutrino Factory accelerator complex layout (not to scale).*

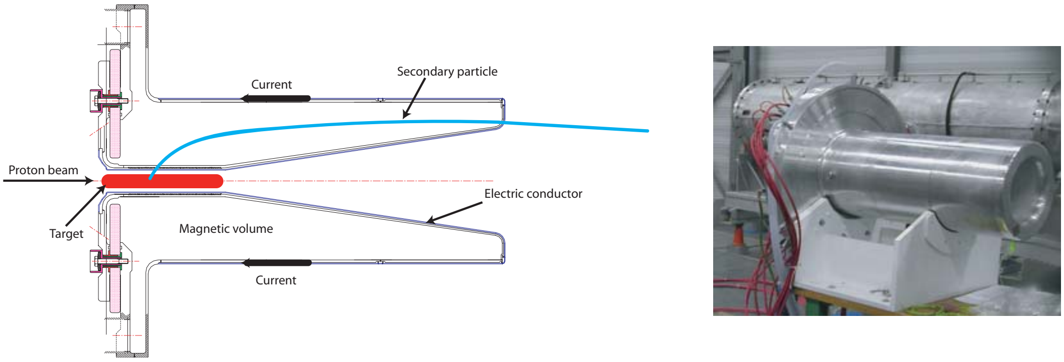

Figure 1.14: *Horn concept (left) and prototype of NuFact horn.*

Bunching and Phase Rotation

The muons from the decaying pions are bunched using a system of RF cavities with frequencies that vary along the channel. A second series of RF cavities with higher gradients is used to rotate the beam in longitudinal phase-space, reducing the energy spread of the muons.

Cooling

A solenoid focusing channel with high-gradient 201 MHz RF cavities and either liquid-hydrogen or LiH absorbers is used to reduce the transverse phase-space occupied by the beam. The muons lose, by $\mathrm{d}E/\mathrm{d}x$ losses, both longitudinal- and transverse-momentum as they pass through the absorbers. The longitudinal momenta is compensated by re-acceleration in the RF cavities.

Acceleration

The central momentum of the muons exiting the cooling channel is 220 MeV/c. A superconducting Linac with solenoid focusing is used to raise the energy to 1.5 GeV. Thereafter, a Recirculating Linear Accelerator raises the energy to 5 GeV, and a pair of Fixed-Field Alternating Gradient rings accelerate the beam to at least 20 GeV.

Storage Ring

A compact racetrack geometry ring is used, in which 35% of the muons decay in the neutrino beam-forming straight sections. If both signs are accelerated, one can inject in two superimposed rings or in two parallel straight sections. This scheme produces over $6 \cdot 10^{20}$ useful muon decays per operational year and per straight section in a triangular geometry.

1.7.3 Machine parameters choice

Stringent limits for the accelerator design and constraints on different NuFact parameters, are imposed by proposed physics goals.

The neutrino energy and the neutrino flux are probably the most critical parameters. Both are limited by technology and cost, while from the physics viewpoint they should be as high as possible: fig. 1.15 describes some physics possibilities for different combinations of neutrino energy and neutrino flux. At least 10^{20} muons per year with an energy greater than 20 GeV are required to observe CP violation.

The third important parameter is the distance of the far detector, first because the detector should be placed far enough to have a large oscillation probability, second because the neutrino interaction with matter will discriminate the sign of Δm^2_{23} thanks to the MSW effect, and finally because the

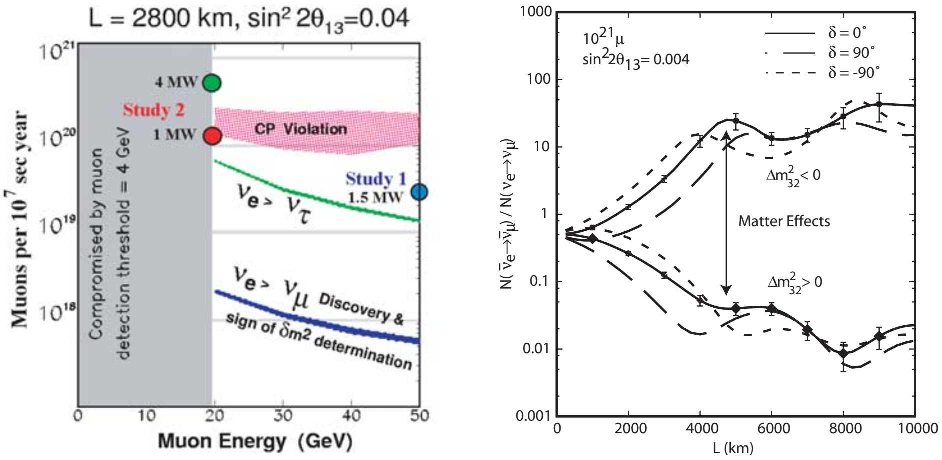

Figure 1.15: *Physics reach versus beam intensity and energy (left, [63]) and baseline influence on the mass splitting recognition and CP measurements (right) [57]*

magnitude of CP violating asymmetry is distance dependent. This parameter, however, is probably the more risky, since it depends on an even rough knowledge of θ_{13}, for at least an upper limit.

Considering for example the CERN site for the neutrino factory, possible detector locations are shown in fig. 1.16. One far detector could be placed at the Gran Sasso Laboratories at a distance of ≈700 km and the far one in the Canary Island or in the North Pole region.

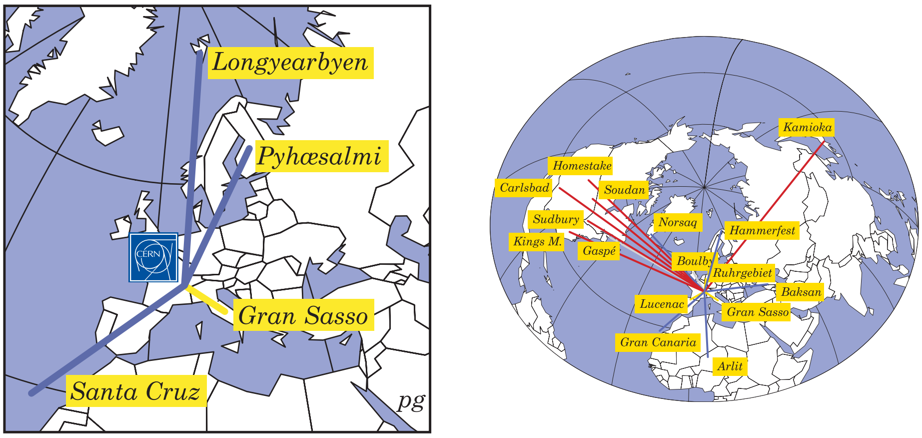

Figure 1.16: *Different possible detector locations that have been identified for a NuFact built at or near CERN.*

1.8 Issue of hadron production modelling in Monte Carlo simulation

Many aspects of neutrino experiments rely on a precise knowledge of hadron production yields both for the prediction of the absolute fluxes as for the energy spectra. Conventional neutrino beams using accelerators are produced by the decay of pions and kaons which in turn are produced by the interactions of protons on a production target (in general made of heavy metals). In order to be able to predict with a good confidence the neutrino flux, the production cross-section of these hadrons has to be known either via precise modelling or via measured data. The need for a precise knowledge becomes larger when ever-increasing precision is required for the neutrino experiments.

The calculation of atmospheric neutrino fluxes relies on the knowledge of pion and kaon production cross-sections of protons impinging on N_2 and O_2 targets, the largest components of air. In this case neutrino physics shares a common interest with experiments studying cosmic-ray muon fluxes. Usually carbon is used as target material in production measurements instead of nitrogen and oxygen, because it is easier to produce a solid target with a mass number A near N_2 and O_2 instead to use a cryogenic target to have N_2 and O_2 in a liquid state.

Finally, the need for more precise and more intense neutrino beams has lead to a design effort towards the construction of Neutrino Factories. The design of the production target region and focusing system to achieve the most efficient production of these muons requires precise knowledge of the production of low momentum pions on nuclear targets.

Simulations of particle production in hadronic interactions fall into two categories: theoretical models and parameterisation driven models.
A summary of the different available models in GEANT4 and their range of validity is present in fig. 1.17.

Some theoretical models are based on calculations on the intranuclear cascade such as Bertini [64] and the Binary Cascade [65]; others include also a quantum molecular dynamics modelling. These models are reliable at proton momenta less than few GeV/c, but are usually not applicable to energy of about or greater than 10 GeV. Another advanced model used in simulation is CHIPS [66] that covers both low energy lepton interactions and hadron proton interactions.

Other theoretical models are based on the String model, such as DPMJET [68], QG and FTF (GEANT4) [69] and FRITIOF [70]. These models were developed mainly for energies, greater than 50 GeV, for example for

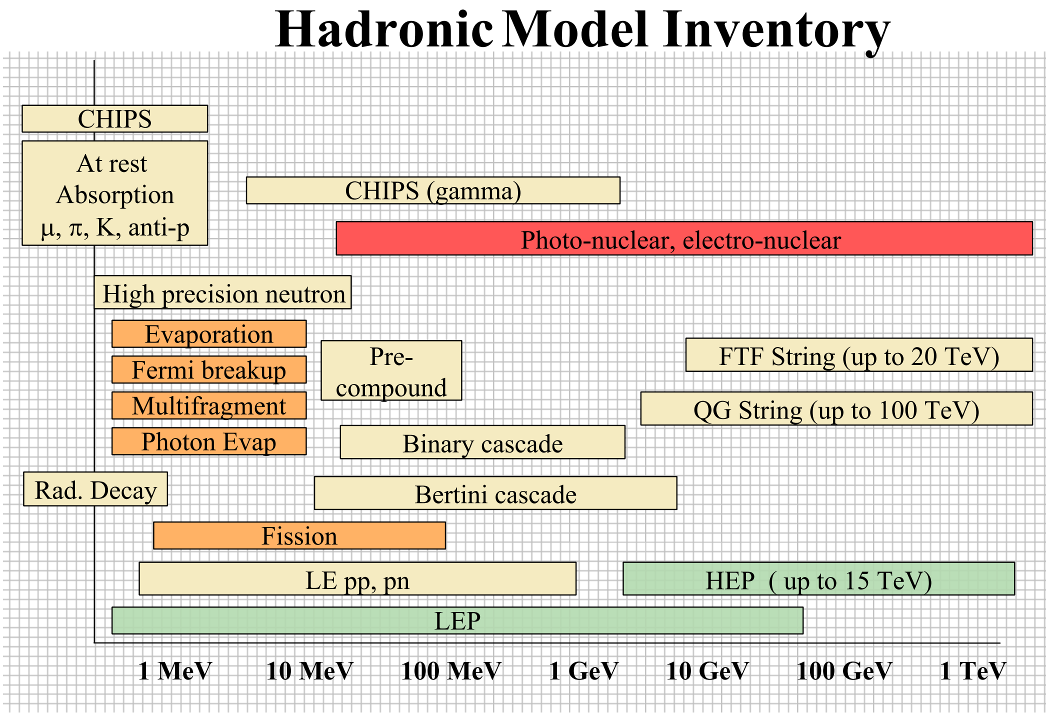

Figure 1.17: *Hadronic Model Inventory [67] of Geant4*

cosmic ray calculations. Their results usually have an uncertainty up to a factor of 5 in the pion yield at momenta less than 1 GeV/c on heavy nuclei for proton beam momenta between few GeV/c up to 30 GeV/c (the region that is especially interesting for the NuFact).

The generators based on the parameterisation of data suffer from the absence of data in the interesting NuFact energy region and usually cover only a forward angular region. That is mainly because in the past several experiments have been performed (see *e.g.* refs. [71, 72, 73]) using single arm spectrometers. More modern experiments use open-geometry set-ups [74, 54, 75]. The measurements of the previous experiments are affected by several (for neutrino physics) limitations. The most obvious ones are the sparse measurements, with low statistics and a limited acceptance that makes extrapolation difficult. The latter type of experiment has the capability to cover a large kinematical area in one exposure, thereby reaching a significantly smaller overall normalization uncertainty. However, the primary proton energies used were binned according to the energies of the used accelerator. This leads to the fact that different models are somehow tuned to reproduce some sets of data, or are validated only with respect to some primary energy or

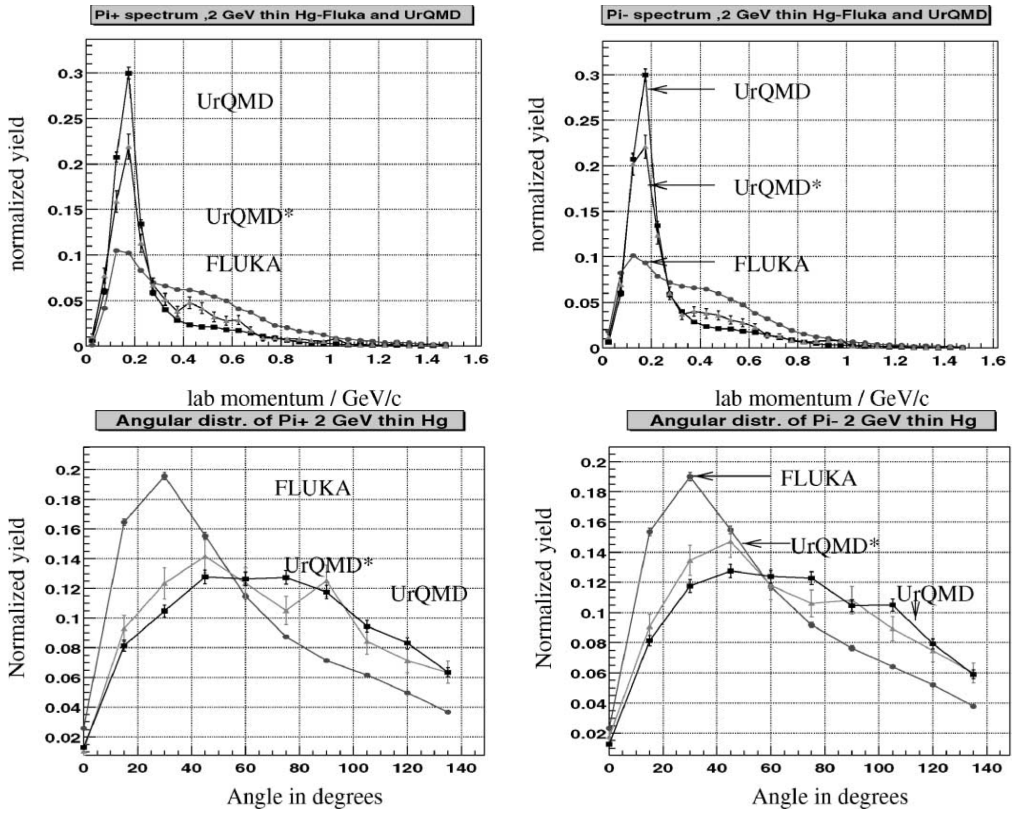

Figure 1.18: *Pion spectrum, on the top, and angular distribution, on the bottom.*

material and not others. The first consequence is that, even if two models have the same range of validity they often do not give the same results when an extrapolation either in primary energy or material is required.

An example that shows the different results of two generators is shown in [76]. They compare the pion production obtained using the particle generations from FLUKA'99 [77] and UrQMD [78]: fig. 1.18 shows a comparison of rapidities, spectra and angular distributions for π^+ and π^- produced by a proton beam with kinetic energy of 2 GeV hitting a mercury target, which is the present base line of the CERN neutrino factory project. Another example that compares the total pion yield obtained using the particle generation FLUKA98 and MARS [79] is shown in fig. 1.19 [80]. One can examine the total pion production from a thin target of 1 mm thick mercury target, that corresponds to approximately 0.7% of the nuclear inelastic interaction length. The vertical axis has been normalized to the total incident protons. One concludes that the two codes give good agreement for total pion production in the incident proton kinetic energy range of 1-16 GeV. The most

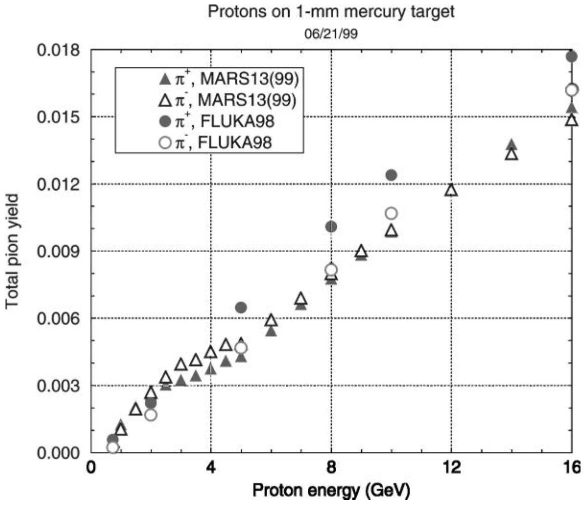

Figure 1.19: *Total pion yield from a thin mercury target.*

significant discrepancy can be seen for the positive pion production in which FLUKA gives approximately 25% higher yields for incident energies greater than 4 GeV.

The only viable solution is to provide a large set of hadronic production cross sections, by varying both the primary energy and the target material, in order to provide a database either to build a new data-driven model or to tune the existing ones: that is the main aim of the HARP experiment.

1.9 Relevance of hadron production measurements in the neutrino physics

1.9.1 Relevance in the present oscillation experiments: K2K and MiniBooNE

The calculation of the flux and neutrino flavours composition of a neutrino beam requires a precise measurement of the interaction cross-section between the beam particles and the target material. In the case of the K2K and MiniBooNE experiments, the dominant component of the beam (muon neutrinos) comes from the decay of positive pions produced in the collisions between the incident protons and the target. To compute the ν_μ flux one needs a 4π parametrization of the differential cross section which, in order to be reliable, must be based on a wide-acceptance and precise measurement.

In the K2K analysis, the determination of the far/near ratio was the leading energy-dependent systematic error. To compute this quantity a Monte Carlo program simulating all relevant beam-line geometry and materials, and all relevant physics processes, is used. In this simulation, the neutrino flux prediction uncertainty is dominated by the uncertainties in the forward π^+ production from the interactions of the 12.9 GeV/c protons in the aluminium target material. By using the recent HARP results on pion production measurements obtained for the same proton beam momentum (12.9 GeV/c) and nuclear target material (aluminum) as those used to produce the K2K neutrino beam, the total F/N error is reduced by a factor 2 across all energies with respect to the previous results based on the simulation.

The result of the pion production measurements of HARP experiment [81] is incorporated into the K2K beam MC simulation to estimate the neutrino spectra at ND and SK and the energy dependence of the F/N flux ratio in the absence of neutrino oscillations. The F/N flux ratio, Φ^{SK}/Φ^{ND}, predicted by the HARP π^+ production measurement for primary hadronic interactions with the systematic error evaluation discussed above, in the absence of neutrino oscillations, is shown in fig. 1.20 as a function of neutrino energy. The flux ratio uncertainty as a function of the neutrino energy binning used in K2K analysis is at the 2-3% level below 1 GeV neutrino energy, while it is of the order of 4-9% above 1 GeV. The dominant contribution to the uncertainty in F/N comes from the HARP π^+ measurement itself. In particular, the uncertainty in the flux ratio prediction integrated over all neutrino energies is 2.0%, where the contribution of the HARP π^+ production uncertainty is 1.4%. The dotted histograms in fig. 1.20 show the central value predicted by using the Cho-CERN compilation for primary hadronic interactions, which was used in K2K prior to the availability of HARP data. In this case, the same Sanford-Wang [82] functional form of π^+ production is employed to describe a CERN compilation of π^+ production measurements in proton-beryllium interactions, which is mostly based on Cho et al. data [15]. A nuclear correction to account for the different pion production kinematics in different nuclear target materials is applied. We find that the predictions of F/N flux ratio by HARP and Cho-CERN are consistent with each other for all neutrino energies. Note that the difference between Cho-CERN and HARP central values represents a difference in hadron production treatment only.

Among the available parametrisation, K2K uses in neutrino oscillation analysis the one predicted by the HARP measurements since the HARP pion production measurement was done in the same conditions as K2K experiment: the proton beam momentum and the relevant phase space of pions responsible for the neutrinos in K2K are the same. In particular, the measured momentum region of the HARP experiment reaches below 2 GeV/c

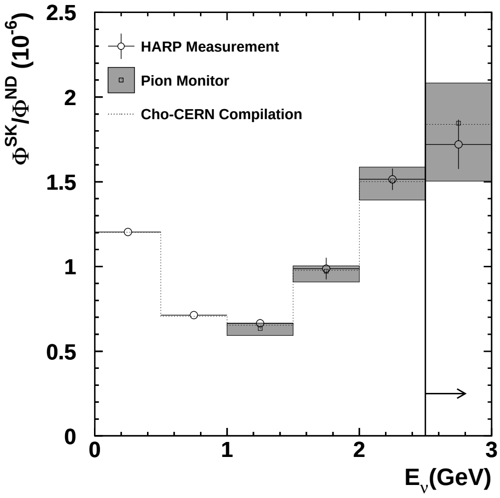

Figure 1.20: *Prediction for the K2K muon neutrino F/N flux ratio in absence of oscillations. The empty circles with error bars show the central values and systematic errors on the muon neutrino flux predictions from the HARP* π^+ *production measurement discussed in the text, the empty squares with shaded error boxes show the central values and errors from the pion monitor measurement, and the dotted histograms show the central values from the Cho-CERN compilation of older (non-HARP)* π^+ *production data.*

down to 0.75 GeV/c where the K2K Monte Carlo is insensitive.

MiniBooNE, at Fermilab was designed to address the yet unconfirmed oscillation signal reported by the LSND collaboration. MiniBooNE will search for the appearance of electron neutrinos in a beam that is predominantly muon flavour with an L/E similar to LSND but with substantially differing systematics. One important systematic arises from the prediction of the fluxes of different neutrino flavours at the MiniBooNE detector.

The MiniBooNE neutrino beam is produced from the decay of π and K mesons as results of collisions of 8.9 GeV/c protons from the Fermilab Booster on a 71 cm beryllium target. The neutrino flux prediction is generated using a Monte Carlo simulation implemented in Geant4 [83]. Primary meson production rates are presently determined by fitting the empirical parameterisation of Sanford and Wang [82] to production data in the relevant region. Prior to the availability of the HARP cross-section results [84] the fit was dominated by cross-section data from the Brookhaven E910 experiment at 6.4 and 12.3 GeV/c [85].

The results being for protons at exactly the booster beam energy, are a critical addition to the global Sanford-Wang parameterisation fits. Using the Monte Carlo we can illustrate the direct impact of these data on the Mini-

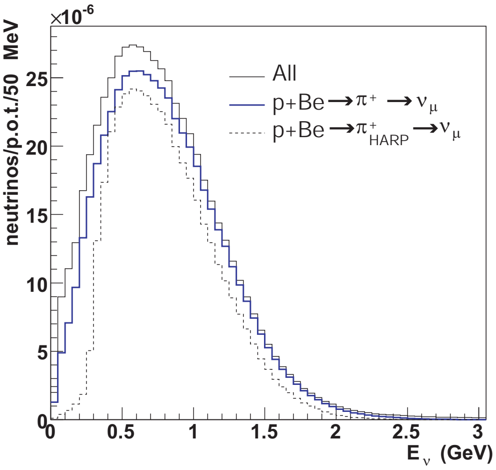

Figure 1.21: *Predicted muon neutrino flux at the MiniBooNE detector from a Geant4-based simulation of the booster neutrino line at Fermilab. The black curve is the total muon neutrino flux, while the blue curve is the fraction of* ν_μ*'s coming from the decay of* π^+ *created in proton-beryllium collisions. This primary production of positive pions is based on a parameterisation of the HARP* π^+ *cross-section measurements presented here and represents the primary source of* ν_μ*'s at MiniBooNE.*

BooNE flux predictions. The dominant channel leading to a muon neutrino in the detector is $p + Be \rightarrow \pi^+ + X \rightarrow \nu_\mu$. Fig. 1.21 shows the total ν_μ flux (black) according to the simulation as well as the fraction coming directly from the sequence listed above (blue).

1.9.2 Relevance in the future experiment: NuFact

The design and optimization of a Neutrino Factory design requires the knowledge of the pion production, in terms of double differential cross section, but also of the absolute yields by varying the primary proton energy.

The proton energy has a primary impact on the design of the proton driver. A proton driver that provides 4 MW of protons with an energy up to 8 GeV on a fixed target can be built as a linac [86] while for proton energies above 8 GeV one aims for a Rapid Cycling Synchrotron [87]. It is mandatory to understand what is the proton energy which maximizes the pion yield in the acceptance of the Neutrino Factory, because it has a major impact on the machine design.

The acceptance of the Neutrino Factory is intended as the maximum volume in the 6D phase space described by the coordinates (x,x',y,y',E,t) of pions that, once decayed into muons, are transported from the target to the muon storage ring without being lost. In term of accelerator physics, the transverse acceptance is the maximum volume in 6D phase space occupied by the 90% particles. However, it is not straightforward to relate this accelerator physics quantity to what is measured in a hadron production experiment like HARP, which are particle yields or cross sections in bins of angles or transverse momentum. Thus in the following, all the acceptances are described using more convenient quantities, such as energy, momentum and transverse momentum.

The energy acceptance of the neutrino factory is mainly given by the acceptance of the phase rotation section. In the design described in section 1.7.3 the phase rotation accepts muons of 200 MeV±100 MeV, which translates into pion momenta between 140 MeV/c and 700 MeV/c. This can be simply deduced from the kinematics of the two body decay and it is shown in fig. 1.22. For a given pion energy, a range of different muon energies can be produced, considering that the muon energy is fixed in the pion frame by the two body decay kinematics. However, if the muon is produced in the pion rest frame in the direction of the pion boost, it has more energy than a muon produced in the opposite direction once transported in the laboratory frame. Since pions are not accelerated before decaying into muons, this energy range is the one that has to be studied at production from the target.

The transverse acceptance of the neutrino factory, however, cannot be directly translated into a phase space region to be studied at the production. The transverse acceptance is roughly defined by the radius of the decay

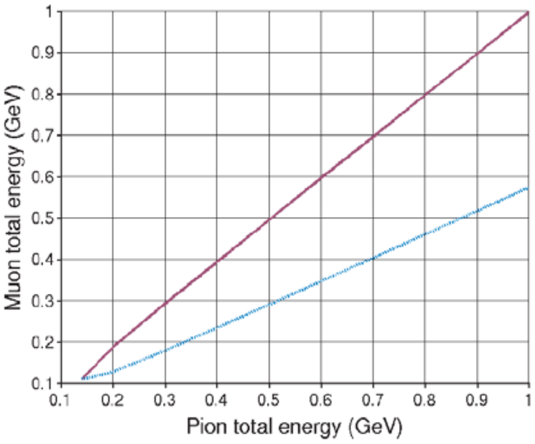

Figure 1.22: *A pion of a given total energy (x-axis) could produce a muon with a total energy (y-axis) in between the two lines.*

channel solenoids, which is 60 cm, and by the magnetic field of the solenoids, which is 1.8 T, and together they give a 80 MeV/c of transverse momentum. However, pions are focused by a specific device meant to feed as many pions as possible inside this acceptance, by focusing them. Two different systems have been studied for this purpose, both manipulating the pion transverse momentum in two different ways.

A possible design foresees the use of a magnetic horn, where particles are focused by a magnetic field which decreases like the inverse of the distance from the beam axis. The horn focuses only the particles which actually enter the magnetic volume enclosed into the current conductors. According to the last CERN design, the horn can focus the particles with an initial angle between 330 mrad and 610 mrad (see fig. 1.14). To understand the real efficiency of the horn, but also to propose a different design, a knowledge of the pion double differential cross section for this momentum range is mandatory. However, one also needs to know the yields or the phase space of the particles which do not cross the magnetic volume, since those particles are mostly, except for possibly their energy, in the acceptance of the Neutrino Factory.

The focusing by a solenoid requires somehow a different knowledge, in the sense that the solenoid does not capture particles with a transverse momentum larger than 250 MeV/c due to its magnetic field and its aperture. More than the double differential cross section, in this case it is more important to know the integral of the differential cross section for a transverse momenta below 250 MeV/c.

The measurements of the HARP experiment cover the interesting angular and momentum region for beam momenta from 1.5 GeV/c to 15 GeV/c for a large range of target nuclei. These measurements of the double differential cross section of positive and negative pions will allows the optimization of the design of the Neutrino Factory: in the choice of the target, of the energy of the proton driver and in the design of the focusing system.

Chapter 2

HARP experiment

The PS214 hadron production experiment [54] at the CERN Proton Synchrotron carried out a program of measurements of secondary hadron production, over the full solid angle, produced in thin and thick nuclear targets by beams of protons and pions with momenta in the range 1.5 – 15 GeV/c.

The main motivations of the experiment are: to measure pion yields to determine the optimum energy of the proton driver of a future neutrino factory; to improve substantially the precision of the calculation of the atmospheric neutrino flux; to provide input for the flux calculation of accelerator based neutrino experiments such as K2K and MiniBoone; and to provide a large set of data to improve hadronic models in Monte Carlo simulation models.

For these reasons, HARP was designed to cover the full solid angle. This was achieved by the combination of a Time Projection Chamber (TPC) in which the target was embedded, with a forward spectrometer featuring a dipole magnet for momentum measurement. The identification of primary particles in the beam was important for the cross section normalisation, as was the identification of secondaries both at large angles in the TPC and at small angles in the forward region. The experiment was approved by CERN's Research Board in February 2000 and collected data in the years 2001 and 2002. The experimental setup was decommissioned at the end of 2002.

2.1 Introduction

The experimental layout consists of four main functional parts: the beamline along with the detection and identification of incoming beam particles, the trigger detectors, the large-angle spectrometer housing the target and the forward spectrometer.

The beamline selects secondary particles with positive or negative charge emerging from a primary target in the extracted proton beam from the PS accelerator, and delivers them via the T9 transfer line to the HARP target where their interactions are then studied. It covers the momentum range between 1.5 GeV/c and 15 GeV/c. Particle identification in the beamline is provided by two gas Cherenkov detectors (beam Cherenkov A and B: BCA, BCB) and a pair of time-of-flight counters (TOF-A, TOF-B). Four multi-wire proportional chambers (MWPC) measure the position and direction of the beam particles upstream of the target. Several scintillation counters serve to trigger on single incoming beam particles.

The global layout of the HARP experiment is shown in fig. 2.1. It covers a total length of 13.5 m along the beam direction. The large-angle spectrometer, composed of the TPC and a set of multi-gap resistive plate chambers (RPC), is housed in a solenoid magnet. The TPC is used for tracking and particle identification (PID). Its particle identification capabilities are complemented by the RPC serving as time-of-flight detectors which surround the TPC.

The forward spectrometer measures particles produced in the forward direction at angles up to $\sim 14.3°$. It is built around a dipole magnet for momentum analysis, with large planar drift chambers (NDC) for particle tracking, and three detectors used for particle identification: a time-of-flight wall (TOFW), a threshold Cherenkov detector (CHE) and an electromagnetic calorimeter (ECAL).

The origin of the HARP coordinate system is placed in the centre of the target. The z-coordinate points in the direction of the beam, the y-coordinate upward, and the x-coordinate to the left when looking in the direction of the beam. HARP collected a total of $\sim 420 \cdot 10^6$ triggers with different target and beam settings in 2001 and 2002. A summary of the collected data is shown in table 2.1.

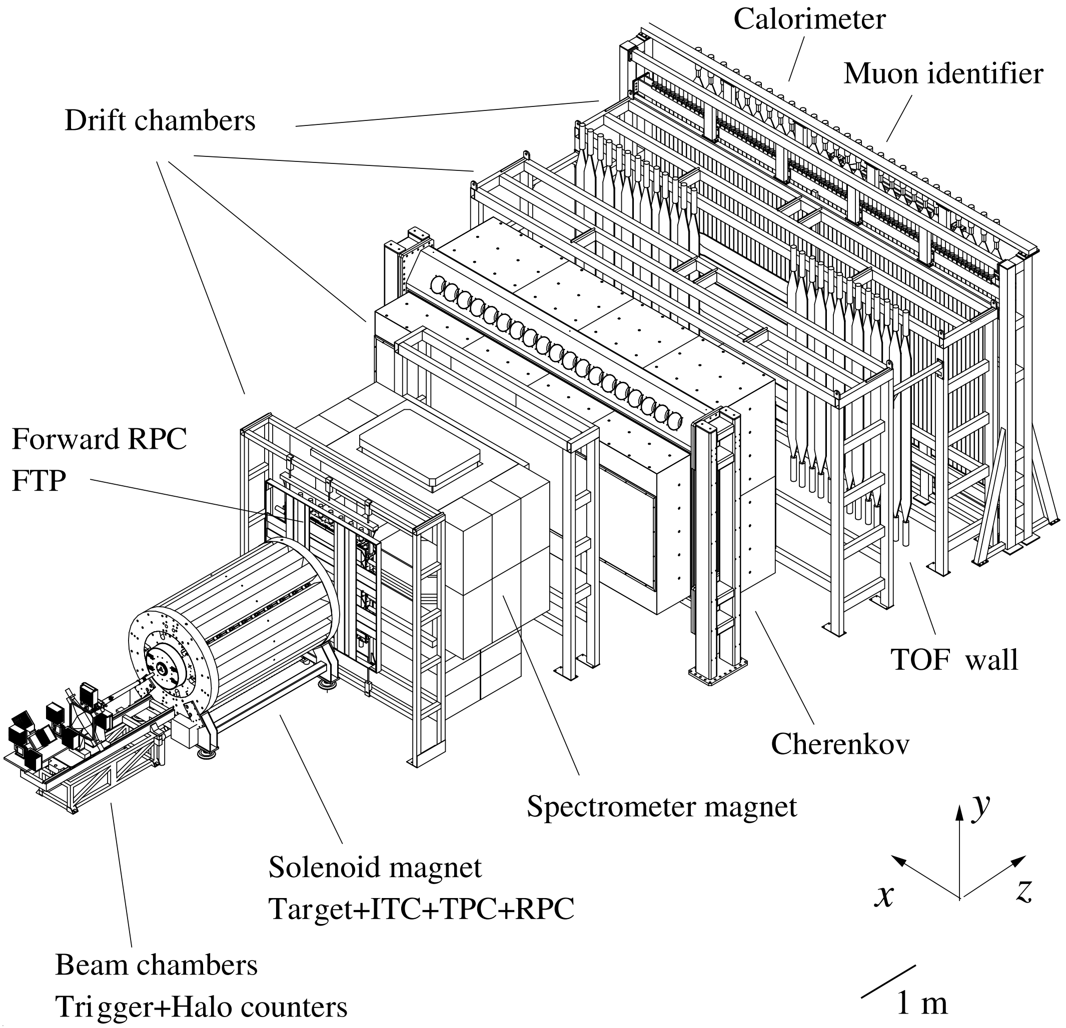

Figure 2.1: *Overall layout of the HARP detector. The different sub-detectors are shown. The target is inserted inside the TPC. The convention used for the coordinate system is drawn in the figure.*

Target	**Momentum** (GeV/c)	**Length** ($\lambda_{\rm I}$)	$\lambda_{\rm I}$ (mm)	**Events** (10^6)
Be	3, 5, 8, 12, 15	2%, 5%, 100%	408.0	37.4
C	3, 5, 8, 12, 15	2%, 5%, 100%	381.0	30.7
Al	3, 5, 8, 12, 15	2%, 5%, 100%	395.5	34.5
Cu	3, 5, 8, 12, 15	2%, 5%, 100%	150.2	36.6
Sn	3, 5, 8, 12, 15	2%, 5%	110.4	23.7
Ta	3, 5, 8, 12, 15	2%, 5%, 100%	112.0	38.2
Pb	3, 5, 8, 12, 15	2%, 5%, 100%	174.4	44.9
N	3, 5, 8, 12, 15	6 cm		13.0
O	3, 5, 8, 12, 15	6 cm		15.5
H	3, 5, 8, 12, 15	6, 18 cm		32.0
D	3, 5, 8, 12, 15	6 cm		21.0
MiniBooNE	+8.9	5%, 50%, 100%,	408.0	22.6
		replica target	394.5	
K2K	+12.9	5%, 50%, 100%,		15.3
		replica target		
H_2O	+1.5	10%, 100%		6.4
Pb, Ta, Cu	+1.5	5%		3.2

Table 2.1: *Main datasets collected by HARP at the CERN PS in 2001-2002. Data were all taken with both positive (mainly p, π^+) and negatively (mainly π^-) charged beams, except where explicitly indicated. Some sets include dedicated empty target runs. $\lambda_{\rm I}$ is the interaction length for the given material. An analysis on pion produced by proton beam with a momentum of 5 Gev/c hitting a tantalum target with a thickness of 5% of a nuclear interaction length is described in chapter 6.*

2.2 Targets

HARP aimed to collect data on a large range of target nuclei. Both solid and cryogenic targets were used to cover a range from small to high atomic weight, to attempt to understand the cross section scaling dependence with respect to the Z of the different materials. Moreover, to study the effect of secondary interactions, targets of different thicknesses have been analysed.

Seven elements (Be, C, Al, Cu, Sn, Ta, Pb) were chosen to provide solid targets, covering the atomic number range from 4 to 82. In order to observe the produced particles with the minimum amount of scattering or re-interaction, most measurements were made with thin disc targets (2% and 5% of one interaction length, λ_I). Because of the size of the beam, the targets are all 30 mm in diameter. Particles produced at 90° with respect to the beam axis would therefore see a significant amount of material. To ensure that corrections for secondary interactions are satisfactorily modelled and corrected, data have been also collected with thick targets, a full interaction length long.

Finally, data have also been collected with replica targets from two accelerator neutrino experiments, MiniBooNE [16][*] and K2K [35][†], with the intention of reducing the systematic uncertainties on the calculated neutrino fluxes of the experiment.

Data have also been taken with cryogenic targets of H_2, D_2, N_2 and O_2. Data taken with H_2 and D_2 targets are fundamental to distinguish nucleon-induced contributions to the cross-sections from nuclear effects. Data collection with O_2 and N_2 targets yields direct information for the precise prediction of atmospheric neutrino fluxes.

The cryogenic targets required a particular housing due to the fact that they were in liquid or gaseous form. They are contained in an envelope with a diameter of 35 mm and made from a 125 μm thick mylar foil. The entrance window has a diameter of 20 mm, thus defining the effective diameter of this target. The target cylinder is connected to the target support by a copper ring with an external radius of 18 mm and internal radius of 10 mm. The target is surrounded by aluminised mylar superinsulation layers and placed inside a cylindrical aluminium cryostat, 60 mm in diameter and 0.6 mm wall thickness, of similar shape to the solid target arm. The endcap of this tube (thickness of 250 μm) is positioned to avoid being crossed by large angle

---

[*] The MiniBooNE replica targets are made of Beryllium and have a three-wing shape, with the wings pointing at 120° of each other, like the bisector of an equilateral triangle. They are 406 and 163 mm long, with a 29 mm diameter.

[†] The K2K replica targets are made of an alloy containing 98% Aluminium and are 650 and 200 mm long, with a 29.9 mm diameter.

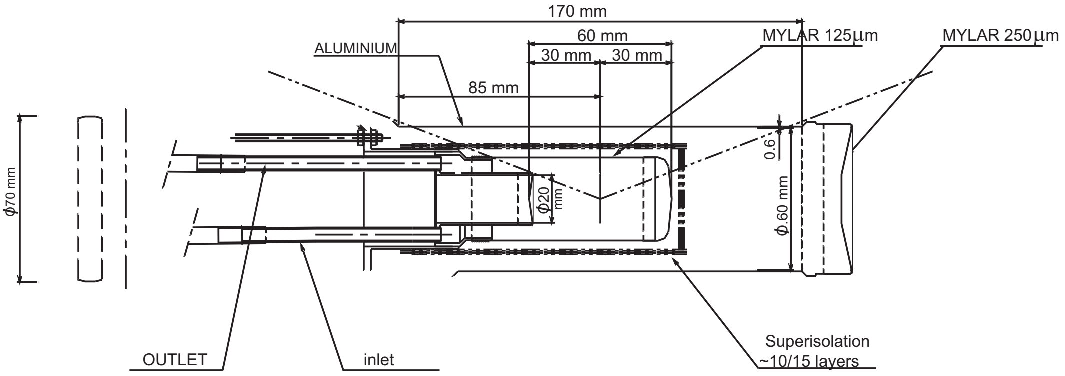

Figure 2.2: *Technical drawing of the cryogenic target with a length of 60 mm.*

particles and to avoid multiple scattering and reinteractions. Fig. 2.2 shows a technical drawing of the short cryogenic target.

The Hydrogen 180 mm target has the same geometry of the short cryogenic target but the mylar tube that contains the Hydrogen has a length of 180 mm. Also the aluminium cryostat is the same in the two cases.

2.3 Primary Beam instrumentation

The beam instrumentation upstream of the target includes a pair of gas threshold Cherenkov counters (BCA and BCB), two scintillation halo counters (HALO-A and HALO-B), a beam time-of-flight system (TOF-A and TOF-B), a set of four multi-wire proportional chambers (MWPC) and two special scintillation counters (BS and TDS). Their role is twofold: to provide the detection, tracking and identification of incoming primary beam particles (BCA, BCB, TOF and MWPC) and to generate primary signals for the trigger decision (TOF-B, BS, TDS, HALO counters and optionally BCA and BCB). A schematic view of the relative position of all beam and trigger detectors is shown in fig. 2.3.

The task of beam particle identification is shared between the beam Cherenkov counters and the beam time-of-flight system. Below 3 GeV/c, the beam Cherenkovs are used to tag electrons or positrons. The TOFs are capable of resolving the more massive beam particles such as pions and protons. At 5 GeV/c the π/p-separation is made jointly by the beam TOF and one of the Cherenkovs (usually BCB), while the other Cherenkov (BCA) is used to tag $e^{\pm}$. At higher momenta the $e^{\pm}$-contamination drops to below 1% and at the same time the beam TOF system becomes unable to efficiently separate pions and protons. The task of π(/K)/p-separation is performed by the beam Cherenkov detectors, as shown in fig. 2.4.

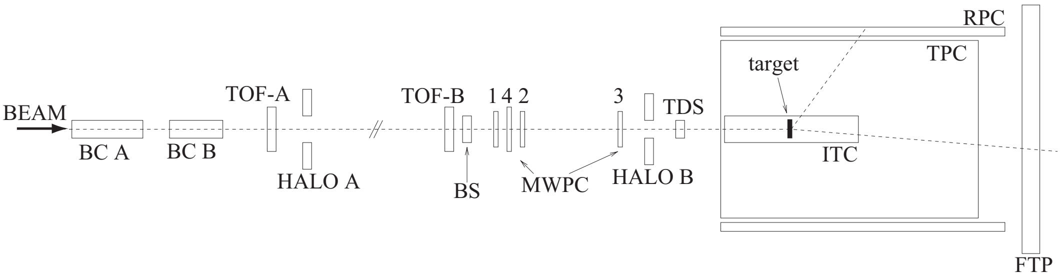

Figure 2.3: *Schematic view not to scale of the arrangement of all trigger and beam equipment. Detailed descriptions are given in the text. The beam enters from the left. The MWPCs are numbered: 1, 4, 2, 3 from left to right.*

The tracking of beam particles is performed by the beam MWPCs located near the target. They are accurately aligned with respect to the nominal HARP coordinate system.

The measured tagging efficiency of both counters for pions and $e^{\pm}$ is close to 100%. The limited K-tagging capability at ≥12 GeV/c (fig. 2.4) is sufficient given the relatively small fraction of kaons in the beam (<1%). Kaons are rare because 1) the probability of being produced in the PS internal target is not too large, and 2) their life time is quite short compared to the length of the transfer line T9 at the end of which HARP was placed.

The beam time-of-flight system with a 21.4 m-long base is used for beam particle identification up to 5 GeV/c. In addition, the beam momentum can be accurately determined by comparing the measured velocities of pions, protons and deuterons of the same beam, as illustrated by fig. 2.5. Two iden-

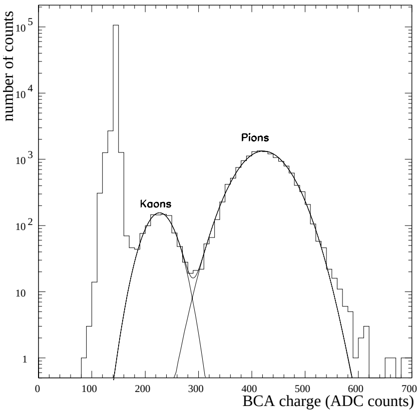

Figure 2.4: *Pulse-height spectrum from the BCA Cherenkov counter for a positive proton beam at 12.9 GeV/c.*

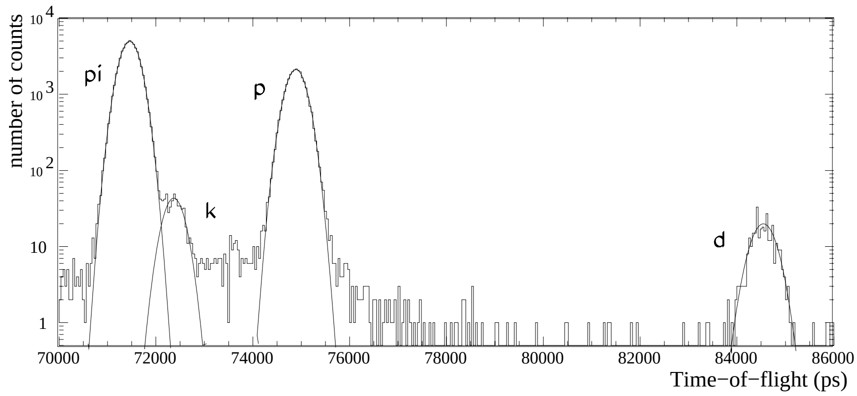

Figure 2.5: *Example for beam particle identification with time-of-flight and a nominal beam momentum of 3 GeV/c. Electrons have been rejected with the Cherenkov counters.*

tical scintillation hodoscopes, TOF-A and TOF-B [88] provide the average time-of-flight resolution of ≈ 100 ps.

Four beam MWPCs are used for the off-line reconstruction of the beam particles, as well as for real-time beam tuning and beam-quality monitoring. They measure the beam particle position and the angle at the target with an accuracy of <1 mm and <0.2 mrad per projection. They are located close to the target in order to reduce multiple scattering effects between the track measurement and the target. The HV settings are chosen so as to maintain the efficiency between 99% and 100% for each chamber.

A beam muon identifier is placed at the downstream end of the HARP detector. Beam muons need to be identified since they would lead to a wrong interaction cross-section when accounted for as pions. At high momenta the most effective way to tag them is through non-showering in a sufficiently deep, longitudinally segmented calorimeter. At low beam momenta, beam muons, which generally result from kaon and pion decays along the beamline, are hardly discriminated from pions but are strongly bent by the magnetic dipole field of the HARP spectrometer.

2.4 Trigger detectors

The detectors used for triggering can be divided into two groups: beam particles are detected upstream of the target, whereas the detection of secondaries emerging from the target relies on downstream detectors and detectors surrounding the target. A schematic view of the relative position of all trigger and beam equipment is shown in fig. 2.3.

Two HALO counters (A, B), made of two scintillator slabs each with a central hole, serve to veto events in which the beam particle is accompanied by a second particle in the halo of the beam. The hole diameter of 3 cm is consistent with the target diameter.

The beam scintillator (BS) starts the decision logic of the trigger system. It is located a few centimetres downstream of TOF-B. In coincidence with a TOF-B hit it represents the lowest-level trigger (strobe). As a consequence, the timing of all trigger signals is given by the original BS signal, *i.e.* BS provides the timing reference for all ADC gates, TDC start and stop signals.

The Target Defining Scintillator (TDS) is a scintillator disc of 20 mm diameter and 5 mm thickness which is viewed by four photo-multiplier tubes. The TDS is designed to have a very high efficiency and to define a subset of beam particles which are guaranteed to hit the target. Therefore, it is located as near as possible to the entrance of the TPC and its 20 mm diameter is smaller than that of the target which is 30 mm. The TDS gives a signal if at least one PMT recorded a hit. An efficiency of well above 99.9% is assured. The TDS has a sufficiently good time resolution ($\sim$ 130 ps) and stability to be used as an additional detector for the beam TOF system.

The Inner Trigger Cylinder (ITC) provides a trigger for large-angle secondaries emerging from the target. It is mounted inside the inner field cage of the TPC and consists of an aluminium/carbon tube with a length of 1300 mm and an inner and outer diameter of 76 mm and 92 mm respectively. Six layers of scintillating fibres (each of diameter 1 mm) are glued on the tube (see fig. 2.6). Triggering on a logical OR condition of all 24 channels provides a combined efficiency for a single track detection of well above 99%.

Downstream of the solenoid, the Forward Trigger Plane (FTP) covers the small angle region complementary to the ITC. It is made of two planes of scintillator slabs. The efficiency of the FTP for single tracks is larger than

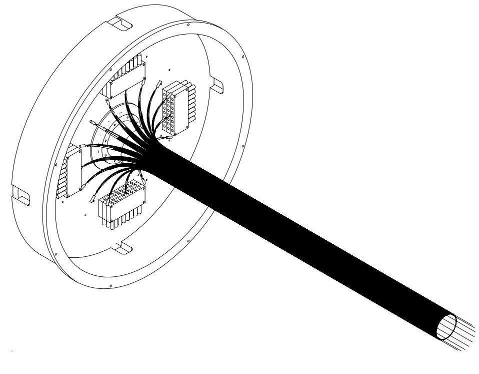

Figure 2.6: *Sketch of ITC. It is inserted into the inner field cage of the TPC. The compartment with the PMT housings is fixed outside the magnetic field on the upstream solenoid end-cap.*

98%.

2.5 The large angle spectrometer

The large-angle spectrometer includes a Time Projection Chamber (TPC) and a system of Resistive Plate Chamber (RPC) counters located inside a solenoid magnet. The detector has to measure and identify large-angle tracks in the angular region 0.23 rad $\leq \theta \leq$ 2.44 rad with respect to the beam direction. Particle identification is obtained mainly via the $\mathrm{d}E/\mathrm{d}x$ measurement from TPC. At higher momentum the p/π separation is made by combining the $\mathrm{d}E/\mathrm{d}x$ and of time-of-flight information.

2.5.1 Time Projection Chamber

An acceptance as close as possible to the full solid angle coverage is required to measure the total and differential cross section of particle production for the largest possible fraction of the secondary phase space. HARP has chosen a TPC with the target located at the centre of the active volume, where the inner field-cage surrounds the beam pipe. The target is placed in a truncated inner field cage, whose geometry is determined by the fact that, in the laboratory frame, the interaction products are boosted in the forward direction. As a consequence the Time Projection Chamber can track and identify particles in the large-angle region between 0.23 rad and 2.44 rad. The dimensions and parameters of the various elements are summarized in table 2.5.1. The beam enters the inner field cage from the upstream end of the TPC, and impinges on a target placed about 50 cm downstream of the pad plane (see fig. 2.7).

The outer and inner field-cage (OFC and IFC) dimensions are 154.1 cm and 79.9 cm long respectively and they have a diameter of 82 and 10.2 cm; they are made of 8 mm and 2 mm thick Stesalit® (65% glass fibres + epoxy) cylinders. The amount of material in the radial direction has been kept to the minimum, compatibly with the small dimensions of the detector and with the need to build an interaction trigger around the target region. Before reaching the 2 mm Stesalit® wall of the inner field-cage, particles emerging from the target first have to traverse the Inner Trigger structure, made by a 1 mm thick bakelite support and three 2 mm thick layers of scintillating fibres. Following simulation results with the Maxwell software package [89] for the electric field geometry and the Garfield package [90] for the electron drift, the inner field cage and the outer field cage were both built with a double interleaved strip pattern. The first set is made by a conductive pattern on the surface of the field-cages; the second one is provided by aluminized Mylar

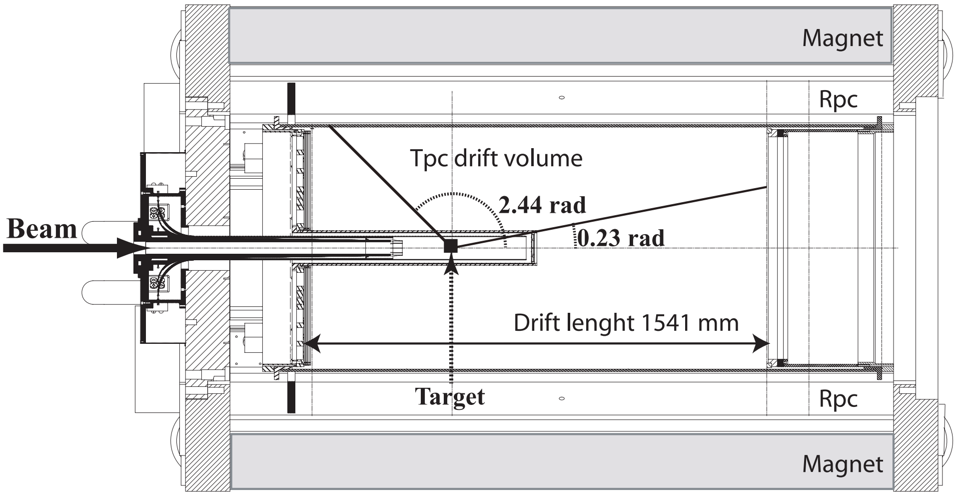

Figure 2.7: *Schematic layout of the TPC. The beam enters from the left. Starting from the outside, first the return yoke of the magnet is seen, closed with an end-cap at the upstream end, and open at the downstream end. Inside the yoke the cylindrical coils are drawn in grey. The field cage is positions in the middle of this magnetic volume. The inner field cage is visible as in insert from the left. It contains the ITC trigger counter and target holder.*

strips (25 μm thick) positioned close to the field-cage surface by means of Stesalit rods, which also support the voltage degrader by a system of resistors (R=262 kΩ). The strips have a width of 1 cm and a gap of 1 mm. This pattern avoids electric field inhomogeneities and high field gradients, which would produce sparks or corona currents in Ar gas. Fig. 2.8 and fig. 2.9 show the IFC and OFC with the aluminized Mylar strips.

The capability of the experiment to collect large data samples is required to obtain a precise measurement of the different double differential cross sections. The design goal of 500 events per 400 ms spills required a very careful study, since a rate of $\approx$ 1 kHz is challenging for a TPC of this size. The sources of dead time in a TPC are 1) the drift time, determined by the drift velocity in the gas volume, and 2) the readout time of the front-end electronics. Both have to be reduced as much as possible.

The gas mixture and the applied drift electric field have been chosen to ensure that the dead time due to the drift time is $< 10\%$ of the total dead time. The gas mixture eventually retained for the HARP TPC is Ar/CH_4 91%/9%. For the chosen drift electric field $E = 111$ V/cm, the drift velocity is about 5.1 cm/μs, which keeps the total drift time of 30 μs within the required limits. The OFC high-voltage membrane is set at 17.1 kV and the IFC at 8.4 kV.

Item	**Dimension/value**
Active length (OFC drift length)	1557 mm
OFC inner/outer diameter	816 mm / 832 mm
IFC length	776 mm
IFC inner/outer diameter	102 mm / 106 mm
Field cage strip width/pitch	10 mm / 1 mm
Field gradient	110 V/cm
Number of readout pads	3972
Pad dimensions	6.5 mm × 15 mm
Anode wire Voltage	1820 V
Anode wire (W + Au) diameter/pitch	20 μm / 4 mm
Distance between pad plane and anode wires	5 mm
Cathode wire (Cu + Be) diameter/pitch	70 μm / 2 mm
Distance between anode wires and cathode plane	5 mm
Gating grid wire (Cu + Be) diameter	70 μm
Gating grid wire pitch (per plane)	4 mm
Gating grid effective wire pitch	2 mm
Distance between cathode plane and gating grid	6 mm
High-voltage end-plate thickness (aluminized mylar)	50 μm
Gas mixture	Ar (91%), CH_4 (9%)

Table 2.2: *Dimensions and parameters of the TPC.*

During the TPC operation, the HV at the downstream end of the IFC is different by about 2% from the HV value on OFC at the same z position. This effect causes unwanted electric field components associated with track distortions (see section 4.7).

The total drift time of the TPC corresponds to 300 samples (one sample each 100 ns); additional samples (30 before the start of the triggered event's drift time and 30 after the end) are saved to check for piled-up events. Advanced processing capabilities, like real-time zero suppression, pre- and post-sampling, tail cancellation and data compression, are available to reduce the data volume. The event rate goal could essentially be met, with a total dead-time per event usually of about 600 μs; different target thicknesses and beam energies made this figure very significantly, primarily depending on particle multiplicity in the chamber.

The TPC is inserted in the solenoid magnet operating at a field of 0.7 T that permits the momentum determination. Its magnetic volume has a diameter of 0.9 m and a length of 2.25 m. The operating current is 889.4 A. The magnet is closed by a 15 cm thick cap on the upstream end, with a 15 cm diameter hole for the incoming beam and the target support. The cylindri-

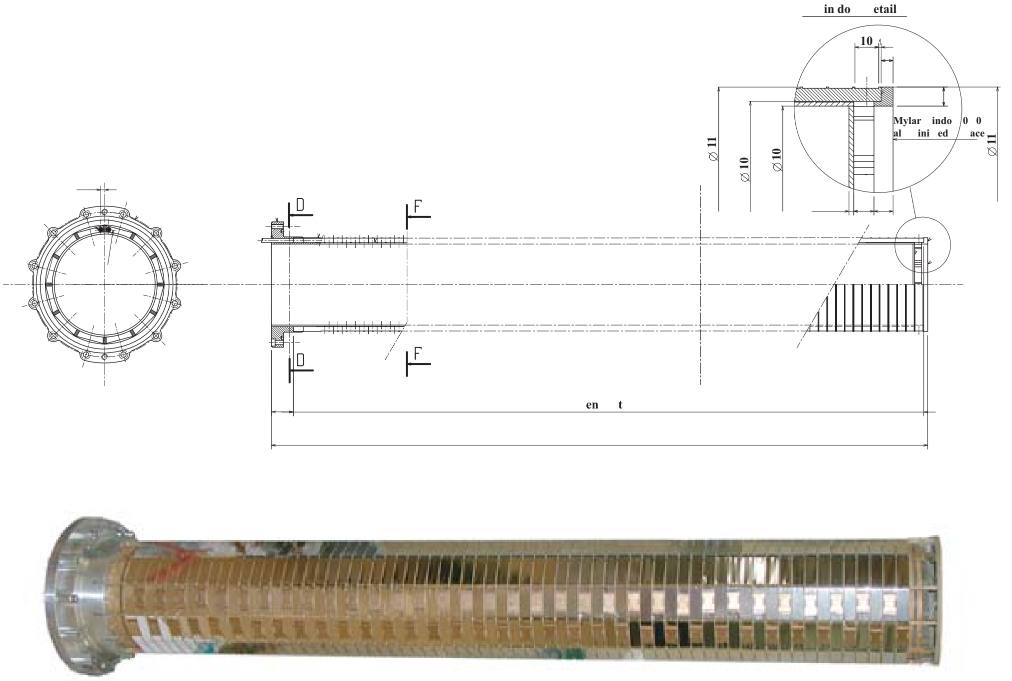

Figure 2.8: *On the top a schematic drawing of the inner field cage and on the bottom a photo with the aluminized Mylar strips.*

cal volume is left open at the downstream end for the passage of secondary particles to the forward spectrometer. The TPC detector is positioned in the most homogeneous part of the magnetic field volume.

Its magnetic field was measured using a set of 48 Hall probes mounted on a rotating axis. Within the volume of the TPC the field along the z axis is known accurately and differs by at most 3% from the nominal 0.7 T value (downstream and at large radii). The radial component of the field is typically less than 0.5% except at large radii where it locally represents up to 1% of the main field. There is no azimuthal field component. The field calculation, based on OPERA® software [91], was iterated until it agreed to better than 0.5% with the measurements.

The TPC readout structure, made of wire chambers readout by pad planes, are placed at the upstream face of the TPC cylinder, to minimize the amount of material in the downstream direction. The HV end-plate is made by a light-construction Mylar membrane.

Charge amplification in front of the pad plane is provided by a set of wire planes. When the ionization electrons reach the readout chamber at the

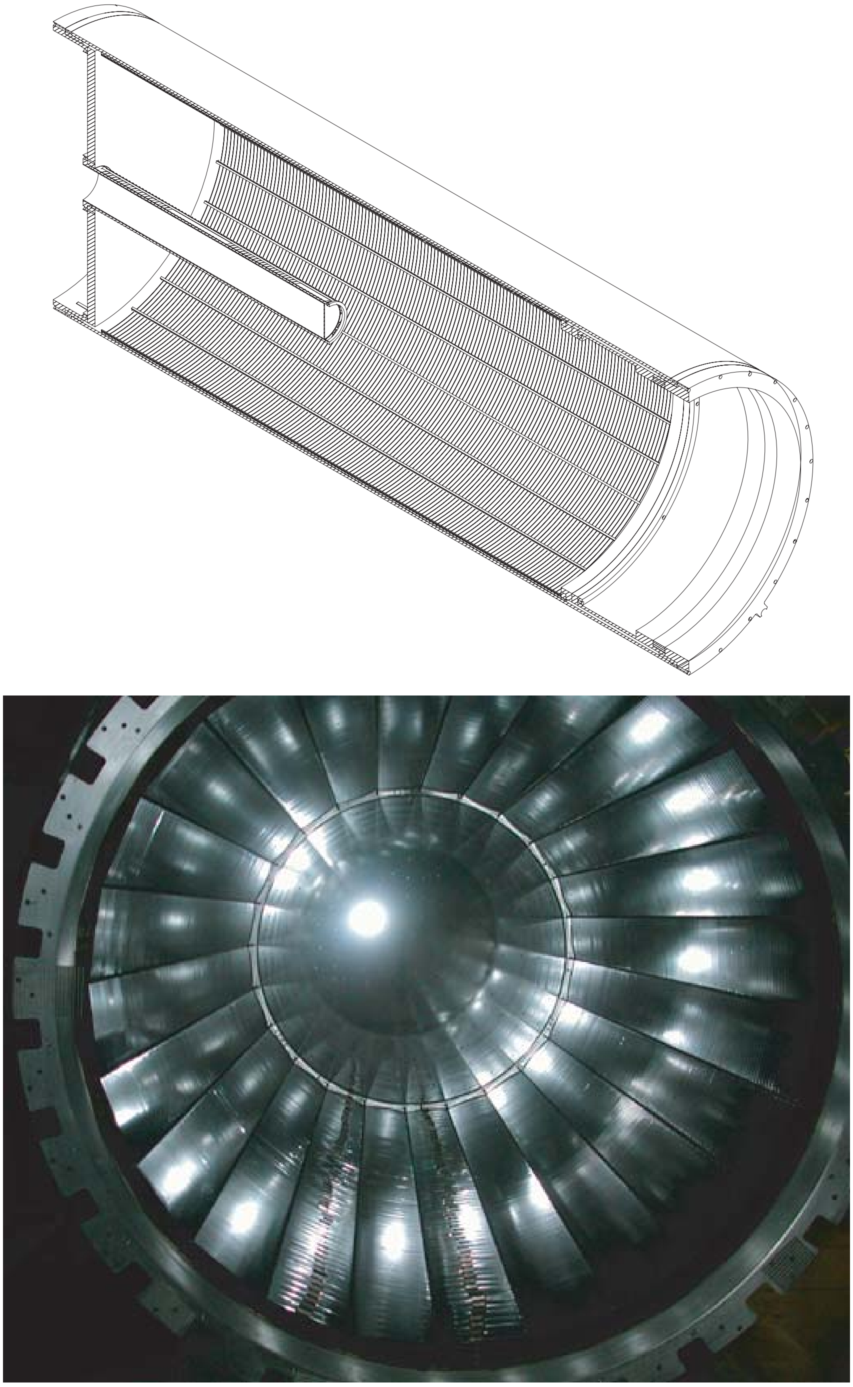

Figure 2.9: *On the top a transverse view of the outer field cage and on the bottom a photo with the aluminized Mylar strips.*

upstream end of the TPC, they first encounter the gating grid consisting of two interleaved single-wire planes at a base voltage of −67 V and a sweep voltage of ±35 V. To reduce the ion feed-back into the drift volume the gating grid is normally kept closed, and only opened during the drift time of a triggered event. Electrons passing the gating grid are multiplied by the anode wire plane (set at 1830 V) located in between the cathode wire plane and the pad plane (both kept at null potential).

To reduce dead space due to mechanics and supports, wire planes are constructed by stringing a single wire over an hexagonal frame. The wire diameter is 20 μm for the anode wire, 50 μm for the gating grid wire, and 70 μm for the cathode wire. The wire pitch is 4 mm for all planes. The use of a single wire provides equilibrium of wire-tension forces on both sides of the wire-support spokes, which have a width of 6 mm only. Fig. 2.10 shows the photos and the drawings of wire plane. Further parameters and dimensions of the wire planes are given in table 2.1.

Given the limited dimension of the TPC, a compromise had to be found between the conflicting requirements of providing many measurement points

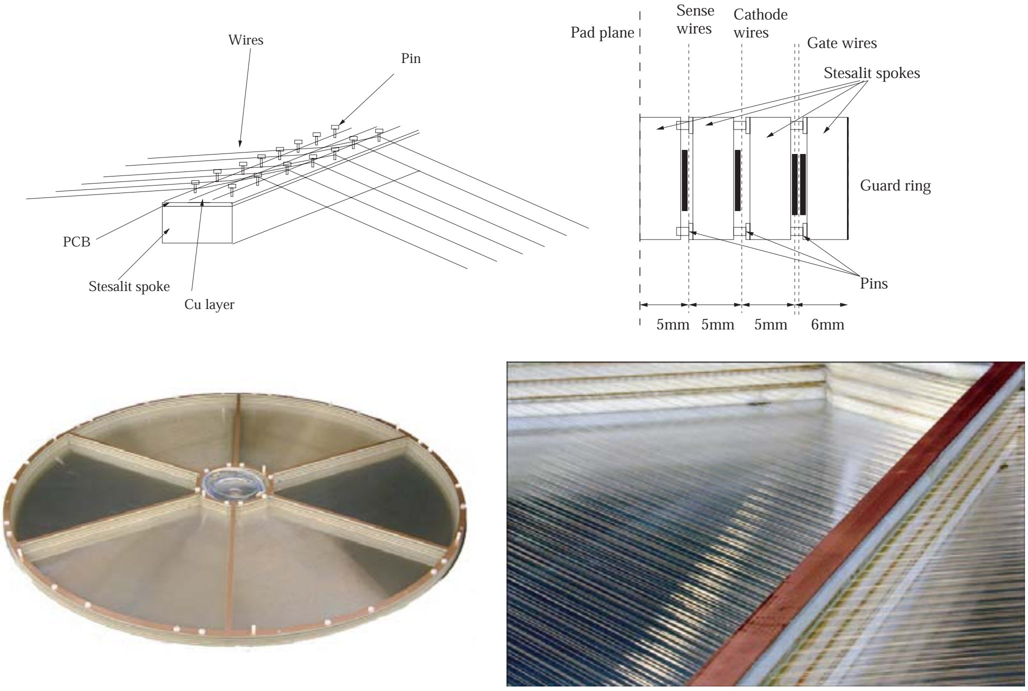

Figure 2.10: *Top: on the left a detail of the spoke where the wires increase the radius of the hexagon; on the right a schema of the wire and pad plane structure. Bottom photos of the wire plane*

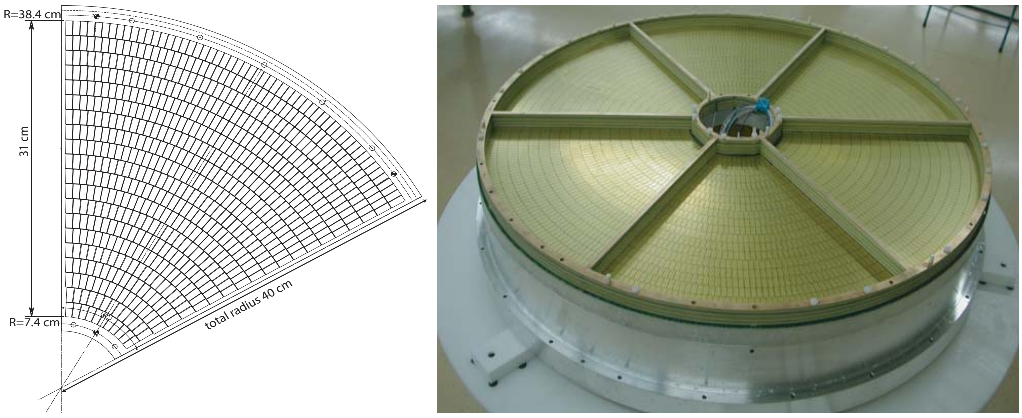

Figure 2.11: *On the left: mechanical drawing of a sector of the TPC, the layout of the pads is indicated. On the right: a photo of the pad plane.*

along high p_T tracks and the need not to spoil the point resolution by reducing too much the ionization statistics per pad. The choice was been made to subdivides radially the pad plane, made of 6 independent sectors, into 20 rows of pads. The pad dimensions are about 6.5×15 mm^2 and there are from 11 (at the inner radius) to 55 (at the outer radius) such pads per row and per sector. The transverse pad dimension and the anode to pad distance have been optimized for a FWHM of the pad response function corresponding to the size of the pad, thus ensuring enough charge sharing between adjacent pads. Fig. 2.11 shows a mechanical drawing of the TPC pad layout and a photo of the pad plane.

The pad plane is made in standard PCB (printed circuit board) technology. The sectors are 6-layers PCBs, carrying 662 pads on one side, and the front-end preamplifiers on the other. The pads are connected to ALCATEL® SMB302 preamplifiers/shapers, whose typical signal rise-time is $\approx$ 150 ns. The preamplified signals are fed, via bundles of pico-coaxial cables, to 48 channel flash ADC (FADC) cards, located in VME crates; 14 such cards were needed to read out each sector. The FADC cards were developed as a prototype [92] of the ALICE TPC [93] front-end system; due to their attractive performance they were adopted by the HARP and CERES [94] experiments. Each FADC card provided 10 bit, 10 MHz sampling, giving several samples during the typical duration of the signals, and allowing a complete waveform analysis during the off-line reconstruction.

A full description of calibration procedure and of the detector performance is given respectively in chapter 4 and in chapter 5.

2.5.2 Resistive Plate Chamber system

Resistive Plate Chambers (RPCs) were chosen as a time-of-flight system in the large and medium angle acceptance region for particle identification at momenta in which the $\mathrm{d}E/\mathrm{d}x$ measurement in the TPC cannot distinguish between electrons and pions (100–250 MeV/c). The basic requirements for the RPC design were a good time resolution of about 200 ps and an efficiency close to 100%. Based on these requirements, multi-gap RPCs were chosen [95].

The RPC system consists of 46 identical chambers, 10 mm thick, 150 mm wide, and 2 m long. Thirty of them are arranged as a barrel around the TPC providing full coverage in azimuth and covering polar angles from 0.30 rad to 2.48 rad with respect to the beam axis. The chamber dimensions and shape were chosen such that two overlapping layers of RPCs fit into the ~25 mm radial free space between the TPC and the coils of the solenoidal magnet, see fig. 2.12. The remaining 16 RPCs are installed downstream of the TPC, perpendicular to the beam before the FTP trigger. They are arranged in four groups of four overlapping RPCs each, and cover the angular region 105 mrad to 280 mrad. The RPCs were operated in avalanche mode with a gas mixture of 90% $C_2F_4H_2$, 5% SF_6, and 5% C_4H_{10}. The HV was −6 kV over two gas gaps.

The efficiency and time resolution of the RPCs have been measured for a few chambers in a dedicated beam exposure; intrinsic time resolutions of

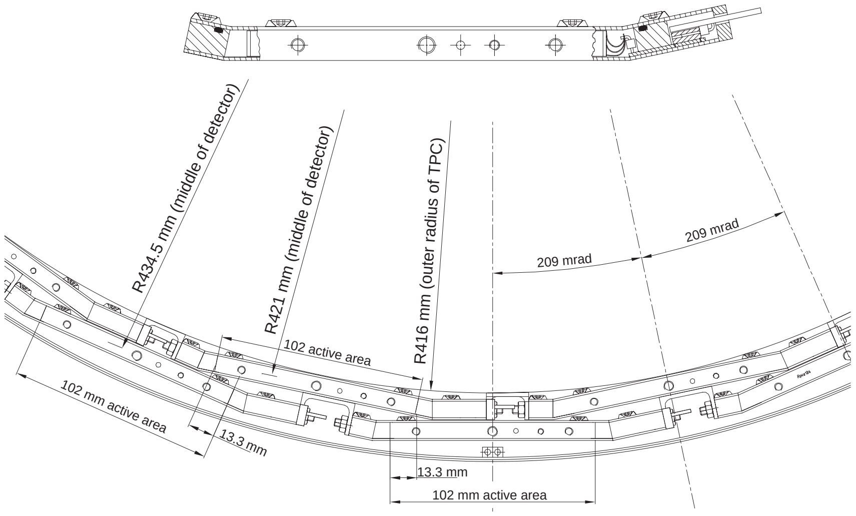

Figure 2.12: *Cross-section through single RPC and arrangement of barrel RPCs around the TPC.*

~150 ps and ~98% efficiency over a HV plateau of a few hundred volts were found. The efficiency was determined using two RPCs as trigger and then checking for the presence of a hit in the third RPC. Particle intensities in this run were 3 kHz/cm^2 in the centre of the beam (compared to rates below 1 Hz/cm^2 in normal data taking).

An estimate of the time resolutions for the RPCs installed in the detector has been obtained by studying negative pion tracks passing through the overlap region between two neighbouring chambers. The spectrum (accumulated over all RPC pads) of the time difference between two measurements of the same track in two overlapping RPC pads has a width that corresponds to the convoluted time resolutions of the two RPCs, leading to a resolution of $\sigma = 203$ ps, if both pads are assumed to contribute equally. The resolution measured in this way includes uncertainties related to the time-slewing correction, the impact point corrections [96, 97] and correction of temperature drift of RPC time response. A linear dependence of the RPC time response on ambient temperature was found, with a slope as big as 49±5 ps/deg, and was corrected for on run-by-run basis individually for each pad. It has been observed that the time resolution is independent of particle momentum but varies with pad position along the beam and measured charge of the signal (see fig. 2.13).

Fig. 2.14 shows the capability of the RPCs to distinguish between differ-

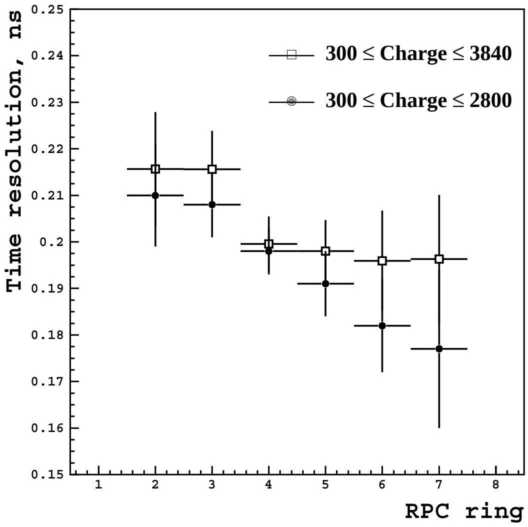

Figure 2.13: *Pad resolution averaged over rings of pads with the same z-position as a function of the pad number for two ranges of signal charge.*

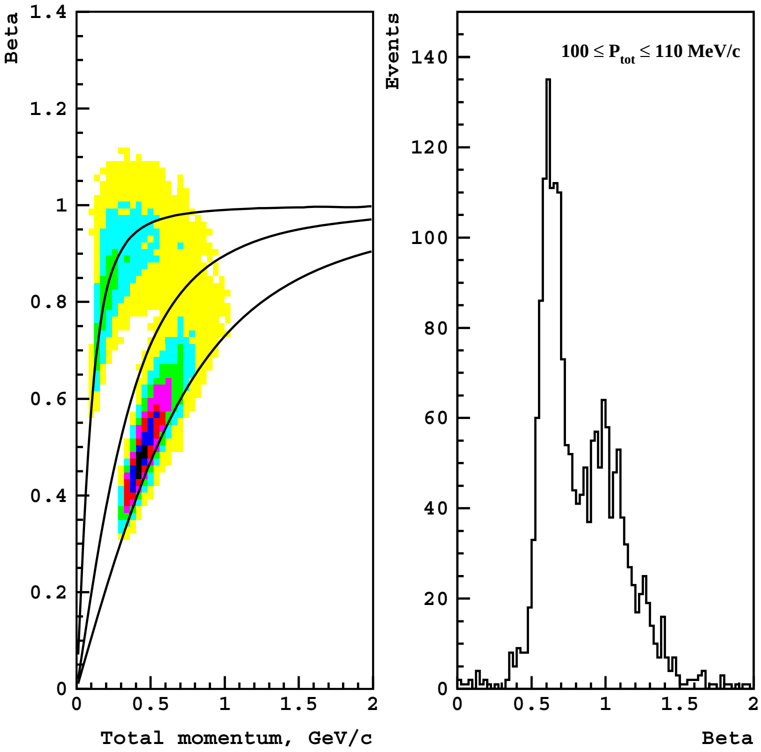

Figure 2.14: *$\beta = v/c$ versus momentum plot for positive tracks (left). β is calculated from the time-of-flight measured with RPCs (pion time-charge correction applied for all tracks) and the track length reconstructed in the TPC. The nominal β versus p lines for pions, kaons, and protons are shown by solid lines. The proton line passes below the proton "island" because of a systematic time shift of proton signals when pion time-charge correction is applied to them. The one-dimensional projection of β in the indicated momentum range (right).*

ent particles as extracted from runs with 8 GeV/c beam on 5% λ_{int} Cu, Ta and Pb targets for positive secondaries. The left plot shows tracks of all momenta, while the right one is the one-dimensional projection of the indicated momentum slice.

Fig. 2.15 demonstrates the particle identification power of combined measurement of time-of-flight by RPC and energy losses by TPC. Islands of electrons and pions can be easily discerned up to momenta of 150 MeV/c. For higher momenta more sophisticated mathematical procedures are to be applied for assigning identification tags to reconstructed tracks.

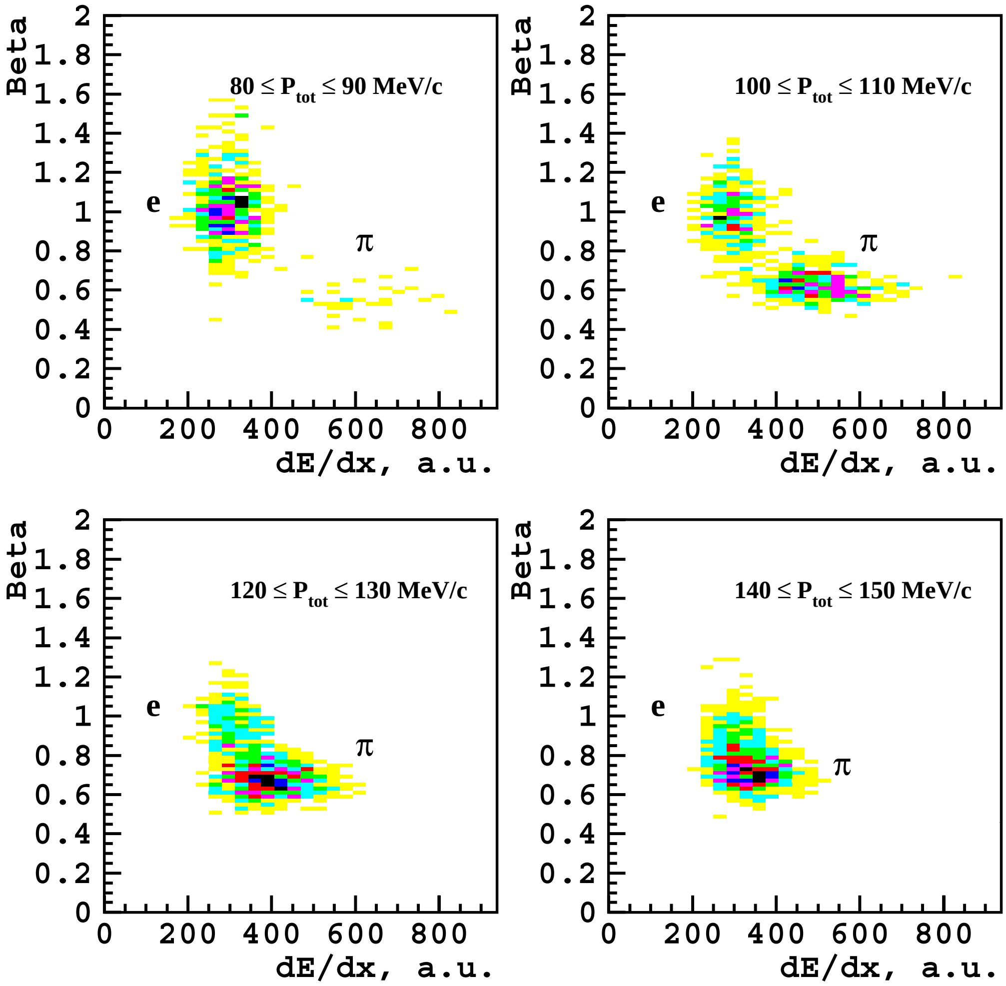

Figure 2.15: *β versus dE/dx (in arbitrary unit, a.u.) for the same tracks as in fig. 2.14 in the indicated momentum region. Islands of pions and electrons are clearly discernible.*

2.6 The forward spectrometer

The forward spectrometer measures high-momentum tracks produced at small angles ($\theta \leq 250$ mrad) via a set of drift chambers. Particle identification is performed by combining information from a threshold Cherenkov counter (at lower momenta), a time-of-flight wall (TOFW, at higher momenta) and an electromagnetic calorimeter.

The dipole magnet used for momentum measurement in the forward spectrometer has a non-homogeneous field: its vertical component B_y is 0.5 T in the central region and rapidly approaches zero outside its aperture. Secondary particles leaving the TPC pass through an integral field of $\int B_y\, dL$ of 0.66 T·m.

2.6.1 Drift chambers

A set of large drift chambers[‡] is placed upstream and downstream of the spectrometer magnet (see fig. 2.1) to act as a tracking device for the forward going particles. Five modules of the NOMAD drift chambers (NDC) are used: one directly upstream of the dipole magnet, one directly downstream of the magnet, and three modules more downstream, covering a larger lateral surface between the Cherenkov detector and the TOFW. Each NDC module consists of four chambers.

The dimensions of the NDC modules (3 m $\times$3 m) allow for full coverage of the forward solid angle as defined by the aperture of the spectrometer magnet. A charged particle can leave up to 12 hits in each traversed module, which allows a fairly accurate segment reconstruction, though each chamber represents 2% of a radiation length. Three more drift chambers were used as preshower in front of the electromagnetic calorimeter.

Each chamber is made of four panels of light composite materials delimiting three 8 mm gas gaps. The very efficient NOMAD gas mixture, Ar (40%) - C_2H_6 (60%), could not be used because of the stricter CERN safety rules, and a classical, non flammable mixture: Ar (90%) - CO_2 (9%) - CH_4 (1%) was chosen instead. The central gap is equipped with sense wires at 0° with respect to the vertical axis, the direction of the magnetic field; in the outer gaps the wires are at $+5^\circ$ and -5°. This small stereo angle allows for 3-D reconstruction with full precision in the horizontal direction, essential for the momentum measurement via track bending in the spectrometer magnet.

To extract the performance of the chambers (spatial resolution and hit

---

[‡] These chambers have been re-used from the NOMAD experiment [98], where they served both as a target for neutrino interactions and as a tracker for the produced charged particles.

efficiency) an alignment of all wires had to be performed. We have used samples of cosmic events recorded via a special trigger requiring a coincidence between the forward trigger plane (FTP), the time-of-flight wall (TOFW) and the cosmic wall (CW). The alignment parameters are validated also using beam data taken with a thick target. The resulting residual distribution gives a spatial resolution of about 340 μm, sufficient for the requirements of the HARP experiment.

Reconstructing long tracks allows us to compute hit efficiencies per chamber plane. Fig. 2.16 shows their distribution for the five tracking modules (NDC1 to NDC5, 12 consecutive planes each). The average efficiencies for the central modules (NDC1, NDC2 and NDC5) lie between 80% and 85%, much less than in NOMAD (>95%): this loss of performance can again be attributed to the change of gas mixture and electronics.

Tracks are reconstructed in two stages. In the first stage a segment reconstruction algorithm builds track segments in each module. A special software implementation of the Kalman filter technique [99] is then used for the matching of track segments and for hit collection, taking into account multiple scattering and the exact field map of the spectrometer magnet. To increase track reconstruction efficiency not only tracks with good upstream and downstream segments, with respect to the dipole magnet are considered, but also tracks with short upstream segments or even with only some hits

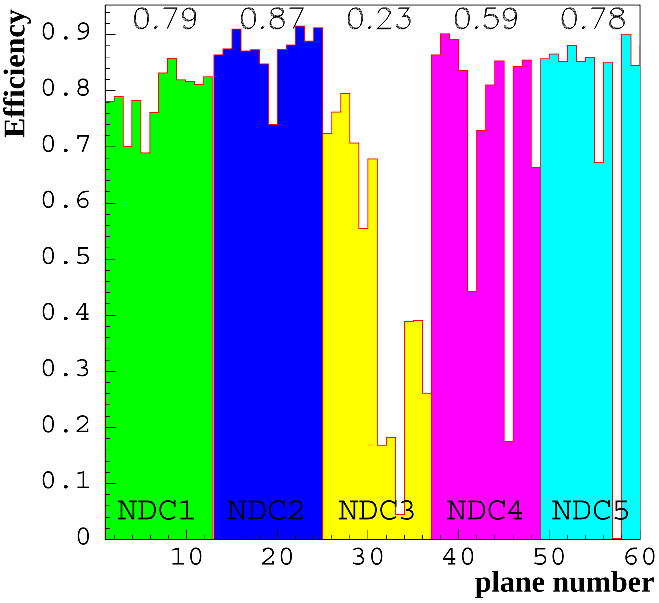

Figure 2.16: *Hit efficiencies of the drift chamber planes. Different modules of drift chambers (from NDC1 to NDC5, 12 consecutive planes each) are shown by different colours. The average efficiency for each NDC module is also given.*

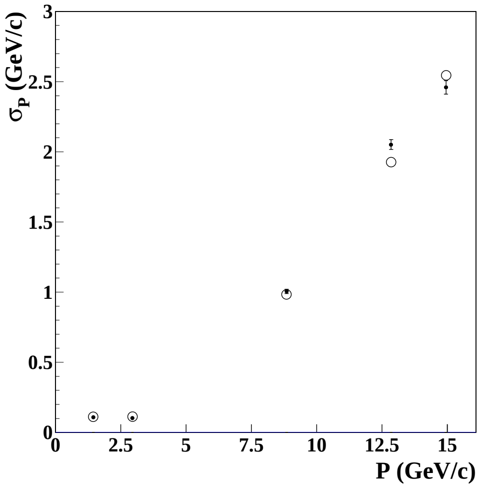

Figure 2.17: *Momentum resolution of the drift chambers: the data (points with error bars) taken using several well-defined discrete beam momenta and no target. Also shown (open circles) the corresponding resolution found using Monte Carlo simulation.*

upstream imposing a vertex constraint. The resulting efficiency for forward track reconstruction amounts to ∼ 80% in the region of interest for physics analysis. The momentum resolution achieved is shown in fig. 2.17.

2.6.2 Cherenkov detector

In the forward direction, the particle identification capabilities of the TOFW are supplemented by a threshold gas Cherenkov detector located immediately downstream of the NDC module after the dipole bending magnet. The radiator gas chosen is perfluorobutane C_4F_{10}. In addition to its environmentally safe properties, its high refractive index allows the detector to be operated at atmospheric pressure in threshold mode to separate secondary pions from protons.

The particles traverse about 2 m of the radiating medium and generate photons that are deflected by about 2.35 rad upwards or downwards by two large cylindrical mirrors 6 m long and with a radius of curvature of 2.4 m. The reflecting layers of aluminium with a protective coating of magnesium fluoride were evaporated on appropriately bent 3 mm thick polycarbonate panels. The average reflectivity of the mirrors was about 90%. A modular structure of assembled honeycomb panels supports the mirrors. The goal of the mechanical design was to obtain a large rigid structure with the minimal mass budget along the path of the dominant flux of particles. The light collection system was optimized using the Zemax-EE v.10 optical design software. A light collection efficiency of about 80% was reached.

In order to identify a particle crossing the active volume a calibration must be performed which assigns the total number of photo-electrons to an individual cluster. In 2002, the detector was equipped with light emitting diodes. Each PMT is equipped with a diode emitting a tiny pulse of light during the inter-spills of the normal data taking. In this way the single photo-electron peaks and the pedestals of each channel can be determined.

Signals in the detector are grouped into clusters, each giving a total number of photo-electrons and a position in the x-y coordinate; since position is computed as a centre of gravity of the hit PMTs, the y coordinate of a cluster is something abstract, showing how much the signal is shared between the upper and lower rows of photomultipliers, while the x coordinate is directly related to the passage of the charged particle through the gas volume. Using runs at varying energies and selecting the beam particles in a proper way a plot for the light yield versus momentum can be obtained, as shown in fig. 2.18.

The curve adjusted to the data is:

$$N_{phel} \propto N_0 \cdot (1 - 1/n^2 \cdot (1 + (\frac{m_\pi}{p})^2))$$

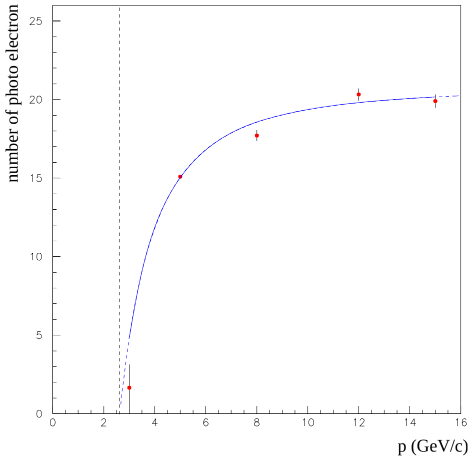

Figure 2.18: *Pion light yield as a function of particle momentum: the dots are the experimental points taken at five different beam momenta (3, 5, 8, 12 and 15 GeV/c). The solid curve is a fit to the data with the function described in the text. The dashed vertical line marks the threshold for light production from pions in a gas with refractive index* $n = 1.0014$.

where the parameter N_0 is the number of photo electrons in the regime of high momentum ($p \to \infty$), n is the refractive index of the gas mixture (constant) and m_π is another parameter of the fit (related to the threshold value) which should be close to the mass of the selected species (pions in this particular case). For the selected sample the fit gives: $N_0 = 20.9 \pm 0.2$ and $m_\pi = 139 \pm 3$ MeV/c^2. This result is in agreement with the value for the pion mass.

The performance of the apparatus can be inferred from the data themselves by exploiting the redundancy of the HARP spectrometer. Information from the NDC reconstruction is used to infer the position of the Cherenkov light cone axis on the PMT plane. Combining the information from the NDC tracks, the Cherenkov hits and the energy measured in the calorimeter, one can discriminate between electrons and pions. An example is shown in fig. 2.19 for a 3 GeV/c run. The scatter plot of the number of photo-electrons from Cherenkov hits versus the energy seen by the electromagnetic calorimeter exhibits two well-defined populations. The pion-like sample is characterized by a low number of photo-electrons (the pions being just above the threshold of 2.6 GeV/c) together with a small energy release in the electromagnetic calorimeter. The electron-like sample is instead characterized by a high number of collected photo-electrons per Cherenkov hit and a typical energy close to the nominal 3 GeV/c measured with the electromagnetic calorimeter.

2.6.3 TOF wall detector

The requirements for the forward time-of-flight wall (TOFW) called for a time resolution of $\sigma \simeq 250$ ps to separate pions from protons at 4σ up to 3.5 GeV/c, on the basis of a 10 m flight path, and a good transverse segmentation to avoid particle pile-up on single counters. Particle identification is achieved by combining leading-edge time measurements (from TDC) with pulse-height information for time-walk corrections (from ADC).

The intrinsic counter resolution of the TOFW has been measured as $\sigma_0 \sim 160$ ps (see [100] for details).

The initial timing calibration (determination of the delay constants of each channel at time $T = T_0$) has been made periodically with cosmic ray runs. In between, the drift of these delays, as a function of the running time T, was traced by a laser calibration system. The precision on the time calibration constants, as determined by the cosmic-ray run and traced by the laser system, was estimated to be ~70 ps.

During the data taking, the time-of-flight of particles produced at the target is obtained from the difference between the times measured in the TOFW and in the TOF-B counter, which has an intrinsic time resolution

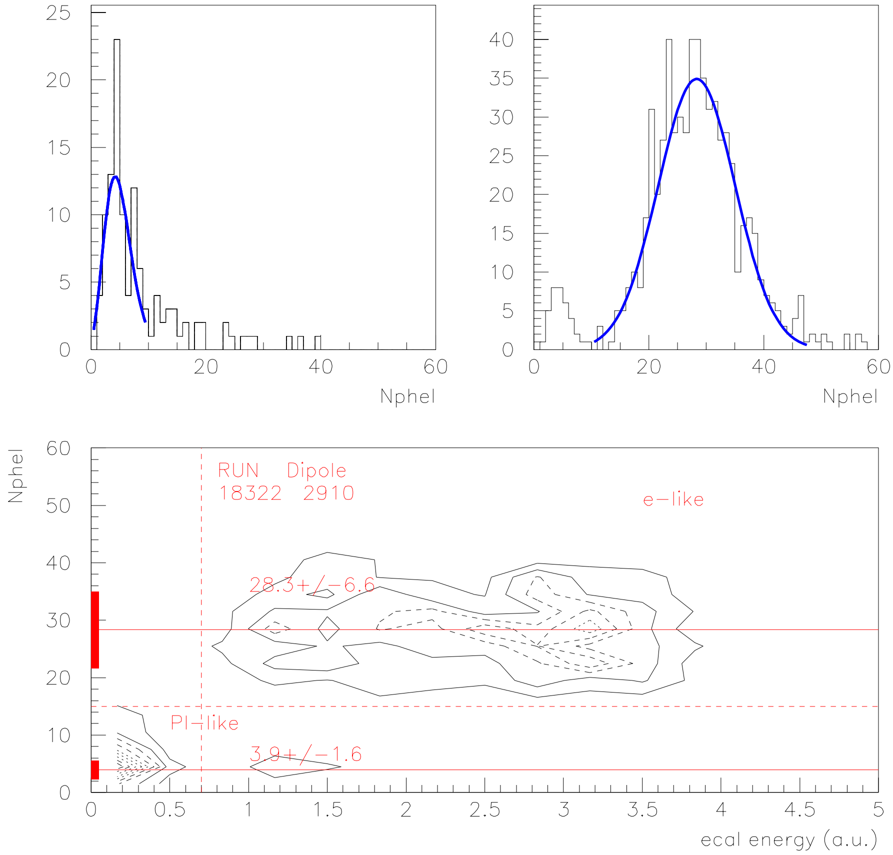

Figure 2.19: *Scatter plot of the number of photo-electrons per Cherenkov cluster versus collected calorimeter energy, showing a clear difference in two populations (namely π-like and electron-like samples). Notice that the energy scale, here shown as arbitrary units, is consistent with GeV within few percent (see the calorimeter section for further details). The red bands on the left side represent the average number of photo-electrons with their uncertainty, resulting from a fit which is shown on the top of the picture.*

of about 100 ps, or from a combination of TOF-A, TOF-B and TDS, with an intrinsic resolution of $\sim$ 70 ps. Therefore the final time resolution on the time-of-flight measurement is $\sim$200 ps, considerably better than the design value of 250 ps.

Particle identification by the HARP TOFW relies on the combination of particle momenta, as measured from the drift chambers, and the time of flight between a start signal and a stop signal from the TOFW itself. The previous calibration issues are essential for the quality of the extracted TOF PID and thus the determination of particle masses. After the calibration procedure, π and p are separated at better than 5σ at 3 GeV/c incident momentum, as shown in fig. 2.20.

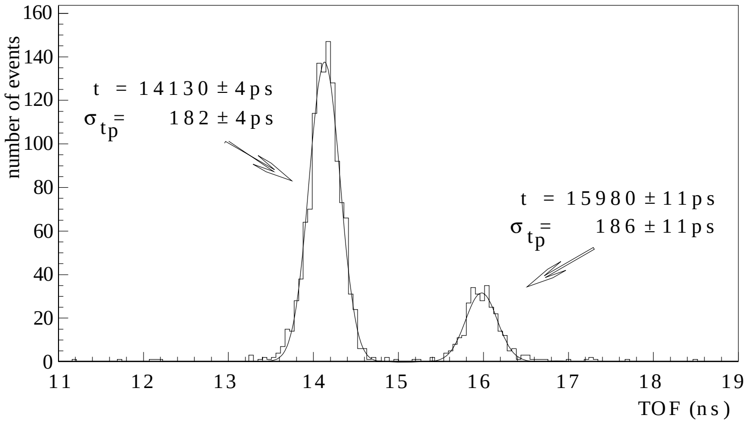

Figure 2.20: *Particle identification with the TOFW detector (pions on the left, protons on the right), with a 3 GeV/c incident unseparated hadron beam. The pion and proton peaks are clearly visible. The time-of-flight is computed between TOF-B and the TOFW system.*

2.6.4 Electron Identifier

The electron identifier was designed to provide electron-pion separation when charged pions, accompanied by knock-on electrons, are occasionally identified as electrons by the Cherenkov counter.

The additional capability of detecting π^0's was achieved by placing a passive converter of 20 mm thick iron in front of the electron identifier to convert a good fraction of photons from π^0 decays. The π^0's are then identified through the two-photon invariant mass reconstructed under the assumption that both photons originate from the target centre.

The sequence of components of the Electron Identifier in the downstream direction is the following:

- an iron photon converter (2 cm thick);
- three NOMAD drift chambers;
- two planes of existing calorimeter modules from the CHORUS experiment [101];
- a plane of scintillators (cosmic wall[§]) to generate a cosmic-muon trigger (in coincidence with the TOFW) to monitor the response of the calorimeter modules.

[§] the cosmics wall is an array of 32 scintillators of 3.20 m × 0.20 m.

Dedicated cosmic ray data samples, taken using the muon trigger mentioned above, were used to provide the calorimeter calibration for equalization of the response in different modules and the measurement of the attenuation length.

The measured energy resolution is about $23\%/\sqrt{\mathrm{E(GeV)}}$ at all energies, well above the nominal value of $(13.8\pm0.9)\%/\sqrt{\mathrm{E(GeV)}} + (-0.02\pm0.04)\%$, obtained by the CHORUS collaboration using test-beam data [101]. Simulation studies have shown that the resolution observed in the data can be explained as a convolution of the detector resolution with the spread of the electron beam energy at the entrance of the spectrometer. The calorimeter resolution can therefore be assumed to be consistent with the nominal value. In addition, results for the measured attenuation length show that the refurbished modules give results consistent with the ones obtained in the CHORUS experiment.

The calorimeter is capable of providing stand-alone particle identification on the basis of the total energy deposition and of the longitudinal shower development, evaluated from the ratio of the energy deposition in the two calorimeter planes. The two-dimensional distribution of total calorimeter energy and ratio of the energy in the first and second plane is shown in fig. 2.21 for 3 GeV particles: the electrons are well separated from the pions.

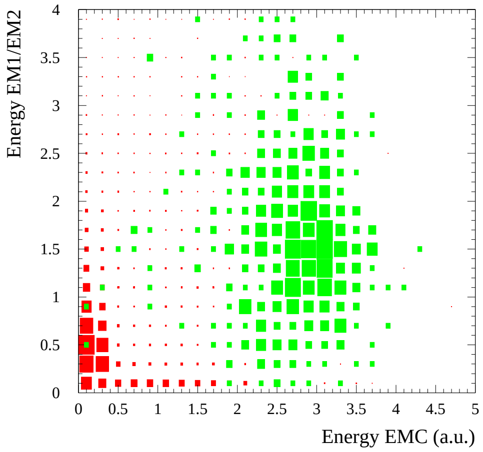

Figure 2.21: *Two-dimensional distribution of total calorimeter energy (in arbitrary unit, a.u.) and ratio of the energy in the first and second plane for 3 GeV particles. Electrons, identified with the beam Cherenkov, are shown in green/lighter, pions in red/darker.*

Chapter 3

TPC Reconstruction

3.1 Introduction

This chapter describes a general view of HARP software framework and of the HARP simulation. Moreover the full reconstruction procedure algorithm and the simulation developed for the TPC is reported in detail.

The TPC reconstruction chain can be divided into the following steps: 1) a calibration algorithm calibrates the signal; 2) a clustering algorithm searches for the spatial points in the TPC; 3) a pattern recognition algorithm associates a group of points to form a track; 4) a fitting algorithm evaluates the helix parameters of a defined track; 5) a vertex fit algorithm evaluates the helix parameters using also the vertex information; 6) a particle identification algorithm performs the PID using the $\mathrm{d}E/\mathrm{d}x$ information; 7) an energy loss algorithm evaluates the energy loss by the particle crossing the different materials before entering in the gas.

A detailed simulation has been implemented for the HARP TPC detector, describing all the physics processes involved in the generation of signals and reproducing their measured performance. Moreover, the behaviour of the front-end electronics is reproduced to perform the digitization, sampling and packing of data. At the end of this chain the data are available in the same format as raw data.

3.2 HARP Software framework

The HARP software environment is based on an Object Oriented (OO) design implemented in C++. Within this framework the software is organised into packages, each with a specific task defined by the user requirements. The HARP software components described in fig. 3.1 have been developed

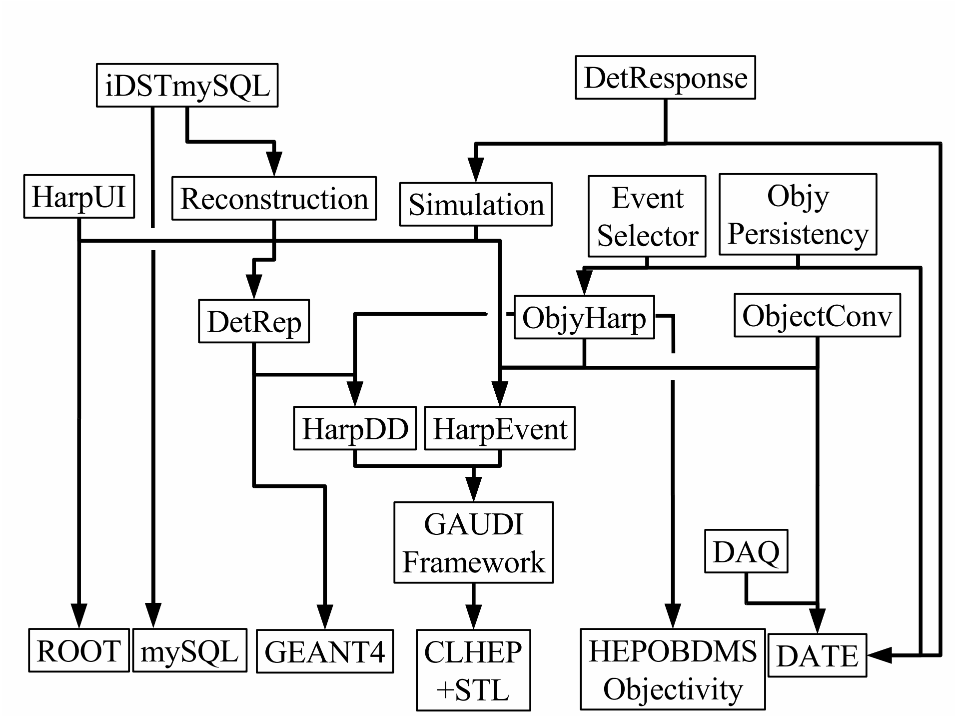

Figure 3.1: *HARP Software architecture. The various components are explained in the text.*

and used for detector calibration and performance studies, trigger and background studies, beam particle identification, on-line applications, studies of data quality, and large scale event reconstruction productions for data analysis.

A short description of the functional specifications of these software components is given in the following:

- DAQ is the data acquisition software based on the DATE [102] package.
- HarpEvent is the component implementing the HARP transient event model, including a structured description of settings, reconstruction objects, Monte Carlo (MC) information, etc. It is based on the Gaudi framework developed by the LHCb [103] experiment.
- HarpDD is the component implementing the HARP detector geometry and materials data in a neutral-representation format. It also contains the alignment and calibration data description.
- DetRep is the component creating the various geometrical representations of the detector objects most suitable for use by the physics

applications. It is based on the GEANT4 [83] solid modelling.

- ObjyHarp is the component implementing the HARP persistent event model. It is based on ObjectivityDB database, and mirrors the transient event model. In 2003, HARP migrated its data to Oracle, thus an equivalent component implementing the HARP persistent event model in Oracle exists.

- ObjectCnv is the component implementing the unpacking of the raw data and the construction of the transient C++ objects used by the physics applications. It can use transparently both on-line data and stored off-line data, as well as Monte Carlo output.

- ObjyPersistency is the component implementing the adapter to use the Objectivity or Oracle databases, while allowing the physics applications not to depend at compile time on the input/output (I/O) solution.

- EventSelector is the component implementing the event selection and data navigation functionality.

- Simulation is based on GEANT4 [83]. It has also been used for the T9 beam line simulation.

- Reconstruction is the component implementing the computation of reconstructed objects at various levels. It uses a dedicated package for Kalman filter operations.

- HarpUI is the component implementing the event display. It was used also on-line. It is based on ROOT [104].

- DetResponse is the component implementing the digitization of the main detectors.

- iDSTmySQL is the component implementing the DST concept for distribution in the collaboration. It contains the persistent-capable physics objects (including reconstruction, simulation, geometry, and event model objects). It supports both a neutral file format and Linux mySQL.

3.3 TPC Reconstruction

The reconstruction of the tracks in the TPC proceeds trough a number of distinct steps:

1. The calibration algorithm calibrates the signals of different pads as a function of time, equalises their gains, and masks the noisy and dead channels.
2. The cluster algorithm [105] reconstructs 3D points.
3. The distortion correction algorithm [106] corrects the point positions using a correction map of the static distortions (described in section 4.7).
4. The pattern recognition algorithm searches for track candidates.
5. The fit algorithm based on a helix model [107] calculates the momentum and the charge of the particle.
6. The vertex algorithm [108] recalculates the momentum using all points of a TPC track and also the 'vertex' point.
7. The particle identification (PID) algorithm [109] evaluates the mean energy loss of the particle in the gas that will be used for particle identification at the analysis level.
8. The energy loss algorithm [110] evaluates the energy loss by the particle passing in different materials (target, ITC, inner field cage) before entering in the gas and calculates the momentum of the particle at the production point in the target.

In the following sections we describe the reconstruction algorithms. The calibration procedure is described in chapter 4 and the PID algorithm is described in section 5.8.

3.3.1 Cluster algorithm

The input for the cluster algorithm is the time-ADC series, with a maximum length of 30 μs, one for each pad. As described previously, the TPC signal of each pad are sampled every 100 ns by a FADC. The first step of the algorithm is to extract from this series a single signal in a continuous time interval, to define in the following step the hit. So we divide the time series whenever the ADC is below a software threshold equal to 5 ADC counts or the time step is bigger than 100 ns (the binning of time series), as illustrated in fig. 3.2.

A hit is defined by the characteristics of this signal:

- position in the xy plane defined by the pad, row and sector number where the signal is collected

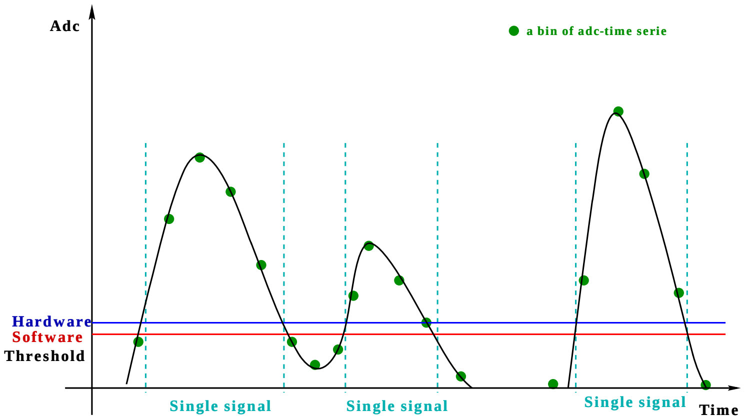

Figure 3.2: *Time series with the hardware and software threshold. The vertical lines divide the time series into single signals.*

- time defined by the z coordinate calculated using the time series of the signal,
- ADC value evaluated by the integral of the signal ADC.

In the second step one groups the hits that belong to the same cluster. These hits should be neighbours in the xy plane (same row number and consecutive pad number) and in time (along z direction). In the last step one calculates the cluster position.

Hit definition: z coordinate

The response of the HARP TPC read-out electronics to a fast input signal (transfer function) is well approximated by a gamma distribution [111]:

$$\Gamma = \frac{t^2}{\tau^2}\, e^{\frac{-t}{\tau}} \tag{3.1}$$

with τ such that the FWHM for a signal is 240 ns, i.e. $\tau = 70$ ns. The factor τ depends (among others) on:

- the shaping time of the electronics,
- the longitudinal diffusion of ionization electrons in the gas,
- the track inclination and the radial extent of the pads.

The signal induced on a pad by a single electron has a shape which is dominated by the transfer function (see fig. 3.3). Although the natural width

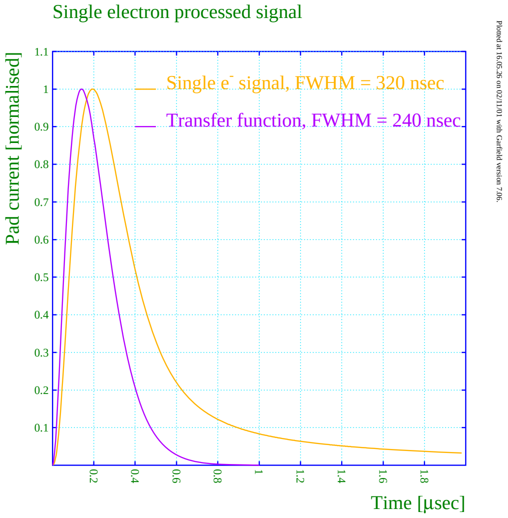

Figure 3.3: *The signal induced by a single electron has a shape dominated by the transfer function that is well approximated by a gamma function.*

of the signals is only a few ns, the long tail is reflected in the 35% increase of the FWHM to 320 − 330 ns, i.e. $\tau = 95$ ns.

The signal induced inside the read out cell is produced by different electrons that follow various drift paths (see fig. 3.4). The difference in drift time associated with these paths (see fig. 3.5) is called the collection isochrony. For the HARP TPC read-out cell, the collection isochrony is of order 100 ns, a minor contribution to the overall signal width.

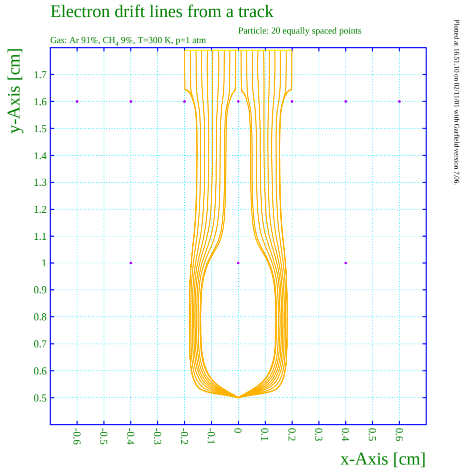

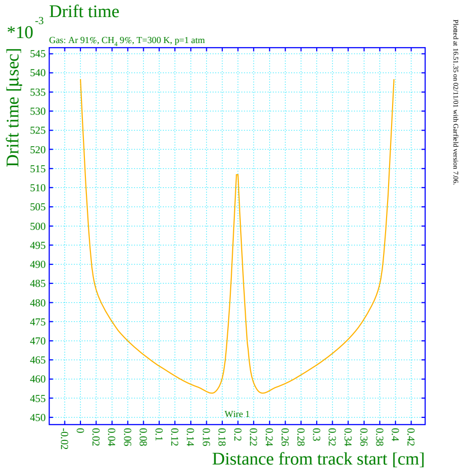

Figure 3.4: *The electron drift lines from a track parallel to the padplane.*

Figure 3.5: *Drift time associated with various drift paths.*

A track near, and parallel to, the pad plane will produce the same shape as that of a single electron signal, marginally broadened by collection isochrony (FWHM of 330 ns). When the track is inclined, some electrons have a shorter drift path to the read-out cell than others: this is defined as the drift isochrony. With a pad width of 1.5 cm and a drift velocity of 5.5 cm/μs, a track inclination of 20° leads to a maximum drift time difference over a pad of 100 ns, at 60° this increases to 470 ns. Up to track angles of 60°, the FWHM is therefore marginally affected by drift isochrony. Beyond this, for inclinations of 80° and more, the width increases rapidly (see fig. 3.6, approximately as the squared sum of the width corresponding to 0° and a tan(angle) term where the angle gives the track inclination with respect to the beam (orange line in the fig. 3.7).

The pulse length seen by a pad increases with the track inclination, which enhances the probability of observing large ionization deposits and large avalanche fluctuations. This leads to a fine structure in the signals, with a corresponding fluctuation in the FWHM.

Due to transverse diffusion, some ionization electrons produced from track ionization reach anode wires facing pads neighbouring the pad toward which the electron would have drifted in the absence of diffusion.

This reduces the number of electrons that contribute to the signal, and thus increases the probability to see spikes in the signal. The effect competes with variations in the energy and species of the particles that traverse the

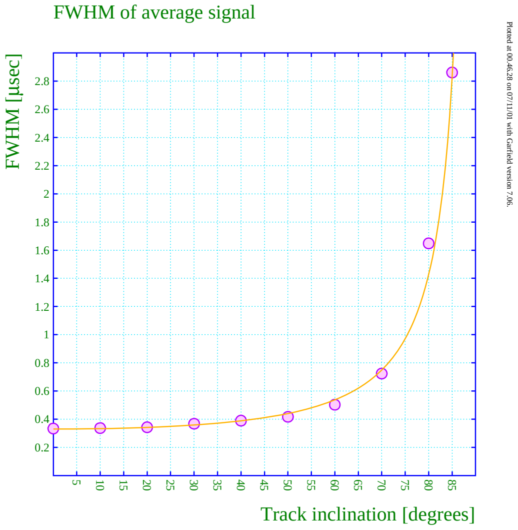

Figure 3.6: *The FWHM increases rapidly, approximately as the squared sum of the* 0° *width and a* tan*(angle) term. Points represent simulated data.*

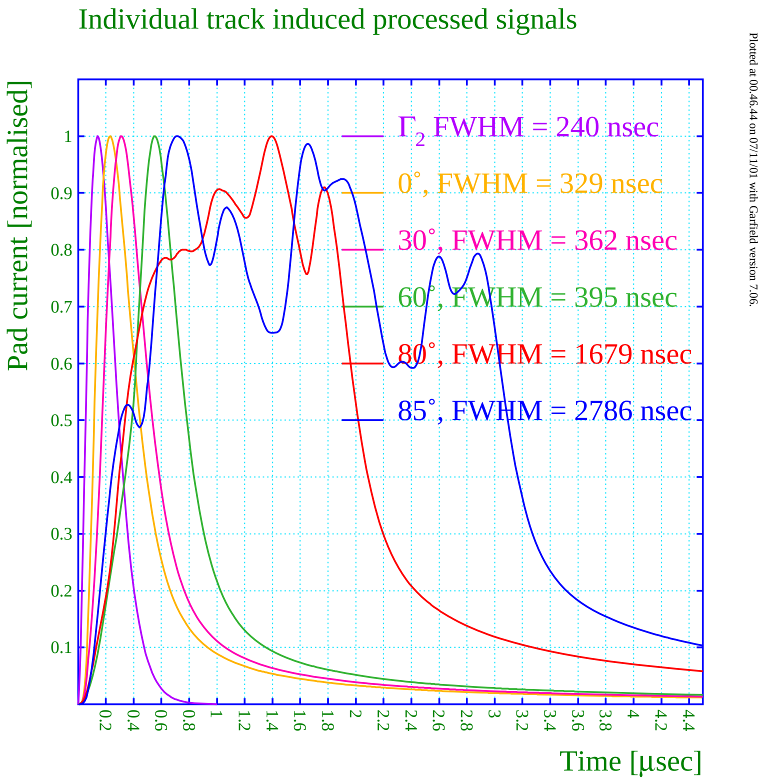

Figure 3.7: *Signal shape with different track inclinations [112].*

TPC. The HARP TPC gas (91% Ar and 9% CH_4) in a magnetic field of 0.7 T has a transverse diffusion coefficient of approximately 200 μm/$\sqrt{\text{cm}}$. Over the maximum drift distance of 150 cm, this leads to a dispersion of 2.5 mm, which is negligible compared to the pad width of 15 mm. We therefore do not expect transverse diffusion to have a visible impact.

Longitudinal diffusion increases the FWHM of the signals. The HARP gas has a longitudinal diffusion coefficient (at all magnetic fields) of approximately 380 μm/$\sqrt{\text{cm}}$ and a drift velocity of 5.2 cm/μs at $B = 0.7$ T. Over the maximum drift distance of 150 cm, this leads to a dispersion of 90 ns. This has a measurable impact only for the tracks that are parallel to the pad plane.

For reconstruction purposes, we need an estimator to extract a z-coordinate from a signal shape. We evaluate different time estimators by a Garfield simulation [90] that includes a simulated signal to electronic noise ratio of order of 10% . The best estimator should have minimal sensitivity to the track inclination and have the smallest RMS possible. The absolute magnitude of a constant bias is not relevant, it will be easily corrected.

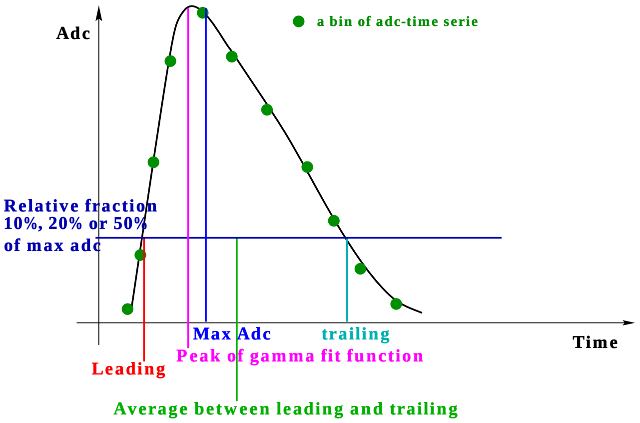

Figure 3.8: *Different time estimators*

We have considered the following options (see fig. 3.8):

- leading edge timing at constant relative fraction (10%, 20% and 50% of the maximum ADC value);
- trailing edge timing at constant relative fraction (10%, 20% and 50% of the maximum ADC value);
- the mean of the leading and trailing edge at a constant relative fraction (10%, 20% and 50% of the maximum ADC value);
- time corresponding to the maximum ADC value;
- time of the peak of the gamma fit function;

By a Garfield simulation we compare the RMS and the bias of the different time estimators. The mean of the leading and trailing edge, with a threshold at 20%, appeared to be the best method [105]. Taking the noise into account, we should count on a z-resolution of order 1 mm for small track inclinations, and of several mm for large angles. Using mean timing, inclination induced biases would reach the level of a few mm at large angles with a noise of 10%.

However, during the data analysis, an unforeseen problem led to a change of the theoretical best time estimator: we discovered a cross talk effect within the multi layer TPC mother boards (as explained in section 4.5). This effect usually generates a signal that is delayed with respect to the real signal. In fact these distortions increase the smearing of the points along z and they create an asymmetry in the residual distribution due to this systematic effect; moreover they decrease the number of points associated to a track. So we concluded that the most robust and precise time estimator is defined by the leading edge time [113].

Hit definition: xy coordinate

The position of a hit in the xy plane is given by the centre of the pad identified by a Sector-Row-Pad number on the TPC pad plane.

Hit definition: ADC

The ADC of an hit is defined as the discrete integral of the ADC series, with the request that the ADC should be larger than a given threshold (5 ADC counts).

Cluster definition

We clusterize the hits in two directions: along the z direction and along the $r\phi$ direction. We obtain two continuous coordinates (z and $r\phi$) and one discrete coordinate along the r direction that is given for each pad by the central radial position of its row. For each row we group the hits of contiguous pads that have a difference in time of less than 600 ns. In the cases where the neighbour pad is considered dead (noisy and dead pads are treated as dead), we accept also the neighbours to the dead pad.

Cluster position in $r\phi$

We have analysed the pad response function to define the method to calculate the cluster position in $r\phi$. E. Gatti et al. [114] have formulated an expression for the pad response function, making assumptions on the electronics noise and making some simplifications for the signal shape. These expressions contain one free parameter (k_3) which depends on the ratio of anode pitch to anode-cathode distance as well as on the anode wire diameter. This parameter has been fitted for various configurations by E. Mathieson and J.S. Gordon [115]. The Mathieson-Gatti function is :

$$\xi(k_3) = a\ k_1\ \frac{1 - tanh^2(b \cdot k_2)}{1 + k_3\ \tan^2(b \cdot k_2)} \tag{3.2}$$

$$k_1 = k_2 \frac{\sqrt{k_3}}{4\ arctan\sqrt{k_3}}\ , \qquad k_2 = \frac{\pi}{2}\ \left(1 - \frac{\sqrt{k_3}}{2}\right)$$

where a and b are two normalization parameters.

The pad response function for the “TPCino” [116], prototype of the HARP TPC, is well described by a Mathieson-Gatti function, as shown in fig. 3.9. The experimental pad response function of the HARP TPC is well described by the Mathieson-Gatti function in the central part, although it

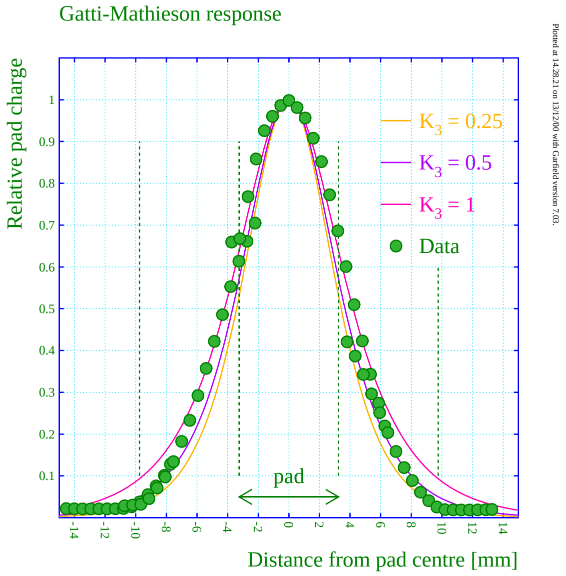

Figure 3.9: *The experimental pad response function for the TPCino (prototype of the HARP TPC) is compared to the Mathieson-Gatti function for 3 different values of* k_3 *(for the TPCino* k_3 *should be equal to 0.5).*

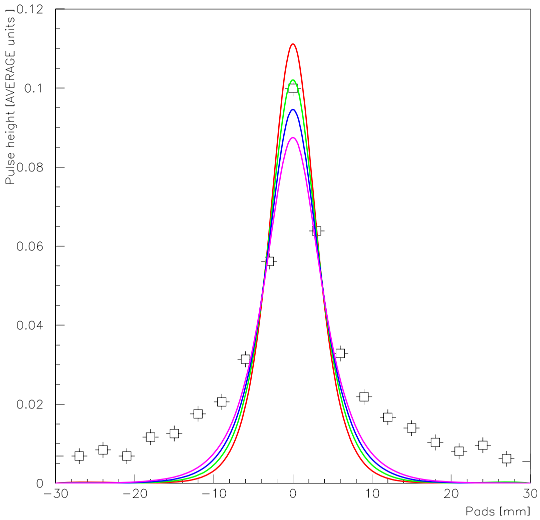

Figure 3.10: *The experimental pad response function is compared to the Mathieson-Gatti function for four different values of* k_3 *(red line* $k_3 = 1$*, green line* $k_3 = 0.75$*, blue line* $k_3 = 0.5$ *and magenta line* $k_3 = 0.25$*); for HARP TPC* k_3 *should be 0.5 [112]. On the* x *axis there is the distance in mm of each pad from the cluster position.*

has long tails (see fig. 3.10). These tails are mainly due to cross talk effects and to dead regions in the pad plane [105]. However the experimental pad response function is symmetric, therefore we define the cluster position as the position barycentre of hits that belong to this cluster, weighted by the hit ADC, as:

$$r\phi_{cl} = \frac{\sum_i r\phi_i \; ADC_i}{\sum_i ADC_i}$$

This definition of the position in the $r\phi$ plane uses as radial position r the central radius of the row.

Cluster position along z

The time position of the cluster is defined by the time of the first hit. Choosing this estimator to evaluate the parameters of the track in the plane perpendicular to the pad plane, one should use the smallest radius of the row for the forward tracks and the largest one for the backward tracks. Therefore the radial position should be defined in different ways in the pad plane and in the plane perpendicular to the pad plane. As explained in section 3.3.3 the fit algorithm consists of two consecutive steps: a circle-fit in the xy plane and a straight line fit in zs_{xy} plane*. Thanks to this feature of the HARP fit we can use different radial positions for the two steps of the fit. In the circle fit the time (z) position of the cluster is not used, therefore the cluster position is defined by the central radius of the row. The linear fit is evaluated twice: the first time to determine the track direction and the second time to evaluate precisely i) the track angle with respect to the z axis, and ii) the z position of the vertex. Technically, in a first iteration the cluster assigns to all points the central radius of the row as radial position. Then we evaluate the track parameters in two steps using the same fit algorithm. Knowing the dip angle of the tracks, we move the points on the helix circle towards the smallest radius of the row for backward tracks and to the largest radius of the row (for forward tracks). After such a reclustering algorithm, we evaluate the fit a second time: the results of the circle fit will be unchanged, and we obtain the correct results for the linear fit.

3.3.2 Pattern Recognition

The pattern recognition algorithm looks for tracks using as input the 3D points defined by the cluster algorithm. This algorithm uses a general framework for track finding in multi dimensional space [117], here applied to the

---

*The s_{xy} coordinate is defined by the arc length between a point and the impact point on the circle in the xy plane.

3D case. This method does not assume any track shape a priori (helix or otherwise). The algorithm first builds a network of all possible links between the points, then it builds a tree of connected clusters, starting from a seed. As the tracks are expected to be less dense in the outer region of the TPC, the links with larger radius are chosen as seeds. In searching for points to be added to the seed link, the line between the two outer points is followed toward the TPC axis. The criterion for adding a new point is defined by a truncated cone as shown in fig. 3.11. The cone size is given by three parameters: a starting radius (SR), a forward acceptance (FA) and an opening angle (θ), all tuned to obtain the best performance. The cone is centred around the linear fit of the track segment (link) found up to that point (considering not more than the last 5 points). After adding new points to the track candidate the axis is re-fitted and the search continues iteratively. Only the best track candidate is retained, while the other candidates are rejected and their points used to look for other tracks. The track finding efficiency is estimated to be 98-99 % with simulated data for an ideal TPC with a nominal resolution and it is 92-96 % for a TPC with unequalised gains and with dead and hot pads [118]. To estimate this efficiency we used Monte Carlo data with a single particle in each event with a complete angular and momentum distribution as defined by the TPC acceptance. The efficiency is defined by the $N_{reconstructed}/N_{simulated}$.

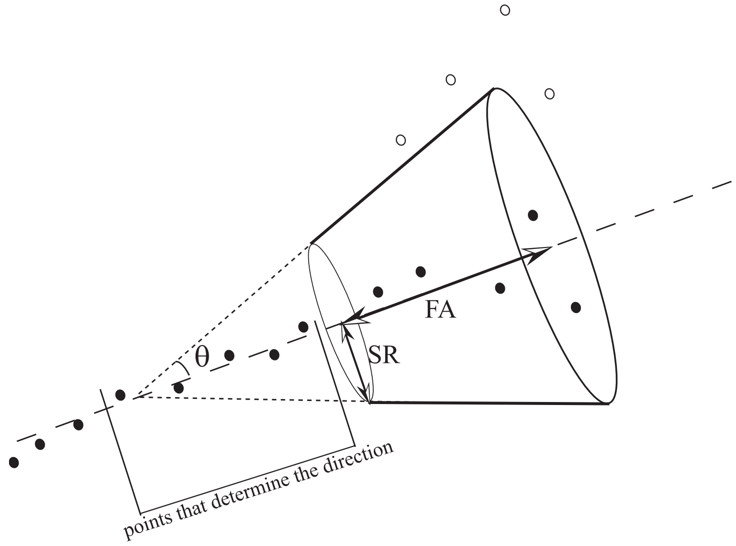

Figure 3.11: *The criterion for adding a new point is defined by a truncated cone.*

3.3.3 Fit Algorithm

The fit algorithm applies an helix fit to the points of the tracks found by the pattern recognition. This fit algorithm is also able to fit the tracks with more than one turn along the helix. The fit algorithm consists of two consecutive steps: i) a circle-fit in the xy plane that defines three parameters (d_0, ϕ, ρ), and ii) a straight line fit in zs_{xy} plane that defines the other two parameters (z_0, s_{xy}). These five parameters (shown in the fig. 3.12) describe the helix in space. They follow the same sign convention as in the TASSO and ALEPH [120] experiments, [121] and are chosen as follows:

- ρ is the inverse of the radius of curvature in the s_{xy} plane. Its sign describes the direction associated to the track: positive if the direction is clockwise and negative if the direction is anticlockwise.
- d_0 is the impact point in the xy plane, i.e. the minimum distance between the track and the z-beam axis in the xy plane. Its sign indicates if the helix encircles the z-beam axis (positive sign) or not (negative sign).
- ϕ_0 is the emission angle in the xy plane at the impact point, i.e. the angle between the x axis and the oriented tangent (the tangent direction is given by the sign of ρ) to the track at the impact point.
- z_0 is the z coordinate of the impact point.
- $\tan(\lambda)$ is the tangent of the dip-angle, with λ defined as the angle between the z-beam axis and the s_{xy} coordinate.

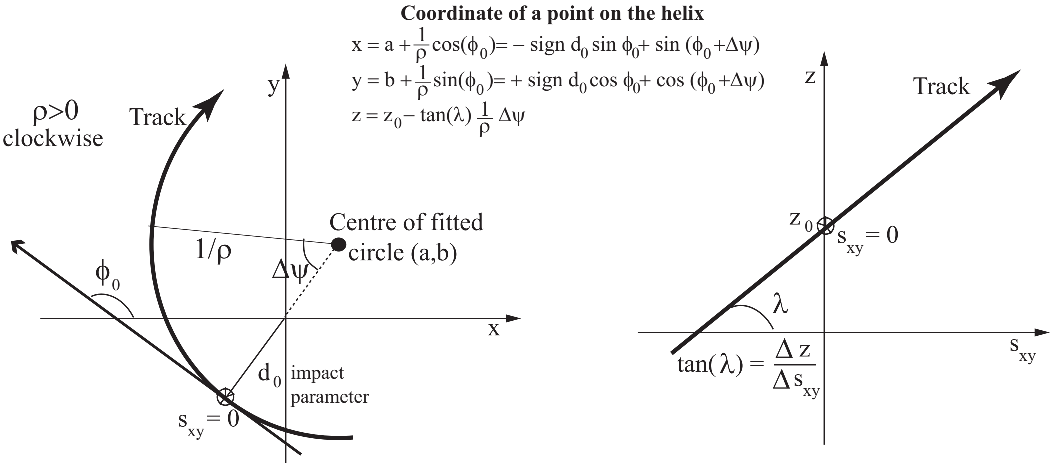

Figure 3.12: *The helix parameters in the xy plane on the left and in zs_{xy} plane on the right.*

By these parameters and these conventions one can describe an unique helix with a direction associated to the motion along the helix itself. The same helical trajectory could be described by different parameters if the direction associated is opposite (for example a different sign of ρ). To set the direction associated to a track, one can define two semicircles starting from the diameter passing through the impact point. The track direction is chosen to be outgoing from the impact point towards the semicircle that contains the majority of points. This definition of track direction depends on some preconditions: in our case one supposes that all tracks come from the beam axis. For particles that are not coming from the z-beam axis (for example cosmics or secondary particles) this direction only has a conventional meaning [122] and should be cross-checked using other information (timing information parameters). Therefore no physics interpretation in terms of particle direction or charge should be assigned to the sign conventions on the fit parameters. In fact the sign of the parameters depends on the track direction associated, that could be the opposite of the particle direction (determining the charge and vector momentum).

As explained below the fit has used as weights the precision of each cluster. An error flag, as explained in details in the appendix A, is associated to each fitted track. The aim of these flags is to indicate that the helix fit results are within the mathematical limits of the algorithm in combination with some geometrical factors; the decision on how to treat the fitted tracks according to their error flags it is left to the user.

The circle fit in the xy plane

The first step in the fitting procedure is a circle fit based on a least square method [123]. The n points, given in a plane by their coordinates $(x_i,\ y_i)$, should satisfy the circle equation:

$$(x_i - a)^2 + (y_i - b)^2 = R^2 \tag{3.3}$$

where R is the radius and (a, b) are the coordinates of the circle's centre. One can find the circle's parameters by minimizing their mean square rectilinear[†] distance to the circle. This distance is defined as

$$\rho_i = \sqrt{(x_i - a)^2 + (y_i - b)^2} - R^2 \tag{3.4}$$

Therefore the function to minimize is:

$$M(a, b, R) = \sum_{i=0}^{n} \left((x_i - a)^2 + (y_i - b)^2 - R^2\right)^2 \tag{3.5}$$

[†] The relevance of the choice of rectilinear distance is further explained at the end of section 3.3.3

where n is the number of points.

It has been found [123] that the computation accuracy can be improved by transferring the origin of the coordinates to the centre of gravity of the points and by minimizing the alternative function:

$$K(a,b,R) = M(a,b,R)R^{-2} = \sum_{i=0}^{n} \left(\frac{x_i + y_i}{R} - 2\frac{a}{R}x_i - 2\frac{b}{R}y_i + \frac{a^2 + b^2 - R^2}{R} \right)^2 \tag{3.6}$$

Equating to zero the derivatives of this function, a second order nonlinear system of equations is obtained:

$$\begin{cases} Fa + Hb - a\gamma = P \\ Ha + Gb - b\gamma = Q \\ 2Pa + 2Qb + \gamma^2 = T \end{cases} \tag{3.7}$$

The coefficients in this system are defined as:

$$F = \frac{1}{n}\sum_{i=0}^{n} 3x_i^2 + y_i^2 \qquad H = \frac{2}{n}\sum_{i=0}^{n} x_i y_i \tag{3.8}$$

$$P = \frac{1}{n}\sum_{i=0}^{n} x_i(x_i^2 + y_i^2) \qquad G = \frac{1}{n}\sum_{i=0}^{n} x_i^2 + 3y_i^2 \tag{3.9}$$

$$Q = \frac{1}{n}\sum_{i=0}^{n} y_i(x_i^2 + y_i^2) \qquad T = \frac{1}{n}\sum_{i=0}^{n} (x_i^2 + y_i^2)^2 \tag{3.10}$$

where $\gamma = R^2 - a^2 - b^2$. Then one can solve the system (3.7) considering as variable only γ, obtaining the following fourth degree equation:

$$\gamma^4 + A\gamma^3 + B\gamma^2 + C\gamma + D = 0 \tag{3.11}$$

where

$$\begin{array}{ll} A = (-F - G) & C = T(F + G) - 2(P^2 + Q^2)] \\ B = (FG - T - H^2) & D = T(H^2 - FG) + 2(P^2G + Q^2F) - 4PQ \end{array}$$

This equation has four roots; in order to obtain the first approximation to the root one looks for, one can use the solution evaluated by another method. In this method a new variable ($z = x^2 + y^2$) can be introduced in the circle equation (3.3); in this way (3.3) is transformed into the following linear regression equation:

$$z = \alpha x + \beta y + \gamma \tag{3.12}$$

where

$$\alpha = 2a \quad , \quad \beta = 2b \quad \text{and} \quad \gamma = R^2 - a^2 - b^2$$

After transferring the origin of the coordinate system to the centre of gravity of the set $(x_i,\, y_i)$, one obtains the normal equation for the parameters α, β and γ:

$$\begin{aligned} \alpha \sum_{i=0}^{n} x_i^2 + \beta \sum_{i=0}^{n} x_i y_i &= \sum_{i=0}^{n} x_i \left(x_i^2 + y_i^2\right) \\ \alpha \sum_{i=0}^{n} x_i y_i + \beta \sum_{i=0}^{n} y_i^2 &= \sum_{i=0}^{n} y_i \left(x_i^2 + y_i^2\right) \\ n\gamma &= \sum_{i=0}^{n} \left(x_i^2 + y_i^2\right) \end{aligned} \tag{3.13}$$

Therefore one has a solution for

$$\gamma_0 = \frac{1}{n} \sum_{i=0}^{n} x_i^2 + \sum_{i=0}^{n} y_i^2 \tag{3.14}$$

γ_0 is obtained as a by-product when calculating the coefficients of (3.11). Since γ_0 is the first good approximation one can minimize round-off errors dividing all coefficients of (3.11) by γ_0^4. The new equation, related to the variable $x = \gamma/\gamma_0$, is

$$x^4 + A_0 x^3 + B_0 x^2 + C_0 x + D_0 = 0 \tag{3.15}$$

where the coefficients are

$$\begin{array}{ll} A_0 = A/\gamma_0 & B_0 = B/\gamma_0^2 \\ C_0 = C/\gamma_0^3 & D_0 = D/\gamma_0^4 \end{array}$$

The fourth degree equation is solved iteratively using the Newton method (starting value $x_0 = 1$) with an accuracy of 10^{-12}. Once γ is known, the parameters a, b, and R can be calculated. The sign of R remains to be determined.

The direction associated to a track is determined by the majority of the points: the direction is defined as starting from the impact point towards the semicircle that contains the majority of points (as shown in fig. 3.13). The sign of R is positive if the direction is clockwise in the xy plane and negative if the direction is anti-clockwise. To accomplish the direction associated to a track by this definition, the asymmetry of the experimental points is evaluated:

$$A_{sym} = \frac{1}{R}(a \cdot Y_{cg} + b \cdot X_{cg}) \tag{3.16}$$

where X_{cg} and Y_{cg} are the coordinates of the centre of gravity of the points, in which the origin has been translated to perform the circular fit.

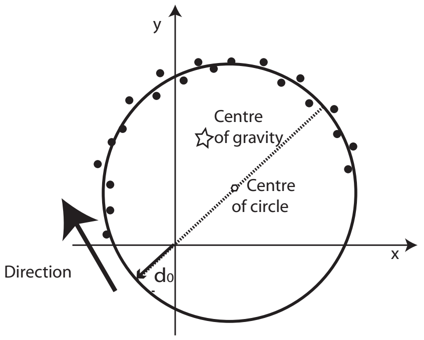

Figure 3.13: *The majority of points determine the direction associated to a track.*

This sign convention corresponds to the most usual case of a particle originating from the target and exiting the chamber. In some case that does not correspond to the particle direction: for example this is true for particles produced in the target and that turn in the xy plane by less than 2π. If the particle turns by more than 2π, the direction and the sign associated to the radius are only a convention. Similarly, the sign of the radius is not the charge of the particle, for example in the case of a cosmic ray that passes in the TPC crossing the blind region of the inner field cage. In this case the cosmic ray is reconstructed as two different tracks that have the same radius as absolute value but with the opposite sign (see fig. 3.14).

Once the circular fit is performed, the helix parameters ρ, ϕ_0 and d_0 can be evaluated using the following formulae:

$$\rho = \frac{1}{R} \tag{3.17}$$

$$\phi_0 = \arctan 2 \left(\frac{b}{a} \right) + sign \cdot \pi/2 \tag{3.18}$$

$$d_0 = |R| - \sqrt{a^2 + b^2} \tag{3.19}$$

where *sign* is the sign of the radius and (a, b) are the circle centre coordinates. The same circle for a given d_0 but with opposite direction associated to a track can be described by a set of parameters differing by the sign of ρ and by a difference of π in ϕ.

The linear fit in the $s_{xy}z$ plane

The second part of the fit procedure is a linear fit in the zs_{xy} plane to get the last two helix parameters, $\tan\lambda$ and z_0. The relation of the linear fit is:

$$z = z_0 + s_{xy} \tan\lambda \tag{3.20}$$

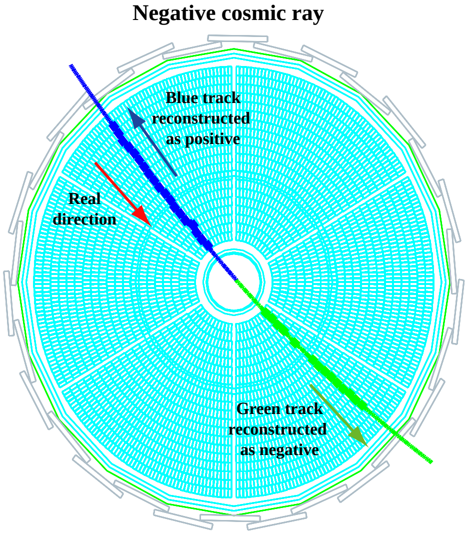

Figure 3.14: *A cosmic ray crossing the blind region of the inner field cage. It is reconstructed as two different tracks that have the same radius as absolute value but with the opposite sign.*

To perform the linear fit, which is done using the least square method, one has to calculate the value of s_{xy} of the experimental points. The value of s_{xy} can be derived from the knowledge of R, d_0 and ϕ_0. The s_{xy} coordinate is defined by the arc length between a point and the impact point on the circle in the xy plane, therefore

$$s_{xy} = R\Delta\psi \tag{3.21}$$

where $\Delta\psi$ is the angle between the point and the impact point in the plane xy with respect to the centre of track circle, as shown in the fig. 3.15.

To evaluate $\Delta\psi$ one can consider the vectorial ($vepr$) and scalar product ($scpr$) in the reference system of the centre:

$$vepr = |\vec{r}_{d_0} \times \vec{r}_{point}| = r_{d_0} r_{point} \sin\Delta\psi = (d_{0x} - a)(P_y - b) - (P_x - a)(d_{0y} - b)$$

$$scpr = \vec{r}_{d_0} \cdot \vec{r}_{point} = r_{d_0} r_{point} \cos\Delta\psi = (d_{0x} - a)(P_x - a) + (d_{0y} - b)(P_y - b)$$

Using these relations one can evaluate

$$\Delta\psi \;=\; \arctan\left(\frac{vepr}{scpr}\right) \tag{3.22}$$

The equation (3.20) implies that $s_{xy} = 0$ at $z = z_0$ (the impact point). The TPC tracks however can start either after ($s_{xy} > 0$) or before ($s_{xy} < 0$) the impact point. Therefore the track points are ordered along the z direction:

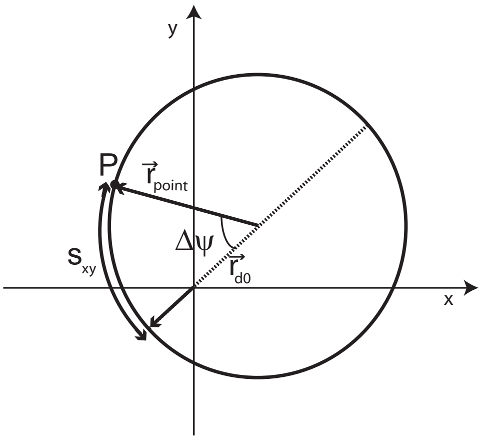

Figure 3.15: *The angle $\Delta\psi$ is the angle between the point and the impact point in the plane xy with respect to the centre of track circle.*

the points with z coordinate before z_0, following the direction given by the sign of R, stay in a semicircle where s_{xy} is negative, the points in the other semicircle have s_{xy} positive (see fig. 3.16).

To obtain easily the sign of s_{xy}, one considers $\Delta\psi \in (-\pi, \pi)$ in the equation (3.22). In the case of a clockwise direction in the semicircle where s_{xy} is positive, $\Delta\psi$ is negative $(-\pi, 0)$. In the other semicircle where s_{xy} is negative, $\Delta\psi$ is positive $(0, \pi)$. Therefore instead of (3.21) the following equation should be used:

$$s_{xy} = -\, R\Delta\psi \tag{3.23}$$

Following the order along z it could happen that a track point will pass

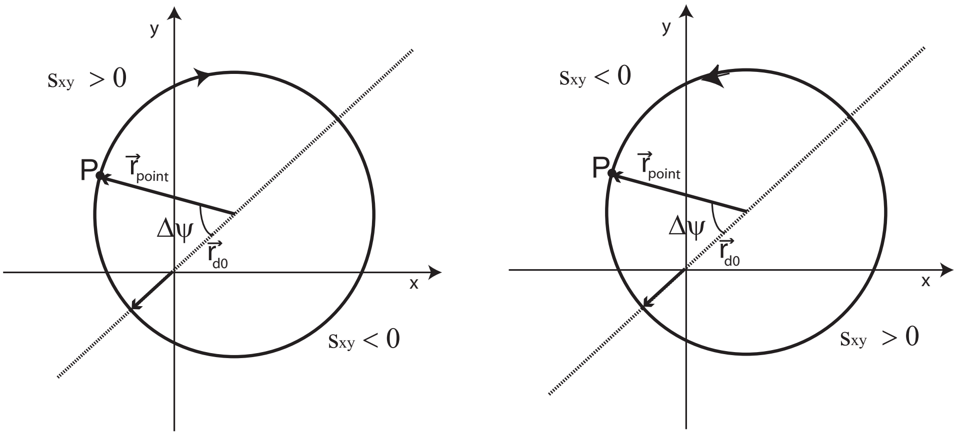

Figure 3.16: *The sign of the angle s_{xy} changes with the direction assigned to the track.*

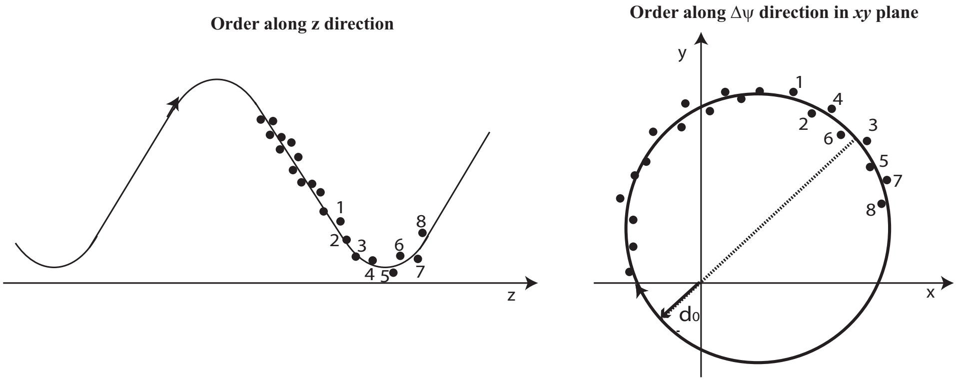

Figure 3.17: *Smearing of points*

into the other semicircle with $s_{xy} < 0$. If a phase is not added one obtains some discontinuities in s_{xy}. Therefore the 2π phase should be added to $\Delta\psi$, to get s_{xy} as a continuous and increasing function. In case of a very long spiralling track the phase should be added more than once. This also allows a fit to tracks with more than one turn along the helix. Moreover the points have a smearing and it could happen that the order along z does not correspond to the order along $\Delta\psi$ (as show in fig. 3.17). This means that sometime one should add the phase to one point but not to the next one, considering the order along z. To avoid this problem the points are ordered around the first one where the phase is changing ($\Delta\psi$ of points $\in (\Delta\psi_{phase\,change} - 174$ mrad, $\Delta\psi_{phase\,change} + 174$ mrad$)$) along $\Delta\psi$. In this way one can easily add 2π phase when the track passes through the change of phase.

One can emphasize that in case of more turns along the helix, the direction associated to the track is completely arbitrary, as well as the coordinate of the impact point along z (z_0), due to the periodicity of the helix function. Moreover, there are cases for which it would not be even sufficient to invert the sign conventions to obtain the correct direction arrow. In fact considering the same example of a cosmic ray (shown in fig. 3.14), we note that if the sign convention is inverted, one obtains again one branch with the right direction (and charge) and one with the wrong direction (and charge), with respect to the known correct physics interpretation.

Fit with weights

By studying the residuals of the clusters along r and $r\phi$ on the collected data, different classes of precision can be observed [124], depending on the number of hits that belong to a cluster and if a cluster is near or not a dead region. This classification and the relative population of the classes was also quantified using simulated data. The precision associated to each class, or in other words the error in $r\phi$, is not statistical nor analytically continuous, but it is systematic and discretized. The error defined along the $r\phi$ and r directions can be transformed along the x and y directions (δx, δy) in a conservative way using the upper limit:

$$\delta x = |\delta_\phi \sin\phi| + |\delta_r \cos\phi| \tag{3.24}$$

$$\delta y = |\delta_\phi \cos\phi| + |\delta_r \sin\phi| \tag{3.25}$$

Moreover, we remind that the fitting procedure uses two metrices: one for the weight, that is just scalar, and one for the distance between the point and the helix that should be minimized in the fit. These two metrices are used simultaneously in the fit procedure and they should be coherent.

If the errors were well behaved (statistical, Gaussian, continuous), the transformation of the error from $r\phi$ to xy would be correct if the error in $r\phi$ and in r are correct; but in the case of the HARP TPC the usual estimation of the error in r ($r/\sqrt{12}$) is inappropriate. Different shape of the pads, different inclination of the wire with respect to the pads, different angle between the track and the pad for radial and not radial tracks. Moreover it has been shown that the errors are not well behaved [124] in the sense explained above.

Thus the same weight metric used in the ALEPH algorithm is adopted, which is more suitable for errors of systematic nature. Since the original method minimises the linear distances between the points and the circle, the weighting procedure is correct only for tracks crossing the pads perpendicularly. The direction is unknown before the fit, so as first approximation we consider the tracks as radial. As in the ALEPH algorithm, the errors are included by modifying all expressions of the following type:

$$\frac{1}{n}\sum_{i=0}^{n} x_i y_i = \frac{1}{n}\frac{\sum_{i=0}^{n} x_i y_i\, w_i}{\sum_{i=0}^{n}\, w_i} \tag{3.26}$$

where w_i is the weight associated to each point.

This method associates the same weight (w_{xy}) to the x, y and xy terms, and the weight w_z to the term including the z coordinate. The upper limit, defined by the arithmetical sum of the projection of w_x and w_y component along the direction perpendicular to the radial position of the cluster, was used to define the weight w_{xy}. The weight is calculated using a linear evaluation of the errors and not on the arc because the fit minimises the linear distance of the point to the track. If the weight would be evaluated using the error on the arc one should use the error defined along $r\phi$ found by the Monte Carlo data: but in order to have the two coherent metrices in the fit, one should then also use the distance on the arc in the fit minimization. The various precautions taken in the mathematical transformations described in this section allowed the fit algorithm to be tolerant to, and performant with, slightly non radial track as well.

Momentum reconstruction

The momentum is reconstructed using the following formulas:

$$\begin{aligned} p_x &= a\,B\,Q\,R\,\cos\phi_0 \\ p_y &= a\,B\,Q\,R\,\sin\phi_0 \\ p_z &= p_t\,\tan\lambda \end{aligned} \tag{3.27}$$

where $a = 0.299 \cdot 10^{-3}$ GeV s/(c T m^2), B indicates the magnetic field in Tesla, whose nominal value is 0.7 T, and Q is the sign of ρ. The particle momentum is given in units of GeV/c.

Performance

The fit algorithm is validated using an analytical unit test ('*stub*'), reconstructing user-defined points. The efficiency and the precision of the fit procedure and of the TPC reconstruction chain were tested using Monte Carlo data [118].

On the target data, the track fit algorithm can fit 99.83% of physics tracks. The physics tracks have at least 12 points and they are in the angular region between 20° and 120°. 96.55% of the sample of physics tracks have no error flag, for the remaining 3.28% the angular information is calculated, but the momentum evaluation is limited, due to the geometrical limitation of the HARP TPC. The meaning and the statistics of the error flags are explained in the Appendix A.

3.3.4 Vertex algorithm

The next step of TPC reconstruction is the vertex algorithm that improves the momentum resolution of the particles.

The target is located inside the TPC and it is a cylinder coaxial with the TPC, with a radius of 15 mm for solid targets. The MWPCs reconstruct the beam tracks and evaluate the extrapolated point in the target with a resolution of about 1 mm in the xy plane [81]. This point is designated in the following, as the 'vertex point'.

By adding the vertex point in the fit procedure, we can increase the track length by about 30%: the sagitta increases from ∼300 mm to ∼376 mm in the case of a track that contains points on the 1^{st} and 20^{th} row. In this way we improve the momentum resolution (as explained in section 5.4.4), but we can use the vertex point in the fit algorithm only if the track passes by that point. In fact if we fit with the vertex all tracks we distort the momentum for all particles that do not come from that point (that is not the production vertex for these tracks): for example, secondary particles or particles that lose a lot of energy in the material (target and materials that surround the target region), which have a trajectory in the gas different from the original one that started from the vertex point. The selection of tracks, to be refit using also the vertex point, is done on the basis of the minimum distance from the vertex point in the xy plane and on the minimum distance along z (called z_0'). This last distance is multiplied by $\cos(\lambda)$ to take into account the λ dependence of the resolution of z of impact point (as explained in section 5.6). The accepted distance in the xy plane is 3σ of the original impact point resolution evaluated using the cosmic rays as explained in section 5.6. The resolution of $z_0' \cdot \cos(\lambda)$ is calculated as the half width of the $z_0' \cdot \cos(\lambda)$ distribution (this width includes the target size and the detector resolution) using the following formula:

$$\sigma_z = \sqrt{(\mathrm{FWHM})^2 - \left(\frac{\text{length of target}}{2}\right)^2}$$

We select the tracks that have $z_0' \cdot \cos(\lambda)$ smaller than half the length of the target plus $3\sigma_z$. This distance depends of the target length and it is calculated for each collected data setting.

The vertex algorithm applies the same helix fit explained in the previous paragraph, using all points of the track and the vertex point. The vertex point is defined in the xy plane by the point extrapolated to the target of the MWPC track. The z coordinate is the average of the z coordinates of the impact point with respect to the MWPC extrapolated point of all selected tracks for each event. A low weight (as the points with the worst resolution) is assigned to this point to avoid distortions of the fit results for the tracks selected.

3.3.5 Energy loss

The particles are produced in the target and cross part of the target, the ITC and the inner field cage that surround the target. The length of the material crossed depends on the trajectory of the particle.

Moderately relativistic charged particles, other than electrons, lose energy in matter primarily by ionisation and atomic excitation. The mean rate of energy loss (or stopping power) is given by the Bethe-Block formula [125]:

$$-\frac{dE}{dx} = Kz^2 \frac{Z}{A}\frac{1}{\beta^2}\left[\frac{1}{2}\ln\frac{2m_e c^2 \beta^2 \gamma^2 T_{max}}{I^2} - \beta^2 - \frac{\delta}{2}\right]$$

where

- ze is the charge of the particle,
- Z and A are the atomic number and atomic mass,
- m_e is the mass of electron,
- c is the speed of light in vacuum,
- β is v/c (v is the particle velocity),
- γ is $1/\sqrt{1-\beta^2}$,
- K is $4\pi N_A r_e^2 m_e c^2$ with N_A is the Avogadro's number and r_e classical electron radius,
- I is the mean logarithmic excitation energy,
- δ is the density effect correction,
- T_{max} is the maximum kinetic energy which can be transfered to a free electron in a single collision.

In this form, the Bethe-Bloch equation (shown in fig. 3.18 for different materials) describes the mean energy loss of pions in a material to about 1% accuracy for momenta between about 40 MeV/c and 6 GeV/c. These limits cover well the region of interest of HARP TPC.

The aim of the HARP experiment is to obtain the double differential production cross section of hadron, so we need to evaluate the momentum at the production point in the target. Due to the energy loss this differs from the one measured in the TPC gas.

In this last step of the reconstruction chain we recalculate the momentum of the particle taking into account the material crossed by the particle. Of course the energy loss depends on the type of the particle, thus we evaluate the momentum, after the energy loss correction, for different particle type hypotheses (p, π, K, e) given the possibilities to apply the PID only at the analysis level.

Using the track information obtained by the first fit (if the energy loss is not small, applying the vertex algorithm we would distort the track momentum), the algorithm calculates the extrapolated point to the inner field cage and ITC volumes. Then it determines the energy of the particle before the material (before the energy loss) and calculates the new momentum and the helix parameters. This allows to evaluate the nearest point on the new helix to the MWPC extrapolated point. In this way one can estimate the length of the target region effectively crossed by the particle and applies the

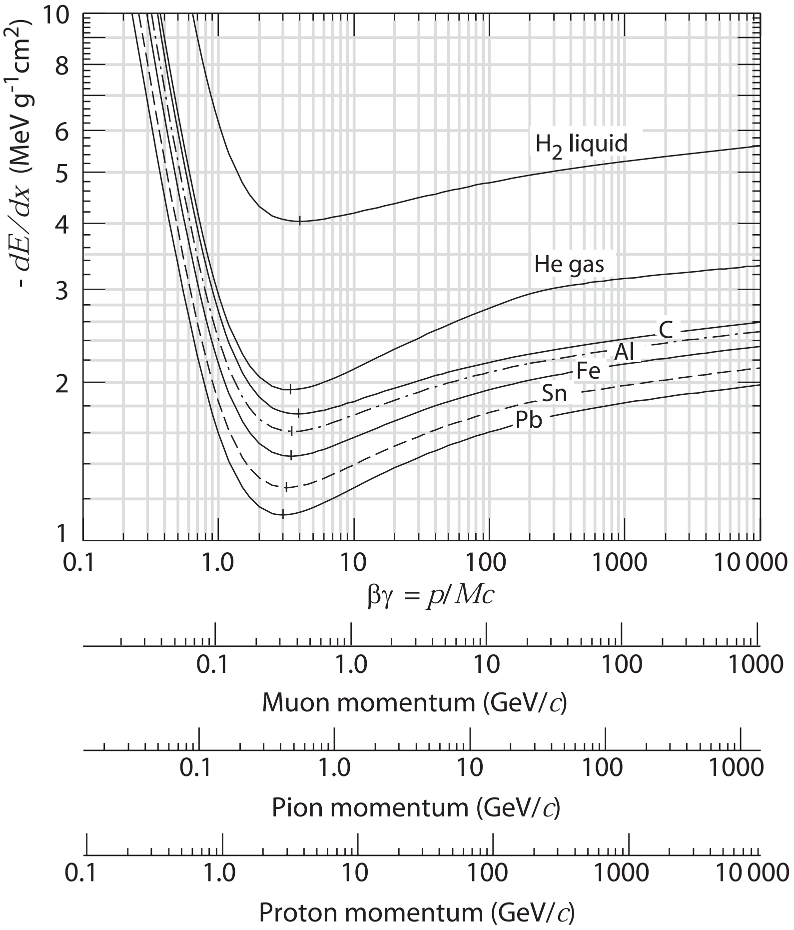

Figure 3.18: *Mean energy loss rate in liquid Hydrogen, gaseous helium, carbon, aluminum, iron, tin, and lead [125].*

second step of the energy loss correction. Finally the momentum and the energy of the particle at the production point in the target are calculated . The dimensions and type of the materials are directly read from the official HARP geometry in DetRep package.

3.4 HARP Monte Carlo simulation

One of the main external packages in the HARP software is GEANT4 (G4). It is used as a toolkit interfaced to the Gaudi framework [103]. All GEANT4 components including the UI interface are initialized and executed via Gaudi algorithms and services, which allows the same user interface both at reconstruction and simulation level.

A complete set of GEANT4 physics processes are available for the simulation of particle transport and physics interactions inside the HARP detector. For electromagnetic interactions the standard G4 package is used [83]. For performance studies in the TPC the G4 low-energy package was applied which allows us to see the behaviour of gaseous detectors. For the simulation of hadron nucleus interactions the set of G4 physics processes provided for LHC detectors are used [126].

The simulation of the HARP sub-detector response is subdivided in three main steps:

- GEANT4 simulation of particle transport, giving the energy deposition in sub-detectors and the creation of Monte Carlo hits;
- simulation of electronic signals;
- application of efficiency functions, resolution functions, and dead channel data and creation of Monte Carlo digits in the same format as experimental data.

The true Monte Carlo information is also recorded. Only beam particles and energetic particles produced inside the target are stored. The complete history of each event is available during the event simulation, which allows for all Monte Carlo hits to be associated with these initial particles. The true Monte Carlo information is propagated to simulated detector response (digits) and to reconstructed objects.

3.5 TPC Monte Carlo

The basic simulation of the HARP TPC is done in two steps. The physics processes reproduce the generation of drift electrons and their signals in the wire chamber of the TPC. The electronics part performs the sampling, digitization and packing of the data. At the end of the simulation chain the data are available in the same format as real physics data and are unpacked and reconstructed with the same software.

3.5.1 The physics processes

For all charged particles in the TPC gas volume which have a non-zero energy deposit, drift electrons are generated and tracked to the cathode wire plane. Then, the avalanche to the nearest wire is reproduced and its induced charge distributed to the pads. The result is a charge time series for each pad which received at least one charge deposit.

Generation of drift electrons

The generation of drift electrons is made on a step-by-step basis, where a step is a G4 step (typical step in HARP TPC simulation is 2 mm). The number of drift electrons is calculated by the total energy deposit for a step and the energy required to produce an electron-ion pair, which is an averaged value taking into account primary and secondary ionization.

The electron drift can be simulated in two ways: they can be single drift electrons or they can be grouped to one charge cluster per step. The latter way is faster and has no relevant differences with respect to the first method.

Tracking of drift electrons

At first, electrons are drifted to the cathode wire plane. The new position of the electron is calculated by adding a Gaussian smearing in both transversal and longitudinal direction. The amount of this diffusion depends on the gas choice and the strength of the magnetic field which especially suppresses the transversal component. In particular, a low transversal diffusion is essential for a good space resolution of the TPC. The values used for longitudinal (378 $\mu\text{m}/\sqrt{\text{cm}}$) and transversal (208 $\mu\text{m}/\sqrt{\text{cm}}$) diffusions are the ones found by a Garfield simulation including all characteristics of the HARP TPC [127].

Avalanche to the wires

The electron is moved to the nearest wire in the anode wire plane, after checking that the position of an electron is not in one of the blind areas of the spokes. Normally, the electron would travel directly to the nearest wire, i.e. perpendicular to the wire. However, in the wire chamber the electric field is not parallel to the magnetic field which causes the so-called wire $\vec{E} \times \vec{B}$ effect. Due to this $\vec{E} \times \vec{B}$ component of the fields the electron direction contains a component $\Delta\phi$ parallel to the wire. The deviation angle depends on the fields, the gas and the geometry of the wire chamber (typically this angle is about 30 degrees). The electron movement is simulated taking this distortion effect into account. At this point the gas gain (that has an exponential distribution) is also calculated and assigned to the electron.

Calculation of the charge in a pad

The amount of charge induced by an avalanche at a certain position onto a particular pad is determined by the pad response function. The charge for a pad is calculated taking into account the distance from the final avalanche position and the geometry of the pad.

3.5.2 The electronics behaviour

The behaviour of the following two electronic components has to be reproduced: the amplifier on the motherboard and the FEDC which is used for the TPC read-out.

Amplification and ADC sampling

The sampling is made in bunches. Each bunch is expected to be the charge deposited from a single original track and well separated in time (by 2 samples=200 ns) from other bunches. After each bunch, the charge time series is checked for the presence of a later charge which belongs to a new bunch.

For each bunch, the pulse shape is applied which is the transfer function of the amplifier. It is assumed to be a gamma function of the form:

$$\Gamma = \left(\frac{t}{\tau}\right)^2 \cdot exp\left(-\frac{t}{\tau}\right) \tag{3.28}$$

where τ is calculated from the length of the original bunch. Dedicated simulations of the electronics of the HARP TPC have shown that values between 70 ns and 300 ns are expected for different track inclinations (and therefore bunch lengths) [4]. Thus, τ for a given bunch length is found by interpolation to meet this requirement. t is the time between the first charge deposit of this bunch and the end of the current sample.

The samples of the bunch are calculated by weighting the transfer function with the sum of charges deposited. Each ADC is multiplied with scaling factors to match the range of ADC values of the real TPC which is 0 to 1023 (10 bit). At this point an eventual difference of the pad gains can be applied. A relative error on the equalization constants can also be applied.

Bunching the raw ADC time series

To simulate the operation mode of the FEDC cards that are used for the TPC readout, the raw ADC time series have to be bunched. Mainly, the application of a threshold (i.e. real-time zero suppression) has to be performed here. In addition, a minimum number of samples above threshold is required. Post- and pre-samples must also be added. A bunch is considered as the necessary number of samples above threshold with their pre- and post-samples and the corresponding sample numbers (i.e. the time). Samples which overlap due to post- or pre-samples are merged.

Packing

The simulation chain is completed by packing of the MC result into raw (binary) data format as delivered by the DAQ readout of the FEDC. The FEDC packs data in 32 bit words. For each pad there is a 32 bit header containing:

- the software address (bits 31 to 16)
- the hardware address (bits 15 to 9, not used)
- the total number of 10 bit words for that pad (bits 9 - 0)

with the number of sectors, rows and pads.

The event data is packed into 10 bit words (ADC values are between 0 and 1023) of which three are contained in one 32 bit word. Bunch by bunch it is followed by the (10 bit) time of the last time sample in the bunch and the (10 bit) total number of 10 bit words for this bunch. Unused bits are set to zero (an example is shown in table 3.1).

These raw data from the front-end electronics is then gathered sector by sector and tagged with event and data headers. Their exact format is determined by the DATE DAQ software.

bits	29-20	19-10	9-0
word 0	ADC2	ADC1	ADC0
word 1	ADC5	ADC4	ADC3
word 2	9	time6	ADC6
word 3	soft	hard	12

Table 3.1: *Data packing for a pad which contains one bunch with seven samples. The seven ADC values ADC0- ADC6 are followed by the time time6 of the last sample and the total number of 10-bit words for this bunch, i.e. 9. The pad data block is finished with the total number of 10-bit words for the pad (12) plus hardware and software address. In all 32-bit words bits 30 and 31 are not used and set to zero.*

Chapter 4

TPC Calibration

4.1 Introduction

The calibration of the HARP TPC has to be applied to obtain the optimal performance of the detector and permit the correction of some unwanted effects that distort the drift of the ionisation electrons inducing a wrong particle parameter reconstruction.

The first step of the calibration is the evaluation of the electron drift velocity in the TPC gas and of the TPC time calibration. The drift velocity calculation (described in section 4.2) and a global time calibration (described in section 4.3) allow to determine the z track positions. A further time calibration pad by pad is required due to a problem of the acquisition electronic that shifts the signals by 100 ns on about 30% of the pads.

The response of the pads and their electronics to induced charges is neither constant in time nor equal between pads. Therefore, methods were developed to characterize the behaviour of the electronics, to track the variations of the response in time and to equalize the response between pads. This equalisation procedure is described in section 4.4.

In the TPC front-end electronics a cross-talk effect has been observed for about half of the channels. It affects the tracking and momentum resolution, as the energy resolution of the TPC. The study to model the effect and to correct the data is described in section 4.5.

The HARP TPC exhibits two effects that produce distortions in the particle trajectories. The first one, called static distortions and constant during all data taking, is due to a voltage misalignment of the order of 150 V between the inner field cage and the outer field cage. The study of the voltage misalignment permits to determine a method to correct the static electric and magnetic distortions due to this misalignment. The second effect, called dynamic distortions, changes with time, shows a dependence from the time in the spill and a sensitivity to the beam characteristics (for example intensity or alignment with respect to the target) and data taking conditions. This distortion causes a variation of the TPC behaviour within each spill due to the charging of the chamber. One possible explanation of the charging effect can be explained by the presence of positive ions generated by the beam crossing the detector. The ions accumulate in the chamber increasing the perpendicular component of the electric field, but the charge distribution, and therefore the electric field distortions, could be not uniformly distributed along ϕ (the azimuthal angle). This effect is not present in the first part of the spill and this permits a selection, different from run to run, of the events not affected by this kind of distortion. In this way we keep only a part of the data without affecting the overall efficiency of the detector, changing only the amount of data available for the final analysis. In this way the errors have a larger statistical uncertainty but without a strong systematic uncertainty associated to the done corrections. The static distortions are described in section 4.7 and the dynamic distortions in section 4.6.

4.2 Drift velocity

One fundamental parameter of the TPC is the drift velocity that allows to determine the z position of the track points. The drift velocity depends on composition, temperature and pressure of the TPC gas. It is fundamental to study its time variation from run to run. The typical method consists of identifying the z coordinate of the vertex of the tracks generated in the target and in the endcap of the inner field cage and of measuring the difference of time between these two points. The drift velocity can be calculated by this time measurement and by knowing the positions defined by the geometry.

4.2.1 Procedure for thin solid targets

We follow two alternative procedures to calculate the drift velocity [128], namely:

1. using the distribution of the z coordinate of the track impact point, we can evaluate the time distance between the target and the endcap of the inner field cage whose positions are known;

2. using the time position of the endcap of the inner field cage calculated using the z of the track impact point and the time position of the mylar plane of the high voltage that is positioned at the end of the drift volume, we can evaluate the time distance between these two planes, whose distance is known.

These procedures have the advantage of using time differences, being therefore free from any absolute time determination.

First procedure: target vs. endcap of the inner field cage

Using the distribution of the z coordinate of the track impact points in μs (z divided by the drift velocity used in the reconstruction chain) for thin targets (Ta 5% λ_I and Pb 5% λ_I at 3, 5, 8 and -3 GeV/c) we evaluate, by a Gaussian fit, the centre of the z coordinate of the target and of the endcap of the inner field cage, for all tracks selected requiring: no error flag, $|\lambda| < 523$ mrad, more than 11 points per track, coming from the target region (about 3 times the target size). This selection is applied only in the first 50 events in a spill to avoid the dynamic distortions [129] with a beam particle recognised as proton or pion and crossing the target. The distributions and the Gaussian fit results for Ta thin target (5%λ_I) are shown in fig. 4.1. The Δt is defined by the difference between the z-time coordinate of the target and of the endcap of the inner field cage. By this time interval and the known position of these two points we calculate the drift velocity.

Considering for the Δt the error associated by the Gaussian fit (as defined in [130]) to the peak of the stesalit endcap (8 ns as maximum value) and as error associated to Δz (0.5 mm including mechanical imprecision and the uncertainty on the target position), we can evaluate an error of 0.010 cm/μs on the drift velocity ($\Delta x/\Delta t$). The results are summarised in the table 4.1.

Second procedure: endcap of the inner field cage vs. mylar plane

We evaluate the position of the stesalit endcap of inner field cage as in the first procedure. The time position of the end of the drift volume has a known position defined by the mylar plane. This time is studied using the time series of the hits associated to each cluster [105] belonging to a forward track ($\lambda > 1.29$ rad). We select only the last time of all time series of the cluster with largest z. This time is shifted with respect to the real time position of the cluster by about 200 ns due to the tail created by the electronic transfer function. The error of this position corresponds to the sigma of the Gaussian fit of this distribution (sigma has an average of 288 ns as shown in fig. 4.2 for Ta thin target, 5% λ_I), that includes also the contribution due to a possible curvature of the mylar plane. Considering that the error on the stesalit peak is negligible if we compare to this, we can assign this error to Δt. Using the known distance between these two planes and the time difference we can calculate the drift velocity. Considering the error associated to Δt and the one on Δx (that is 0.5 mm including mechanical imprecision and the

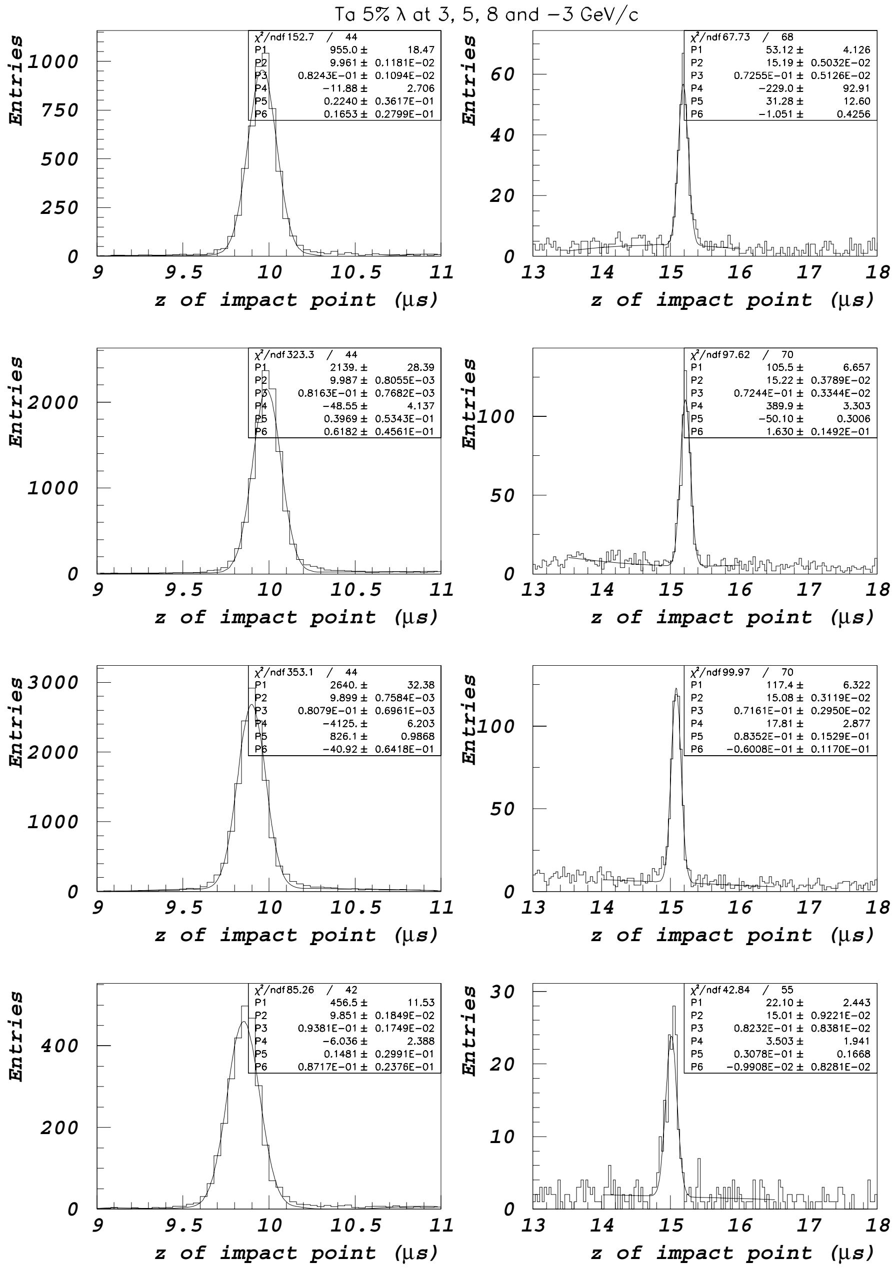

Figure 4.1: *The target (on the left) and the stesalit endcap (on the right) peaks of the distribution of the z coordinate of the impact point for Ta* 5% λ_I *at 3 (first row), 5 (second row), 8 (third row) and -3 (last row) GeV/c. The distribution are fitted by a double Gaussian fit.*

Setting	Target position (μs)	Endcap position (μs)	Drift velocity ($cm/\mu s$)
Ta thin target 5% λ_I 5.6 mm at 3 GeV/c	$9.961 \pm 1 \cdot 10^{-3}$	$15.186 \pm 5 \cdot 10^{-3}$	5.085 ± 0.010
Ta thin target 5% λ_I 5.6 mm at 5 GeV/c	$9.987 \pm 1 \cdot 10^{-3}$	$15.216 \pm 4 \cdot 10^{-3}$	5.081 ± 0.010
Ta thin target 5% λ_I 5.6 mm at 8 GeV/c	$9.899 \pm 1 \cdot 10^{-3}$	$15.082 \pm 3 \cdot 10^{-3}$	5.126 ± 0.010
Ta thin target 5% λ_I 5.6 mm at -3 GeV/c	$9.851 \pm 2 \cdot 10^{-3}$	$15.013 \pm 9 \cdot 10^{-3}$	5.147 ± 0.010
Pb thin target 5% λ_I 8.5 mm at 3 GeV/c	$9.999 \pm 1 \cdot 10^{-3}$	$15.186 \pm 5 \cdot 10^{-3}$	5.094 ± 0.010
Pb thin target 5% λ_I 8.5 mm at 5 GeV/c	$9.990 \pm 1 \cdot 10^{-3}$	$15.176 \pm 4 \cdot 10^{-3}$	5.095 ± 0.010
Pb thin target 5% λ_I 8.5 mm at 8 GeV/c	$9.934 \pm 1 \cdot 10^{-3}$	$15.085 \pm 2 \cdot 10^{-3}$	5.130 ± 0.010
Pb thin target 5% λ_I 8.5 mm at -3 GeV/c	$9.909 \pm 1 \cdot 10^{-3}$	$15.053 \pm 5 \cdot 10^{-3}$	5.137 ± 0.010

Table 4.1: *Summary of the results for the first method (target vs. stesalit endcap) for Ta thin target (5% λ_I) and Pb thin target (5% λ_I) at 3, 5, 8, -3 GeV/c.*

uncertainty on the target position), we can obtain an error of about 1.8% on the drift velocity. The results are summarised in the table 4.2.

Conclusions

The results of the two methods are in good agreement within their respective error for all settings. The drift velocity has a maximum variation of 1.3% that is more than the error associated to the first method (0.2%), thus allowing a calculation of the drift velocity setting by setting. Note that the analysing of a setting that is far in time during the data taking period, such at Sn thin target (2%λ_I) at 5 GeV/c shows, a drift velocity equal to 5.234 ± 0.010 cm/μs, hence a clearly enhanced variation. We use the most precise method (target vs. stesalit endcap) to evaluate the drift velocity for each setting with a solid thin target.

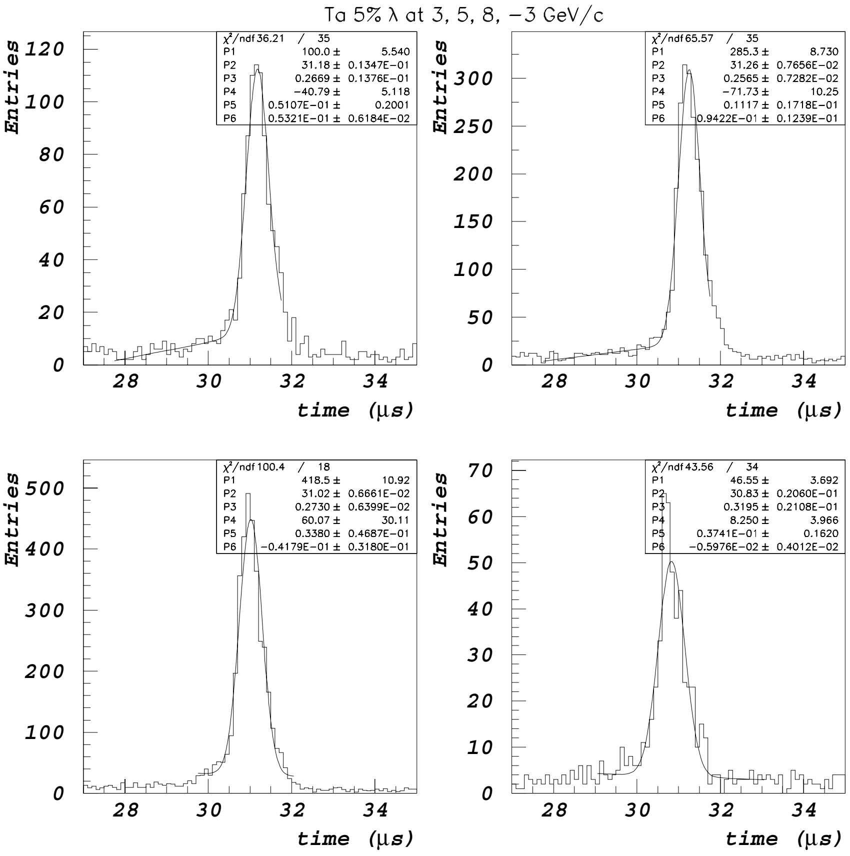

Figure 4.2: *The time position of the end of the drift volume that has a known position defined by the mylar plane for Ta* 5% λ_I *at 3 (first row on the left), 5 (first row on the right), 8 (second row on the left) and -3 (second row on the right) GeV/c. The distribution are fitted by a double Gaussian fit.*

Setting	Endcap position (μs)	Mylar position (μs)	Drift velocity (cm/μs)
Ta thin target 5% λ_I 5.6 mm at 3 GeV/c	$15.186 \pm 5 \cdot 10^{-3}$	30.979 ± 0.267	5.056 ± 0.101
Ta thin target 5% λ_I 5.6 mm at 5 GeV/c	$15.216 \pm 4 \cdot 10^{-3}$	31.056 ± 0.257	5.041 ± 0.096
Ta thin target 5% λ_I 5.6 mm at 8 GeV/c	$15.082 \pm 3 \cdot 10^{-3}$	30.818 ± 0.273	5.074 ± 0.081
Ta thin target 5% λ_I 5.6 mm at -3 GeV/c	$15.013 \pm 9 \cdot 10^{-3}$	30.632 ± 0.320	5.112 ± 0.097
Pb thin target 5% λ_I 8.5 mm at 3 GeV/c	$15.186 \pm 5 \cdot 10^{-3}$	31.055 ± 0.328	5.032 ± 0.106
Pb thin target 5% λ_I 8.5 mm at 5 GeV/c	$15.176 \pm 2 \cdot 10^{-3}$	31.004 ± 0.289	5.045 ± 0.091
Pb thin target 5% λ_I 8.5 mm at 8 GeV/c	$15.085 \pm 3 \cdot 10^{-3}$	30.829 ± 0.284	5.072 ± 0.086
Pb thin target 5% λ_I 8.5 mm at -3 GeV/c	$15.053 \pm 5 \cdot 10^{-3}$	30.738 ± 0.292	5.091 ± 0.092

Table 4.2: *Summary of the results for the second method (stesalit endcap vs. mylar plane) for Ta thin target and Pb thin target at 3, 5, 8, -3 GeV/c.*

4.2.2 Procedure for cryogenic targets

The cryogenic targets (described in section 2.2) have a geometry completely different from the thin solid targets, therefore we use a different procedure [131] to evaluate the drift velocity. Fig. 4.3 shows the 3D target structure reconstructed from the x and y coordinates of the extrapolated data track point to the target of the MWPC track and z_0. One can distinguish the copper ring at the beginning of the target, the central part of the target composed by liquid Hydrogen and the mylar endcap of the vacuum tube.

We can calculate the drift velocity using the z coordinate of the track impact point (shown in fig. 4.4):

- the time distance between the mylar endcap of the vacuum tube and the endcap of the inner field cage whose positions are known;
- the time distance between the central position of the target (using the initial and final position of the target, as explained later) and the endcap of the inner field cage whose positions are known.

These procedures have the advantage of using time differences, being therefore free from any absolute time determination. Using the two methods we have a cross check on evaluation of the drift velocity.

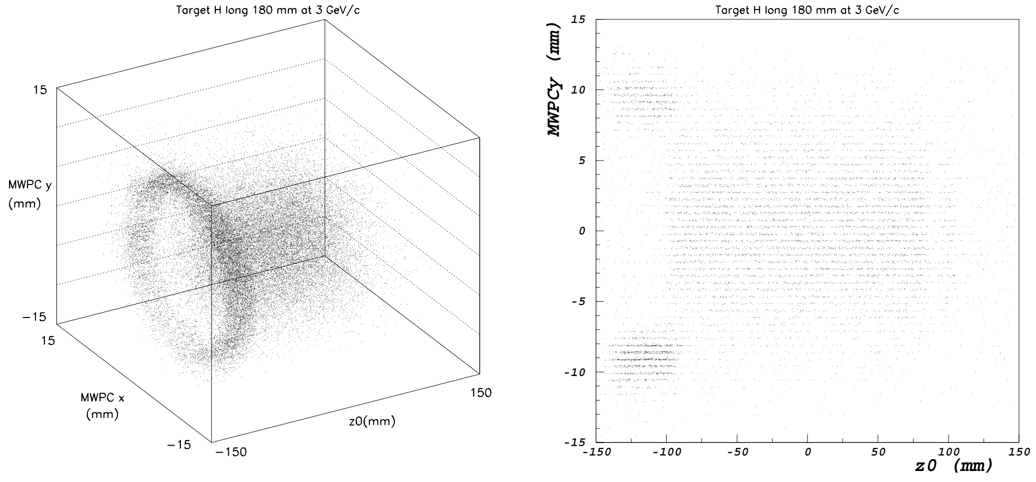

Figure 4.3: *The targets image as reconstructed using the extrapolation point on the xy plane of the MWPC beam track and the z coordinate of impact point of the reconstructed tracks in the TPC. On the left 3 dimensional spectrum and on the right the target slice requiring the x coordinate of the extrapolated point of the MWPC beam track between -2 and 2 mm .*

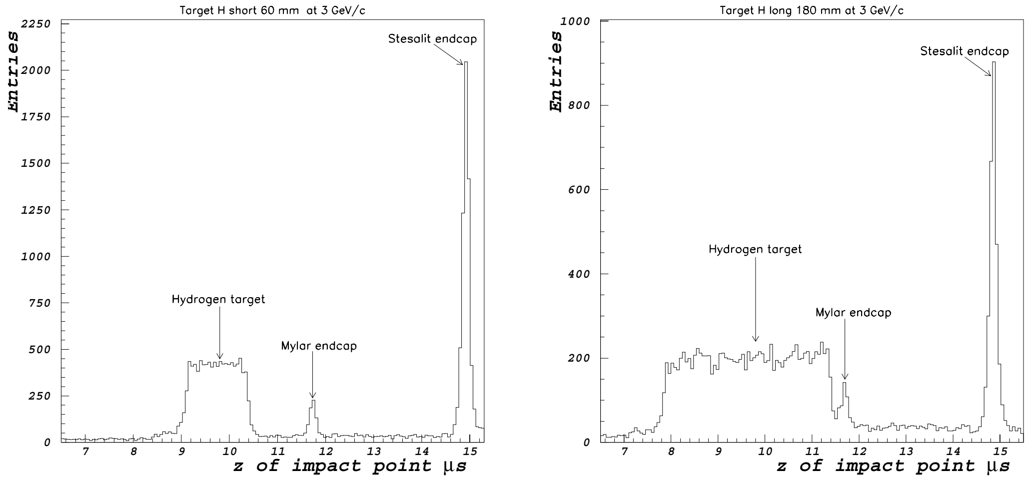

Figure 4.4: *The z_0 distribution of the TPC selected tracks: on the left the target is 60 mm long and on the right is 180 mm long. One can see clearly the Hydrogen part of the target, the mylar endcap (thickness 250μm) of the vacuum tube that surrounds the target, and the stesalit endcap of the inner field cage (thickness 2 mm).*

For this study we use the distribution of the z coordinate of the track impact point in μs (z divided by the drift velocity used in the reconstruction chain) for all tracks selected requiring: no error flag, $|\lambda| < 523$ mrad, more than 11 points per track, coming from the target region on the xy plane. This selection is applied only in the first 40 events in a spill to avoid the dynamic distortions with a beam particle recognised as proton or pion and crossing the target. Moreover, to select the Hydrogen part of the target we select only events where the beam track crosses the target in the central part (radius smaller than 6 mm), avoiding the region of the copper ring. This can be noticed from the fig. 4.3 on the right that shows the distribution of the z_0 versus y coordinate of extrapolated point of the beam track (as reconstructed by the MWPC) in the central slice of the target (x coordinate of extrapolated point of the beam track between -2 and 2 mm), for the H target long 180 mm.

First procedure

The time position of the mylar endcap of the vacuum tube and the endcap of the inner field cage are determined by the distribution of the z coordinate of the track impact point fitting the peaks by a Gaussian; the mean value of these Gaussians are the best estimator of the position of the two endcaps.

The position of the endcap of the inner field cage is well known (268.5 mm in the HARP reference system) while the position of the endcap of the vacuum tube can be measured from the technical drawings (102 mm). In the error we should consider the incertitude due to deformation produced by possible variations of gas pressure. The results are shown endcap in fig. 4.5 for Hydrogen 60 mm target and Hydrogen 180 mm target and they are summarised in the tables 4.3 and 4.4.

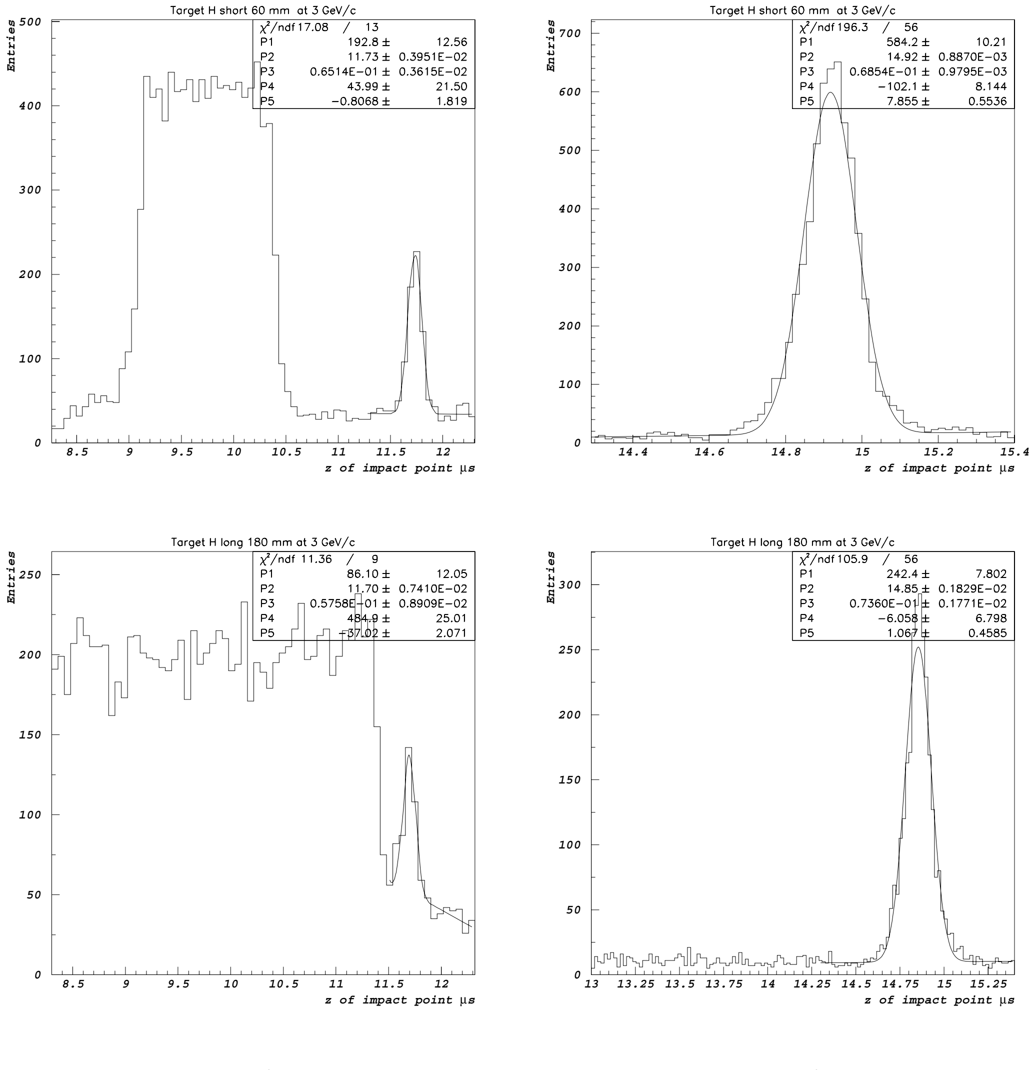

Figure 4.5: *Results for Hydrogen 60 mm target on the top and for Hydrogen 180 mm target on the bottom. On the left, the mylar peak of the endcap of the vacuum tube that surrounds the target is well fitted by a Gaussian and a straight line for background subtraction. On the right, the stesalit peak of the endcap of the inner field cage is well fitted by a Gaussian and a straight line for background subtraction.*

Second procedure

In the second procedure we use the endcap of inner field cage as used in the first procedure and the central position of the target. To determine the central position of the target we evaluate the beginning and the end of the target, then we calculate the average value that corresponds to its central position. The average value has the advantage to avoid systematics due to the resolution (that should be distributed as a Gaussian for both edges). The two edges of the target are not well defined due to the tails created by our resolution on the impact point, so we can calculate the flex point by fitting the distribution with an error function (the results are underlined by the blue line in fig. 4.6) or determine the edge of the distribution (red line in fig. 4.6). The error function is defined by the formula [132]:

$$f(x) = c_1 \left[\frac{2}{\sqrt{\pi}} \int_0^{\frac{x-c_2}{c_3}} e^{-t^2} dt + c_4 \right]$$

We consider as the position of the central point of the target the average of the two values obtained using the fit by an error function and the one that estimates the edge of the distribution. The results are summarised in the table 4.3 and 4.4.

Conclusion

In the first method, the error associated to the drift velocity is calculated by the propagation of the errors using as errors for the time the ones associated by the Gaussian fit [130] and an error of 1.5 mm on the position of the endcap of the vacuum tube (this error contains also the deformation from the nominal position due to the pressure). For the second method, the error associated to the time of the central position of the target is the variation between the two times and the one associated to the position of the target, namely 2 mm, that includes the deformation of the endcaps of the target due to the pressure (as explained in [133]).

The values of the two drift velocity are in good agreement and we consider as drift velocity the one obtained with the first method (with the smallest error).

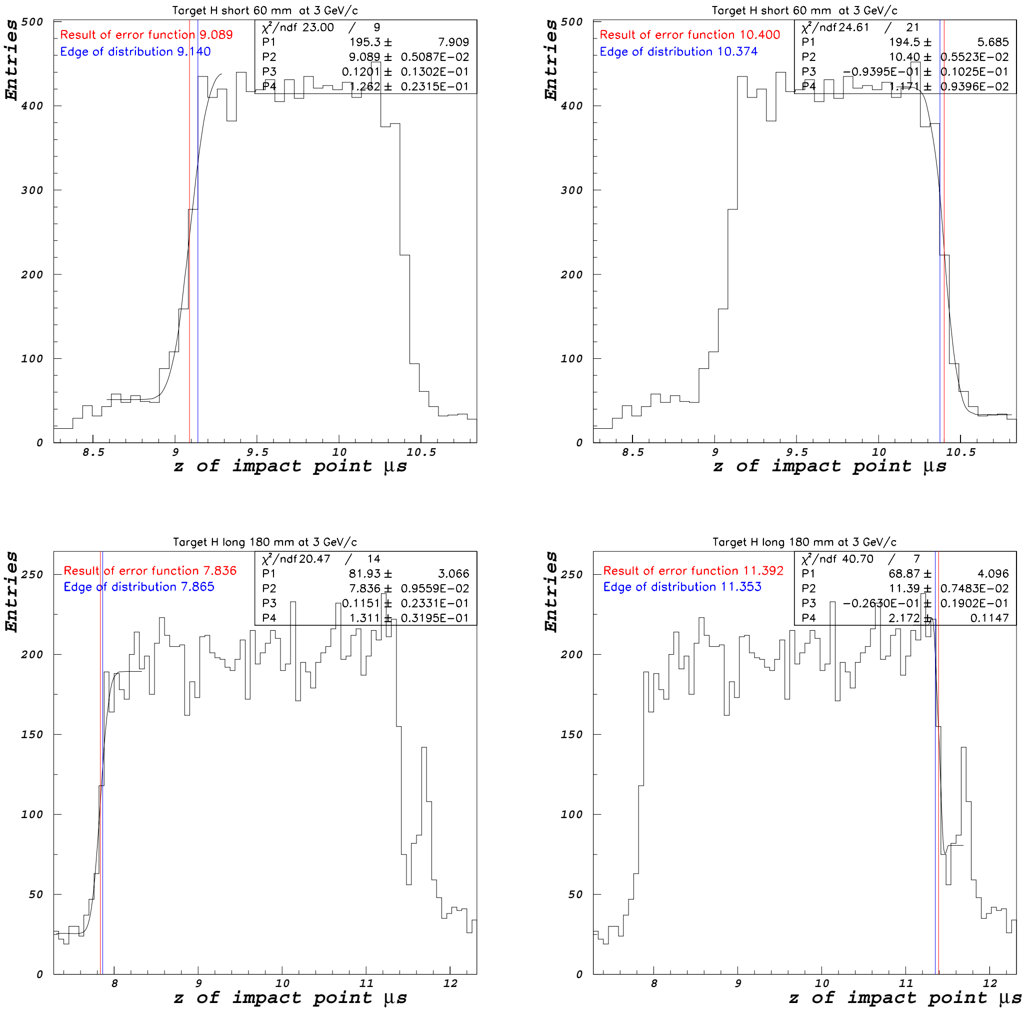

Figure 4.6: *Results for Hydrogen 60 mm target on the top and for Hydrogen 180 mm target on the bottom. The first edge (on the left) and the second edge (on the right) of the target as fitted by an error function to determine the beginning of the target (the flex point in blue) and as determined selecting the edge of the distribution (in red).*

	Position (mm)	Time position (μs)
Central point of the target	0	$9.750 \pm 39 \cdot 10^{-3}$
Endcap of the vacuum tube	102	$11.732 \pm 3.9 \cdot 10^{-3}$
Endcap of the inner field cage	268.5	$14.918 \pm 0.5 \cdot 10^{-3}$
	First method	Second method
Drift velocity cm/μs	5.226 ± 0.047	5.195 ± 0.062

Table 4.3: *Summary of the results for the first and second methods for the target of Hydrogen of 60 mm with a proton and pion beam at 3 GeV/c.*

	Position (mm)	Time position (μs)
Central point of the target	-8	$9.611 \pm 34 \cdot 10^{-3}$
Endcap of the vacuum tube	102	$11.699 \pm 7.4 \cdot 10^{-3}$
Endcap of the inner field cage	268.5	$14.854 \pm 1.8 \cdot 10^{-3}$
	First method	Second method
Drift velocity cm/μs	5.277 ± 0.047	5.274 ± 0.063

Table 4.4: *Summary of the results for the first and second methods for the target of Hydrogen of 180 mm with a proton and pion beam at 3 GeV/c.*

4.3 Time calibration

The time calibration is fundamental because its miscalibration causes a constant shift along z with respect to the real position of the track in the chamber. In addition, the HARP TPC is affected by static and dynamic distortions which have a strong z-dependence, hence any correction algorithm depends on the proper time calibration [128].

There are several sources of miscalibration of the TPC time:

1. The trigger signal has an unknown delay (trigger-delay).
2. The electronics card has a buffer of 1.6 μs, therefore the first time when data are stored corresponds to this value.
3. As shown in fig. 4.7 [134], the trigger signal arrives to the VME master and is recorded as TDC_{in} in the control room; it is also sent to the trigger-clock card inside the experimental area. The signal arrives to the experimental area with a delay Δ_{time1}. When the trigger arrives it is aligned on the time of the next clock signal before entering the ADC cards, this gives a jitter time comprised between 0 and 100 ns. Therefore the flash ADC records data with a delay corresponding to Δ_{time1}+jitter. Then the signal comes back to the control room with a delay Δ_{time2} and the time is stored in TDC_{out}. These two times, Δ_{time1} and Δ_{time2}, are virtually equal except for the jitter time; therefore the flash ADC starts to take data after a time $\sim 0.5 \cdot (TDC_{out} - TDC_{in})$. To evaluate the delay due to the jitter we shift all measured time series by the quantity $(TDC_{out} - TDC_{in}) = \Delta_{time2} + \Delta_{time1} +$ jitter where one TDC count corresponds to 0.8 10^{-3} μs [135]. The difference Δ_{time2} will be evaluated together with the delay due to the trigger signal.
4. a time shift of 100 ns of $\sim$ 30% of pads was discovered after the data taking. It requires a correction.

All measured time bins should be therefore corrected by the following time calibration:

$$time = time_{meas} + [(TDC_{out} - TDC_{in}) * 0.8 \cdot 10^{-3}] - 1.6\mu s + \Delta_{time0} \quad (4.1)$$

where Δ_{time0} is the sum of trigger-delay and Δ_{time2}.

Since July 12^{th} 2002 (from run 15619) the TDC_{out} and/or TDC_{in} are not stored for about 20% of the events. This problem is due to intermittent failures of one discriminator which allows for communication with the master crate. These data are calibrated in time using the mean value of the $TDC_{out} - TDC_{in}$ distribution that is 3.6 μs with a σ of 29 ns [128].

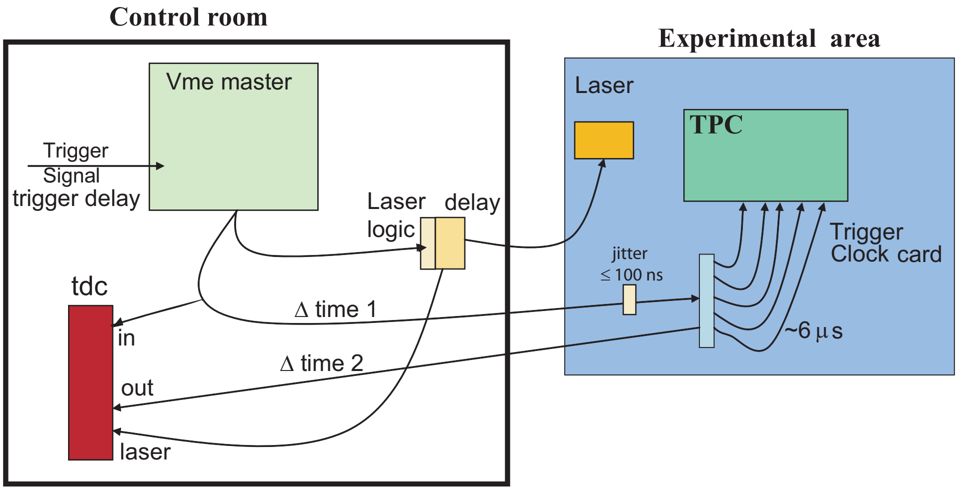

Figure 4.7: *Scheme of the data taking hardware [134]*

4.3.1 Calculation of Δ_{time0}

In order to evaluate the unknown Δ_{time0}, we decided to study the time position associated to the target centre using the distributions of the impact point z coordinate transformed in μs (z divided by the drift velocity) of all tracks selected requiring: no error flag, $|\lambda| < 523$ mrad, more than 11 points per track, coming from the target region (about 3 times the target size). This selection is applied only in the first 50 events in a spill to avoid the dynamic distortions with a beam particle recognised as proton or pion and crossing the target. We evaluated Δ_{time0} for Ta and Pb thin target (5% λ_I) with a length respectively of 5.6 mm and 8.5 mm at 3, 5, 8, -3 GeV/c. Then we evaluate the time associated to the nominal position of the centre of the target, again using the drift velocity calculated as explained in the previous paragraph. The shift between the two times calculated above gives the Δ_{time0}. For the measured target position we assign the associated error by the Gaussian fit to the peak of the distributions of the impact point z coordinate (1 ns). The nominal target position has an error of 0.5 mm due to the uncertainty of the real target position convoluted by an error of 0.2% (as found in the previous chapter) on the drift velocity used to find such nominal time position; thus the total error on the time associated to the nominal target position is of about 22 ns. Therefore by error propagation, the error on the Δ_{time0} is 22 ns.

The maximum spread of the Δ_{time0} for the considered settings is 28 ns using the drift velocity calculated for each setting; this spread is well contained within 2 sigma of the error computed for this method. The results are summarized in table 4.5.

Setting	Measured Target position (μs)	Nominal target position (μs)	Δ_{time0} (ns)
Ta thin target 5% λ_I 5.6 mm at 3 GeV/c	$9.961 \pm 1 \cdot 10^{-3}$	$9.672 \pm 22 \cdot 10^{-3}$	-289±22
Ta thin target 5% λ_I 5.6 mm at 5 GeV/c	$9.987 \pm 1 \cdot 10^{-3}$	$9.679 \pm 22 \cdot 10^{-3}$	-308±22
Ta thin target 5% λ_I 5.6 mm at 8 GeV/c	$9.899 \pm 1 \cdot 10^{-3}$	$9.594 \pm 22 \cdot 10^{-3}$	-305±22
Ta thin target 5% λ_I 5.6 mm at -3 GeV/c	$9.851 \pm 2 \cdot 10^{-3}$	$9.555 \pm 21 \cdot 10^{-3}$	-296±22
Pb thin target 5% λ_I 8.5 mm at 3 GeV/c	$9.999 \pm 1 \cdot 10^{-3}$	$9.682 \pm 22 \cdot 10^{-3}$	-317±22
Pb thin target 5% λ_I 8.5 mm at 5 GeV/c	$9.990 \pm 1 \cdot 10^{-3}$	$9.680 \pm 22 \cdot 10^{-3}$	-310±22
Pb thin target 5% λ_I 8.5 mm at 8 GeV/c	$9.934 \pm 1 \cdot 10^{-3}$	$9.615 \pm 22 \cdot 10^{-3}$	-319±22
Pb thin target 5% λ_I 8.5 mm at -3 GeV/c	$9.909 \pm 2 \cdot 10^{-3}$	$9.602 \pm 22 \cdot 10^{-3}$	-307±22

Table 4.5: Δ_{time0} *calculation for Ta thin target (5%* λ_I*) with length of 5.6 mm and for Pb thin target (5%* λ_I*) with length of 8.5 mm.*

We use a second method for the time calibration to study the possible systematics of the first method. We calculate the time position of the beginning of the target, analysing only the first time above threshold of all time series associated to each track selected as in the first method and requiring also 35 mrad< λ <140 mrad. This selection in λ is used to consider only the almost perpendicular tracks to the beam, avoiding the backward tracks (within two sigma of angular resolution to avoid biasing the sample). By the rising time of this histogram we evaluate the beginning position of the target. The result for the Ta thin target 5% λ_I at 3 GeV/c is shown in the fig. 4.8. In this case the first time is 9.7 ns: after this time the signal increases up to the peak, while before the background is dominant as assured by the histogram weighted on ADC integral. To compare this time with the one found with the first procedure we should add about 200 ns to compensate for the maximum possible bias introduced by the time estimator used by the clustering algorithm*. Moreover one must add 50 ns that correspond to half length of the Ta thin target (5% λ_I). In this way we can compare this result (9.75-9.95 μs) with the one found with the first procedure that is $9.961 \pm 22 \cdot 10^{-3}$ μs.

---

*Note that the time calibration of the first method was determined using the standard cluster time estimator.

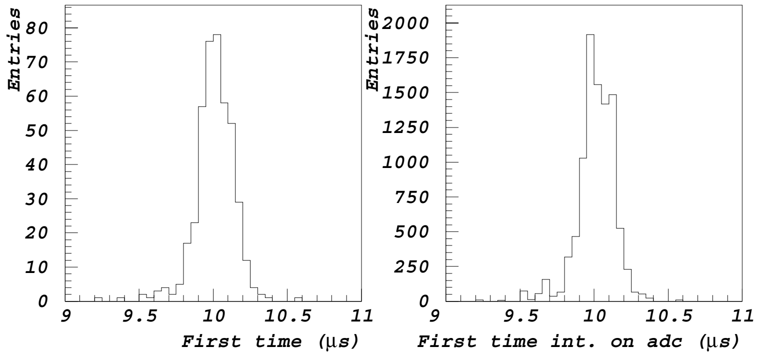

Figure 4.8: *On the left the first time above threshold of all time series associated to each track selected, on the right the first time above threshold of all time series associated to a selected track integrated by the ADC value: for the Ta thin target* 5% λ_I *at 3 GeV/c.*

We obtained similar results for Pb thin target 5% λ_I at 8 GeV/c. Therefore the results of the two methods are in good agreement within the associated error.

4.3.2 100 ns pad time shift

A time shift of 100 ns was discovered for about 30% of pads as reported by [136]. Studying the z_0 distribution in the case of the Hydrogen target at 3 GeV/c one can note a clear shift for sector 5 which is not present in sectors 4 or 6 (see fig. 4.9).

Using the pulser data in which we give, as input, a delta function pulse equal for all pads, one can study the distribution of the time series for each pad. Two kinds of pads can be distinguished by using the mean value and the R.M.S. of this distribution: one class of bad pads has a mean shifted by about 100 ns and a larger R.M.S. with respect to the other class of good pads, as shown in fig. 4.10. As shown in fig. 4.11, the sector 5 has almost all pads shifted and the sector 6 has only few shifted pads. Knowing the two different families it is possible to correct the pad that are shifted by 100 ns. This information for each pad is recorded in the calibration file and the time series are corrected in the calibration algorithm.

The effect of the correction is demonstrated studying the z_0 distribution in the case of the Hydrogen target at 3 GeV/c for sector 5 where almost all pads are shifted and for sector 6 where only few pads are shifted. Fig. 4.12 shows the distribution before and after the 100 ns correction for sector 6 and 5. One can note that, after the correction, the two peaks for both sectors nicely superimpose.

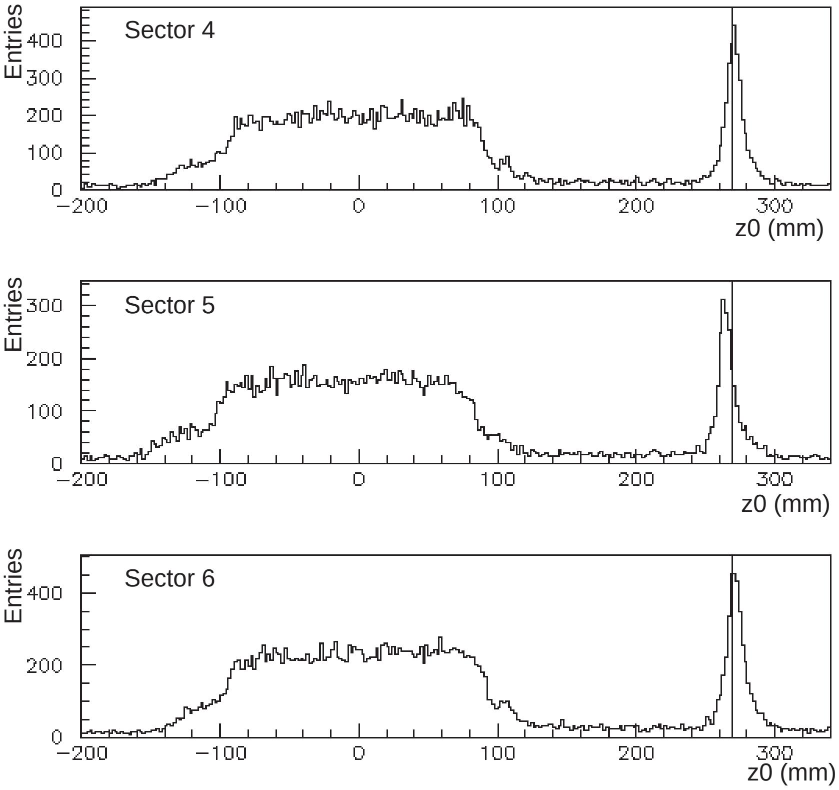

Figure 4.9: *The* z_0 *distribution for sectors 4, 5 and 6. The distribution for sector 5 is shifted with respect to that of the other sectors (as can be clearly seen by observing the endcap peak of the inner field cage on the right).*

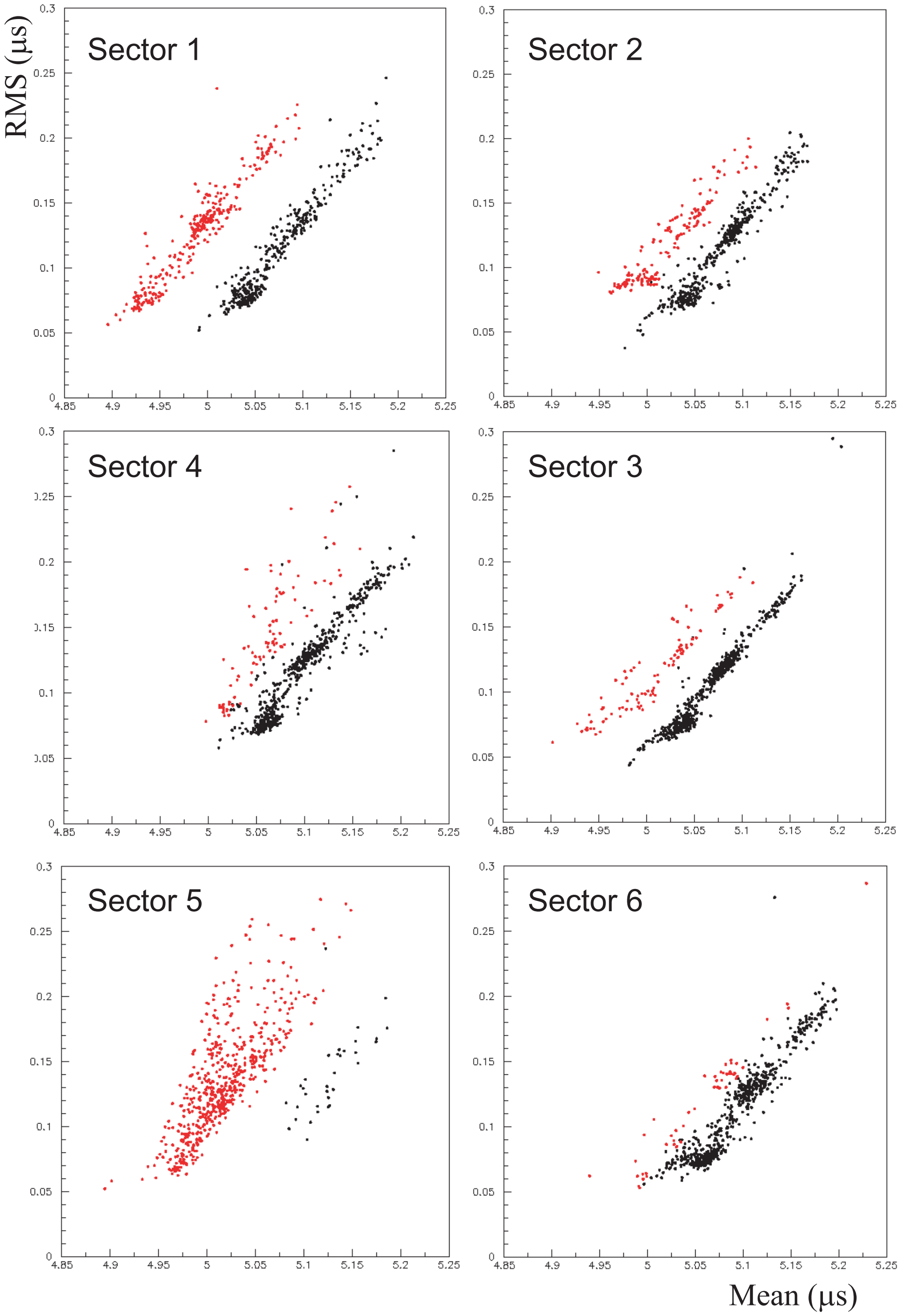

Figure 4.10: *Scatter plots of the R.M.S. versus the mean of the time series distributions. The pads shifted by 100 ns (red dots) are clearly visible with respect to the unshifted pads (black dots).*

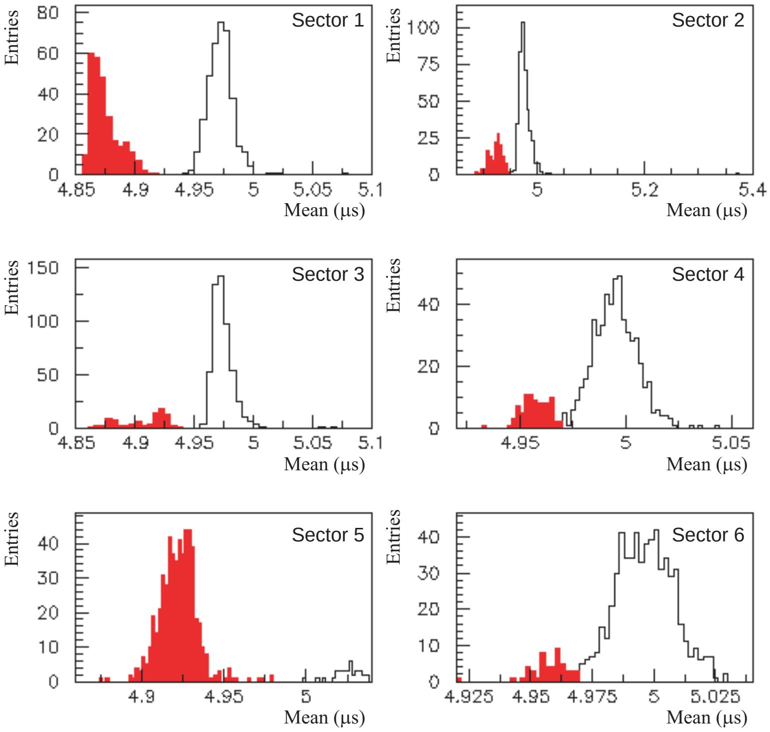

Figure 4.11: *Projections (along the main axis) of the scatter plots in fig. 4.10. The two populations of shifted (red) and unshifted (unfilled) are clearly distinguishable.*

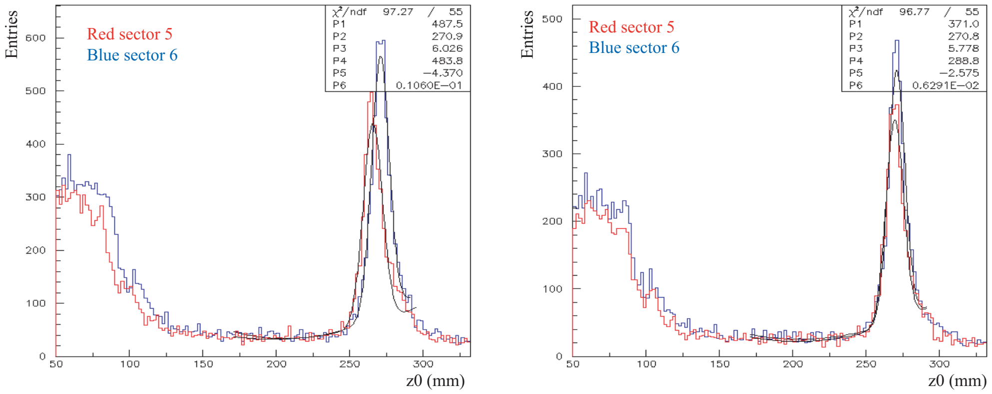

Figure 4.12: *The* z_0 *distribution in the case of the Hydrogen target at 3 GeV/c (run 19419-19455) for sector 5 (in red) where almost all pads are shifted and for sector 6 (in blue) where only few pads are shifted: on the left the distribution before the 100 ns correction and on the right after the correction. The parameters in the plot correspond to the results of the fit of the sector 6 peak by a Gaussian and a polynomial of second degree for the background subtraction.*

4.4 Equalisation

The response of the pads and their electronics to induced charges is not constant in time, nor equal between pads. Therefore, methods were developed to characterize the behaviour of the electronics, to track the variations of the response in time and to equalize the response between pads.

Three different equalisation methods were used to estimate the pad gains: measurement of the electronic response [137], equalisation with radioactive ^{55}Fe and ^{83}Kr sources [138] and a method based on the beam data. They are applied run–by–run, allowing a study of the time variations of the equalisation [139].

4.4.1 Study of the electronic response

In order to characterize the individual electronic channels, in particular their pulse shape, the response to a short pulse applied to each pad separately was measured. Known amounts of charge were injected in each pad and the response of the preamplifiers recorded by the data acquisition system. Three points were taken along the gain curve of each preamplifier, so that a complete channel-by-channel characterization in terms of electronic gain and linearity could be made.

4.4.2 Equalisation with radioactive sources

The calibration with radioactive sources aimed at studying the absolute gain of the pad response and to cross-check the method of run by run equalisation on beam data. This calibration permits also to measure the linearity of the energy response of the detector and to compare the channel-dependent equalisation factors both at low and at high X-ray energies. In fact with these sources we explore the dynamical range 2.9-41.6 keV covering the energy loss from minimum ionizing to low momentum heavy ionizing particles propagating inside the detector. In dedicated measurement periods, we employed radioactive isotopes of ^{83}Kr mixed into the TPC gas and ^{55}Fe sources positioned just outside the HV membrane. The measured X-ray energy spectrum (shown in fig. 4.13) features the peaks 5.9 keV and 3.0 keV for Fe sources, and 41.6 keV and 32.2 keV for Kr. The energy range provided by these sources is useful as an absolute energy calibration tool.

The energy range provided by ^{83}Kr sources that cover almost all the pad plane is useful also for a pad equalisation, collecting the energy release of the γ from the source. For this measurement a 3D cluster algorithm was developed (based on the 2D cluster explained in section 3.3.1). The total energy was calculated by summing the charge measured in neighbouring pads. This procedure therefore restricts the calibration to pads which are not adjacent to boundaries of the readout sectors. The gain of a pad is defined as the mean value of the energy integral when the pad has the largest signal in the cluster divided by the average mean of the energy integral computed on all TPC pads.

4.4.3 Run by run equalisation with beam data

The other method used for the equalisation of the gains of all active pad channels have been applied run–by–run with the Pad Pile-up Pulse method [139], that uses the real conditions of operation in beam of the run (all pulses from each pad) to extract the topological (dead pad map, noisy pad map) and analog (average gain of each pad channel before equalisation) information.

The method is based on the fact that the real tracks are distributed uniformly in ϕ angle. Accumulating all the data taken during a long period in time (the duration of a run) for each pad a ‘super-event’ (ADC-time series integrated on all events) is constructed. With the observation that most tracks have their origin in the target and that the energy-flow through each row of pads is equal, one can restrict the summation to tracks which traverse all pad rows. The latter condition can be met by making a selection of the time-of-arrival of the charge, constraining the ADC readings to those corresponding to tracks which are consistent with originating at the target

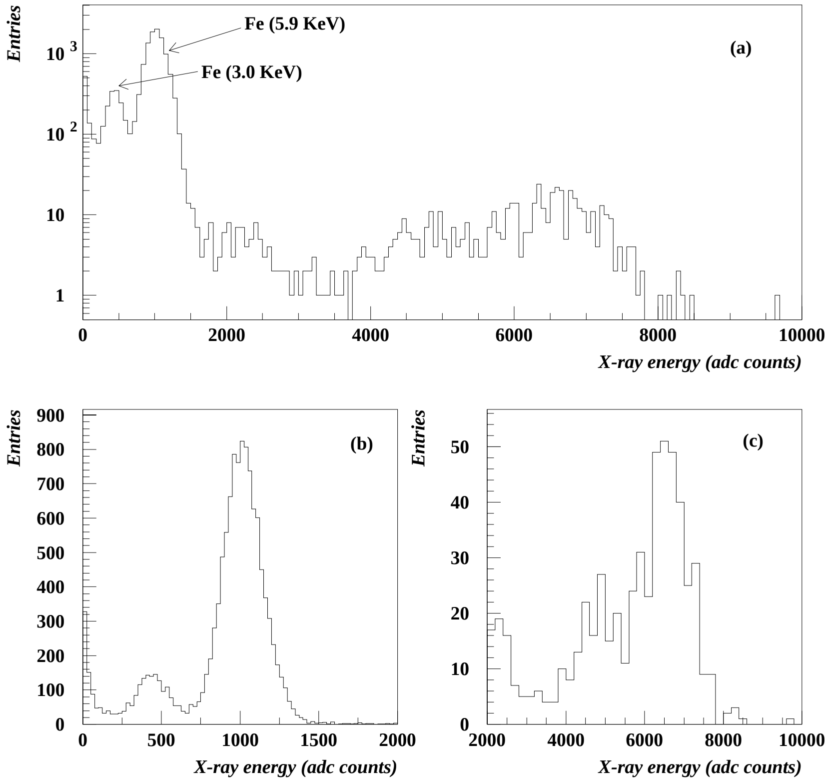

Figure 4.13: *Energy spectra of* ^{55}*Fe and* ^{83}*Kr X-rays absorbed in front of the three pads. The sum of the X-ray energy spectra features clearly the 3.0 and 5.9 keV peaks due to* ^{55}*Fe, plus the 9-14 keV complex peak and the 32.2 and 41.6 keV peaks due to* ^{83}*Kr. (a) Full energy spectrum (counts in logarithmic scale), (b) magnified view of the low energy region below 10 keV dominated by iron events, (c) magnified view of the high energy region where the krypton events are present.*

and traversing the full radius of the sensitive volume of the TPC. With the appropriate geometrical corrections, the average gain of each individual pad can be obtained. Moreover pads with a collected signal 5 times less than the average are set as dead pads and the ones with 2.5 times more than the average are set noisy pads. The equalisation between rows is obtained by normalizing the average $\mathrm{d}E/\mathrm{d}x$ per track point in each row for particle with a minimum energy loss in the gas With this method, the time-dependence can be followed: fig. 4.14 shows the R.M.S. variation of the pad gain observed as a function of time. The average percentage of dead or hot pads is of the order of 15% during all the data taking.

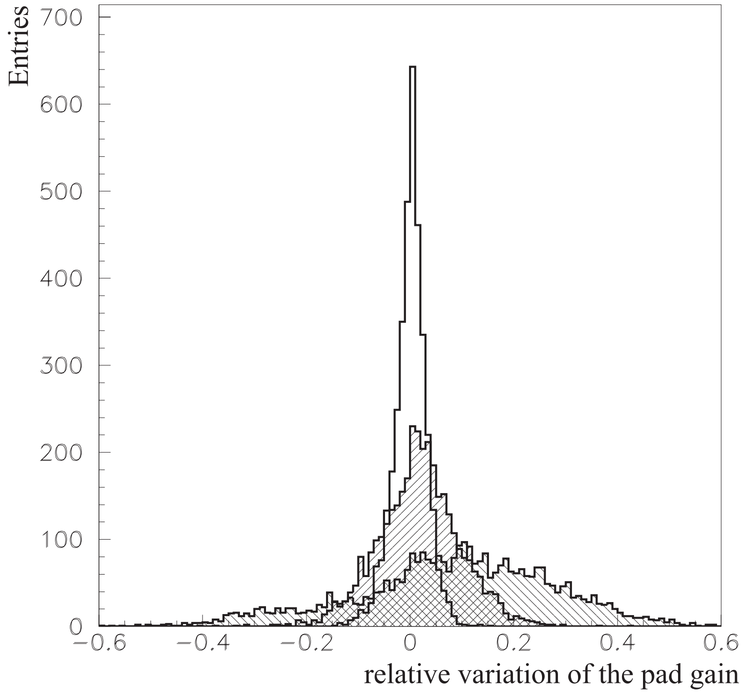

Figure 4.14: *Variation of the pad gains as a function of time. The unfilled histogram shows the relative pad-by-pad difference for two runs taken with 36 hour difference, it has an R.M.S. of* $\approx 3\%$*. The narrower hatched histogram is for two runs taken with a time difference of a week (*$\approx 8\%$ *R.M.S.). The broader hatched histogram is for two runs taken with a time difference of two months (*$\approx 18\%$ *R.M.S.).*

4.5 Cross talk effect

In the TPC front-end electronics a cross-talk effect has been observed for about half of the channels [137] [140]. It affects the tracking and momentum resolution, and also the energy resolution of the TPC. This effect is due to capacitive coupling between the output of one preamplifier and the input of another (possibly the same one, called self-talk) given the physical proximity inside the pad-plane of the connections which carry the signals before and after amplification.

In order to identify the existing cross-talk relations and to model the effect, a series of tests on all pads were performed. The pads were excited by means of a probe connected to a wave generator through a 15 pF capacitor. The wave generator provides a step function, thus a pulse with a shape as a delta function is injected into every pad and the signals generated in any pad has been recorded by the TPC DAQ system. These tests permit to measure

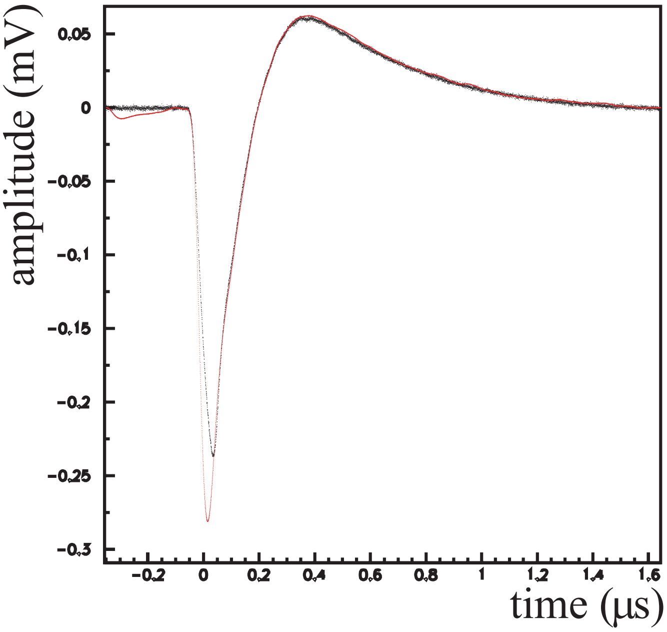

Figure 4.15: *Comparison between observed cross-talk signals (black) and the predicted ones (red)*

the preamplifier transfer-functions thus their electronic gain and to identify the cross-talk couplings.

These studies allowed us to identify and model the effects. It was found that the induced cross-talk signals could be predicted using the Fourier transforms of the signal from the pad inducing the cross-talk signal and the transfer function of the pad on which the cross-talk was induced, along with the capacitive coupling between the two pads (fig. 4.15 shows a cross-talk signal (black) and the model predicted signal (red)).

Using the results of this study we can reproduce the cross talk effect in Monte Carlo data using the measured transfer function for each pad and simulating the cross talk effect modelled by the Fourier transform. Moreover the Monte Carlo was used to design a correction based on the understanding of the capacitive coupling. The signal shapes are corrected by predicting the cross-talk signals using a Fast Fourier Transform (FFT model) and subtracting these predicted cross-talk signals from the measured ones. Unfortunately due to the zero suppression procedure, only positive signals are stored by the DAQ, consequently not all signals could be corrected. An example of Monte Carlo data with the simulation and the correction of the cross talk is shown in fig. 4.16.

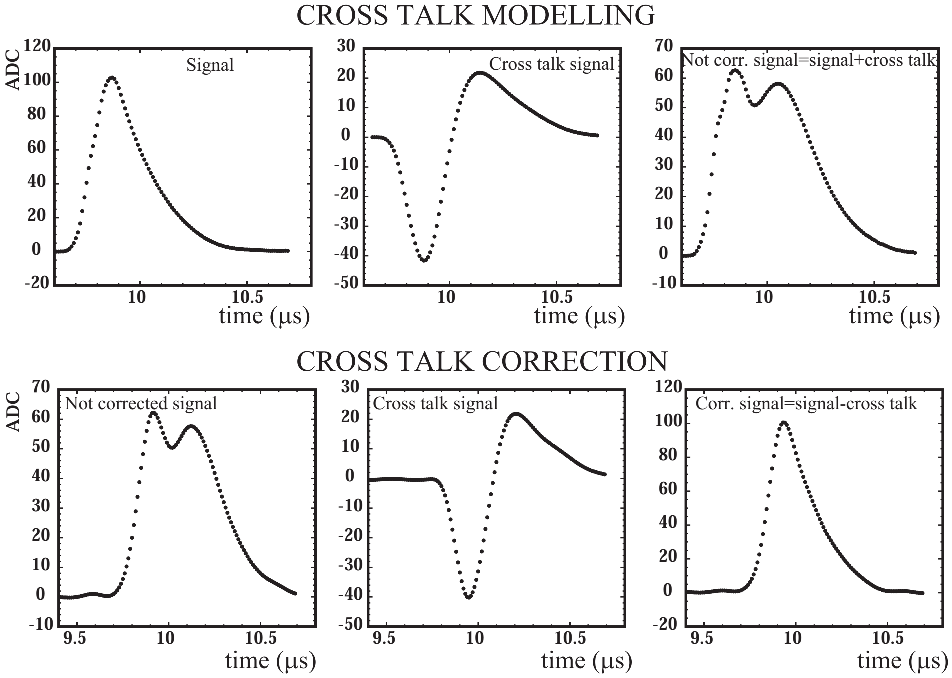

Figure 4.16: *On the top simulation of MonteCarlo signal and the cross talk effect. On the bottom the correction of the signal affected by cross talk.*

4.6 Dynamic Distortions

The HARP TPC exhibits two effects that produce distortions in the particle trajectories. The first one, called static distortions, is constant during all data taking and is due to a voltage misalignment of the order of 150 V between the inner field cage and the outer field cage. The dynamic distortion changes with time and depends on the beam (tuning) and data taking conditions.

In order to study these effects a sensitive parameter is d_0', the impact parameter in the xy plane, i.e. the minimum distance between a track and the beam particle direction determined by MWPC detectors extrapolated to the target on the xy plane the beam axis (determined by MWPC detectors on the beam line) in the xy plane. Its sign indicates if the helix encircles the beam axis (positive sign) or not (negative sign). The resolution can increase the width of the distribution without creating a shift of the peak (see fig. 4.17). A distortion effect, as a $\vec{E}x\vec{B}$ effect distorts the track with a dependence on 1/r, increases the momentum of the track with one sign and decreases the momentum of the track with opposite sign: this increases the absolute value of d_0' with an opposite sign for different charges (see fig. 4.18). If the distortion effect is very strong it can flip the charge of the track: the

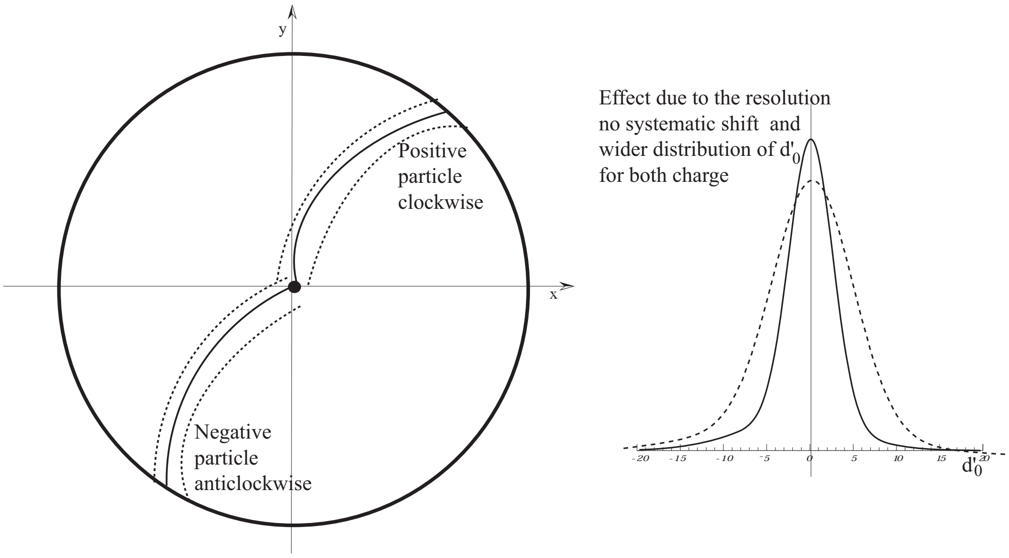

Figure 4.17: *The effect of the* d_0' *resolution increases the width of the distribution without creating a shift of the distribution*

momentum diverges to the 'infinite' value and then it is reconstructed with the opposite sign. Tracks of positive particles reconstructed as positive have a positive d_0' while tracks of positive particles reconstructed as negative have a negative d_0'. Tracks with wrong reconstructed charge create a negative peak in d_0' that can be distinguished by the negative distorted d_0' distribution (see fig. 4.19).

The mean of d_0' for positive and negative tracks presents a clear dependence on the event number during a spill, as shown in fig. 4.20. The dynamic and static distortions seem to be clear $\vec{E} \times \vec{B}$ type effect working in opposite directions. The dynamic distortions are clearly a charging effect of the chamber during the spill. This explains the behaviour of fig. 4.20. At the beginning of the spill the dynamic effect is negligible and the static distortion is dominant (as explained in section 4.7). During the spill the dynamic distortion first compensates the static one and in the second part of the spill will become dominant. We have observed that the effect of the dynamic distortions could become two times larger than the one due to the static distortions at the beginning of the spill.

The effect is the same for all the spills in the same run. The rate of the trigger particles, by opening of the T9 line collimators, for example, can emphasize or minimize the dynamic distortions. Different runs or settings can be affected more or less. The net effect can be some times large and some times almost negligible. As example one can look at the d_0' distributions for setting of Be 2% λ_I at 8 GeV/c runs 9450 and 9455 (fig. 4.21).

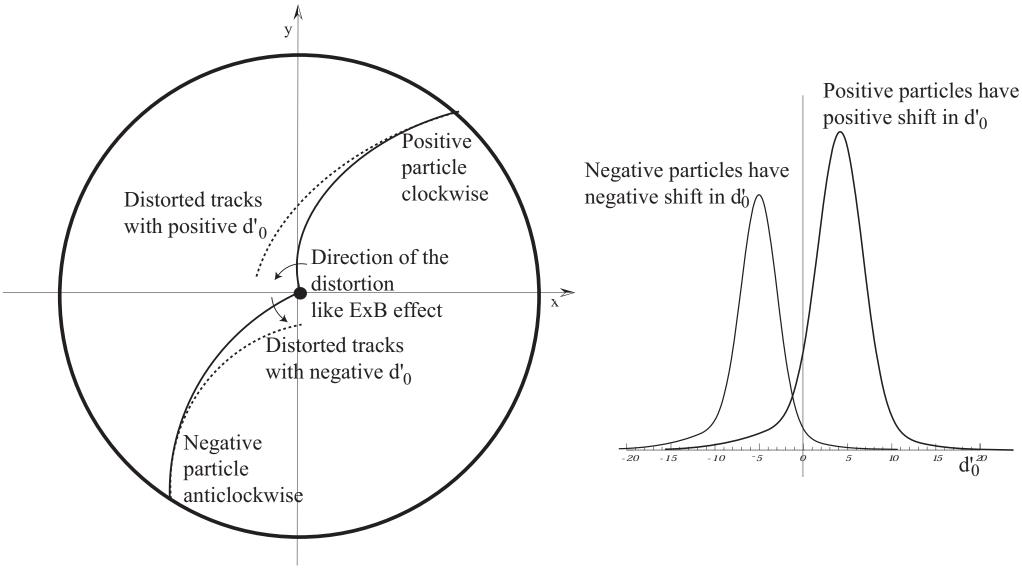

Figure 4.18: *A distortion effect, as a* $\vec{E}x\vec{B}$ *effect, distorts the track with a dependence on 1/r, increases the momentum of the track with one sign and decreases the momentum of the track with opposite sign, this shifts in opposite directions the* d'_0 *distributions of tracks of particles with opposite charges.*

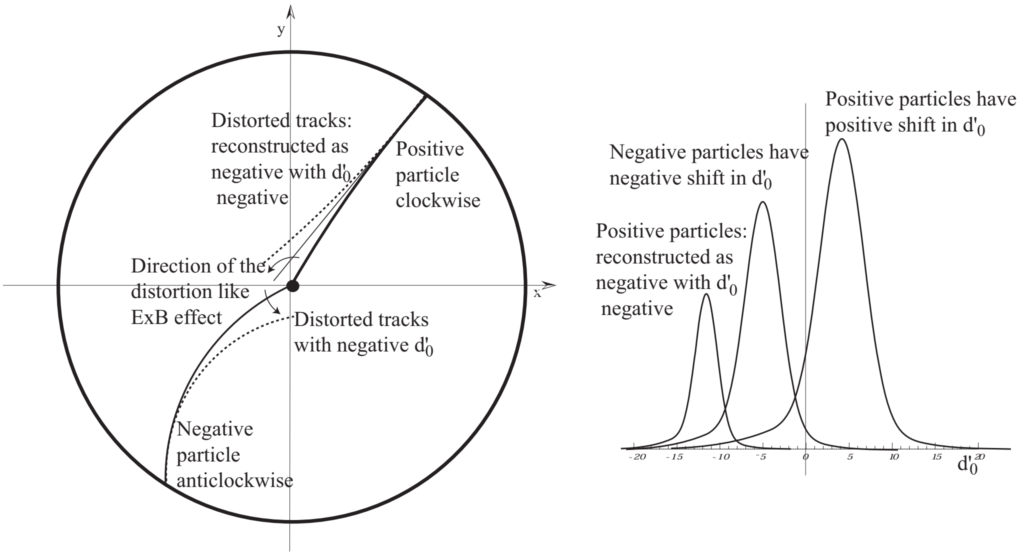

Figure 4.19: *If the distortion effect is very strong it can flip the charge of the track: the momentum diverges to the 'infinite' value and then it is reconstructed with the opposite sign. This creates a second peak in negative* d'_0 *distribution.*

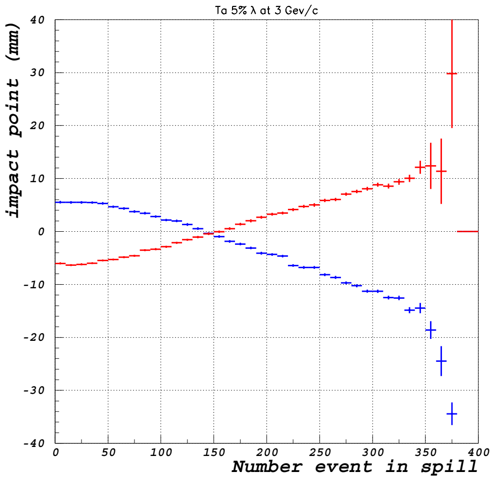

Figure 4.20: *The mean d_0' for the positive (in red) and negative (in blue) pions in function of the event number during a spill before the static distortion corrections.*

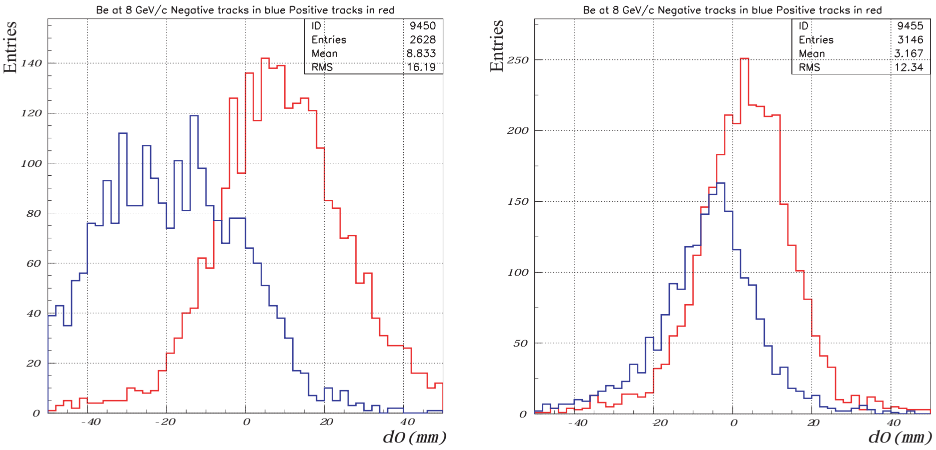

Figure 4.21: *The d_0' distribution for negative (in blue) and positive (in red) pions for Be 2% λ_I at 8 GeV/c runs 9450 on the left and 9455 on the right*

One possible explanation of this charging effect of the chamber during the spill can be found in the effect of positive ions generated by the beam crossing the detector (we see a dependency on the beam tuning). The ions accumulate in the chamber increasing the perpendicular component of the electric field. In the future, it will be studied if the cause is primary ions generated by the spurious beam-induced interactions, or by malfunctioning of the gating grid, or both. Our strategy, for the moment, has not been introduce corrections (which could fix the d_0' but bias the momentum), but simply to select a

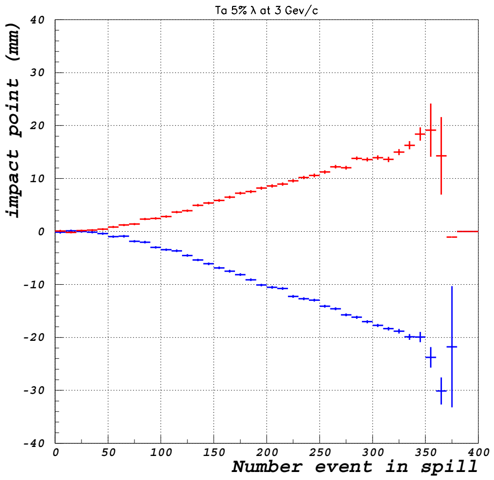

Figure 4.22: *The mean d'_0 for the positive and negative tracks in function of the event number during a spill after the static distortions correction.*

clean subsample of events that are not affected by dynamic distortions. If we study the dependence of d'_0 on the event number in the spill, correcting first for static distortion (as explained in the following paragraph), we see that the dynamic distortions become evident after a plateau (fig. 4.22). Once more it is confirmed that the peak at zero of the d'_0 distribution (observed also in overall distorted runs) is due to un-distorted events [141]. For this reason we decided to use two straightforward selection criteria: 1) keep only events at the beginning of the spill when this kind of distortion is a small fraction of the resolution; 2) in the chosen region we check that the d'_0 distribution has no bias for positive and negative tracks. This kind of selection is different from run to run, because the dynamic distortion has different effect for different runs. In this way we keep only a part of the data without affecting the efficiency, changing only the amount of data available for the final analysis.

4.7 Static Distortions

In order to understand the static distortion effect and to gauge the correction method [106], we studied 2003 cosmic ray data that were taken both with the nominal voltage of the inner field cage and with voltage shifts of +500 V and -500 V to magnify the effect [142]. To evaluate the effective voltage misalignment during the beam data taking in 2002, we analysed the 2002 experimental data (both beam data and cosmic rays).

The cosmic rays taken in 2003 with different voltage misalignment show that our modelling matches well the reality. The cosmic rays taken in two different periods of 2002 and the check on different settings for beam data show that these distortions are stable during all 2002. The same model can correct the distortions for cosmic rays and for beam data at the beginning of the spill.

The effective voltage misalignment for 2003 data turns out to be 101 V, while it is 150 V for cosmic rays taken in 2002 and for 2002 beam data.

4.7.1 Modelling

The motion of charged particles in the gas under the influence of electric and magnetic fields can be described by the following formula [143] that is the solution of the equation of motion:

$$\vec{u} = \mu|\vec{E}|\frac{1}{1+\omega^2\tau^2}\left[\hat{E} + \omega\tau\left(\hat{E}\times\hat{B}\right) + \omega^2\tau^2\left(\hat{E}\cdot\hat{B}\right)\hat{B}\right] \tag{4.2}$$

where $\hat{E}$ and $\hat{B}$ are unit vectors in the direction of the fields, μ is the mobility of the charges in the gas, ω is the cyclotron frequency of the electrons ($\mu = |(e/m)\vec{B}|$) and τ is the average collisions time of electrons in the gas molecules. For the HARP TPC $\mu = 4.3 \cdot 10^{-2}$ cm^2 V$^{-1}\mu$s^{-1} and $\omega \cdot \tau \simeq 3.3$.

In presence of electric and magnetic fields parallel to the cylinder axis (z axis) of the TPC, the drift of charges is parallel to this axis. Instead the component of the electric field perpendicular to the z axis (due to the voltage misalignment) and the inhomogeneities of magnetic field distort the electron drift, that is therefore no longer parallel to the z axis.

The voltage misalignment at the end of the inner field cage distorts the longitudinal component (shown in fig. 4.23) and creates a radial component of electric field (shown in fig. 4.24)

We simulate, with the Maxwell® program [89], the misalignment voltage at the endcap of the inner field cage and we use the magnetic field map in DetRep that represents the measured magnetic field in the HARP TPC. In this way we take into account both electric and magnetic field inhomogeneities. We obtain a map of the azimuthal, radial and along z distortions of the position where the electrons are produced. These distortions depend on the radial and z position where the electrons are produced as shown in the fig. 4.25, 4.26 and 4.27. An algorithm is implemented to correct the point positions using this map.

We produce different maps for different misalignment voltage and we use the data to determine the real misalignment voltage, as described in the following paragraphs.

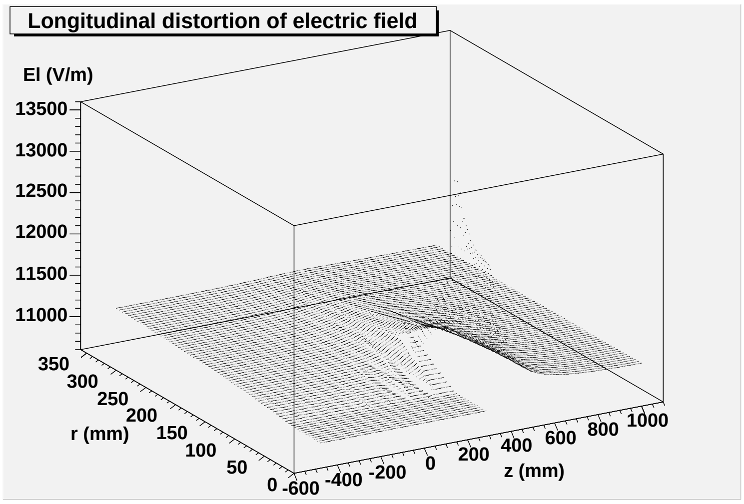

Figure 4.23: *The longitudinal component of the electric field as function of radial and z coordinate. In this plot the misalignment is 101 V; a higher misalignment increases the distortion but the shape is the same (Maxwell® simulation).*

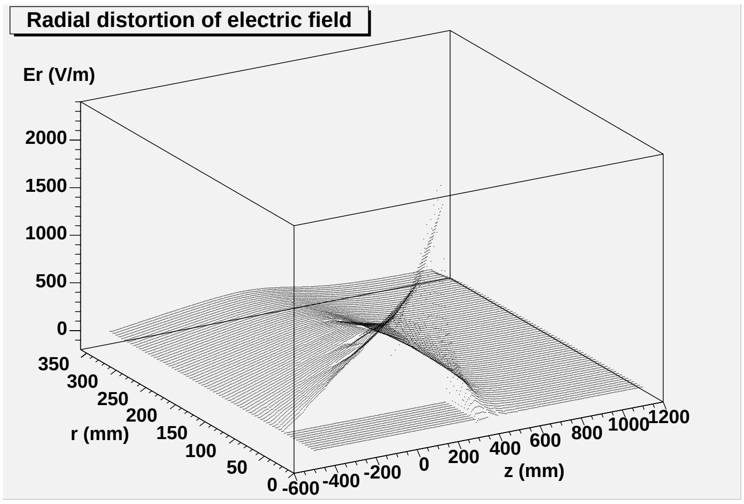

Figure 4.24: *The radial component of the electric field as function of radial and z coordinate. In this plot the misalignment is 101 V; a higher misalignment increases the distortion but the shape is the same (Maxwell® simulation).*

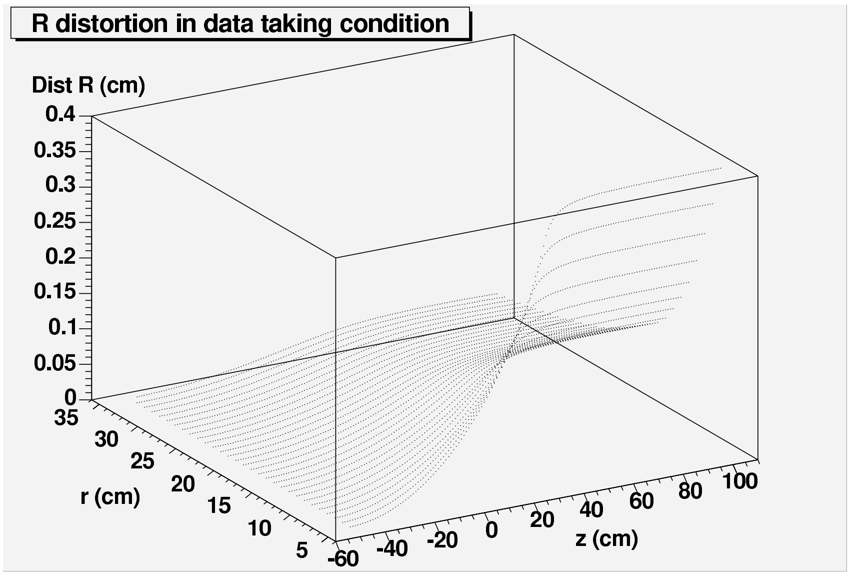

Figure 4.25: *The azimuthal distortion as function of radial and z coordinate. In this plot the misalignment is 101 V; a higher misalignment increases the distortion but the shape is the same (Maxwell® simulation).*

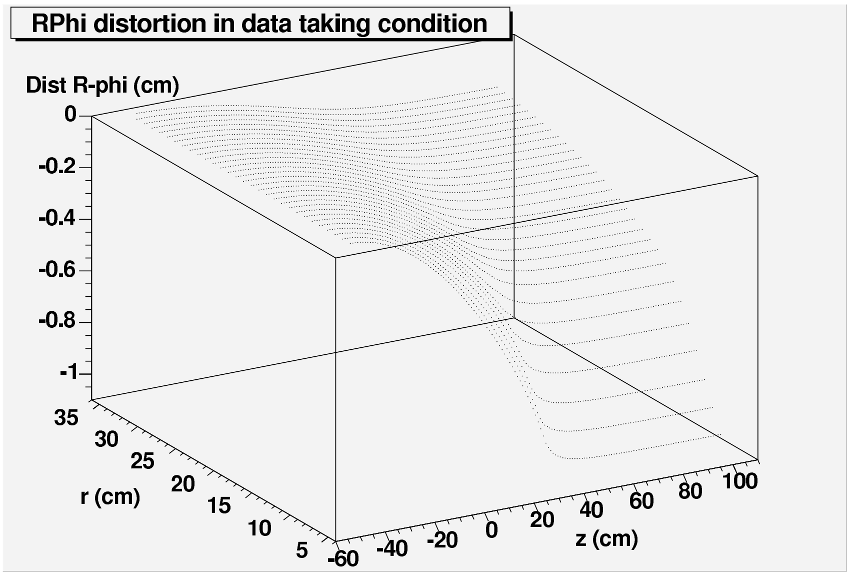

Figure 4.26: *The radial distortion as function of radial and z coordinate. In this plot the misalignment is 101 V; a higher misalignment increases the distortion but the shape is the same (Maxwell® simulation).*

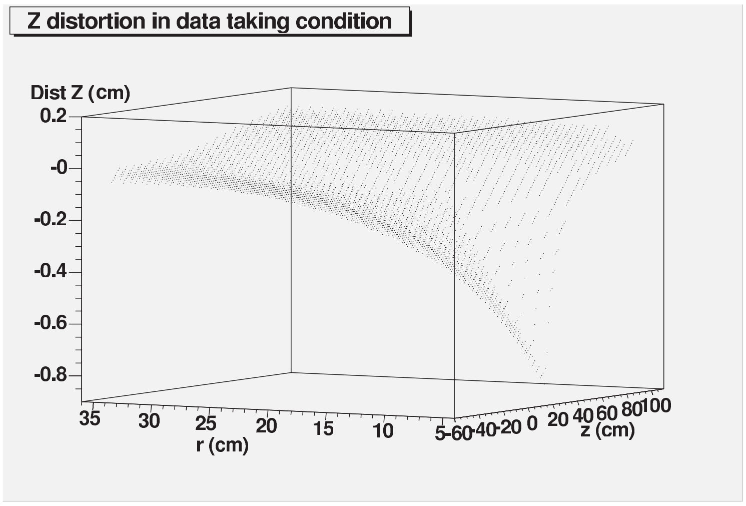

Figure 4.27: *The distortions along z as function of radial and z coordinate. In this plot the misalignment is 101 V; a higher misalignment increases the distortion but the shape is the same (Maxwell® simulation).*

4.7.2 Cosmic rays data taken during 2003

We were forced to move the TPC from its original position to another place of the experimental hall in order to do the cosmic rays 2003 calibration. A complete reproduction of the running condition of 2002 was not granted. The 2003 cosmic rays data were taken with the nominal voltage misalignment, and also with a voltage misalignment increased of + 500 V and -500 V from the nominal position.

These data were taken using as trigger a scintillator detector placed along the beam axis (-380 mm< z <230 mm). In this way we obtained a clean sample of cosmic rays that cross the central part of the TPC and cover the region along z between the padplane and the endcap of the inner field cage. We use these data taken at three different voltages to find the misalignment and to validate the method with higher misalignment (about a factor 3-5 with respect the nominal one).

To deduce the voltage misalignment, we select a cosmic particle if it is reconstructed by two tracks in two opposite TPC sectors. The distance between the two tracks and their different directions permit to evaluate the distortions and the effect of our corrections. These distributions are limited by the intrinsic resolution on the measurements of the impact point and of the track direction. When the residual distortions are small, we can use as best estimator of the real track the global fit considering the two segments as a single track. With this method we find a value of voltage misalignment of +101 V with respect to the voltage necessary to obtain a constant electric field. The fig. 4.28 and 4.29 show the angular resolution and impact point resolution in the xy plane and along z after the correction for static distortions with a misalignment of +101 V.

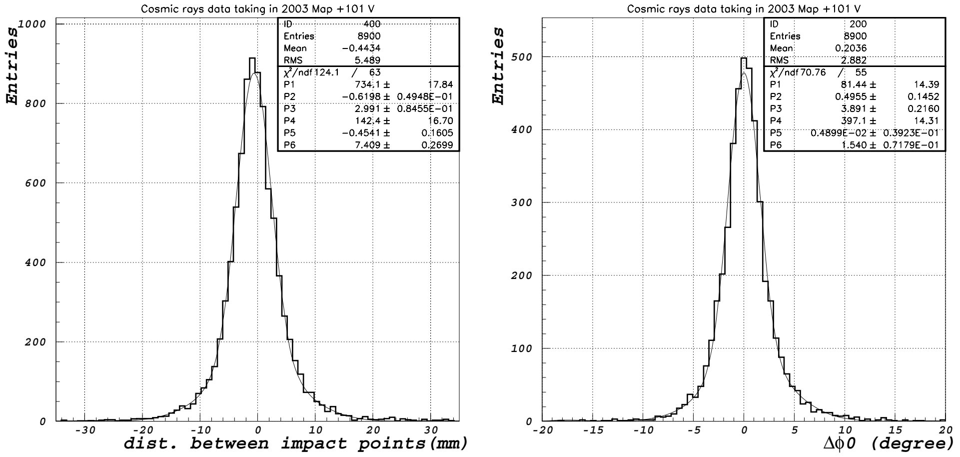

Figure 4.28: *On the left minimum distance between a segment with respect to the global fit. On the right angular difference in the xy plane between global fit and single fit. Both after the correction of the static distortions. The inset reports the results of the double gaussian fit of the distribution.*

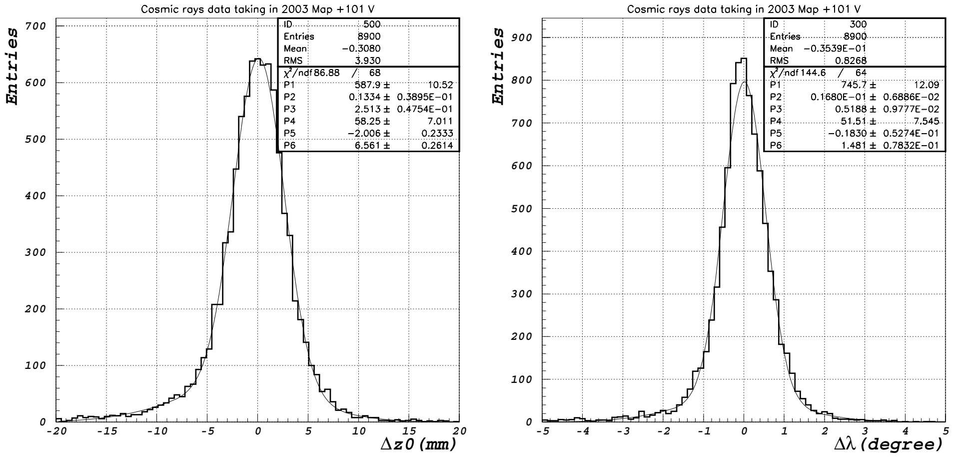

Figure 4.29: *On the left distance along z of the impact point of one segment and the global fit. On the right angular difference with respect to the z axis between global fit and single fit. Both after the correction of the static distortions. The inset reports the results of the double gaussian fit of the distribution.*

4.7.3 Cosmic rays data taken during 2002

The cosmic ray run of 2002 used as trigger the RPC barrel that surrounds the TPC. With this trigger we can study the z dependence of the distortions because the RPCs cover the whole TPC along z, so the sample of cosmic rays collected with this trigger cover the whole TPC along z. During 2002 we took cosmic rays during July and October after the data taking: this permits to verify the stability of the distortions. We obtain the same results for the two periods. In the following, we present the results for cosmic rays taken in October 2002.

These data constitute a less clean sample of cosmic rays crossing the inner part of the TPC and are therefore reconstructed as two different tracks. We select events with only two reconstructed tracks. Moreover to obtain events with single cosmic rays reconstructed as two tracks we analyse the distance along z of the impact point and the angular difference with respect to the z axis between the two reconstructed tracks. The effect of the distortions is small for these quantities. These distributions are shown in fig. 4.30 without any correction for static distortions. The distributions show a clear peak and small tails that includes the events with two different cosmic rays. We applied a cut at 14.25 mm for the z distribution and 2.5 degree for the λ distribution that correspond to 5 σ of these distributions.

The z dependence of the static distortions in the xy plane is shown by a study of the distance between the two helixes obtained by the fit of the two single tracks as function of z and of the angle difference in the xy plane as function of z. These distributions are shown in fig. 4.31. The distortions are

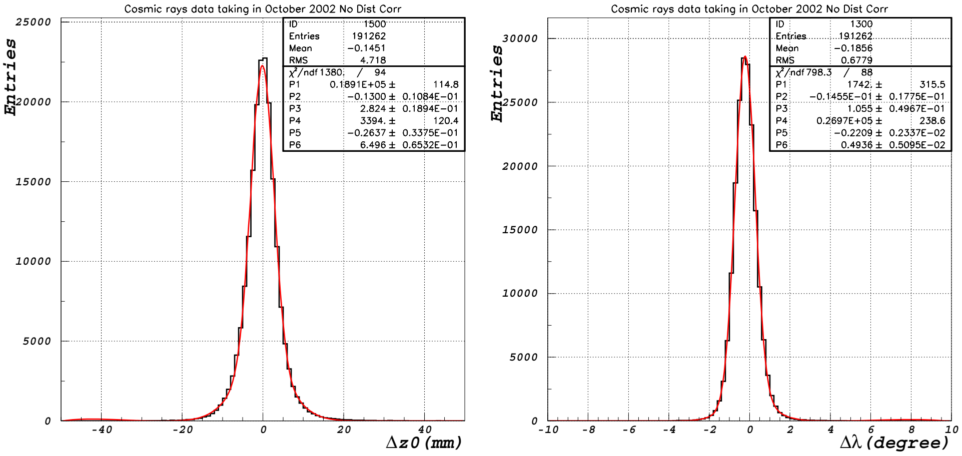

Figure 4.30: *Difference of* z_0 *(left) and* λ *(right) of the two segments without any distortions correction. The inset reports the results of the double gaussian fit of the distribution.*

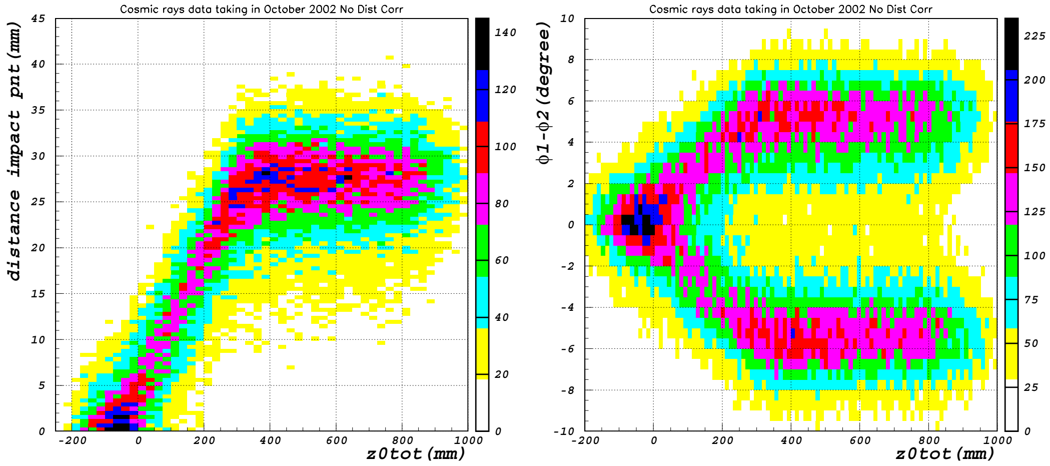

Figure 4.31: *On the left, minimum distance between the two segment as function of* z *of the impact point, before static distortions correction. On the right, angular difference in the xy plane between global fit and single fit as function of* z*, before static distortions correction.*

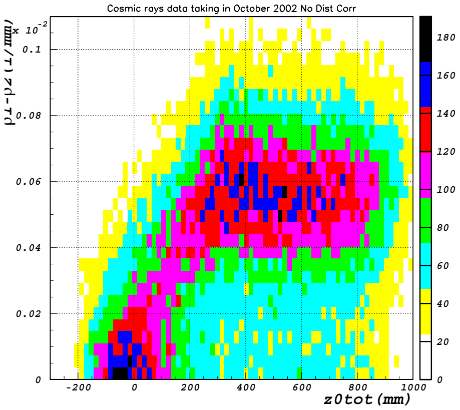

Figure 4.32: *The* ρ *difference in the xy plane between the two segment as function of* z*, before static distortions correction. The distortions are negligible in the first part of the TPC along* z *(the part near to the padplane), then the distortions increase approaching to the endcap of the inner field cage where the distortions of electric field are maximum, and after this point they reach a plateau constant in* z*.*

negligible in the first part of the TPC along z (the part near to the padplane), then the distortions increase approaching to the endcap of the inner field cage where the distortions of electric field are maximum, and after this point they reach a plateau constant in z. Analysing the difference of bending radius (ρ) that is proportional to the inverse of the transversal momentum, we can see that also the momentum is distorted by the static distortion (see fig. 4.32).

To determine the efficiency of the corrections we study the cosmic rays with the largest distortions therefore with a z of impact point larger than 300 mm. By the study of the angular resolution and impact point resolution in the xy plane and along z for all cosmic rays (no selection in z), we find that the misalignment for the cosmic rays taken during 2002 is +150 V. After the distortions correction using this voltage misalignment, the angular resolution in λ is 0.37° and in ϕ_0 is 1.7° and the impact point resolution in the xy plane is 3.7 mm and along z is 2.2 mm (these resolutions are shown in fig. 4.33 and 4.34). We can evaluate the upper limit of this misalignment by studying the residual distortions for different voltages for tracks with a z_0 after the endcap of the inner field cage (where the distortions are maximum). By a linear extrapolation we find that the upper limit is 166 V [106].

Finally, we calculate the angular resolution and the track impact point resolution in the xy plane and along z after the correction of the static distortions in different slices along z to check that there are no residual distortions in any region of TPC. The results are summarized in the table 4.6. We conclude that no residual distortion are present in whole TPC region.

σ	$-0.2 < z_0 < 0.1$m	$0.1 < z_0 < 0.25$m	$0.25 < z_0 < 0.45$m	$z_0 > 0.45$m
Δd_0	3.8 mm	3.1 mm	3.4 mm	3.8 mm
$\Delta\phi_0$	1.7°	1.7°	1.7°	1.8°
Δz_0	2.2 mm	2.3 mm	2.1 mm	2.2 mm
$\Delta\lambda$	0.41°	0.38°	0.35°	0.38°

Table 4.6: *Differences between the fit helix results for the two single tracks for cosmic rays taken in 2002 in different z slices, after the correction.*

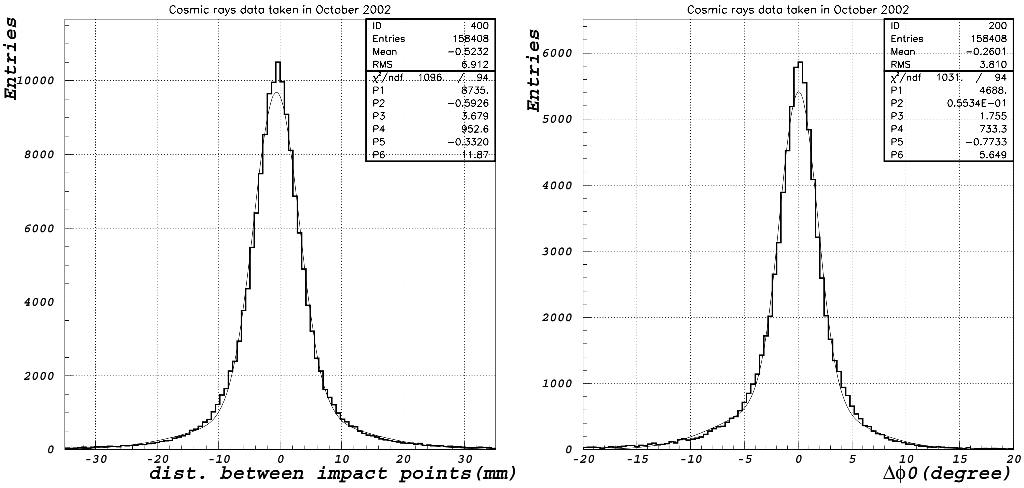

Figure 4.33: *On the left minimum distance between a segment with respect to the global fit. On the right angular difference in the xy plane between global fit and single fit. Both after the correction of the static distortions. The inset reports the results of the double gaussian fit of the distribution.*

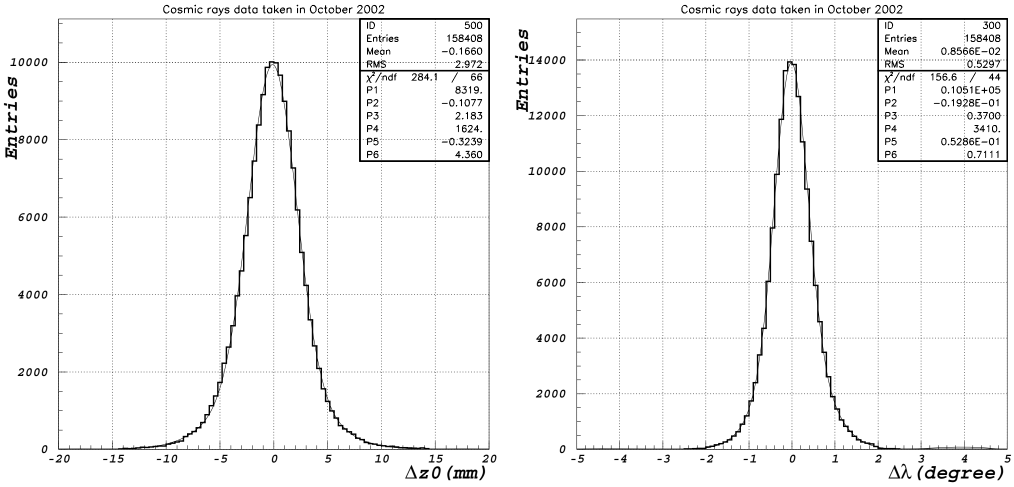

Figure 4.34: *On the left distance along z of the impact point of one segment and the global fit. On the right angular difference with respect z axis between global fit and single fit. Both after the correction of the static distortions. The inset reports the results of the double gaussian fit of the distribution.*

4.7.4 Beam data taken during 2002

In beam data taken in 2002 (the case considered here is data with target of Ta 5% λ_I at 3 GeV/c, but we obtained similar results for all settings analysed), a sensitive parameter to study the TPC distortion is d'_0, the impact parameter in the xy plane.

As explained in section 4.6, the mean of d'_0 for positive and negative tracks shows a clear dependence on the event number during a spill, as shown in fig. 4.35. At the beginning of the spill the dynamic effect is negligible and the static distortion is dominant. During the spill the dynamic distortion first compensates the static one and in the second part of the spill will become dominant [129].

Applying the distortion correction with a misalignment of 150 V the distortions at the beginning of the spill disappear (fig. 4.35). Using the first 10 events in the spill we study the residual distortion with three different voltages for the correction. We can calculate the upper limit of the misalignment by a linear fit of these values. The upper limit is 170 V, consistently with the value computed with the 2002 cosmic data [106].

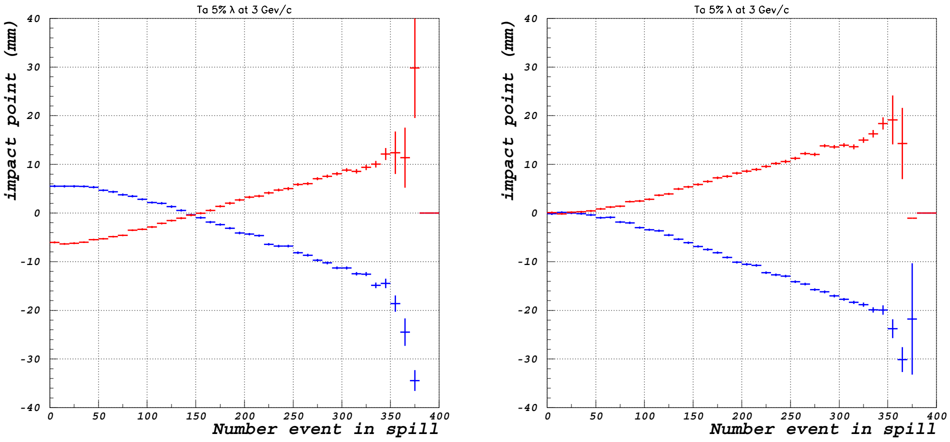

Figure 4.35: *The mean* d'_0 *for positive and negative tracks as function of the event number during a spill, on the left with the voltage misalignment and on the right with static distortions correction for a misalignment of 150 V.*

Chapter 5

TPC performances

5.1 Introduction

The TPC performance can be evaluated analysing data: cosmic ray data and physics target data [144]. Moreover comparing these performance with the Monte Carlo data: permits validation of Monte Carlo simulation that should reproduce the detector performance for physics analysis. In this chapter we describe the study of residuals, the evaluation of the momentum resolution, the angular and impact point resolution. Moreover we evaluate the apparatus efficiency using the Monte Carlo data. Finally, energy loss in the gas allows particle identification by $\mathrm{d}E/\mathrm{d}x$ as described in the last section.

5.2 Data Selection

In this section we explain the data selection criteria used for the determination of the TPC performance that are the same applied for the data analysis.

Cosmic ray data

We select tracks with at least 12 points per each track and no–error flag associated to the fit results. We use a dedicated dead-hot pad map and equalised pad gains for these data. We select cosmic rays that cross the TPC in the central part and that are reconstructed as two tracks (these are identified by the green and blue tracks in fig. 5.1) in two opposite directions. A comparison between the two tracks provides information on the resolution of the reconstructed tracks. In order to improve the reconstruction resolution, we refit the cosmic tracks after adding the point in the middle position between the two reconstructed impact points with respect to the z axis of the two separated tracks. By this method we can evaluate the resolution of the vertex

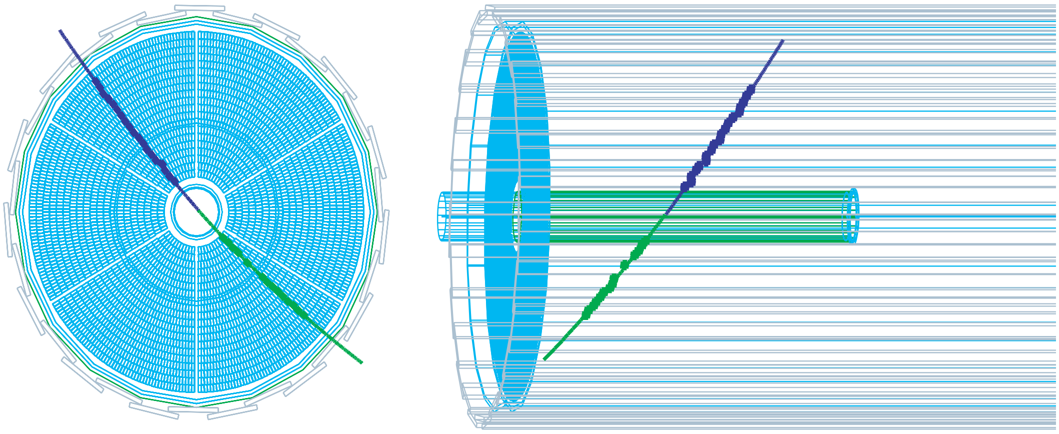

Figure 5.1: *Cosmic ray reconstructed as two tracks (identified by the green and blue tracks) emitted in two opposite directions.*

algorithm used in the data (explained in section 3.3.4)

Definition of cuts for Ta 5% λ_I at 5 GeV/c

We study the 5% λ_I Ta target data with a proton/pion beam at 5 GeV/c. We select events that have only one beam particle hitting the target and with an interaction trigger in the ITC. We study only the first 50 events in the spill to avoid dynamic distortions. We focus this study on the secondary particles emitted by interactions in the target into the large angle region, between 0.35 rad and 2.15 rad. We select tracks that satisfy quality criteria: tracks with at least 12 points, no error flag associated. Moreover to apply the vertex fit we select tracks coming from the target within 2σ of resolution on the impact point, as calculated using cosmic ray data.

Definition of cuts for the Monte Carlo data

The Monte Carlo includes modelling of all known effect and features defining the TPC response, including also the dead map measured for the analysed setting. Dynamic distortions are not modelled because in the data they have been shown to be negligible for the first 50 events in spill. The residual of static distortions after corrections are also negligible. Finally, the modelling of cross-talk is switched off in the software because it was demonstrated not to influence significantly the TPC performance.

We analyse the data produced by a generator of single positive or negative pions and protons (one particle per event) with a interaction point in the target and with a production distribution in the xy plane reproducing the beam distribution in the analysed target data. These data have a uniform angular distribution and a momentum distribution at the production point that decrease linearly with the momentum.

We select Monte Carlo events with only one positive pion entering in the TPC (we reject events where the particle decays or interacts in the material around the target). The Monte Carlo reconstructed particles should satisfy the same quality criteria as for the data: emission from the target, within the large angle region between 0.35 rad and 2.15 rad.

5.3 Residuals

The study of residuals provides an estimation of the errors on the cluster-space points and their possible dependence on selected variables. To evaluate the residuals of a point that belongs to a track, we exclude this point from the group of points used for the track helix fit. Then we calculate the residuals independently for the z-beam direction and for the azimuthal direction.

The residual along $r\phi$ (see fig. 5.2) is defined as the distance along the arc between the cluster position and the associated point on the fit circle. The track point is calculated by the intersection between the 'cluster row circle' and the fit circle. Since the intersections between the 2 circles can give 2 points as result, we choose as "real" the point with the minimum distance to the cluster position.

The residual along r is constant and depends only on the geometrical construction of the TPC: the cluster position is discrete in this direction and the cluster is defined row by row.

The residual along z is the distance between the cluster position and the real point on the fit helix, calculated using the same xy position used in the

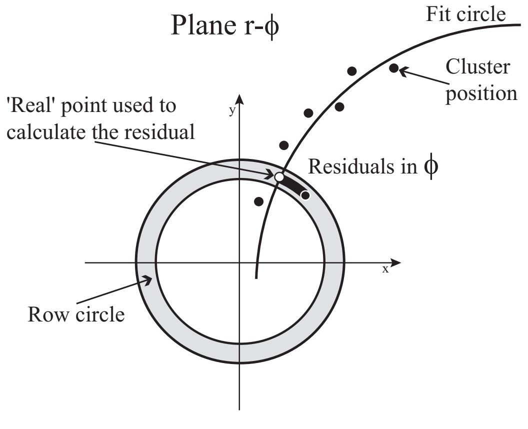

Figure 5.2: *Definition of residuals along $r\phi$ plane.*

calculation of the residuals along $r\phi$.

We consider two categories of clusters: near a dead region and not near a dead region; for both we study the dependence as function of the number of hits used to calculate the cluster position.

A cluster is defined to be near a dead zone if any pad neighbour to the pads that compose the cluster is dead; in such a case part of the signal could be lost. This missing signal creates a systematic effect on the point resolution. This effect is clearly visible in the residual distribution in fig. 5.3 for cluster composed by one hit: the residual distribution can be fitted by two Gaussian centred at about -4 mm and + 4 mm with the same sigma (the systematic shift has different sign if the dead pad is on the right or on the left of the pad that composes the cluster). This effect is negligible for clusters composed by 3 pads: in this case the eventual missing signal would have only a small signal that gives a small systematic shift. Therefore the cluster with 3 hits has better resolution.

The Monte Carlo data reproduce well these effects (see fig. 5.4). The only minor difference is for clusters composed by 4 or more hits: both for the resolution (1.7 mm for the data and 1.5 mm for Monte Carlo) and for the relative population (9% for data and 6% for Monte Carlo). This is due to the missing model of cross talk effect in the Monte Carlo data and the missing correction in the data. In fact one of the effect of the cross talk is the generation of fake signals (see section 4.5). The results are summarised in table 5.1.

We analyse the $r\phi$ residuals distributions for cluster not near a dead region by a double Gaussian fit[*]. We find two components (one larger Gaussian with $\sigma \sim 2.5$ mm and one smaller Gaussian with $\sigma \sim 1$ mm); the two components are always present in the four classes but their contributions change as function of the number of hits used to calculate the position in a cluster (see fig. 5.5). These residuals are well reproduced by Monte Carlo data (see fig. 5.6), as well the population of the different classes is the same as for the data. These results are summarised in table 5.2.

The residuals along the z direction do not change significantly (not more than few hundred μm) with the different classes as function of the number of hits (see fig. 5.7 and 5.9). The Monte Carlo data reproduce well the residuals distribution, as shown in fig. 5.8 and 5.10. The table 5.3 summarises the results and compares both the RMS of the z residual distribution and the sigma of the Gaussian fit.

---

[*] as double Gaussian fit is intended a fit which uses the sum of two independent Gaussians

number of hits in cluster	Target Data σ of Gaussian [mm]	MC Data σ of Gaussian [mm]	% of clusters (Data - MC)
1 hit near dead	3.0-3.1	2.6-2.8	31% - 31%
2 hits near dead	2.2	2.3	36% - 39%
3 hits near dead	1.4	1.3	24% - 24%
more than 3 hits near dead	1.7	1.5	9% - 6%

Table 5.1: *Residuals along $r\phi$ for clusters near a dead region. Results of a Gaussian fit for the four classes of clusters as function of their number of hits for clusters near a dead region (see fig. 5.3 and 5.4). The residuals distribution for 1 hit is well fitted by a double Gaussian fit, due to the systematic shift generated by the dead zone.*

number of hits in cluster	σ of smaller Gaussian [mm] (Data - MC)	σ of larger Gaussian [mm] (Data - MC)	% of clusters (Data - MC)
1 hit not near dead	-	4.4 -3.0	12% - 9%
2 hits not near dead	1.0 - 1.1	2.4 - 2.1	31% - 35%
3 hits not near dead	0.9 - 0.8	2.0 - 1.9	42% - 43%
more than 3 hits not near dead	1.0 - 1.1	2.7 - 2.9	14% - 13%

Table 5.2: *Residuals along $r\phi$ for clusters not near a dead region. The results of a double Gaussian fit for the four classes of clusters as function of their hits number for clusters not near a dead region (see fig. 5.5 and 5.6). The residuals distribution for 1 hit is well fitted by a single Gaussian, for this reason the σ of the smaller Gaussian is not given.*

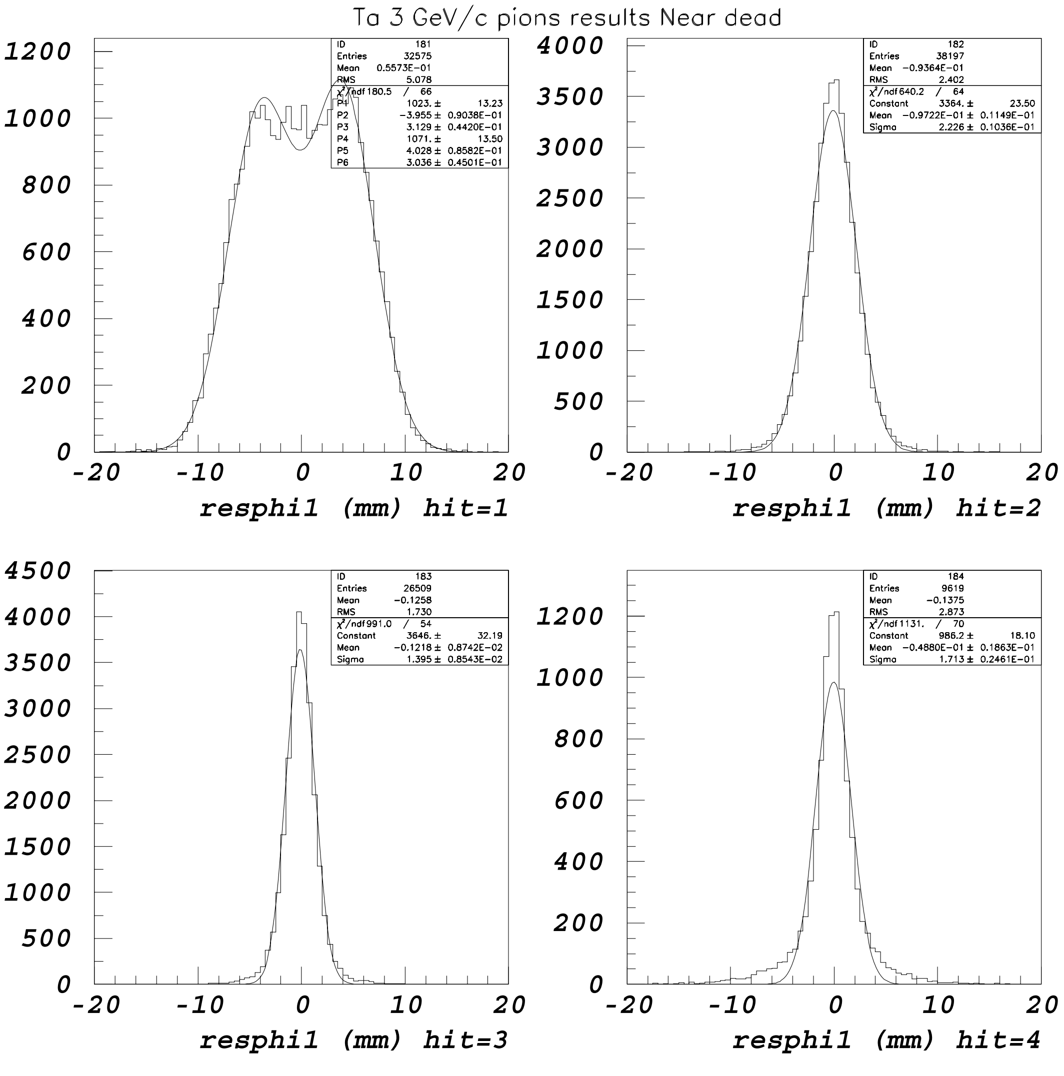

Figure 5.3: *Physics target data. Residuals along the $r\phi$ plane as function of the number of hits in cluster near to a dead region.*

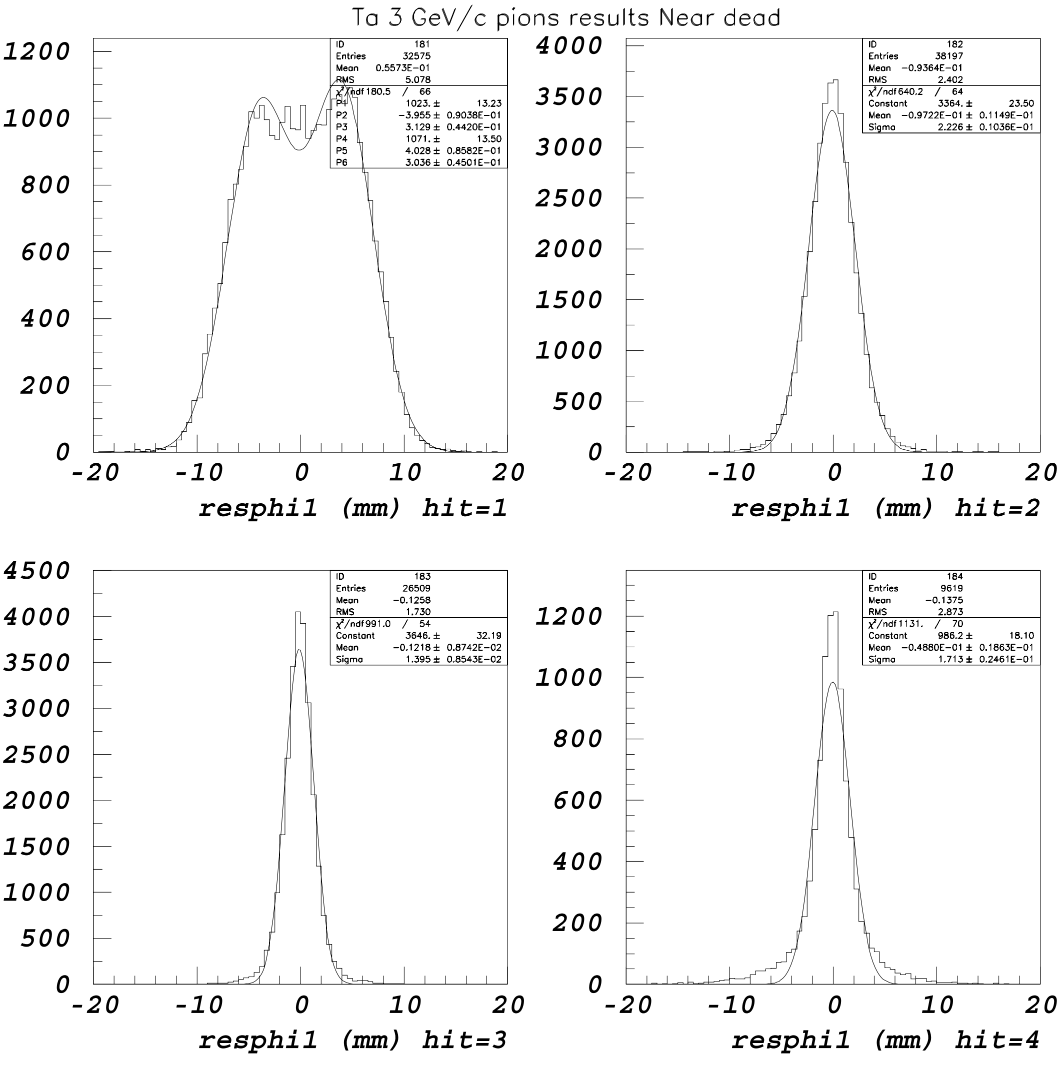

Figure 5.4: *Monte Carlo data. Residuals along the $r\phi$ plane as function of the number of hits in cluster near to a dead region.*

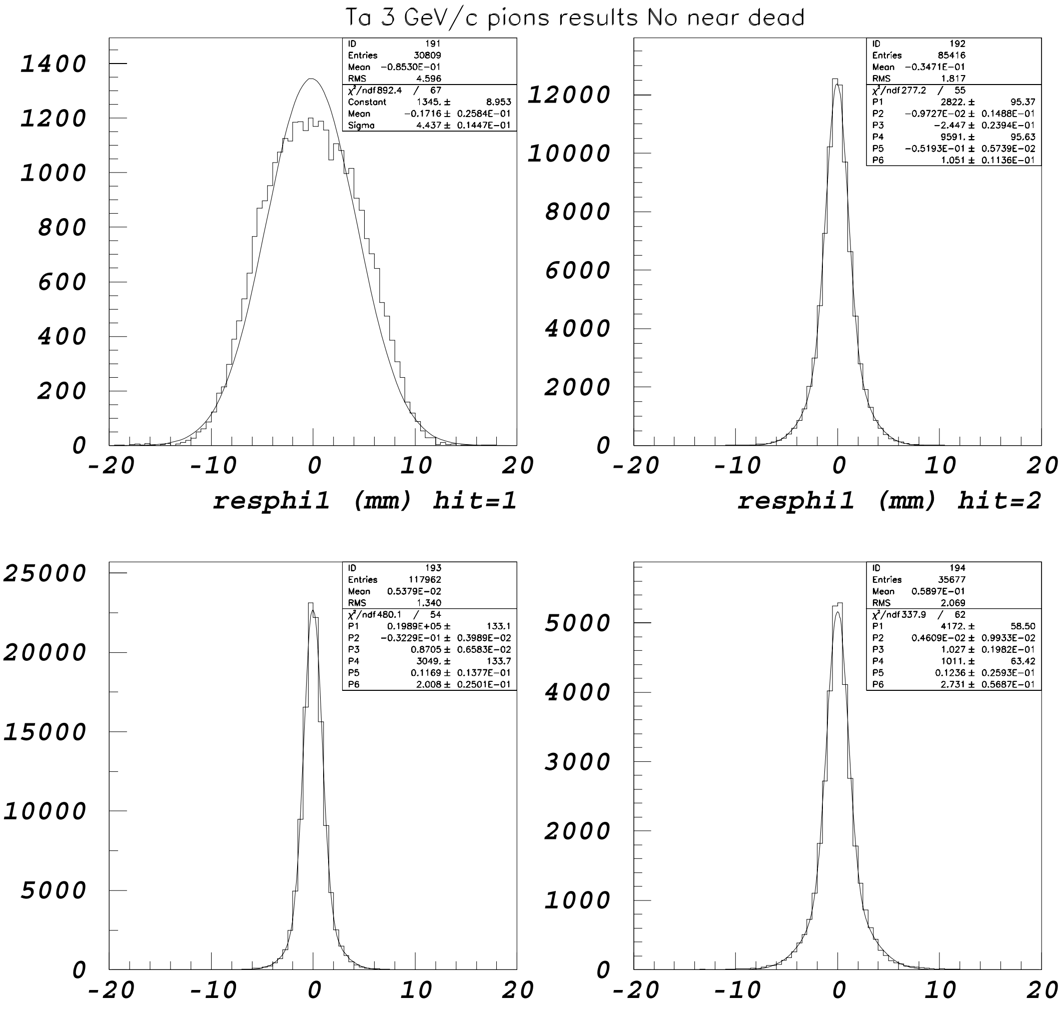

Figure 5.5: *Physics target data. Residuals along the $r\phi$ plane as function of the number of hits in cluster not near to a dead region.*

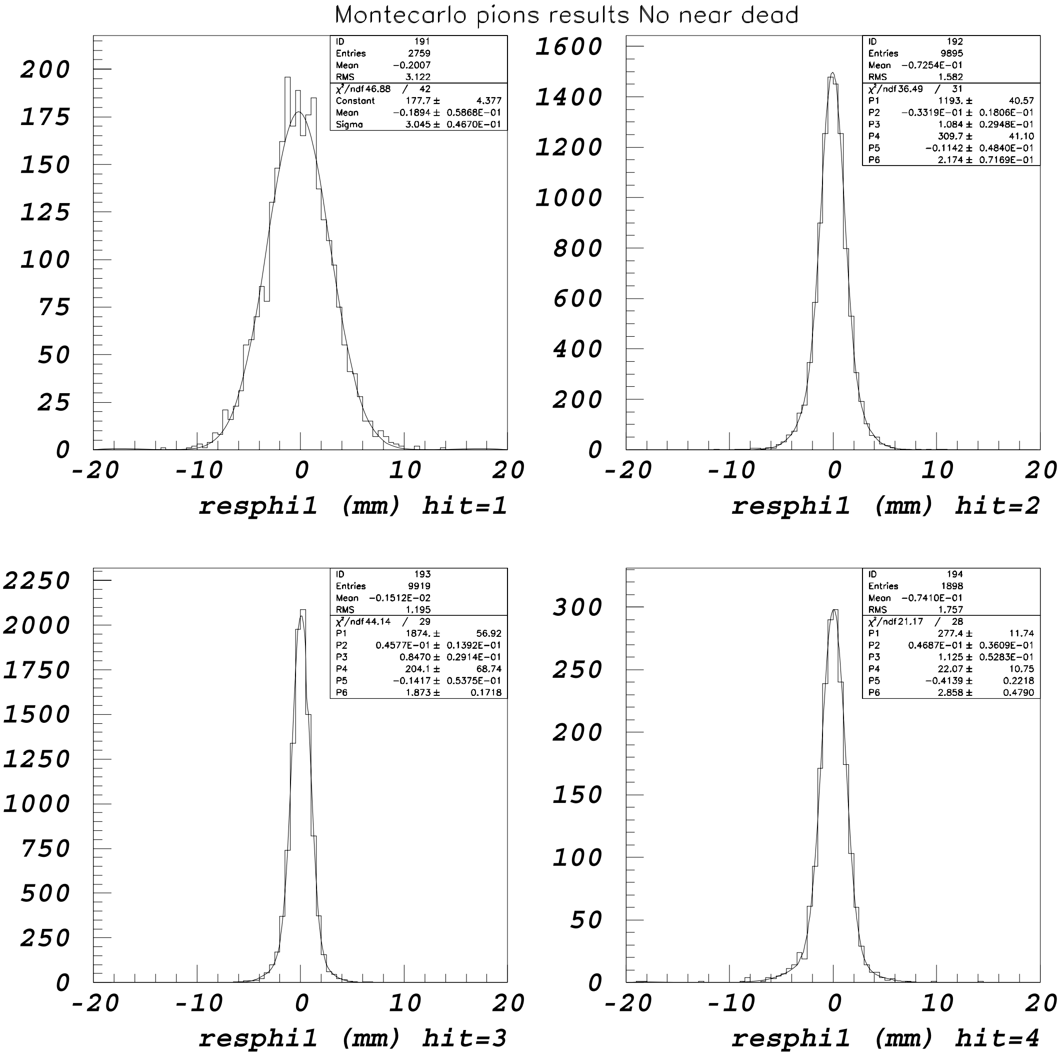

Figure 5.6: *Monte Carlo data. Residuals along the $r\phi$ plane as function of the number of hits in cluster not near to a dead region.*

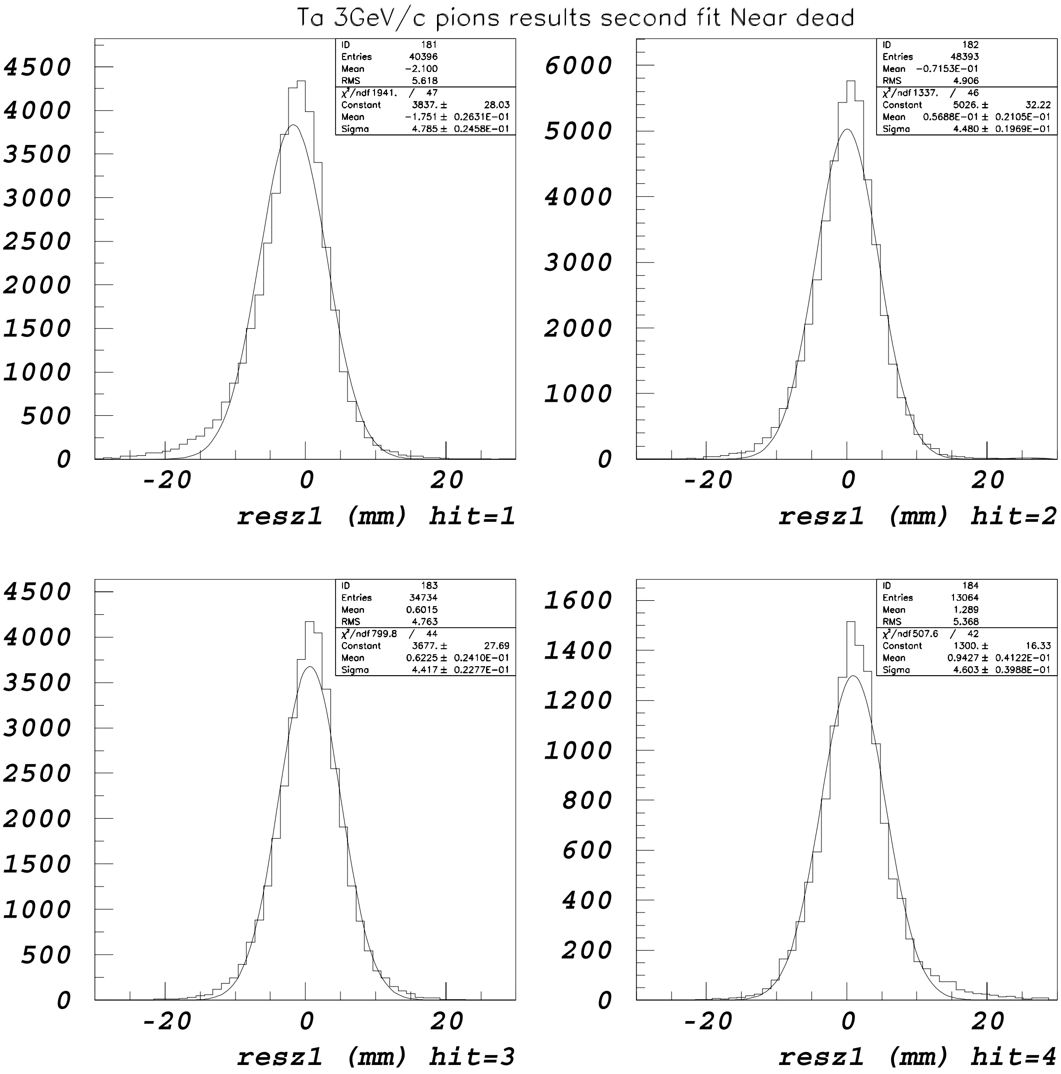

Figure 5.7: *Physics target data. Residuals along the z direction as function of the number of hits.*

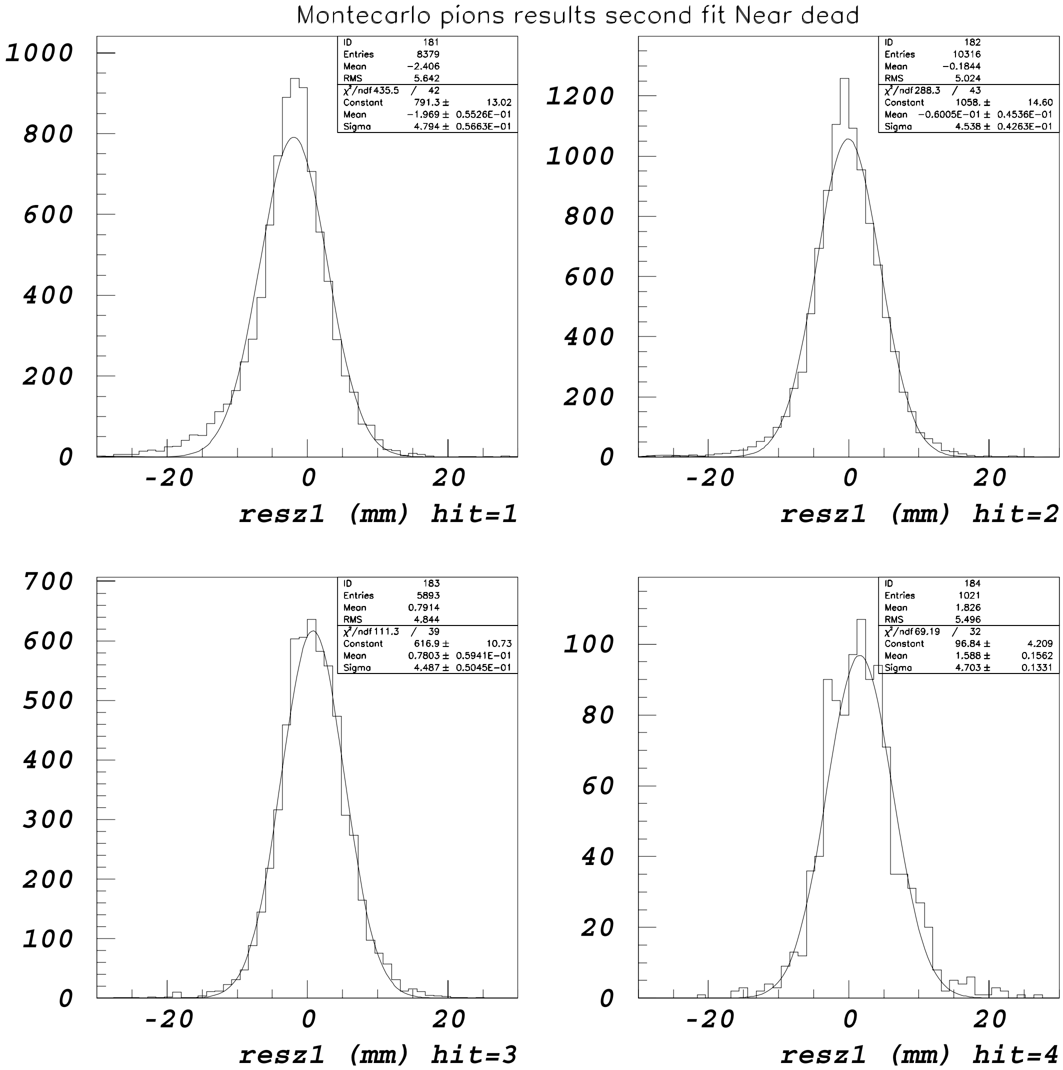

Figure 5.8: *Monte Carlo data. Residuals along the z direction as function of the number of hits.*

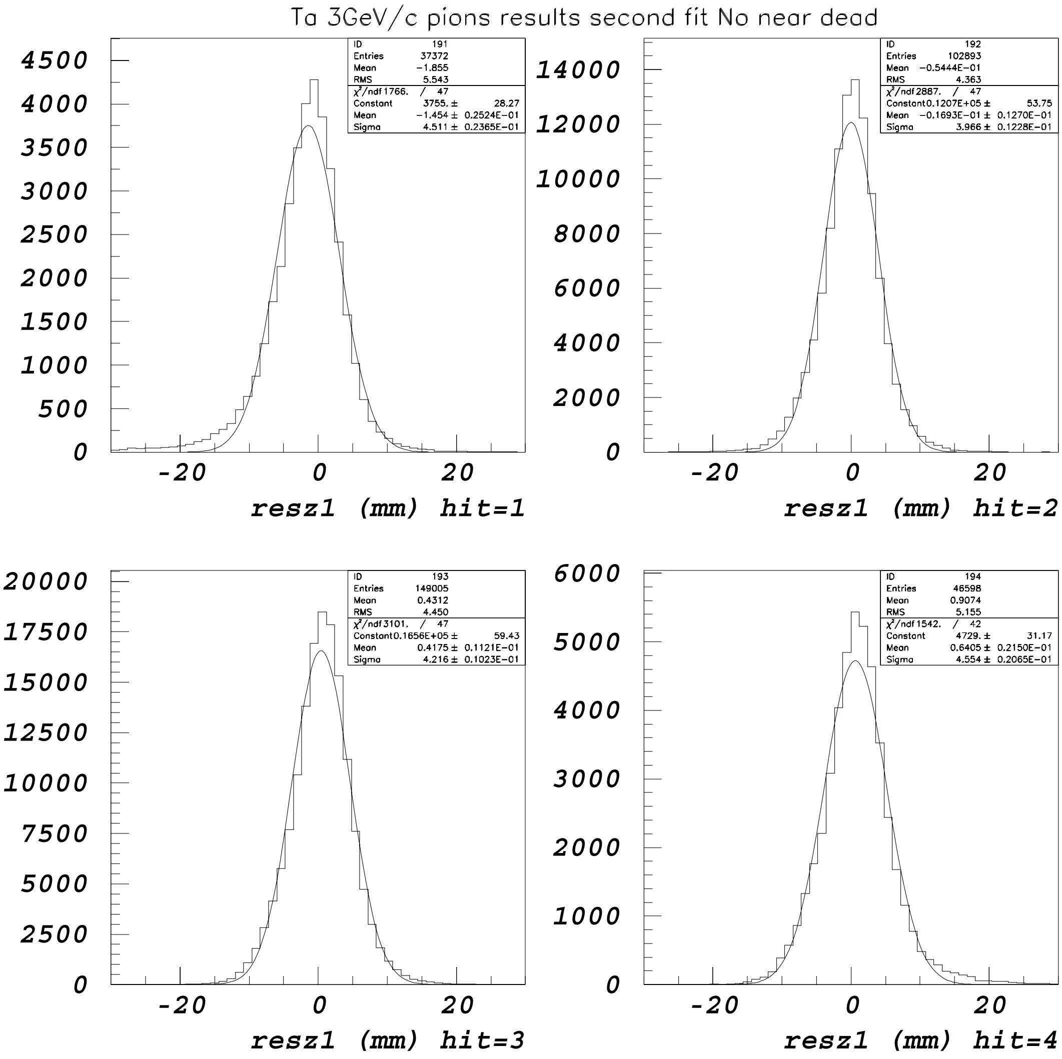

Figure 5.9: *Physics target data. Residuals along the z direction as function of the number of hits.*

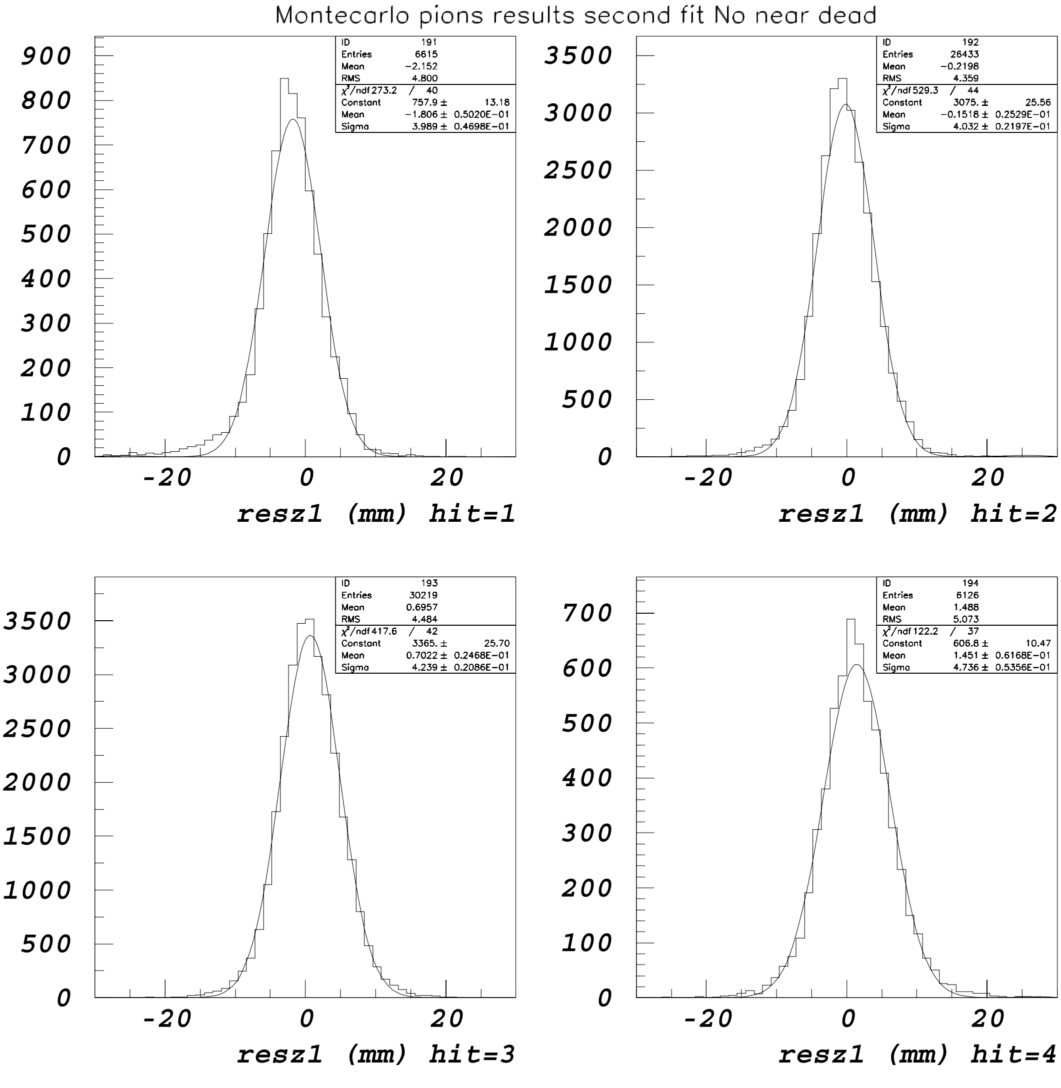

Figure 5.10: *Monte Carlo data. Residuals along the z direction as function of the number of hits.*

number of hits in cluster	RMS of distribution [mm] (Data - MC)	σ of Gaussian [mm] (Data - MC)
1 hit near dead	5.8 -5.6	4.8 -4.8
2 hits near dead	4.9 - 5.0	4.5 - 4.5
3 hits near dead	4.7 - 4.8	4.4 - 4.5
more 3 hits near dead	5.4 - 5.5	4.6 - 4.7
1 hits not near dead	5.5 -4.8	4.5 -4.0
2 hits not near dead	4.4 - 4.4	4.0 - 4.0
3 hits not near dead	4.4 - 4.5	4.2 - 4.2
more 3 hits not near dead	5.2 - 5.1	4.5 - 4.7

Table 5.3: *Residuals along z. The rms and the sigma of a Gaussian fit for the four classes of clusters as function of their hits number used to calculate the cluster position.*

5.4 Study of momentum resolution

To evaluate the transverse momentum resolution we use the cosmic data 2003 and compare the momenta of the two track segments. We calculate also the resolution of the total momentum for the tantalum data using the dE/dx spectrum: dE/dx varies so fast at low energy, selecting a small slice of dE/dx it allows a cross check of momentum resolution. For comparison, the transverse momentum resolution can be calculated with the Gluckstern formula [145], knowing the track information (number of points, track length, point resolution) and the value of the magnetic field in the TPC.

5.4.1 $\Delta p_t/p_t$ for the cosmic ray data

The transverse momentum resolution, $\frac{\Delta p_t}{p_t}$, is given by the ratio between $\Delta\rho$ of the two fits of the 2 single segments and ρ of the fit of the ensemble of the two segments as a single track.

In these evaluations we reject the first point ($p_t < 100$ MeV/c), because the energy loss for muons or pions in the material in the central part of the TPC (basically the inner field cage tube and the scintillator used as trigger) causes variation of the momentum that is not compatible with the method, used to evaluate the transverse resolution.

The application of the static distortion corrections improves the transverse momentum resolution at all momenta.

As shown in [146], the pad gain equalisation increases the linearity of $\frac{\Delta p_t}{p_t}$, while, by weighting the track points as function of the number of hits in the clusters and of the presence or absence of near to dead zones, the resolution improves by about 40%.

After the vertex algorithm that uses also the 'vertex' point the resolution improves by more than a factor two, in fact the slope decreases to 0.27 (0.31 for 2002 data) and also the intercept improves from 0.10 to 0.04 (0.11 to 0.03 for 2002 data) (the results are shown in fig. 5.11 on the right).

5.4.2 Total momentum resolution using the dE/dx distribution

By using the dE/dx distribution we can evaluate the momentum resolution with the physics data. Considering the tantalum data at 5 GeV/c, we select a small range of dE/dx (shown in fig. 5.12) in the proton band where all the protons have about the same momentum. We evaluate the momentum resolution calculating the width of the momentum distribution in this range of dE/dx.

Selecting a band of dE/dx between 1700 ADC counts and 1800 ADC counts (zone 3 in fig. 5.12) we obtain a resolution of 11.9%±0.6% at a trans-

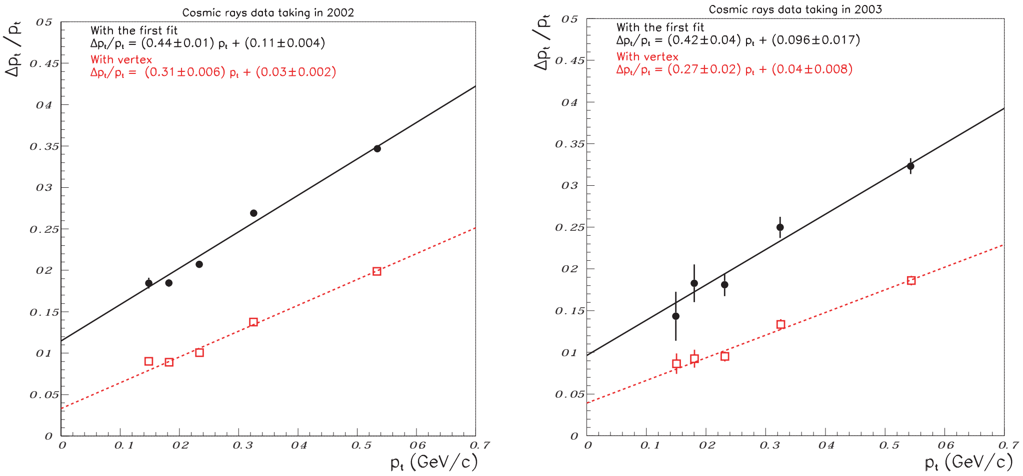

Figure 5.11: $\frac{\Delta p_t}{p_t}$ *as function of the transverse momentum considering all points belonging to a single track. The results of the first fit are represented by the circle points and the black line. The results after the refitting including also the 'vertex' point are represented by the squares and the dashed-red line. On the left the results of cosmic runs of 2002 and on the right the cosmic runs of 2003.*

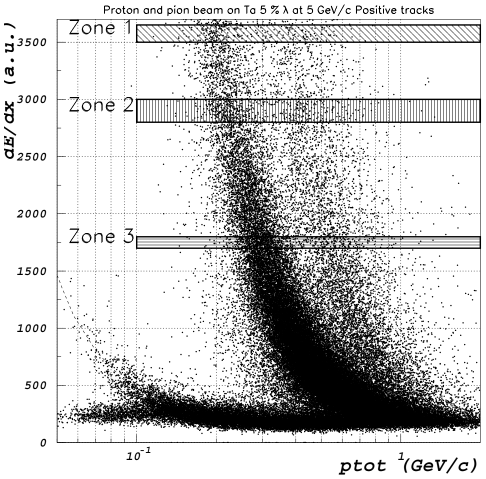

Figure 5.12: *dE/dx distribution for positive particles for Ta* $(5\%\ \lambda_I)$ *data at 5 GeV/c. The box underlines the selection on dE/dx to determine the momentum resolution.*

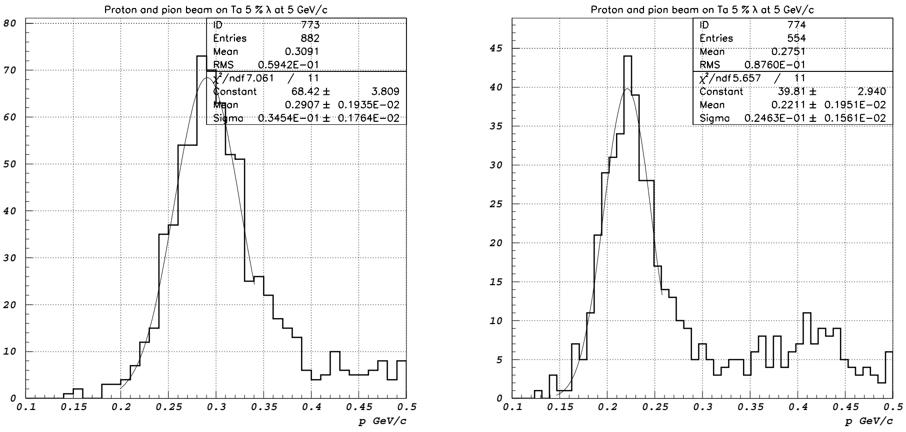

Figure 5.13: *Momentum distribution for protons in the dE/dx the three bands: between 1700 and 1800(on the left), between 2800 and 3000 (on the right).*

verse momentum of 251 MeV/c (this value is the mean of the Gaussian fit of the transverse momentum distribution), in the band between 2800 ADC counts and 3000 ADC counts (zone 2 in fig. 5.12) a resolution of 11.1%±0.7% at a transverse momentum of 199 MeV/c, in the band between 3500 ADC counts and 3650 ADC counts (zone 3 in fig. 5.12) a resolution of 10.0%±1.0% at a transverse momentum of 180 MeV/c. The error contains the statistical error and the systematic error that considers the variation of the momentum in the selected dE/dx range. The results for zone 2 and zone 3 are shown in fig. 5.13.

Considering the angular distribution we can evaluate the correspondent transverse momentum resolution, we can consider negligible the contribution of the angular resolution. These results are in good agreement with the ones found with cosmic data, as shown in fig. 5.14.

5.4.3 Comparison with Monte Carlo data

We evaluate for Monte Carlo data the Δp_t as the difference between the reconstructed momentum and the true momentum when the particle enters in the gas.

Fig. 5.15 shows the transverse momentum resolution for cosmic ray data and for Monte Carlo data. The resolution is similar to the one obtained for the data, even if it is lower by about 1% at low momenta.

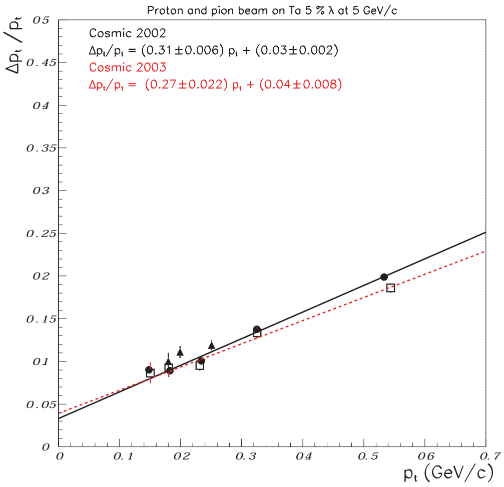

Figure 5.14: $\frac{\Delta p_t}{p_t}$ *as function of the transverse momentum considering all points belonging to a single track including also the 'vertex' point. The cosmic rays taken during 2002 are the squares and the dashed-red line and the cosmic rays taken during 2003 are indicated by the filled circles and the black line. The momentum resolution evaluated using dE/dx are represented by the black triangles.*

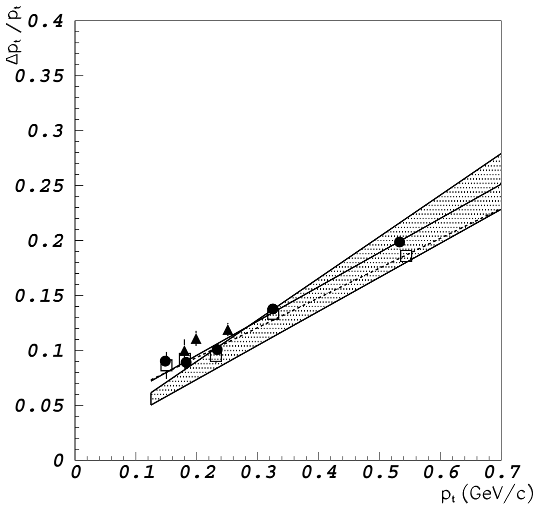

Figure 5.15: *Momentum resolution: the filled circles (open boxes) and the drawn (dashed) straight line refer to the cosmic ray data taken in 2003 (2002). The filled triangles are the resuls evaluated by dE/dx methods. The shaded area refers to a straight line fit to the Monte CArlo calculations.*

5.4.4 Comparison with the Gluckstern formula

It is interesting to compare the results with what can be calculated with the Gluckstern formula [145]:

$$\frac{\Delta p_t}{p_t^2} = \frac{\delta_{r\phi}}{0.3 \cdot B \cdot L^2}\sqrt{\frac{720}{N+4}} \tag{5.1}$$

where $\delta_{r\phi}$ is the azimuthal position resolution of a space point, L is the total visible projected track length in the TPC, N is the number of points per track, B is the value of the magnetic field.

Considering the study in section 5.3, one can consider a resolution in $r\phi$ of 1.3 mm (average resolution of points). Requiring at least 12 points per track, the arc of the visible track length in the TPC is between 165 mm (points in 12 neighbour rows) and 285 mm (points that cover all 20 rows). When the fit uses also the vertex that lies near the TPC axis in the xy plane this arc is between 250 and 370 mm. The average arc length for the cosmic rays is 280 mm and 370 mm using the vertex constraint.

The Gluckstern formula gives, with a magnetic field of 0.7 T, 16 samplings (mean number of points for the cosmic rays), a point resolution of 1.3 mm (the mean sigma of the Gaussian fitted experimental residuals distribution) and a visible length of 280 mm, a p_t resolution of:

$$\frac{\Delta p_t}{p_t} = 47.4\%\, p_t$$

Using also the vertex constraint the visible length becomes 370 mm and this improves the p_t resolution that becomes:

$$\frac{\Delta p_t}{p_t} = 27.1\%\, p_t$$

The use of the vertex in the fit algorithm increases the length of a reconstructable track by about 30% and permits to improve the p_t resolution by about 40%.

Formula (5.1) considers all points with a constant resolution. We input in the formula, as resolution for the points, the mean sigma of the Gaussian fitted experimental residuals distribution. The result obtained is in good agreement with the resolution found experimentally by analysing cosmic ray data. For that data analysis the fitting program used for the track reconstruction is based on a weighted fit that takes into account the different systematics on the points (number of hits, near dead zone, etc.). The coincidence of the resolution results obtained with the 2 different methods, demonstrates that we determined precisely the weights of the points; hence one can obtain some significant improvements in the momentum resolution mainly by improving the point resolution.

5.5 Angular resolution

The angular resolution of tracks can be studied using cosmic rays that cross the central part of the TPC, that are reconstructed as two different track segments. A comparison between the angles in the xy plane and with respect to the z axis of the two track segments with respect to the ones obtained by fitting the two segments as a single track provides information on the resolution of the reconstructed tracks.

We find a resolution for ϕ_0 (the azimuthal angle in the xy plane) of 36 mrad for 2002 cosmic rays and 29 mrad for 2003 cosmic rays. (see fig. 5.16) The difference is due to the difference on momentum distribution (because of the different trigger): the resolution in ϕ_0 is about 45 mrad for momenta less than 200 MeV/c and decreases to less than 26 mrad for momenta larger than 500 MeV/c.

We find a resolution for λ of 9 mrad for both 2002 cosmic rays and for 2003 cosmic rays (see fig. 5.17). The resolution in λ is almost constant for momenta above 200 MeV/c and is about 18 mrad for lower momenta.

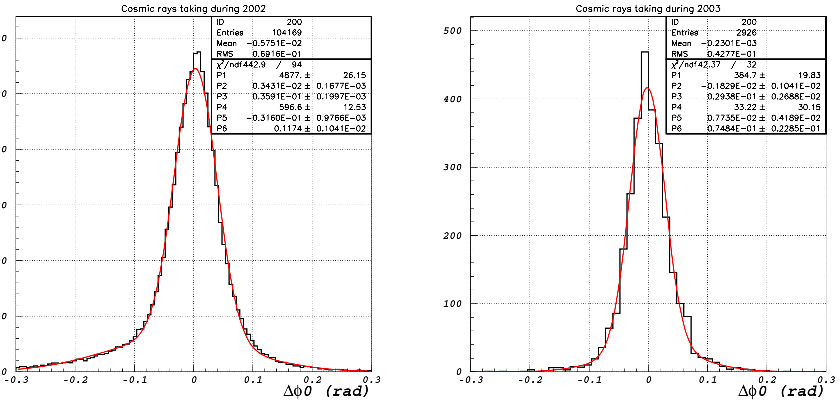

Figure 5.16: *The distribution of the difference between the azimuthal angle ϕ of the projection in the xy plane of the two segments of one cosmic ray crossing the TPC. On the left the 2002 data and on the right the 2003 data. The inset reports the results of the double gaussian fit of the distribution. The resolution is given by the sigma of the first gaussian.*

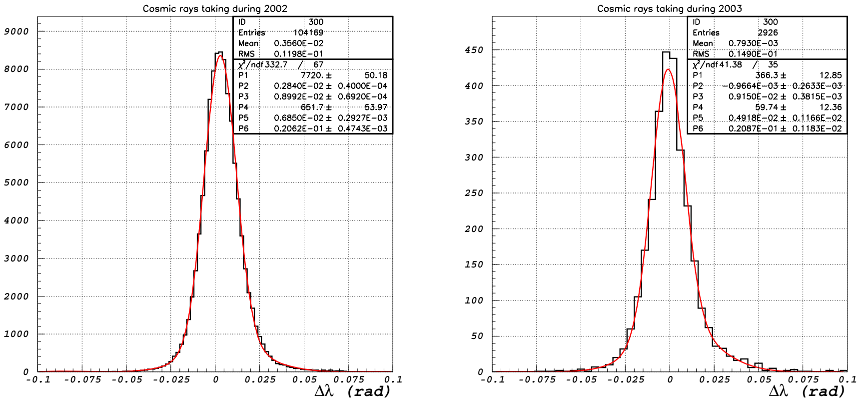

Figure 5.17: *The distribution of the difference between the angles (λ) between the track and the beam axis of the two segments of one cosmic ray crossing the TPC. On the left the 2002 data and on the right the 2003 data. The inset reports the results of the double gaussian fit of the distribution. The resolution is given by the sigma of the first gaussian.*

5.6 Impact point resolution

The impact point resolution can be evaluated by using the cosmic rays and also the distribution of the impact point with respect to the beam position.

5.6.1 Cosmic 2003 data

The impact point resolution of a track has been studied by using cosmic rays that cross the central part of the TPC, and are reconstructed as two different track segments. The impact point resolution is defined by the minimum distance between the impact point of the other segment.

To evaluate the resolution in the xy plane we calculate the minimum distance in this plane between the impact point of one segment with respect to the other segment. We have a resolution in the xy plane of 4.3 mm for 2002 cosmic rays and 3.2 for 2003 cosmic rays (see fig. 5.18). The difference is due to the difference on momentum distribution (because of the different trigger): the resolution of d_0 is about 5 mm for momenta less than 200 MeV/c and decreases to 3.1 for momenta larger than 500 MeV/c.

The resolution along the z axis is calculated by the distance of the z coordinate of impact point of one track segment and the z coordinate of the point on the other track. It is 2.3 mm for 2002 cosmic rays and 2.2 for 2003 cosmic rays (see fig. 5.19).

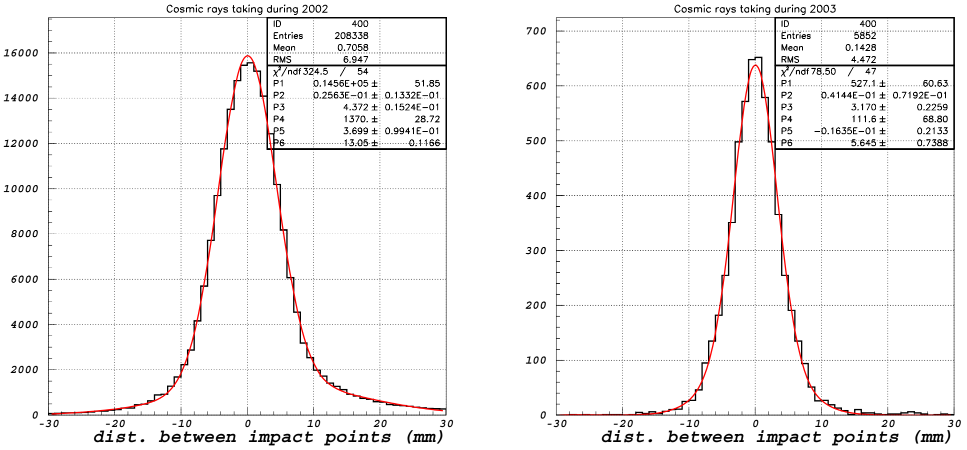

Figure 5.18: *The distribution of the difference between the minimum distance between the impact point of each of the two segments of a single cosmic ray crossing the TPC with respect to the other segment. On the left the 2002 data and on the right the 2003 data.*

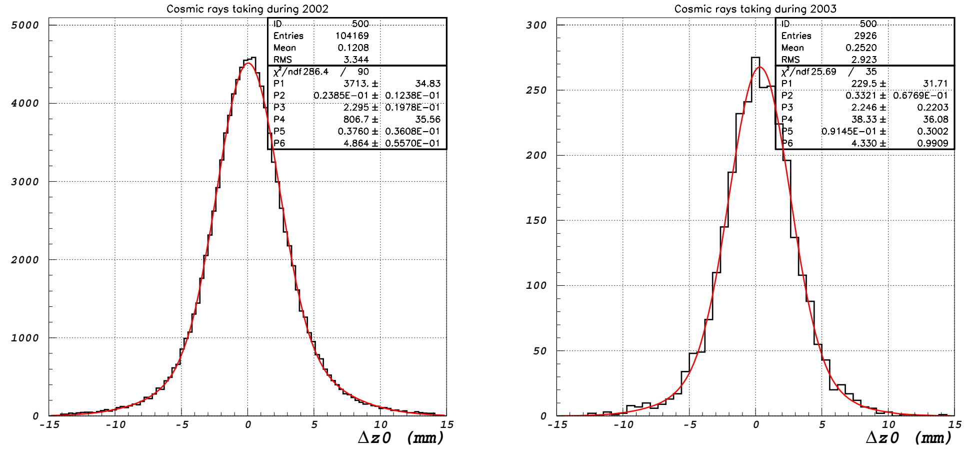

Figure 5.19: *The distribution of the difference between the z coordinates of the impact points with respect the z axis of the two segments of one cosmic ray crossing the TPC. On the left the 2002 data and on the right the 2003 data.*

5.6.2 Impact point resolution in the data with a target

In the beam data on target we evaluate the resolution on the impact point by looking at the distribution of the projection onto the xy plane of the impact point of TPC tracks with respect to the impact point of the beam particle in the xy plane given by the MWPCs.

We apply a cut on $\mathrm{d}E/\mathrm{d}x$ at 300 ADC counts to avoid the tracks that have a large energy loss in the material that does not permit a good reconstruction of the vertex position. The distribution of the impact points (shown in fig. 5.20) can be fitted by a double Gaussian, the larger Gaussian permits to exclude the background from the central peak that estimates the resolution. We obtain a resolution of 3.7 mm that is in good agreement with the value (3.2-4.3 mm) found using the cosmic rays.

We can evaluate the resolution of the coordinate z of the TPC impact point by looking at the distribution of the z coordinate of the impact point with respect to the impact point given by the MWPCs tracks extrapolated to the endcap of the inner field cage. This endcap is made of stesalit and it has a thickness of 2 mm. The distribution (shown in fig. 5.21) is fitted by a Gaussian and a polynomial to subtract the background. We obtain a distribution with a sigma of 3.4 mm. This value is a convolution between the resolution and the stesalit thickness. It is compatible with the resolution of 2.3 mm found in cosmic ray data.

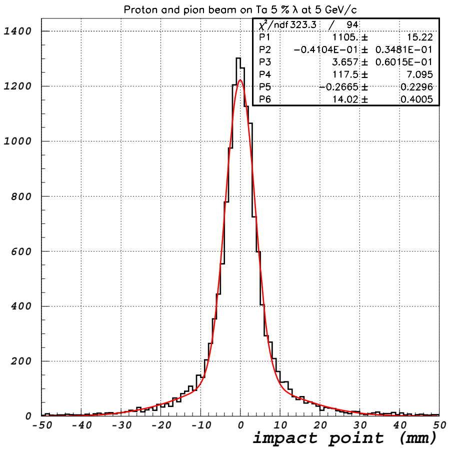

Figure 5.20: *Distribution of the impact point of selected particles coming from the target with respect the beam particle impact point in the xy plane for the Ta (5% λ_I) data at 5 GeV/c of selected particles coming from the target.*

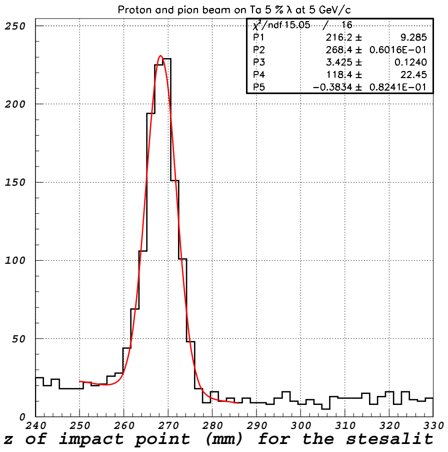

Figure 5.21: *Distribution of the z coordinate of the impact point with respect to the one given by the MWPC tracks extrapolated to the stesalit endcap of the inner field cage for data with target Ta (5% λ_I) data at 5 GeV/c of selected particles coming from the target. The inset reports the results of the fit by a gaussian and a polynomial.*

5.6.3 Impact point resolution for Monte Carlo data

Using the Monte Carlo data we evaluate the resolution in the impact point along z and in the xy plane using the same method as in data. Therefore we can look at the distribution of the projection onto the xy plane of the impact point of the TPC tracks with respect to the beam particle impact point in the xy plane given by the MWPC track. For the Monte Carlo we find 3.2 mm (see fig. 5.22) and in the data 3.7 mm; the tails are similar. The asymmetry of the Monte Carlo distribution is due to the fact that in the Monte Carlo data we select only positive pions.

We can evaluate the absolute resolution along z by comparing the reconstructed z coordinate of the vertex and the truth value. For the Monte Carlo we find 2.7 mm and in cosmic rays 2.3 mm. The differences between the Monte Carlo and data are due mainly to the fact that momentum and angular distributions are different for the two samples of data.

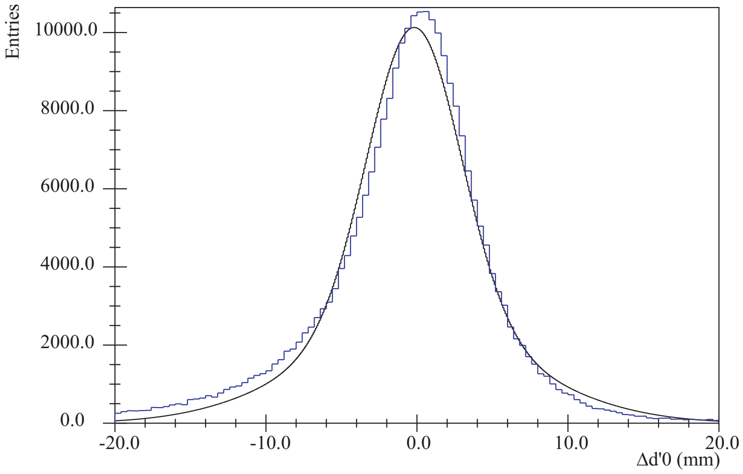

Figure 5.22: *Monte Carlo data: d0' spectrum fitted by a double gaussian.*

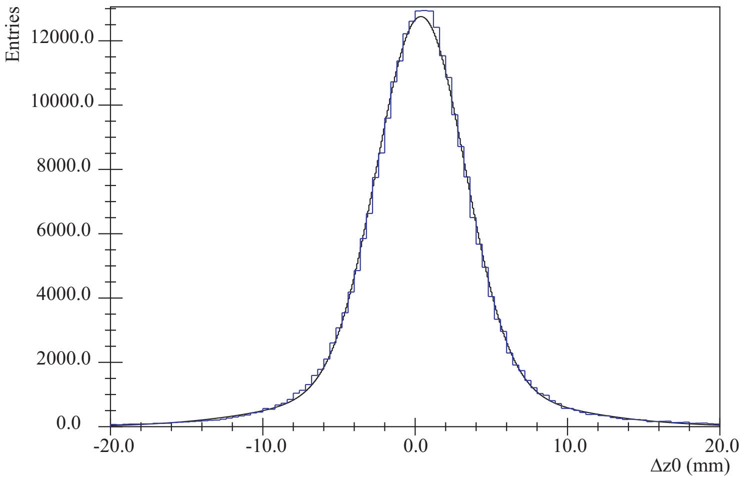

Figure 5.23: *Monte Carlo data: z impact point resolution for positive pions fitted by a double gaussian.*

5.7 Efficiency study

To study the efficiency of our detector we use the Monte Carlo simulation. We select Monte Carlo events with only one positive pion entering the TPC (we reject events where the particle decays or interacts in the material around the target). The efficiency is calculated by the ratio between the number of reconstructed particles and the number of Monte Carlo generated particles.

The global efficiency asking at least one reconstructed track (no requirement on the number of points) is about 92%. When we require that the reconstructed track has at least 12 points and no error flag and coming from the target region the efficiency is $\sim 82\%$ and if we require a successful vertex fit the global efficiency is 68%. The lower efficiency of the vertex fit is due the selection of tracks coming from the target within 2σ of resolution on the impact point.

The fig. 5.24 and 5.25 show the efficiencies for pions as function of the transverse and total momentum. The efficiency is evaluated requiring at least one reconstructed track (no requirement on the number of points) (black line and black circles), requiring also at least 12 points and no error flag (blue line and blue squares) and requiring also the successful vertex fit (red line and red diamonds). One can note that the efficiency is about 30% for low momenta below 100 MeV/c (due to energy loss) and it increases reaching a plateau above 250 MeV/c. The efficiency requiring the vertex fit has a plateaux at about 75%. The fig. 5.26 shows the dependence of the pion efficiency on the polar angle θ. The efficiency is lower for the tracks that are almost perpendicular to the beam and that cross the target in the transverse section (the radius of the target is 15 mm and the length along z is 5.6 mm). These tracks have a higher energy loss. The fig. 5.27 shows the pion efficiency dependencies on the azimuthal angle ϕ_0. Requiring only one track the effect of the sector spokes on the efficiency is small, requiring at least 12 points and no error flag the efficiency becomes lower on the sector spokes and the effect of the dead regions are also more visible. Requiring also the vertex fit (higher resolution) the inefficiency of these region is higher. Fig. 5.28 shows the efficiency for protons: due to the energy loss the protons with a momentum at the production point less than 450 MeV/c are stopped before they enter in the gas. For higher momenta protons have an efficiency about 5% higher than pions. Since the protons ionise gas more than pions, they produce a higher signal and a higher number of points than the pions. Fig. 5.29 shows the dependence of efficiency for protons as function of θ, this dependence has the same shape as for pions.

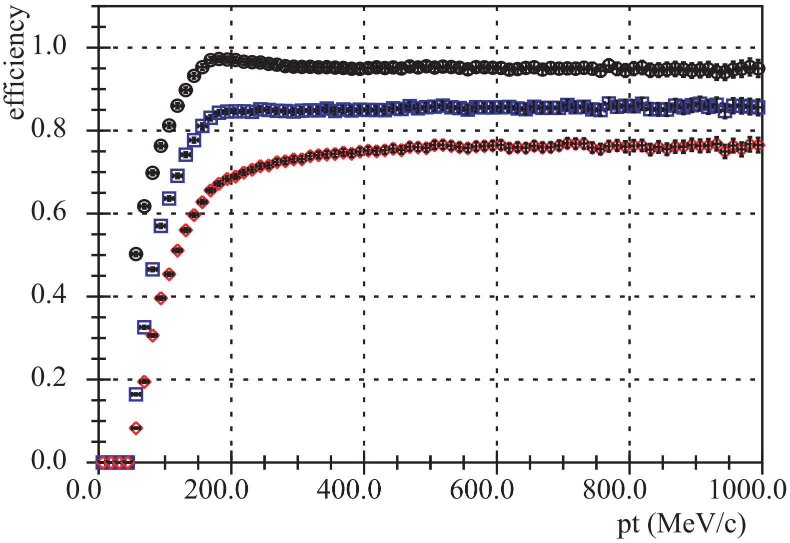

Figure 5.24: *Efficiency for pions as function of the transverse momentum: requiring a reconstructed track (black line and circles), requiring at least 11 points and no error flag (blue line and squares), requiring also the vertex fit (red line and diamonds).*

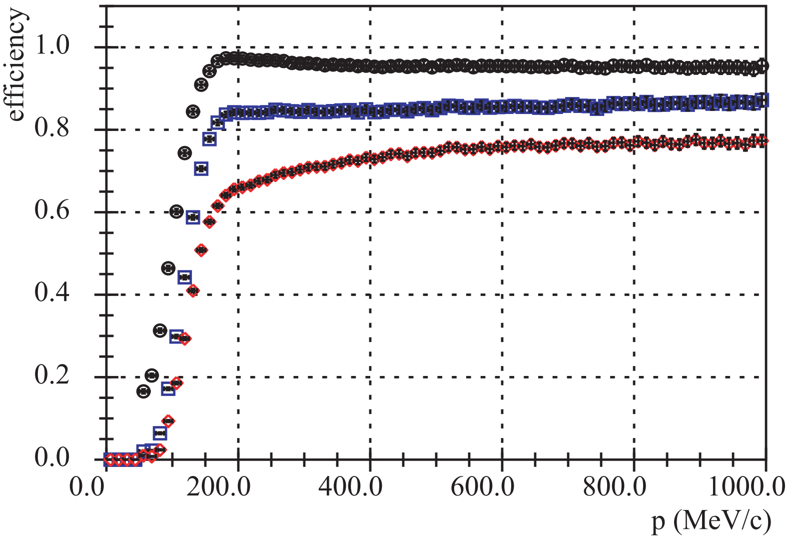

Figure 5.25: *Efficiency for pions as function of the total momentum: requiring a reconstructed track (black line and circles), requiring at least 11 points and no error flag (blue line and squares), requiring also the vertex fit (red line and diamonds).*

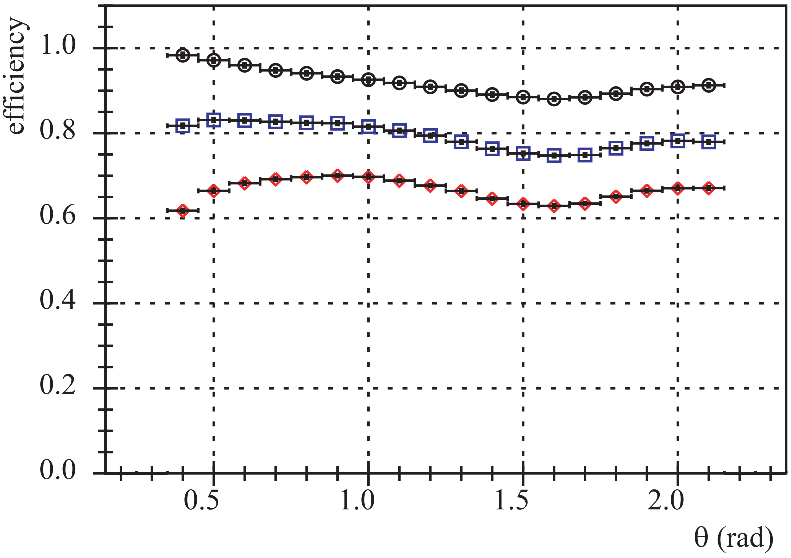

Figure 5.26: *Efficiency for pions as function of the θ angle: requiring a reconstructed track (black line and circles), requiring at least 11 points and no error flag (blue line and squares), requiring also the vertex fit (red line and diamonds).*

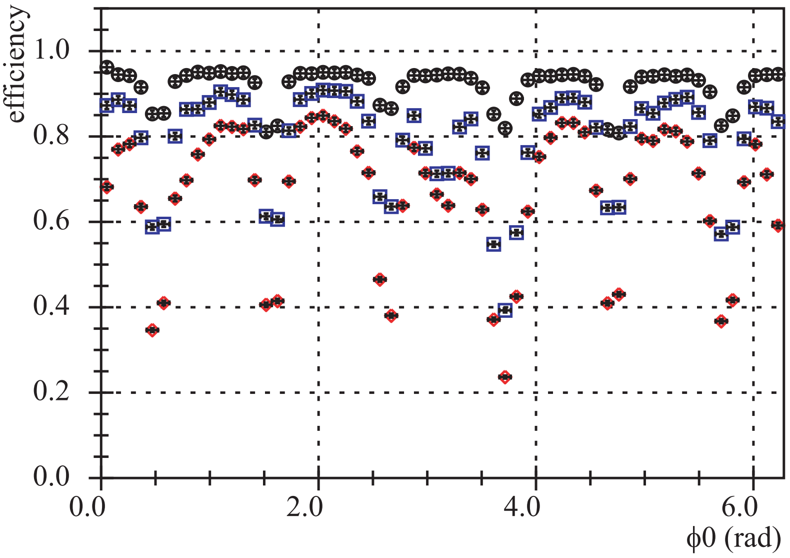

Figure 5.27: *Efficiency for pions as function of the azimuthal angle ($\phi0$): requiring a reconstructed track (black line and circles), requiring at least 11 points and no error flag (blue line and squares), requiring also the vertex fit (red line and diamonds).*

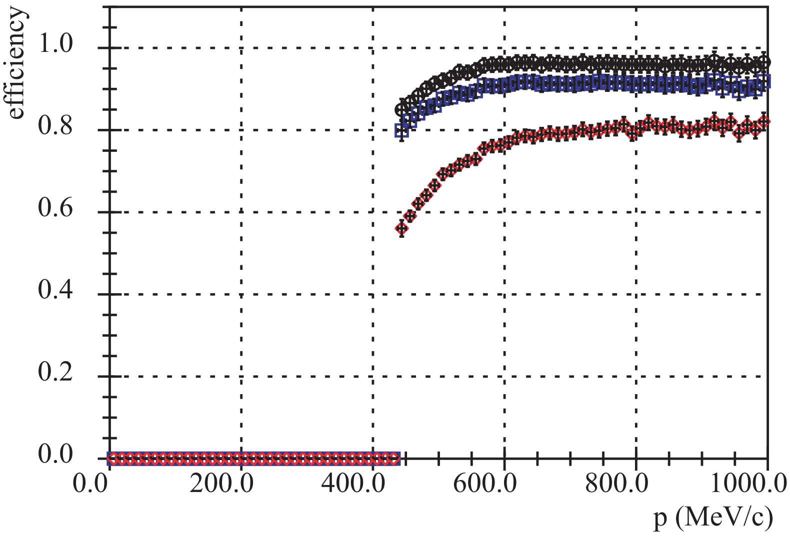

Figure 5.28: *Efficiency for protons as function of the total momentum: requiring a reconstructed track (black line and circles), requiring at least 11 points and no error flag (blue line and squares), requiring also the vertex fit (red line and diamonds).*

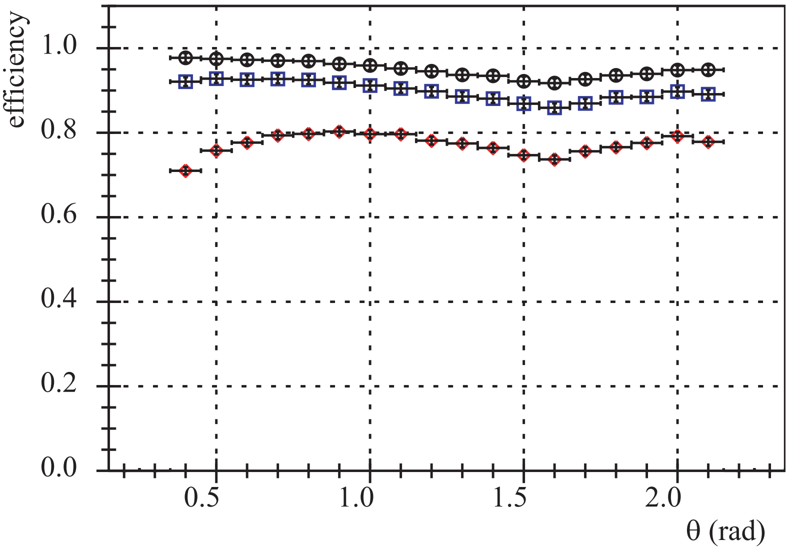

Figure 5.29: *Efficiency for protons as function of the θ angle: requiring a reconstructed track (black line and circles), requiring at least 11 points and no error flag (blue line and squares), requiring also the vertex fit (red line and diamonds).*

5.8 PID capabilities

Charged particle identification (PID) in the TPC can be achieved by measuring the ionization in the gas together with the measurement of the total momentum of the particle.

5.8.1 Energy loss in a gas

For energy loss calculation, a detailed understanding of the ionization process and its stochastic nature is needed. When a charged relativistic particle passes through the gas, it loses energy principally by excitation and ionisation. The mean energy loss is well described by the Bethe-Bloch equation. The parameters of this function depend on the electronic density (composition, pressure and temperature) of the detector gas.

The energy loss resulting from the combined effect of the individual ionizing events would be found to have the characteristic skew probability distribution of a Landau distribution, given the density and thickness of the HARP TPC gas. This makes the experimental determination of the average ionization per unit path length a difficult matter.

The energy loss of the particle in the passage of the gas is proportional to the ions pairs produced in the gas. It enables to identify the particle measuring the number of ionization electrons along the tracks of the particles (or rather an electronic signal being proportional to this number). In the following we refer to it as 'energy loss' although it is really a measurement of ionization.

5.8.2 Method

To evaluate the mean energy loss of a particle crossing the TPC we evaluate for each point the energy loss per length unit ($\mathrm{d}E/\mathrm{d}x$) where:

- $\mathrm{d}E$ is the mean energy loss by the particle in the length $\mathrm{d}x$ or rather the total signal collected by the pad plane for that cluster in a given TPC pads row

- $\mathrm{d}x$ is the segment of the helicoidal trajectory of the particle in the row.

The most probable value of the Landau distribution, and therefore of the mean energy loss, is not the simple average of all $\mathrm{d}E/\mathrm{d}x$ measurements which would be biased by the tail of the Landau distribution. Instead a truncated mean can be a good method to evaluate the most probable energy loss, if this cuts are well tuned to the TPC characteristics. To study and to tune this method for the HARP TPC, we select particles of a given type by a cut on a

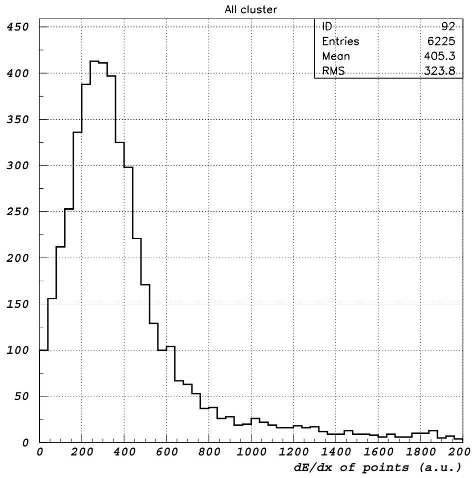

Figure 5.30: *dE/dx (in arbitrary unit, a.u.) spectrum for the points of the 'super-pion'.*

first approximation of dE/dx and in a small momentum range. In this way we obtain the measurement of dE/dx for the same particle repeated several times (later referred as 'super-proton' or 'super-pion'). Hence this technique allows characterization of the dE/dx distributions with high statistics and determination of the truncated mean need to evaluate the most probable value of the energy loss for pions and protons in different momentum bins.

Fig. 5.30 shows the experimental Landau distribution of dE/dx individual measurement in each track point belonging to the 'super-pion'. In this case, the 'super-pion' is defined in momentum range between 150 MeV/c and 200 MeV/c and the mean dE/dx should be less than 500 ADC counts. The best estimator of the most probable value of dE/dx is obtained using the 80% of the integral. This is equivalent to do a truncated mean discarding the 20% of points with highest dE/dx, with no cuts on the points with lowest dE/dx. This estimator gives the best dE/dx resolution evaluated using the pions between 300 and 400 MeV/c.

5.8.3 Resolution

The dE/dx spectrum for positive and negative particles is shown respectively in fig. 5.31 for Monte Carlo data, in fig. 5.32 for the tantalum target (5% λ_I, beam momentum of 5 GeV/c) and for the hydrogen target (length of 180 mm, beam momentum of 3 GeV/c) and in fig. 5.33 for cosmic rays. For the cosmic rays, momentum and dE/dx are computed without splitting the track into two segments, but considering it as a single track. Therefore the average number of points is about 2 times the one obtained for tantalum and for Monte Carlo data. Fig. 5.34 shows the dE/dx distribution for tantalum target data for positive particles with momentum between 375 and 475 MeV/c, produced by a pion beam with a momentum of 5 GeV/c on a tantalum target: the peaks of pions and protons are visible, with a possible evidence of a kaon peak. The deuterons band is present in the tantalum data and negligible in the hydrogen target data. The fig. 5.35 shows the momentum distribution for a small slice of dE/dx for tantalum target data: the two peaks are protons and deuterons.

We can evaluate the dE/dx resolution selecting pions (muons in case of cosmic rays) with a momentum between 300 and 400 MeV/c. In this momentum range for these particles the dE/dx has a minimum as function of the momentum. As shown in fig. 5.36, 5.37 and 5.38, the distribution of dE/dx for these particles is a Landau distribution The peak of the Landau distribution is well represented by a Gaussian, therefore to evaluate the resolution of dE/dx we can fit the peak of the distribution by a Gaussian. We find a resolution of 19.8% for the Ta data, 20.2% for Monte Carlo data and 13% for the cosmic rays. This latter number is consistent with a factor $\sqrt{2}$ improvement since we have about two times the number of points per track.

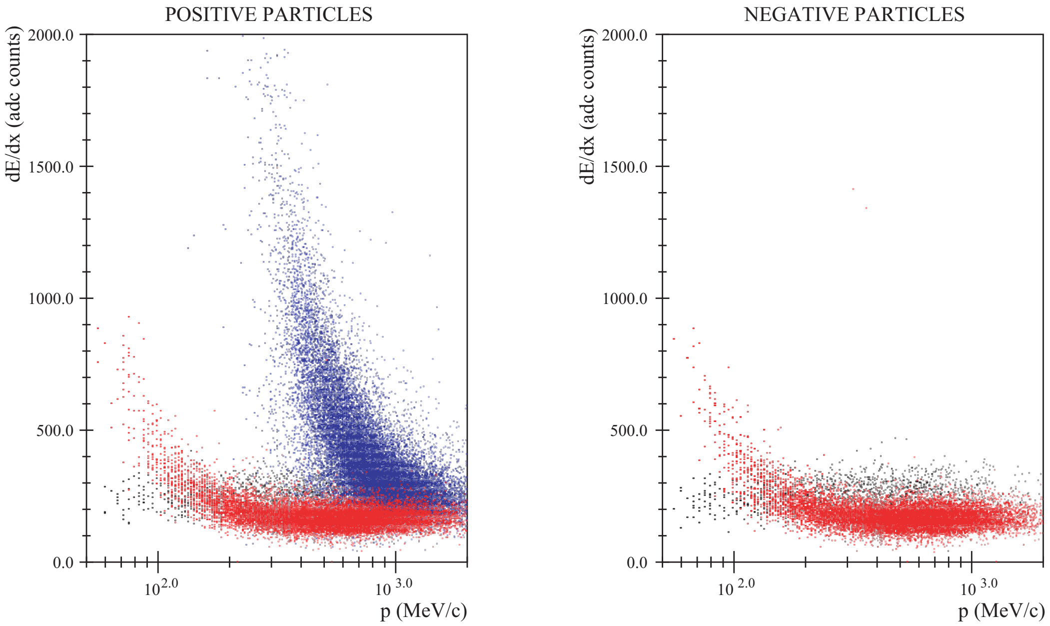

Figure 5.31: *dE/dx spectrum for reconstructed Monte Carlo data, positive particles on the left and negative ones on the right. The red points are the MC truth pions, the black points are the MC truth electrons and the blue points are the MC truth protons.*

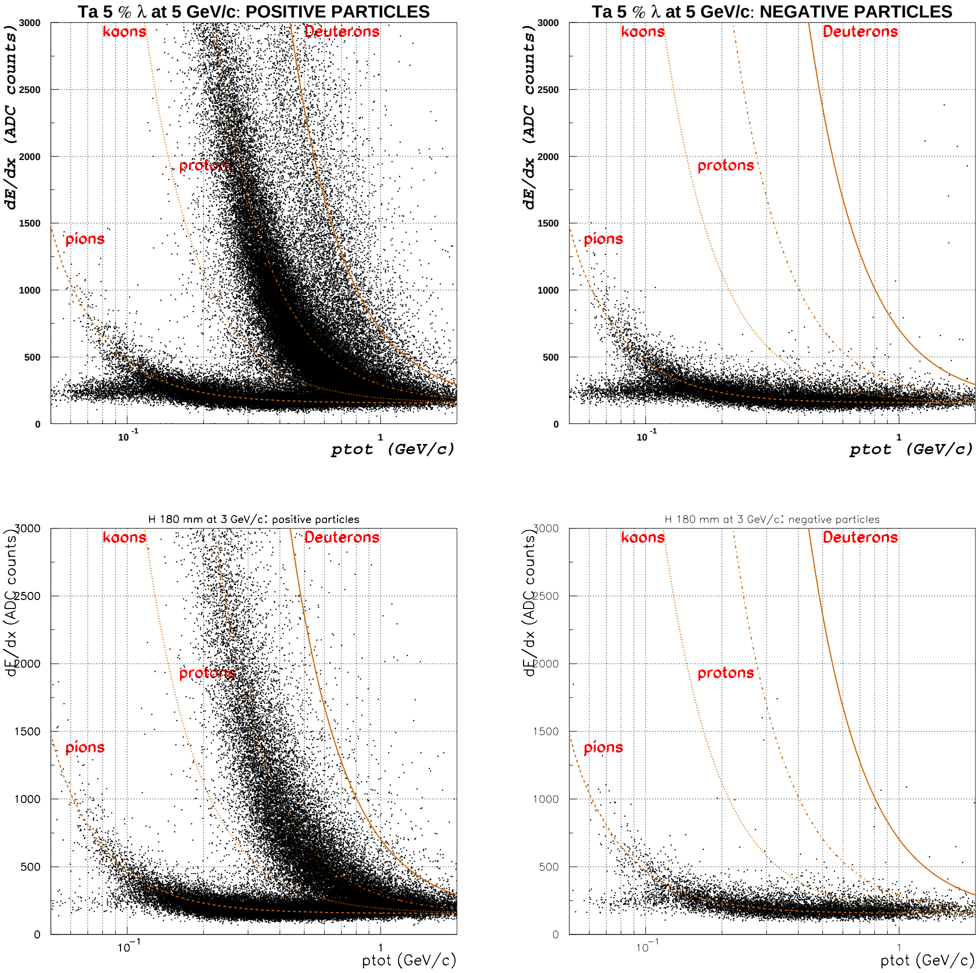

Figure 5.32: *dE/dx spectrum for reconstructed data with a target of Ta (5% λ_I) at 5 GeV/c (on the top) with a target of H (length 180 mm) at 3 GeV/c (on the bottom), positive particles on the left and negative ones on the right. The lines represent the theoretical curves.*

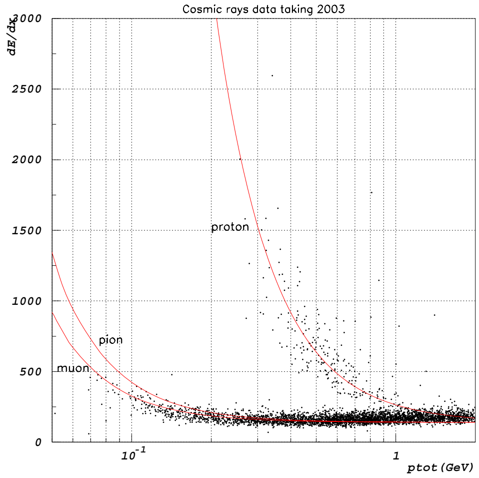

Figure 5.33: *dE/dx spectrum for cosmic rays, the momentum is evaluated by fitting the two segments as a single track and the dE/dx is evaluated by using all points of the two segments, low momentum cosmic rays are clearly muons.*

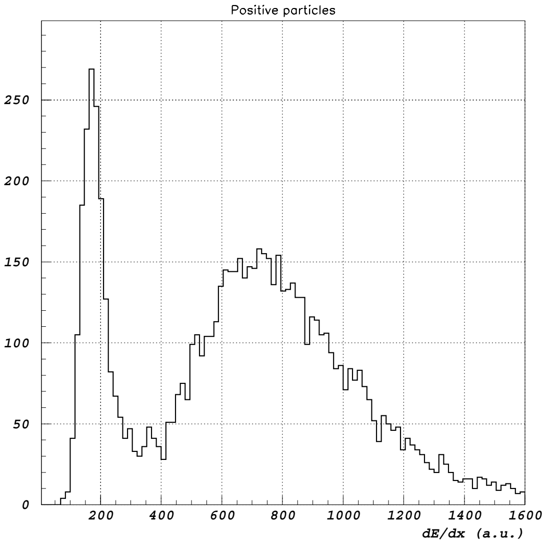

Figure 5.34: *dE/dx (in arbitrary unit, a.u.) distribution for positive particles with momentum between 375 and 475 MeV/c, produced by pion beam with a momentum of 5 GeV/c on a tantalum target. The peaks of pions, protons are well defined, and there is an evidence that kaons are also visible.*

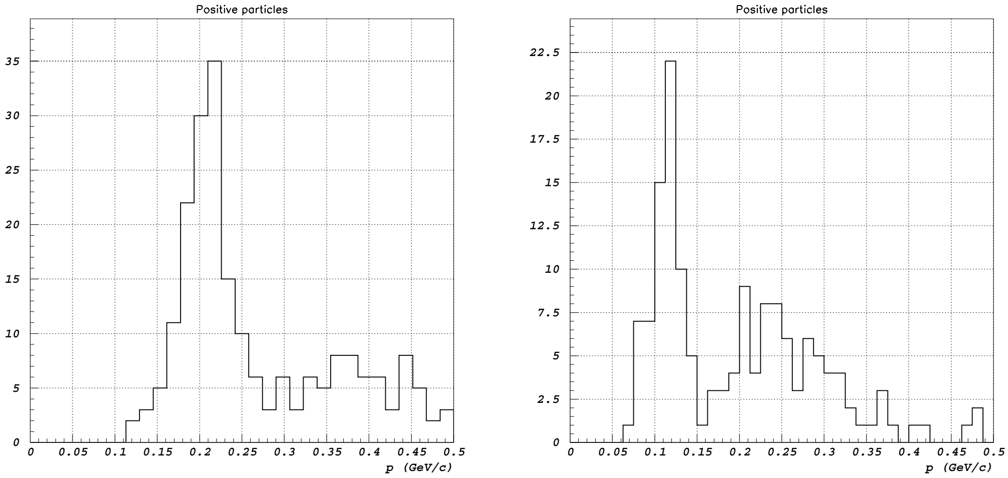

Figure 5.35: *Momentum distribution for positive particles with dE/dx between 3400 and 3500 ADC counts (on the right) and between 7000 and 8000 ADC counts (on the left), produced by pion beam with a momentum of 5 GeV/c on a tantalum target. The two peaks correspond to the protons and deuterons bands.*

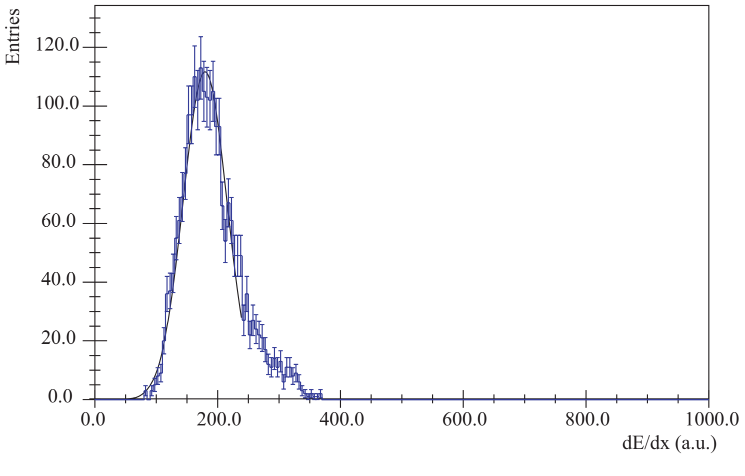

Figure 5.36: *dE/dx (in arbitrary unit, a.u.) distribution for particles with momentum between 300 and 400 MeV/c selecting pions, for reconstructed data with a target of Ta (5% λ_I) at 5 GeV/c.*

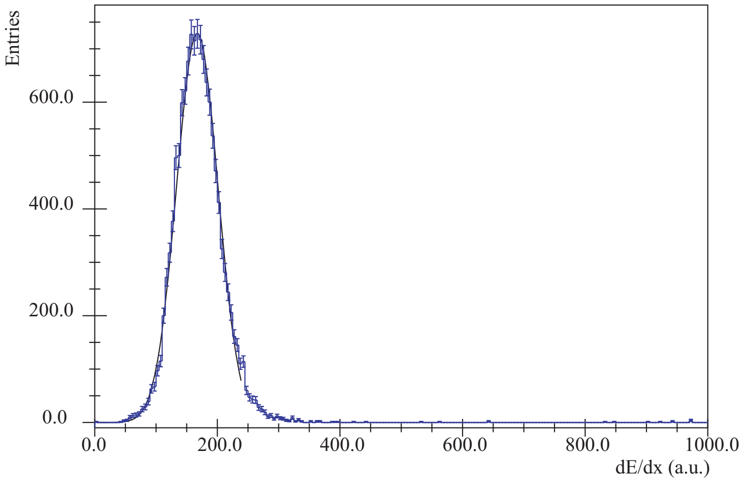

Figure 5.37: *dE/dx (in arbitrary unit, a.u.) distribution for particles with momentum between 300 and 400 MeV/c selecting pions, for Monte Carlo (pions tracks).*

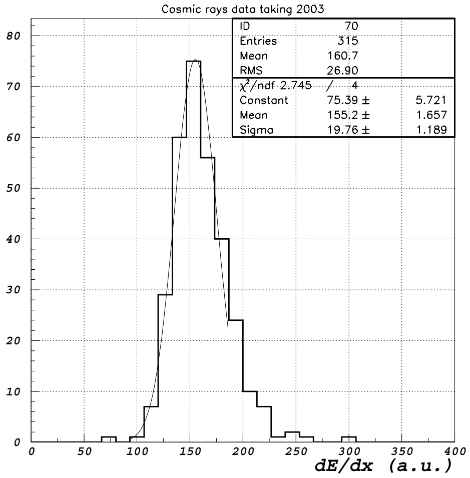

Figure 5.38: *dE/dx (in arbitrary unit, a.u.) distribution for particles with momentum between 300 and 400 MeV/c selecting muons for cosmic rays.*

Chapter 6

Study of TPC performance on pp elastic scattering as physics challenge

6.1 Introduction

Elastic scattering interactions are very suitable for calibration and performance investigations due to the fact that they are well known from previous measurements, they provide additional kinematic constraints and have a well defined final state. The elastic cross section varies from 30% to 10% of the total cross section as function of the beam momentum. At least half of the elastic cross section is in the acceptance of the HARP apparatus. The elastic interactions:

$$p + p \rightarrow p + p$$
$$\pi^{\pm} + p \rightarrow \pi^{\pm} + p$$

have simple kinematical properties and the presence of only 2 charged particles in the final state make these reactions a very suitable calibration tool. The incoming particle is identified by the beam TOF detectors. One of the two emerging tracks from the target escapes in the forward direction usually without being measured in the TPC, and the second one is detected at large angle in the TPC.

By using only the large angle spectrometer it is possible to evaluate the mass of the beam particle scattered in the forward spectrometer (defined as missing mass) [147].

The kinematics of elastic scattering interactions of protons and pions on hydrogen is fully determined by the direction of the forward scattered beam particle. We can evaluate the momentum resolution, the momentum bias and the efficiency of the TPC using events where one particle is detected in the forward spectrometer to predict the momentum and angle of the large angle particle [142].

The cross section measurement can confirm that we have completely understood and evaluated all ingredients to measure any cross section: particle identification, efficiency calculation, beam particle identification, absolute normalization using minimum bias events. In addition, these measurements allow study the momentum bias, in particular as function of the event in the spill. Moreover the efficiency evaluation can be compared with the one determined by the Monte Carlo and their agreement can justify the use of the simulation to determine the efficiency to measure pions.

Data were taken with liquid hydrogen targets with proton and pion beam at momenta from 3 GeV/c to 14.5 GeV/c. The data were collected using a hydrogen cryogenic target with lengths of 60 mm and 180 mm, as described in section 2.2.

6.2 Elastic cross-section measurement using the large angle spectrometer

The analysis is performed within a region of momentum and angle where the detector geometry ensures full acceptance. The choice of a 3 GeV/c beam momentum is convenient, since at this energy the kinematics of the reaction allow most of the cross-section to be in the acceptance of the TPC, and in a 3 GeV/c momentum beam the incoming particles can be identified with high purity by the time-of-flight system.

Typically, the scattered beam particle maintains a momentum close to its initial value, while the recoil proton enters the detector at large angle (from 60 to 80 degrees) and small momentum (a few hundred MeV/c). The large-angle track is easily measured by the TPC, and the initial event sample can be selected by the requirement of track multiplicity ≤ 2. The computation of the efficiency is evaluated using Monte Carlo data. After the subtraction of the background, the number of events counted in the region of the elastic peak is corrected for the efficiency, and then used to directly evaluate the elastic cross-section.

6.2.1 Data selection

The first selection is performed on the base of the incoming beam particle: a) beam width limits in the xy plane: ± 6 mm; b) incoming particle is identified as proton by the beam detectors.

Simple cuts are applied to the overall event properties: only the first 40 events in the spill are selected to avoid the effect of dynamic distortions.

Moreover we select only 1- or 2-prong events in the TPC. The 2-prong events are determined by very loose kinematical cuts: $||\phi_1 - \phi_2| - \pi| < 0.3\ rad$ and $(\theta_1 + \theta_2) < 1.75\ rad$, where ϕ_1, ϕ_2, θ_1, θ_2 are - respectively - the azimuthal and polar angles of the two tracks. Further selection criteria are applied to the large-angle track: the particle is positively charged and well measured over a minimum of 10 points; the reconstructed momentum is in the range $[320, 620]$ MeV/c; the particles come from the target (z'_0 in the range $[-50, +70]$ cm); the particles are recognised as protons with a dE/dx selection.

In the following the analysis of the pp→ pp will be described in details. The πp→ πp analysis has been performed exactly in the same way with the same selection, and the data are presented for both reactions.

6.2.2 Results

First we calculated the missing mass using the large angle track with the proton hypothesis. A missing mass (M_x^2) distribution can be constructed from the quantity:

$$M_x^2 = (p_{\text{beam}} + p_{\text{target}} - p_{\text{TPC}})^2 \quad . \tag{6.1}$$

where p_{beam}, p_{target} and p_{TPC} are the 4-momenta of the incoming beam particle, target particle and the particle scattered at large angle and measured in the TPC, respectively. We fitted the missing mass distributions by the sum of a Gaussian and a second order polynomial to find the bias and resolution in the missing mass (see fig. 6.1, 6.2, 6.3 and 6.4). The value of the mass peak of the proton and the pion is found with excellent accuracy $m_p^2 = 0.9147 \pm 0.0022$ GeV $^2/c^4$ and $m_\pi^2 = 0.110 \pm 0.0007$ GeV $^2/c^4$.

By considering a total useful (as defined by cuts) target length of 12 cm, a target density of 0.0708 g/cm^3 and an efficiency factor for both pp and πp elastic events of 68.9%, the following cross-sections are obtained [147]:

$$\sigma_{pp\to pp} = 6.8 \pm 0.27\ mb\,(6.1 \pm 0.24\ mb) \tag{6.2}$$

$$\sigma_{\pi p\to\pi p} = 2.9 \pm 0.12\ mb \tag{6.3}$$

where the error is the statistical one. Two different approaches to the missing-mass fits were attempted. In the first one, the background is simply modelled by a polynomial (results in the brackets), while in the second one a more refined fit tries to quantify the contributions due to resonances close to the mass peak. The result for $\sigma_{\pi p\to\pi p}$ is unchanged (see fig. 6.3 and 6.4). The reason why we quote two values for $\sigma_{pp\to pp}$ is that the two fits lead to different results. This preliminary analysis cannot rule out any of the two; it has to be noticed, however, that both values are compatible to the one of [148], as quoted below.

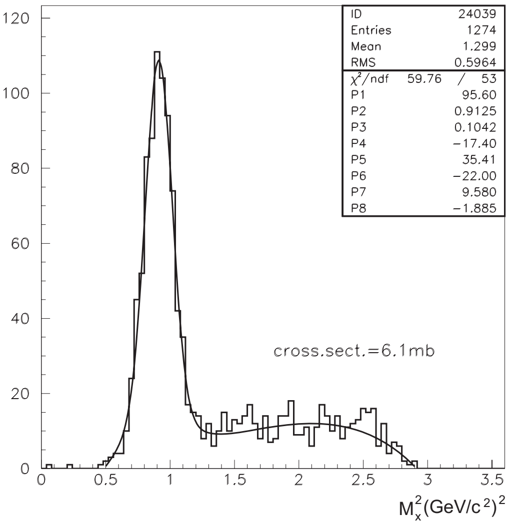

Figure 6.1: *Missing mass distribution in pp scattering. The background is estimated with a polynomial.*

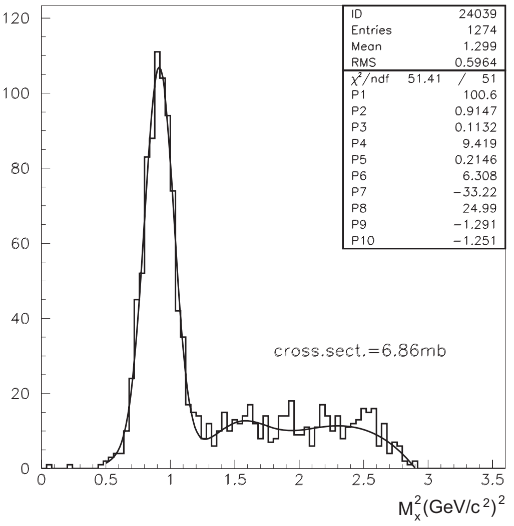

Figure 6.2: *Missing mass distribution in pp scattering. The background is estimated using resonance production.*

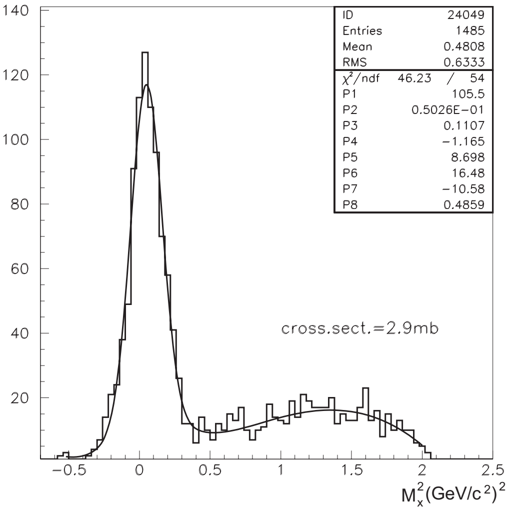

Figure 6.3: *Missing mass distribution in πp scattering. The background is estimated with a polynomial.*

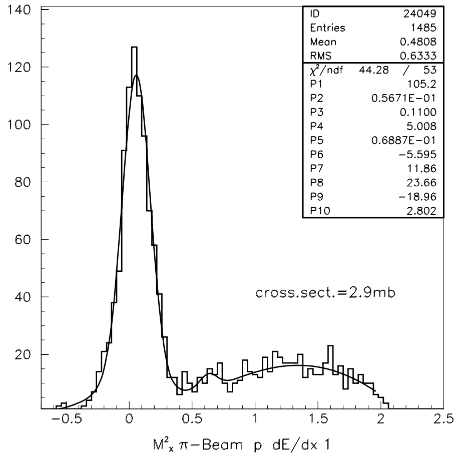

Figure 6.4: *Missing mass distribution in πp scattering. The background is estimated using resonance production.*

The most straightforward comparison is with the measurements by Ambats et al. [148]. The quoted results for the integrated elastic cross-sections are:

$$\sigma_{I,pp\to pp} = 17.2 \pm 0.7\% \pm 4\%\ mb \tag{6.4}$$

$$\sigma_{I,\pi p\to \pi p} = 7.8 \pm 0.3\% \pm 4\%\ mb \tag{6.5}$$

By re-scaling the total cross section to our region of momentum transfer, we obtain:

$$\sigma_{pp\to pp} \simeq 6.6 \pm 0.27\ mb \tag{6.6}$$

$$\sigma_{\pi p\to \pi p} \simeq 3.2 \pm\ 0.14\ mb \tag{6.7}$$

From a purely numerical point of view these values can be considered satisfactory, since they show that - within the error bars - the overall detector efficiency is well understood.

6.3 Calibration with elastic scattering using the forward spectrometer

In the elastic scattering reaction a good fraction of forward scattered protons or pions enter the forward spectrometer. The full kinematics of the event can be determined by a precise measurement of the direction of this forward scattered beam particle, and the direction and momentum of the recoil proton can be precisely predicted. The use of this sample will provide a precious benchmark of TPC performance.

Selecting events with only one track in the forward direction and requiring that the measured momentum and angle are consistent with an elastic reaction already provides an enriched sample of elastic events. A further requirement that only one barrel RPC hit was recorded, and that this hit occurs at the position predicted for an elastic event defines a sample of protons with known momentum vector with a purity of about 99%. At beam momenta in the range 3 GeV/c – 8 GeV/c the kinematics are such that these protons point into the TPC with angles of $\approx 70^\circ$ with respect to the beam direction. With these protons an absolute determination of the reconstruction efficiency and of the bias and resolution of the measurement of momentum and angle are obtained. In addition, a clean sample of protons is available to study the PID for these particles. The measurements obtained with the elastic recoil protons will then be compared with the results of a Monte Carlo simulation allowing to transport the obtained calibrations to positive and negative pions with different kinematics.

Once a clean sample of elastic-scattering events is isolated the efficiency of the track finding and fitting procedure can be measured. It should be kept in mind that the recoil protons in elastic events have a specific distribution in momentum and angle. In particular, the correlation of the forward scattering angle and recoil proton momentum is such that an unavoidable threshold in recoil proton momentum (≈ 350 MeV/c) translates into a minimum angle for the scattered particle. The threshold is relatively high due to the requirement to detect the proton in the barrel RPC systems. This requirement can be removed only in cases where a small amount of background can be tolerated.

Due to the geometry of the rectangular aperture of the dipole magnet in the forward region only two small horizontal sectors of the TPC can be populated with recoil protons above threshold momentum in the 3 GeV/c beam. In the 5 GeV/c beam the situation is much better and all azimuthal angles can be populated, although not yet homogeneously. In the 8 GeV/c beam the population is homogeneous in ϕ, but the error propagation of the measurement of the forward scattering angle into the prediction of momentum and angle of the recoil proton becomes less favourable. Summing up all these arguments, the 8 GeV/c is most suitable for the determination of average efficiency, the 5 GeV/c beam is still useful for efficiency measurements and provides a good sampling of the resolution of the detector, while the 3 GeV/c beam can be used to study the resolution with the most favourable situation for the prediction.

6.3.1 Results

Based on the 5 GeV/c data the track reconstruction efficiency was determined to be 91% ± 1% compared with an efficiency of 93% calculated with the simulation. In the 8 GeV/c beam the efficiency is the same as that for 5 GeV/c data. In the data a $\approx$ 1% can be attributed to TPC readout channels with intermittent connection problems, an effect not simulated in the Monte Carlo. The inefficiency is dominated by the effect of the TPC spokes, as shown in fig. 6.5. The good agreement of the measurements with the simulation justifies the use of the simulation to determine the efficiency to measure pions.

The momentum resolution is at low momentum dominated by the straggling of the energy-loss, therefore a comparison with the simulation is needed. The comparison of the momentum resolution is shown as function of momentum in fig. 6.6. The momentum bias can also be studied with this method. Again a careful correction for the energy-loss is needed. The momentum bias is shown as function of predicted momentum in fig. 6.7. These results can be compared with the momentum resolution of the first fit obtained with the cosmic rays (section 5.4). The results show a difference of about 5% that can be explained by an error on the energy loss correction: in this momentum

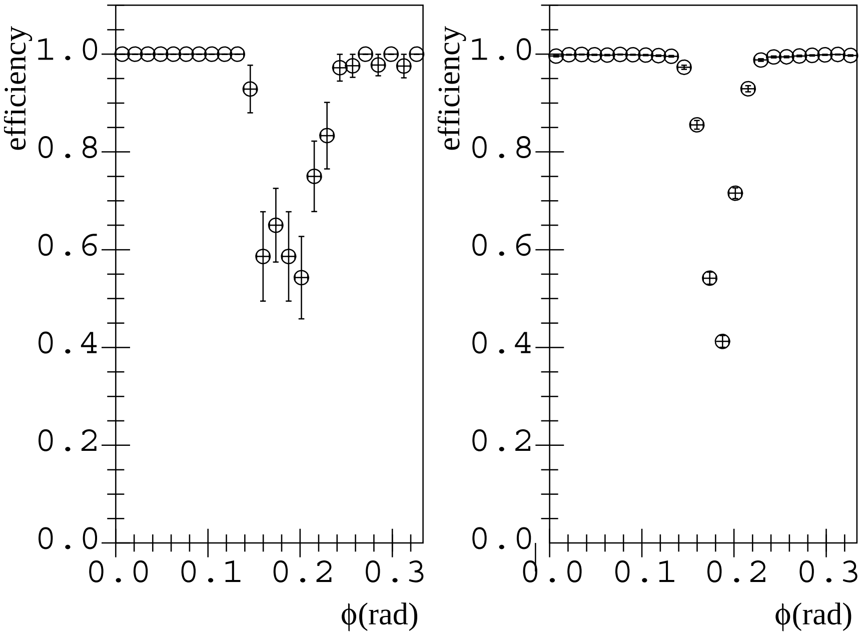

Figure 6.5: *The track finding efficiency as a function of ϕ in radiant within the sectors of the padplane of the TPC for 5 GeV/c p–H data measured with elastic events. The left panel shows the efficiency for recognizing tracks including the fit to a helix in the data, the right panel for the simulation.*

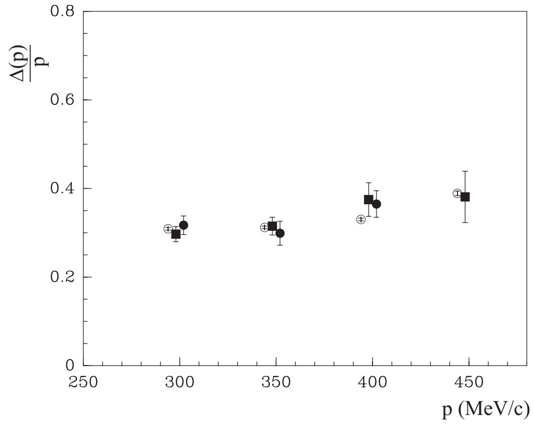

Figure 6.6: *The momentum resolution of the fit without vertex constraint for pp (3 GeV/c: filled squares, 5 GeV/c: filled circles) data measured with elastic events as a function of the momentum predicted by the forward scattered track compared to a simulation of the same sample of events at 5 GeV/c (open circles).*

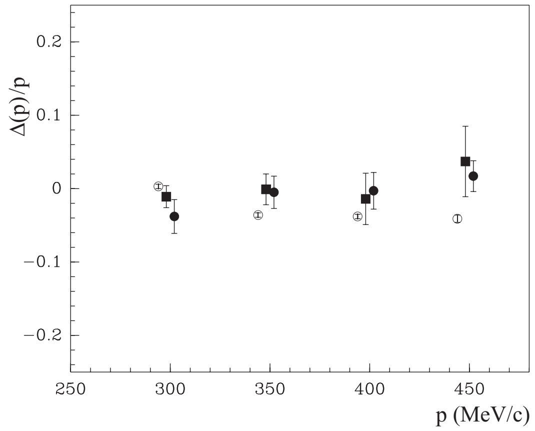

Figure 6.7: *The momentum bias measured with pp (3 GeV/c: filled squares, 5 GeV/c: filled circles) data with elastic events as a function of the momentum predicted by the forward scattered track compared to a simulation of the same sample of events at 5 GeV/c (open circles).*

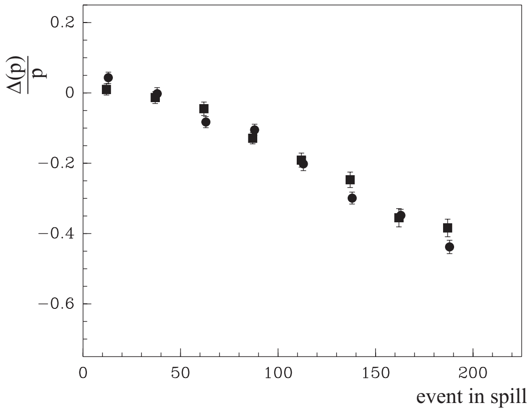

Figure 6.8: *Difference between the average momentum of elastically scattered protons in p–H data (3 GeV/c: filled squares, 5 GeV/c: filled circles) measured in the TPC and the momentum predicted by the forward scattered track as a function of the event number in the spill.*

range, between 300 MeV/c and 400 MeV/c, an error of 15 MeV/c on the energy can explain this difference.

It was verified that the value of θ is not modified by the dynamic distortions. However, the momentum and value of d'_0 is biased as a function of event in spill due to the effect of these distortions as shown in fig. 6.8 and fig. 6.9, respectively. The results of this analysis justify the use of only a limited number of events in each spill in order not to introduce large uncer-

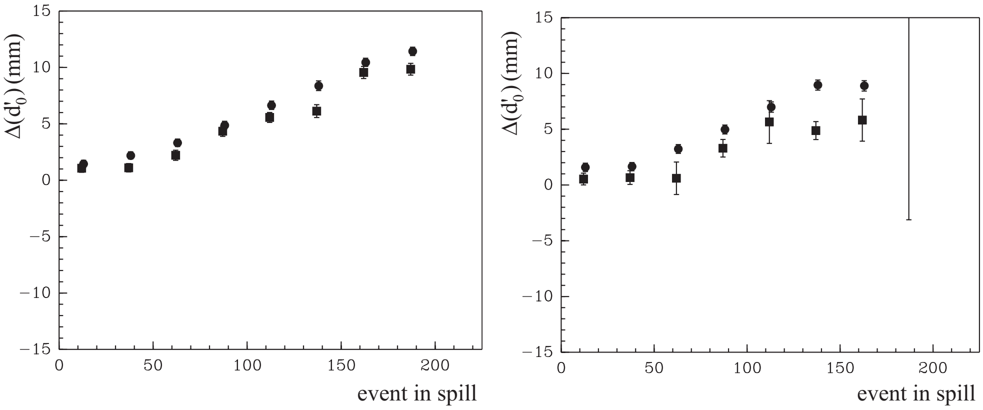

Figure 6.9: *Difference in average* d_0' *as a function of the event number in spill for p–H data (3 GeV/c: filled squares, 5 GeV/c: filled circles) between elastically scattered proton measured in the TPC and predicted by the forward scattered track. The left panel shows the data for low momentum and the right panel for high momentum.*

tainties due to distortions. The maximum effect of the distortions is very well controlled with the elastic scattering events. These results show clearly the correlation between the bias in the momentum and the bias in d_0' distribution. Therefore the d_0' distribution is a good parameter to determine the events selection in the spill to obtain a data sample that is not significantly affected by the dynamic distortions. The cut on d_0' depends on the setting because the dynamic distortions change setting by setting, as explained in section 4.6.

6.4 Conclusions

We have shown agreement of measured elastic cross section with previously measured elastic cross section at the level of ±6% systematic error. We demonstrated also that the track reconstruction efficiency was determined by the simulation as in the data within 2% of difference: this justifies the use of the simulation to determine the efficiency to measure pions. We evaluated that the momentum bias is below 5%. We established that dynamic distortions produce a bias as function of event number in spill which can be tagged by a study of the d_0' distribution and made negligible by applying a suitable cut on the event number in spill.

Chapter 7

Measurement of the production of charged pions by protons collisions on a tantalum target

7.1 Introduction

This chapter describes the measurement of the differential cross section for the production of charged pions generated by a proton beam with momentum larger than 3 GeV/c hitting a tantalum target with a thickness of 5% of a nuclear interaction length. The angular and momentum range covered by the experiment is of particular importance for the design of a Neutrino Factory. An elaborate system of detectors in the beam line ensures the identification of the incident particles. The produced particles were detected using the Time Projection Chamber (TPC) for track recognition, momentum determination and particle identification. Results are shown for the double differential cross-sections $\frac{d^2\sigma}{dpd\theta}$.

7.2 Motivation

The results of this analysis represent one of the main motivations of the HARP experiment: the measurement of the yields of positive and negative pions for a quantitative design of a proton driver and a target station of a future Neutrino Factory (as explained in section 1.9.2). The variables affecting the pion production yields are the primary proton beam energy, the target material and the target geometry (diameter and length). In order to achieve the highest number of potentially collected pions of both charges per unit energy, a pion production measurement should give the information necessary to optimize both the proton beam energy and the target material.

The fig. 7.1 shows the HARP kinematic coverage compared with the typical range of the kinematical acceptance of the Neutrino Factory designs. It is shown that HARP experiment covers the full momentum range of interest for production angles above 0.35 rad. A small part of the small angle region can in principle be covered by measurements with the forward spectrometer. The analysis reported here covers the major part of pions produced in the target and accepted by the focusing system of the input stage of a neutrino factory. The importance of the knowledge of the smaller angles varies with the different types of design being contemplated.

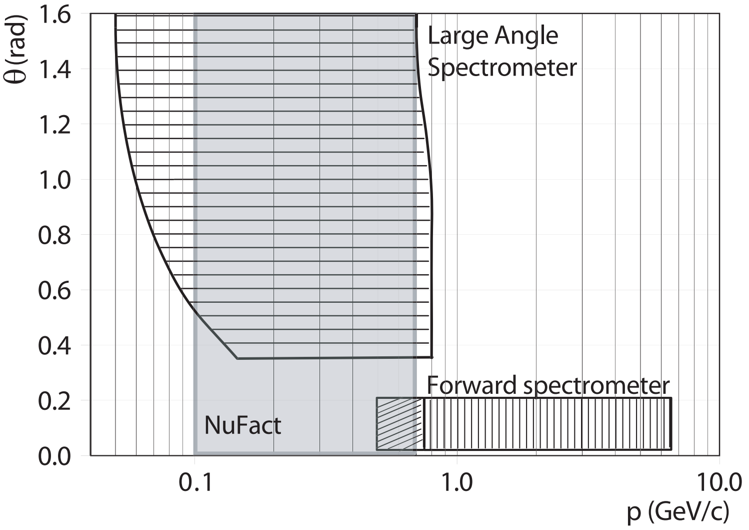

Figure 7.1: *HARP acceptance covered by the forward spectrometer (area with vertical dashed lines) and by the large angle spectrometer (area with horizontal lines). The grey box indicates the most interesting region for the Neutrino Factory.*

7.3 Data selection procedure

The positive-particle beam used for this measurement contains mainly positrons, pions and protons, with small components of kaons and deuterons and heavier ions (see fig.7.2). Its composition depends on the selected beam momentum.

The analysis proceeds by first selecting a primary proton hitting the target, not accompanied by other beam tracks, by requiring a trigger in the ITC. After the event selection, the sample of tracks to be used for the analysis is defined. All beam-selection criteria used for the events with an interaction

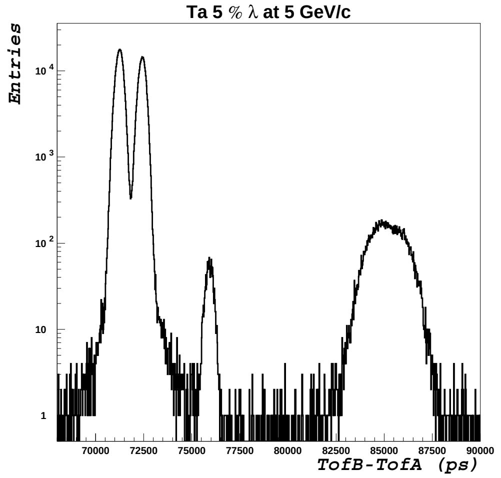

Figure 7.2: *TofB-TofA spectrum for beam particles at 5 GeV/c: the peaks correspond to pions, protons, deuterons and the heavy particles could be tritium or helium isotopes.*

trigger are applied identically to a set of minimum-bias triggers. Therefore, the normalization to the number of incoming protons is possible by counting the beam particles accepted within the interaction and minimum-bias samples. The selection procedure is described below. Table 7.1 shows the number of events and tracks at various stages of the selection.

7.3.1 Events selection

The TOF system of the beam line measures the time-of-flight over a distance of 21.4 m which provides particle identification at low energy (up to 5 GeV/c). At 5 GeV/c the π/p-separation is made jointly by the beam TOF and the Cherenkov (BCB), while the other Cherenkov (BCA) is used to tag $e^{\pm}$. The fig. 7.3 shows the time-of-flight and the Cherenkov signals for the analysed setting: the two peaks identify the protons and pions beam.

A set of MWPCs is used to select events with only one beam particle whose trajectory is extrapolated to the target. Fig. 7.4 shows the beam spectrum at the first face of the target for the analysed setting. The beam is centred at x=0 mma and $y = -4$ mm. We accept events for which the beam hits the target within a circle with a radius smaller than 15 mm.

An identical beam particle selection was performed for events triggered with the minimum bias trigger in order to provide an absolute normalization of the incoming protons. This trigger selected every 64^{th} beam particle coincidence outside the dead-time of the data acquisition system. The beam

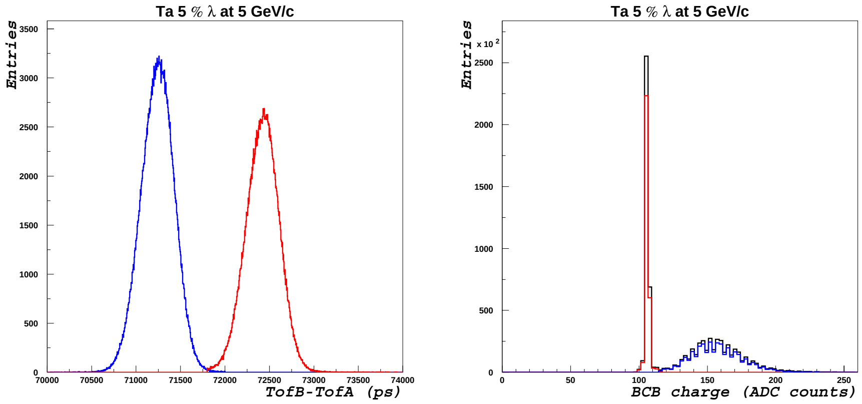

Figure 7.3: *On the left TofB-TofA spectrum shows the two peaks corresponding to the pion (on the left) and to the proton (on the right) and on the right is displayed the pulse-height spectrum from the BCB Cherenkov counter for a positive beam at 5 GeV/c.*

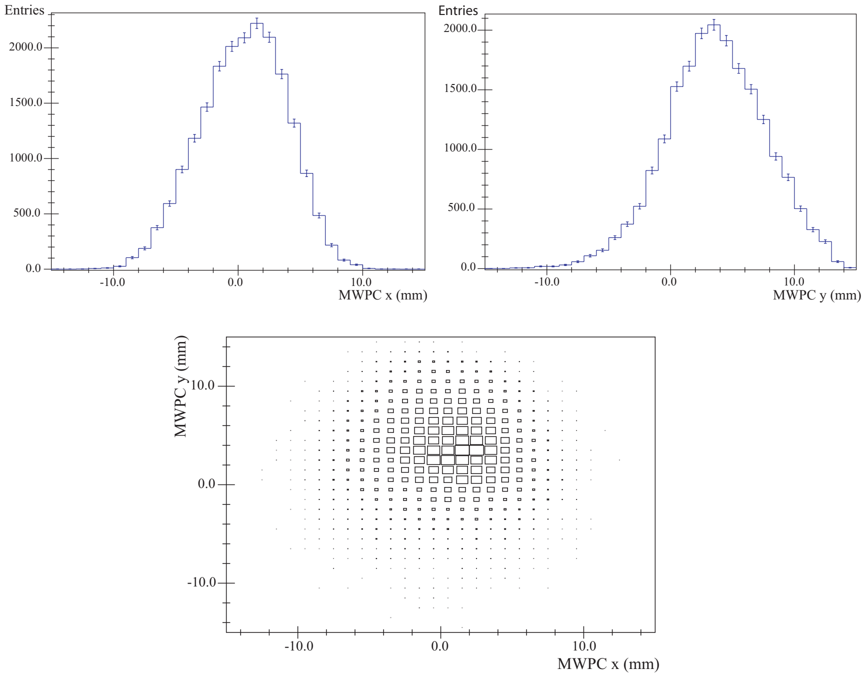

Figure 7.4: *The distribution of the beam particle trajectory extrapolated points to the first face of the target along x (first row on the left), along y (first row on the right) and the xy spectrum (second row). One can note the asymmetry of the beam along y.*

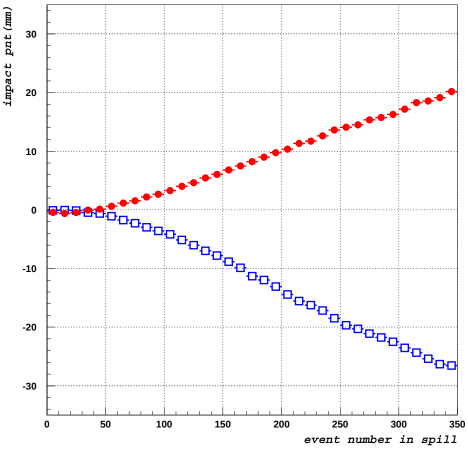

Figure 7.5: *The mean impact point: for the positive (in red) and negative (in blue) pions as function of the event number during a spill after the static distortions corrections.*

particle has to be accepted by the criteria described above and has to be identified as a proton.

To avoid large effects of the dynamic distortions on the analysed data sample, only the first N_{evt} events in each spill are retained. The value of N_{evt} is determined by comparing for each data taking condition the shift in the average value of d'_0 with the distribution of the calibration data set. Fig. 7.5 shows the d'_0 dependencies on the number of events within a spill for the analysed setting. For this setting the value of N_{evt} is 50 compared to a typical total number of events per spill of 350.

7.3.2 Track selection

Not all tracks found in the TPC are suitable for the analysis. Cuts are defined to reject tracks from events which arrive randomly within the 30 μs drift time of the TPC (overlays). In addition, selection criteria are used which preferentially remove tracks produced by interactions of secondary particles. The following cuts were applied to retain well-measured particle tracks with known efficiency and resolution.

Tracks are only considered if they contain at least twelve space points out of a maximum of twenty. This cut is applied to ensure a good measurement of the track parameters and of the dE/dx. Fig. 7.6 shows the distribution of number of points for pions[†]. By requiring at least 12 points, we reject

---

[†] Pion samples obtained by a rough PID selection

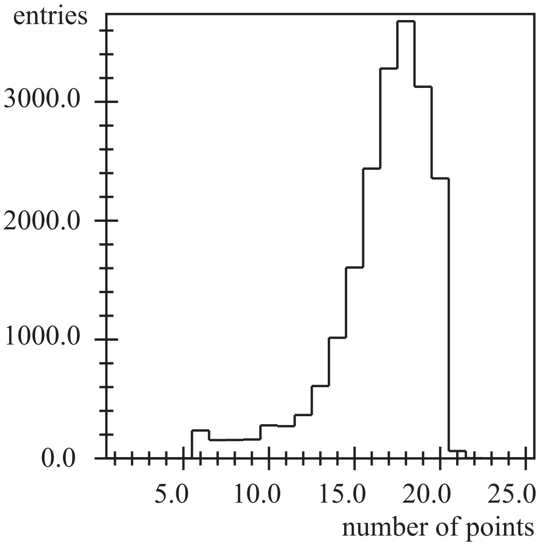

Figure 7.6: *Number of points per pion after event and track selection.*

about 7% of the tracks. The peak of points distribution is 17.8 for pions and 19 for protons, the mean value is 17.2 for pions and 17.8 for protons. This difference is due to different ionization of pions and protons in the selected momentum range below 700 MeV/c.

Furthermore, a quality requirement is applied on the fit of the helix and on the vertex fit. As explained in section 3.3.4, the vertex fit is applied to tracks that have an impact parameter (in the plane perpendicular to the nominal beam direction) inside a fiducial volume defined by the target size and by the resolution in the xy plane and along z. We select tracks with an impact point in the target within 2σ of the impact point resolution (shown in section 5.6).

Fig. 7.7 shows the distribution of d_0' and z_0' for the data taken with 5 GeV/c protons on a tantalum target. Cuts are applied at d_0' smaller than 8.5 mm and $z_0' \cdot \cos(\theta)$ between 7.2 mm and 12.8 mm. The latter cut depends on θ to take into account the θ dependence of the precision. The transverse coordinates of the interaction vertex are obtained by extrapolating the trajectory of the incoming beam particle measured by the MWPCs. The longitudinal coordinate is taken from the nominal target position.

Finally, we accept only tracks with total momentum in the range between 50 MeV/c and 700 MeV/c that have a good momentum resolution and good particle identification. This range meets the requirements of the data needed for the design of the Neutrino Factory and is consistent with the acceptance and resolution of the chamber.

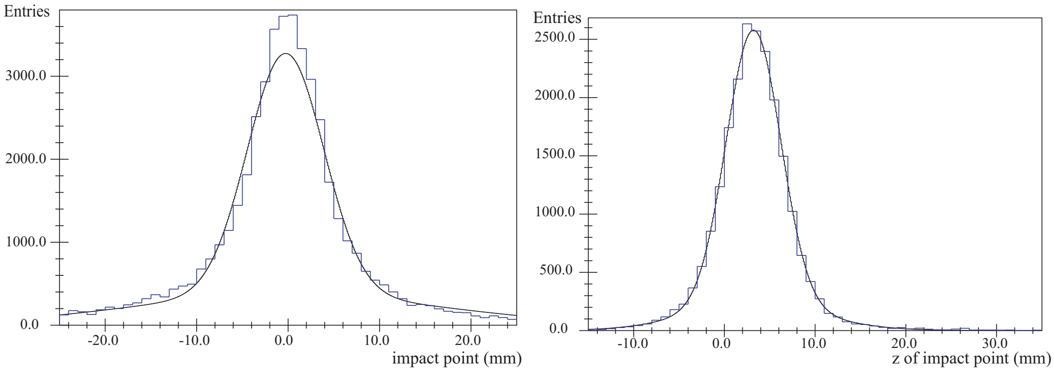

Figure 7.7: *d_0' (on the left) and z_0' (on the right) taken with a 5 GeV/c proton beam hitting a tantalum target.*

Data Set	**5 GeV/c**
Total events processed	2094286
Events with accepted beam proton	615212
Protons on target	546649
Interaction triggers	218115
Events in accepted part of the spill	33400
Pre-scaled triggers with accepted beam proton	7890
Total good tracks	47000

Table 7.1: *Total number of events in the tantalum 5% $\lambda_{\rm I}$ target data with a beam momentum of 5 GeV/c; the number of protons on target is calculated from the pre-scaled trigger count.*

7.4 Analysis procedure

The double differential cross section for the production of a particle of type α can be expressed in the laboratory frame as:

$$\frac{d^2\sigma_\alpha}{dp_i d\theta_j} = \frac{1}{N_{\rm pot}} \frac{A}{N_A \rho\, t} M^{-1}_{ij\alpha i'j'\alpha'} \cdot \left(N^{\alpha'}_{i'j'}(T) - N^{\alpha'}_{i'j'}(E)\right) \tag{7.1}$$

where $\frac{d^2\sigma_\alpha}{dp_i d\theta_j}$ is expressed in bins of true momentum (p_i), angle (θ_j) and particle type (α). The summation over reconstructed indices $i'j'\alpha'$ is implied in the equation. The terms on the right-hand side of the equation are as follows:

- the so called raw yield $N^{\alpha'}_{i'j'}$ is the number of particles of observed type α' in bins of reconstructed momentum ($p_{i'}$) and angle ($\theta_{j'}$). The term ($N^{\alpha'}_{i'j'}(T)$) refers to the data taken with the tantalum target and ($N^{\alpha'}_{i'j'}(E)$) refers to the data taken with no target (Empty target). These particles must satisfy the event, track and PID selection criteria;

- the matrix $M^{-1}_{ij\alpha i'j'\alpha'}$ corrects for the efficiency and resolution of the detector. It unfolds the true variables $ij\alpha$ from the reconstructed variables $i'j'\alpha'$. This matrix corrects the observed number of particles to take into account effects such as reconstruction efficiency, acceptance, absorptions, pion decay, tertiary production, PID efficiency, PID misidentification rate and electron background;
- the factor $\frac{A}{N_A \rho\, t}$ is the inverse of the number of target nuclei per unit area (A is the atomic mass, N_A is the Avogadro number, ρ and t are the target density and thickness);
- the result is normalized to the number of incident protons on target N_{pot}.

This analysis addresses the problem of unfolding by decomposing the correction matrix of eq. (7.1) into distinct independent contributions, which are computed using the real data and Monte Carlo data. The following contributions compose the unfolding matrix:

$$M^{-1}_{ij\alpha i'j'\alpha'} = (M^{PID}_{gv})^{-1} \cdot (M^{enloss}_{gv})^{-1} \cdot \epsilon^{-1}_{ij\alpha} \cdot (M^{p}_{ii'})^{-1}$$

- $(M^{PID}_{gv})^{-1}$ is the correction matrix for the PID efficiency and the purity correction;
- $(M^{enloss}_{gv})^{-1}$ is the term of the unfolding matrix correcting for the energy loss which only depends on the indices g and v representing the momentum when the particle enters in the gas and the momentum at the production vertex, respectively;
- the correction for the efficiency of the apparatus $\epsilon^{-1}_{ij\alpha}$ is the collection of factors applying the corrections that are diagonal in the PID indices. This matrix can thus be factorized as

  $$\epsilon^{-1}_{ij\alpha} = w^{acc}_{ij} \cdot w^{recon}_{ij} \cdot w^{absorption}_{ij\alpha} \cdot w^{tertiaries}_{ij\alpha}$$

  where

  - w^{acc}_{ij} is the correction for the acceptance;
  - w^{recon}_{ij} is the correction for the overall reconstruction efficiency;

  - $w_{ij\alpha}^{absorption}$ is the correction for the loss of particles due to absorption and decay;
  - $w_{ij\alpha}^{tertiaries}$ is the correction for the background of tertiary particles generated by the secondaries produced in the target.

  The first two corrections are the same for pions and protons while the last two also depend on the particle type;

- the momentum bin migration is small for low momentum, but it must be considered for transverse momenta above 300 MeV/c. $(M_{ii'}^{p})^{-1}$ is the simplified unfolding matrix correcting for the momentum smearing which only depends of the indices i and i' representing the true and reconstructed momentum bins, respectively. It was verified that the smearing effect in the angular measurement has a negligible effect, therefore $(M_{ii'}^{\theta})^{-1}$ is the identity matrix.

These corrections will be described in the next sections and the effects of these corrections on the data are shown in section 7.5.

The results are expressed in double differential cross section for positive and negative pions as function of momentum in nine angular bins of 200 mrad each.

7.4.1 Particle Identification

The particle identification (PID) in the large-angle region mainly uses the dE/dx information provided by the TPC. The PID is evaluated with analytical cuts on the plot of dE/dx versus the momentum. The purity and the efficiency is evaluated studying the dE/dx slices in the different momentum bins: by fitting each distribution by a double Landau distribution we can evaluate for the selected pions sample the contamination of electrons (at low momentum) and of protons at higher momentum. The fig. 7.8 shows the PID on the plot of dE/dx versus the momentum, the colour being assigned according to the particle identification after the analytical cut.

Particle separation between protons and pions can be achieved with a purity of about 99% up to 400 MeV/c. Above this value, efficiency and purity are evaluated using the slice fit method, some examples are shown in fig. 7.9 and 7.10. This study is done as function of the momentum in angular bins.

A slightly different approach is needed for background generated by other secondary particles, such as electrons and positrons resulting from π^0 decay or δ-rays. The electron contamination can be evaluated only for momentum less than 125 MeV/c. Above this value it is evaluated using Monte Carlo.

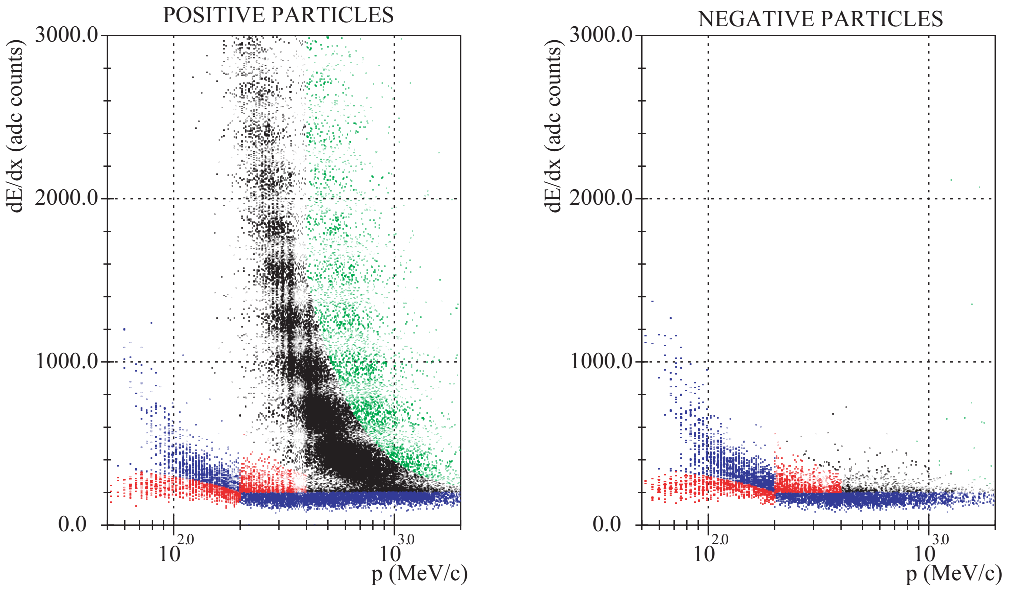

Figure 7.8: *dE/dx spectrum as function of the momentum. The colours identify the different PID regions as used in this analysis.*

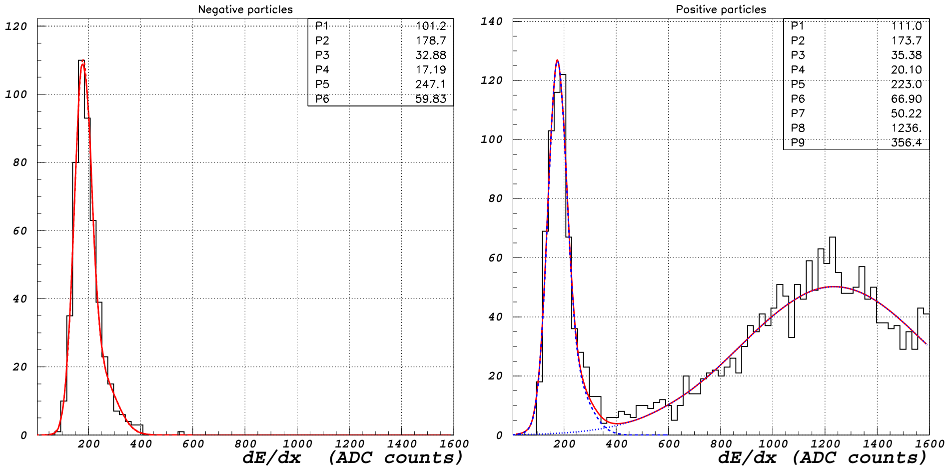

Figure 7.9: *dE/dx slices for negative particles (on the left) and positive (on the right) with momentum between 300 MeV/c and 350 MeV/c*

δ-rays electrons are negligible in this momentum range, as δ-rays are mainly at low momentum as shown in [149]. The assumption made is that the π^0 spectrum is similar to the spectrum of π^+ and π^- or the average of them. In the Monte Carlo simulation we generate a π^0 with the same momentum and angular distribution of π^+, the resulting effects (*i.e.* tracks of conversion electrons) are studied as function of the angular and momentum distribution.

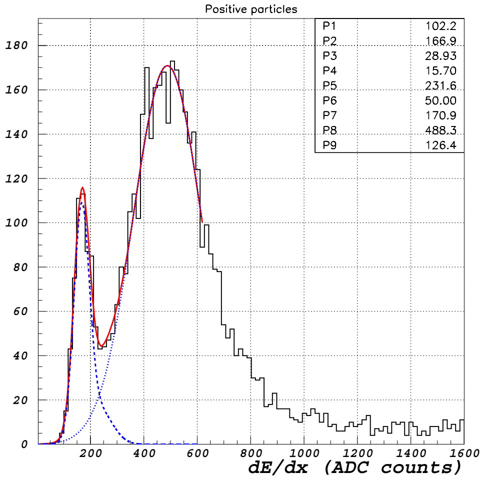

Figure 7.10: *dE/dx slices for positive particles with momentum between 500 MeV/c and 600 MeV/c*

Using the slice for momentum below 125 MeV/c where we can evaluate the electrons in the physics data (see fig. 7.11), we can normalize the simulated data to obtain the same number of electrons and positrons as in the measured data.

The RPC can provide complementary information in PID for pion-electron separation for momentum up to 125 MeV/c and for proton-pion separation, but the data are reduced of about 15% due to the RPC efficiency.

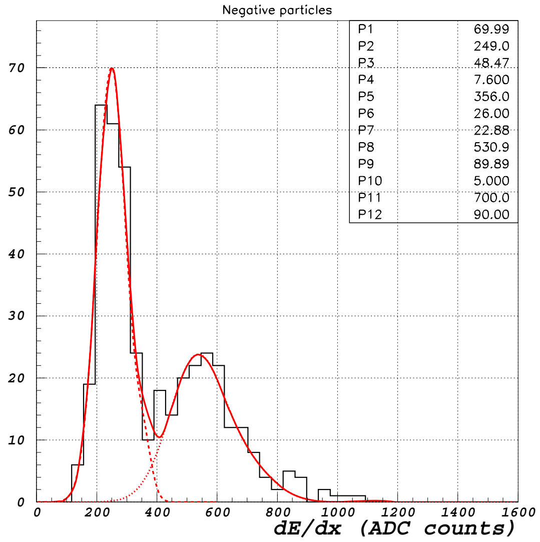

Figure 7.11: *dE/dx slices for negative particles with momentum between 75 MeV/c and 100 MeV/c*

7.4.2 Energy loss study

Particles produced in the target lose energy when they cross different materials before reaching the TPC active volume (ITC and inner field cage). All the geometry and materials are well simulated by the Monte Carlo. We evaluate the pion energy loss by analysing the MCtruth information, namely the value of the kinematic parameters of the particles as produced by the Monte Carlo generator. Using these values as function of angle and of momentum we can evaluate the corrections that we should apply to the reconstructed momentum in the gas to obtain the momentum at the production point. The results are summarised in table 7.2. After 300-400 MeV/c the energy loss is constant and only depends on polar angle (see fig. 7.12).

The energy loss as function of the polar angle is shown in fig. 7.13. It has a peak around $\theta = 90$ degrees when the particles cross radially the target (5.6 mm length and 15 mm radius), and decreases for other angles. For forward tracks the energy loss increases again because the tracks cross more material outside the target, this is clearly shown by comparing fig. 7.13 with fig. 7.14. The difference of energy loss for particles produced at different radius in the target and with the same direction is only few MeV/c for particles of at least 50 MeV/c.

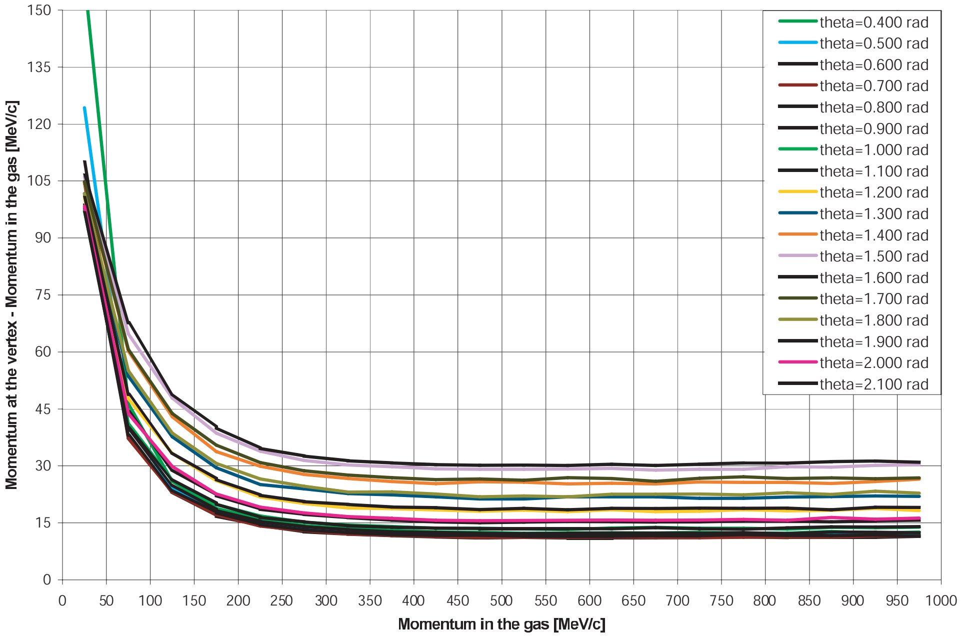

Figure 7.12: *Monte Carlo: momentum lost as function of the momentum in the gas in different momentum bins.*

Mom. loss (MeV/c)	p_{gas} (50-100)	p_{gas} (100-150)	p_{gas} (150-200)	p_{gas} (200-250)	p_{gas} (250-300)	p_{gas} (300-350)	p_{gas} (350-400)	p_{gas} (400-1000)
θ=0.4 rad	46	26	19	16	14	14	13	13
θ=0.5 rad	41	24	18	15	13	12	12	12
θ=0.6 rad	38	23	17	14	13	12	12	11
θ=0.7 rad	37	23	17	14	13	12	12	11
θ=0.8 rad	38	24	18	15	13	12	12	12
θ=0.9 rad	39	25	18	15	14	13	13	13
θ=1.0 rad	41	26	20	17	15	14	14	14
θ=1.1 rad	44	29	22	19	17	16	16	15
θ=1.2 rad	45	33	26	22	20	19	19	18
θ=1.3 rad	51	38	30	25	24	23	22	22
θ=1.4 rad	52	39	34	30	28	27	26	25
θ=1.5 rad	52	44	39	34	31	30	30	29
θ=1.6 rad	58	44	40	35	33	31	31	30
θ=1.7 rad	52	39	35	31	29	28	27	26
θ=1.8 rad	50	39	31	27	25	23	23	23
θ=1.9 rad	49	34	27	22	21	20	19	19
θ=2.0 rad	44	30	23	19	18	17	16	16
θ=2.1 rad	40	27	20	16	15	14	14	14

Table 7.2: *Monte Carlo: momentum lost (because of energy loss) between the production point in the target and the entrance in the TPC gas as function of the momentum in the TPC gas in different momentum bins.*

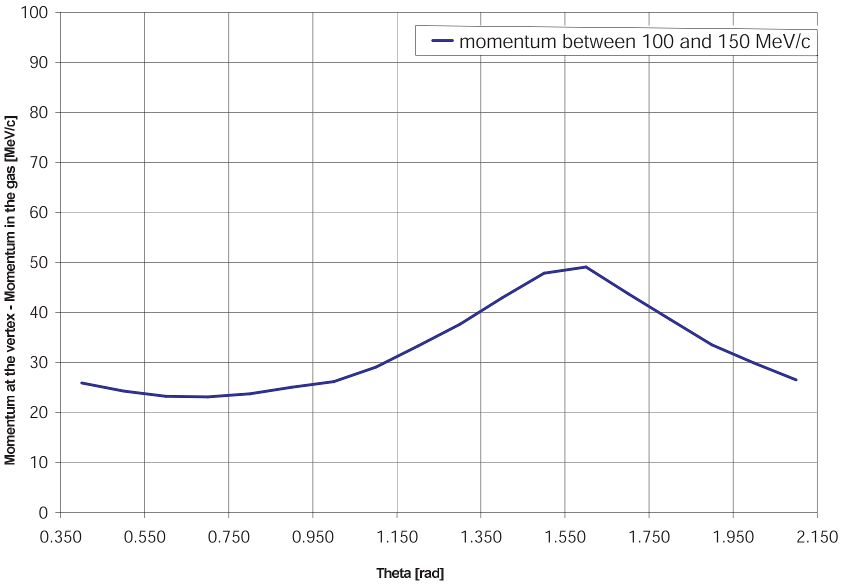

Figure 7.13: *Monte Carlo: momentum lost between the production point in the target and the point where the particle enters in the gas, as function of polar angle for pions with a momentum between 100 MeV/c and 150 MeV/c.*

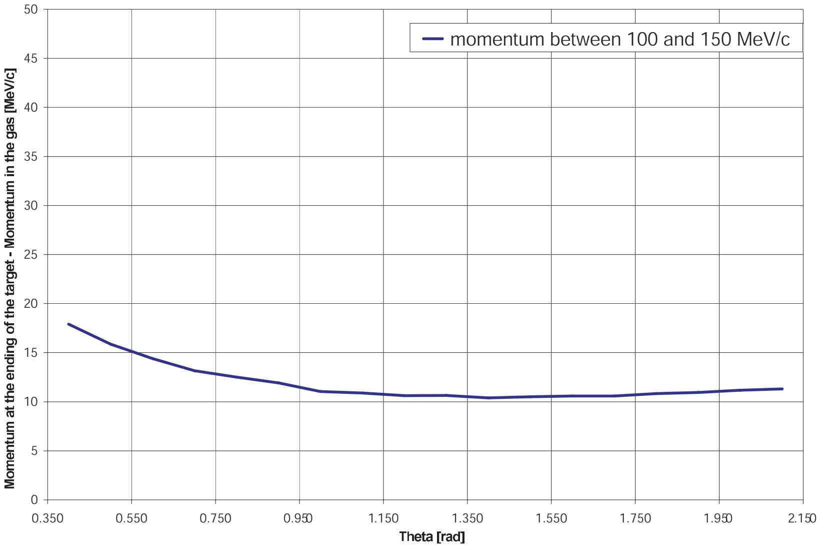

Figure 7.14: *Monte Carlo: momentum lost between the point where the particle exits from the target and the point where the particle enters in the gas, as function of polar angle for pions with a momentum between 100 MeV/c and 150 MeV/c.*

7.4.3 TPC overall efficiency study for pions

The efficiency of the apparatus is related to different factors: 1) reconstruction efficiency, 2) acceptance efficiency, 3) efficiency for the loss of particles due to absorption and decay, 4) the background of tertiary particles generated by interaction of secondaries produced in the target.

The reconstruction efficiency and acceptance can be calculated by the Monte Carlo which reproduces well the resolution seen by the data. These efficiencies are evaluated applying the cuts as done for this analysis on the quality of the tracks and on the angular and momentum acceptance.

An additional correction to be considered is the absorption of pions and protons and the decay of secondary pions in the detector materials that surround the target.

A correction of opposite sign to the one above comes from tertiary charged particles. These can come from interactions of secondaries inside the target (this is a small effect, since the target is only 5% λ_I in thickness) or in the material outside the target area. Another different background could be due to particles produced by interactions of primary protons with material outside the target. This effect can be studied analysing the data taken with empty target settings: the selection criteria which accepts only events from the target region and the good definition of the interaction point reduces this background to a negligible level ($< 10^{-5}$).

The above efficiencies are evaluated using a Monte Carlo, with the method described in section 5.7. The single particle Monte Carlo generator neglects the possible interference of close tracks for the reconstruction efficiency. Due to the relatively low event multiplicity (for the analysed data the average multiplicity* is 2.3) which is spread over a large solid angle this simplification does not introduce a significant error. The efficiency is evaluated as function of the momentum and polar angle and it has been computed separately for true pions and protons, because these corrections are applied after the PID. The pions overall efficiency is shown in fig. 7.15.

7.4.4 Normalization

The absolute normalization of the results is calculated relatively to the number of incident beam particles accepted by the selection and once the factor $\frac{A}{N_A \rho t}$ is applied. The total number of protons on target is counted using prescaled beam triggers that were continuously recorded at the time of data taking. The trigger condition for the prescaled beam triggers only involved

---

*The average multiplicity is defined as the ratio of the number of tracks with at least twelve hits in the TPC (regardless of their momentum, angle or spatial position) and the number of events accepted by the selection criteria with at least one of such tracks.

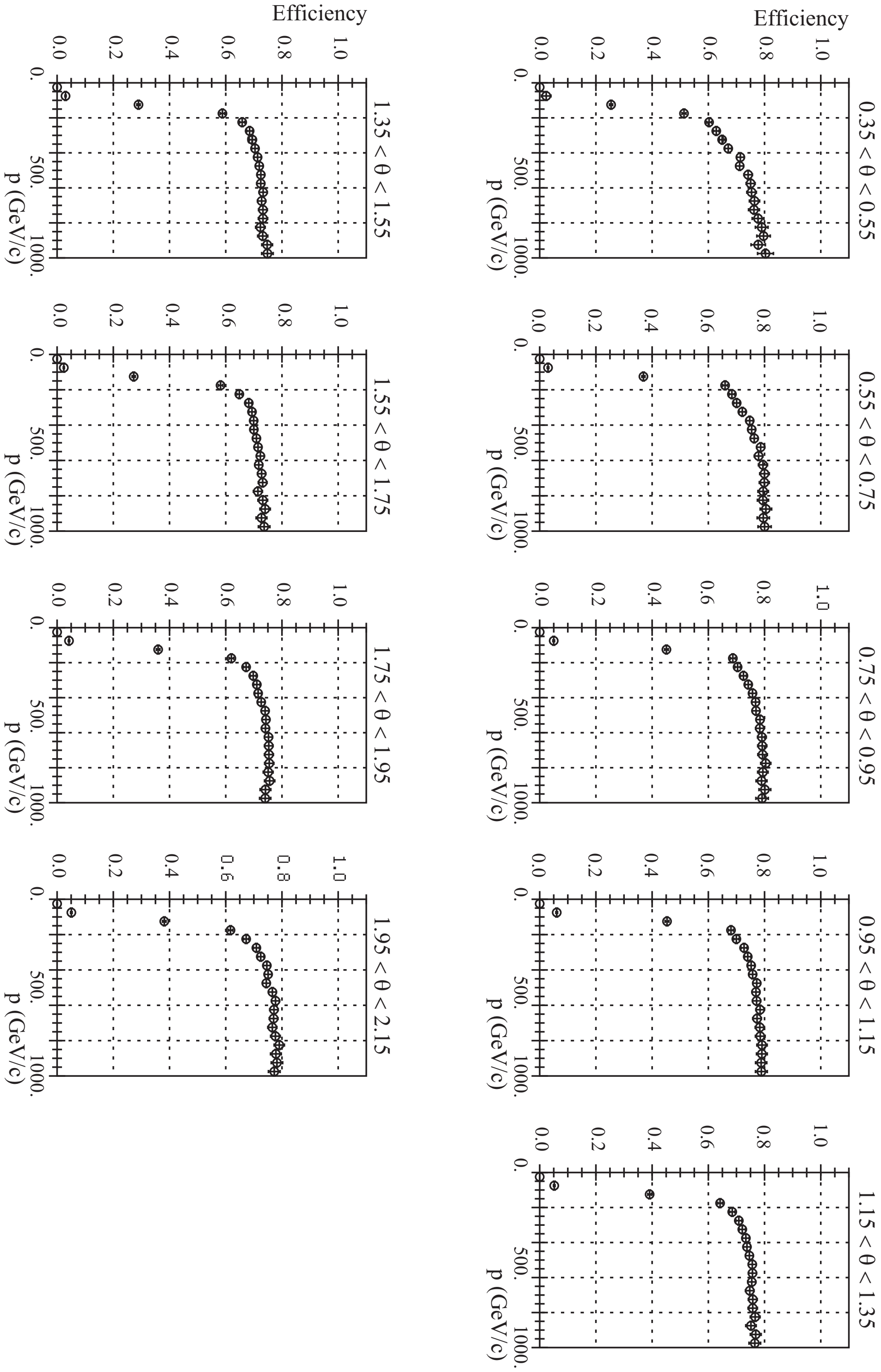

Figure 7.15: *Monte Carlo data. Efficiency for positive pions as function of the total momentum for different polar angle bins of 200 mrad each.*

a simple coincidence of scintillators in the beam line with no requirement of an interaction in the target. Using subsamples of the triggers the prescale factor was checked to confirm it had its preset value of 1/64. Because the selection criteria for beam protons used in event analysis and prescaled beam proton events are the same, the efficiencies for these cuts factorize, and the total normalization is known without additional systematic uncertainty.

Especially at lower momenta, beam particles may miss the target even if their trajectory measured in the MWPCs extrapolates to the target. This 'targeting' efficiency was estimated by counting secondaries produced in the forward direction and measured in the forward spectrometer as a function of the impact radius measured from the centre of the target. The integral of the distribution of number of tracks measured in the forward spectrometer as a function of the maximum radius is shown in fig. 7.16. The measured variation in the target thickness is used as an estimate of an additional uncertainty in the absolute normalization. The target thickness uncertainty cancels in the comparison of data with different incoming beam momenta, while the uncertainty in the efficiency to hit the target introduces an error ($\leq 2\%$) into this comparison.

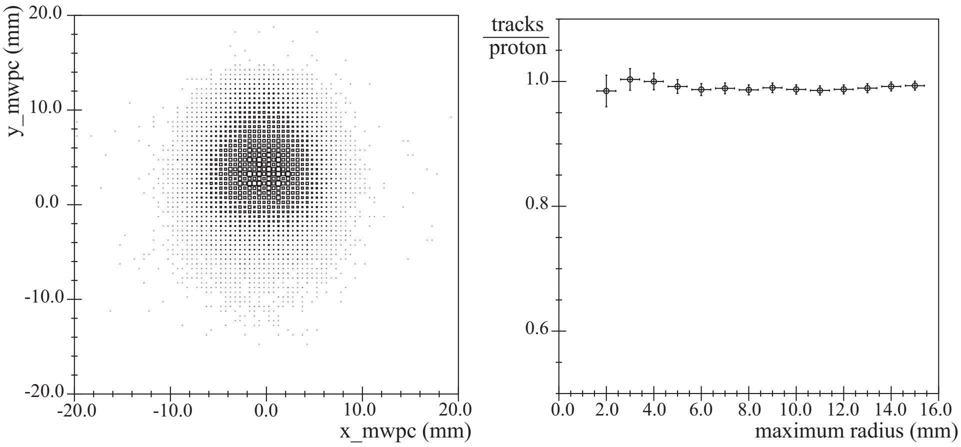

Figure 7.16: *Left panel: impact point of the beam particles onto the target predicted by the MWPC measurement. Right panel: measurement of the efficiency of hitting the target for the beam selection used in this analysis. The correction is measured using tracks in the forward spectrometer.*

7.5 Double differential cross sections for pions produced by proton–Ta collisions

This section shows the pion yields and the double differential cross sections of positive and negative pions as function of total momentum and of the polar angle at the large angle region (0.35 rad $\leq \theta \leq$ 2.15 rad) produced by a proton beam of 5 GeV/c impinging on a thin (5% interaction length, 5.6 mm) tantalum target. These results are obtained using the data selection described in section 7.3. The results with the statistical errors obtained by the different steps of the analysis procedure described in section 7.4 are shown in the following figures:

Fig. 7.17 shows the raw yields for positive and negative particles before any corrections.

Fig. 7.18 shows the raw yields for positive pions (red squares), negative pions (blue circles) and protons (black) after the analytical cut on dE/dx.

Fig. 7.19 shows the raw yields for positive (red squares) and negative pions (blue circles) after the analytical cut on dE/dx and the PID purity and PID efficiency correction.

Fig. 7.20 shows the raw yields for positive (red squares) and negative pions (blue circles) after the analytical cut on dE/dx and the PID purity, PID efficiency correction and the energy loss correction.

Fig. 7.21 shows the raw yields for positive (red squares) and negative pions (blue circles) after the analytical cut on dE/dx and the PID purity, PID efficiency correction, the energy loss correction and the total apparatus efficiency correction.

Fig. 7.22 shows the raw yields for positive (red squares) and negative pions (blue circles) after the analytical cut on dE/dx and the PID purity, PID efficiency correction, the energy loss correction, the total apparatus efficiency correction and with the bin migration corrections.

Fig. 7.23 shows the differential cross section for positive (red circles) and negative pions (blue squares), the error bars represent the statistical errors.

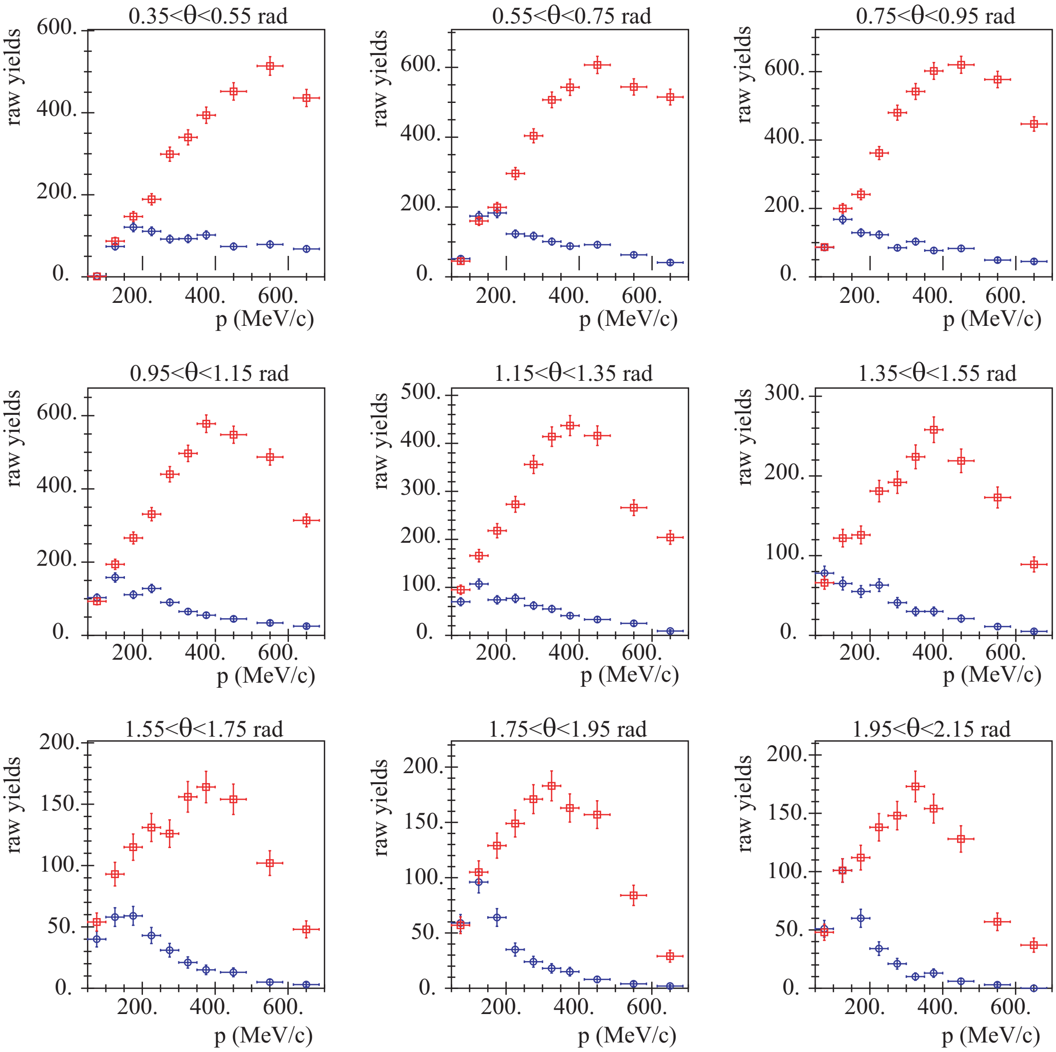

Figure 7.17: *The raw yields as function of total momentum and polar angle for positive (red squares) and negative (blue circles) particles before any corrections.*

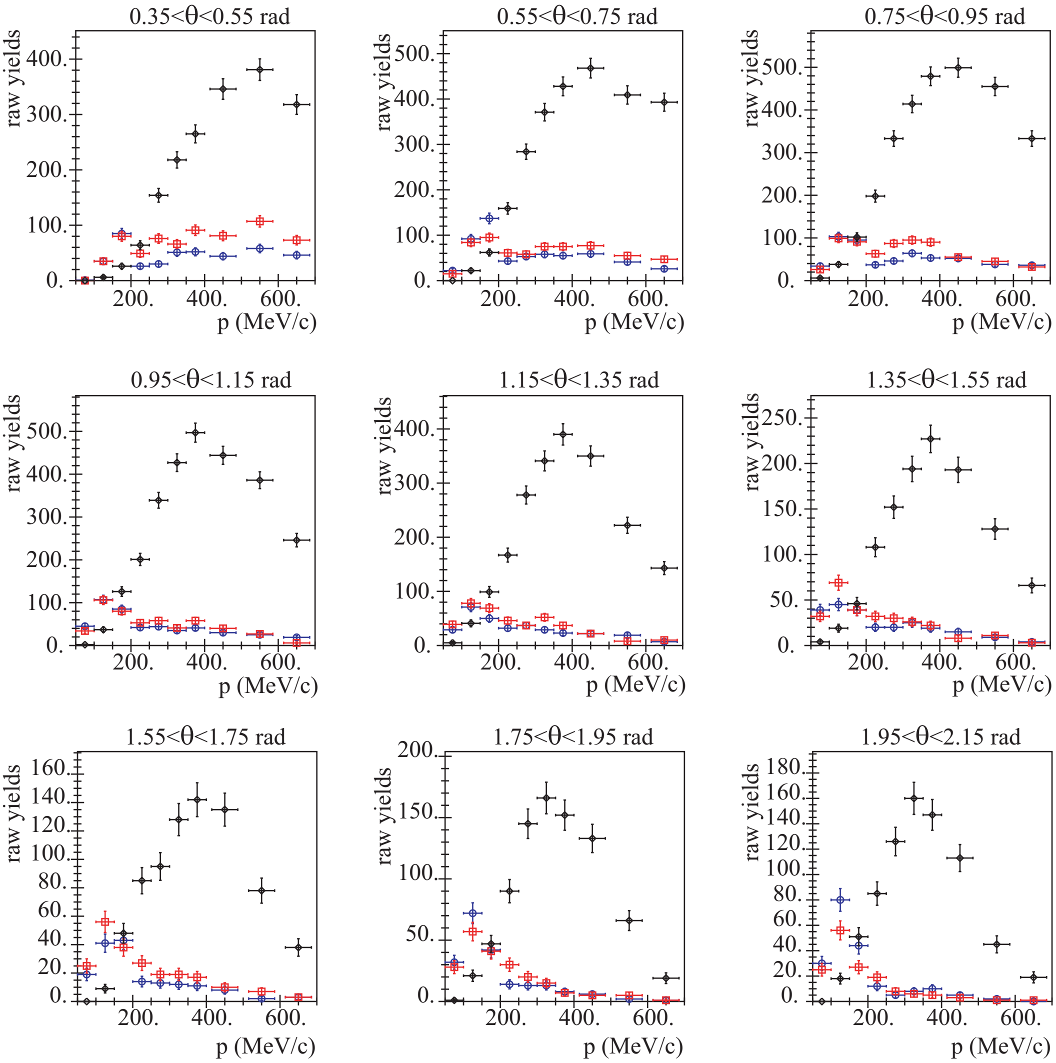

Figure 7.18: *The raw yields as function of total momentum and polar angle for positive pions (red squares), negative pions (blue circles) and protons (black) after the analytical cut on dE/dx.*

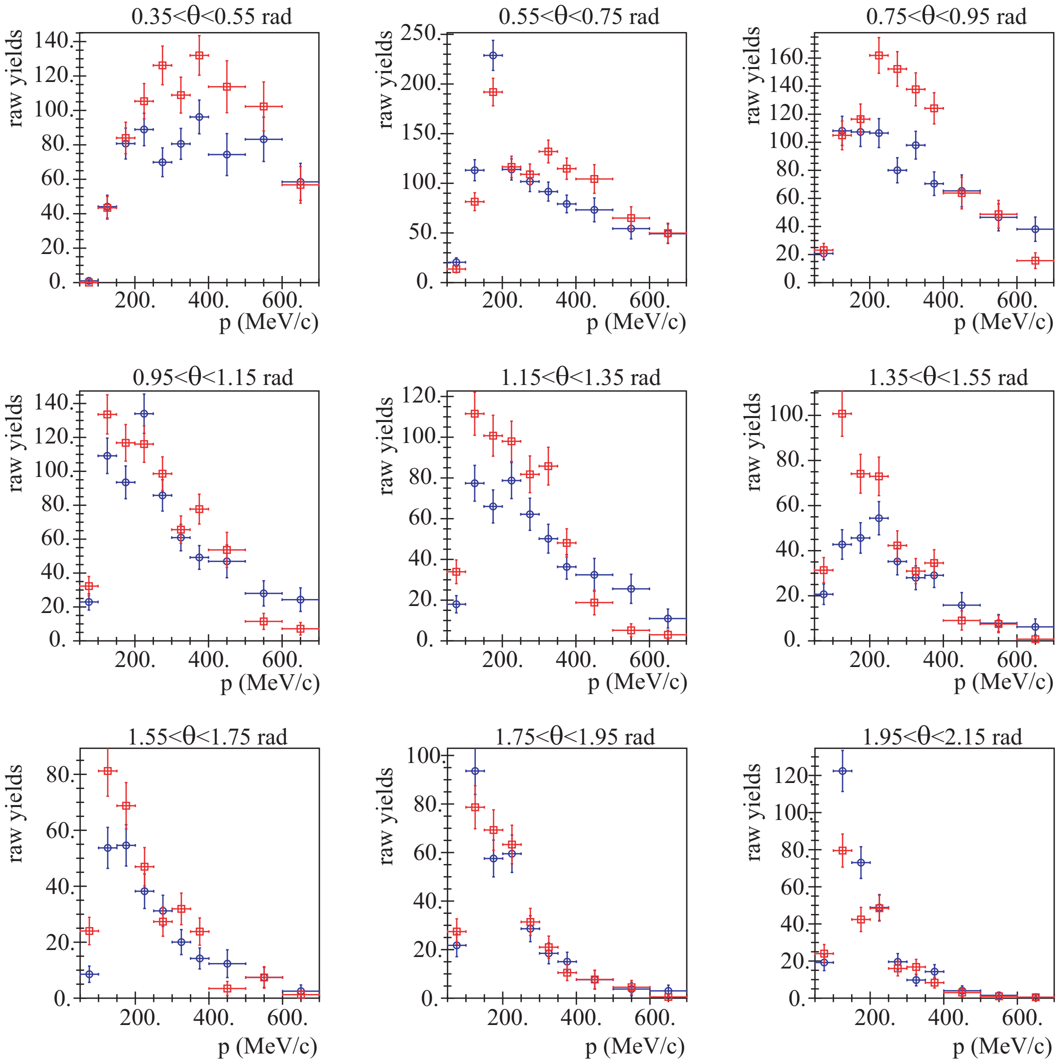

Figure 7.19: *The raw yields as function of total momentum and polar angle for positive (red squares) and negative pions (blue circles) after the analytical cut on dE/dx and the PID purity and PID efficiency correction.*

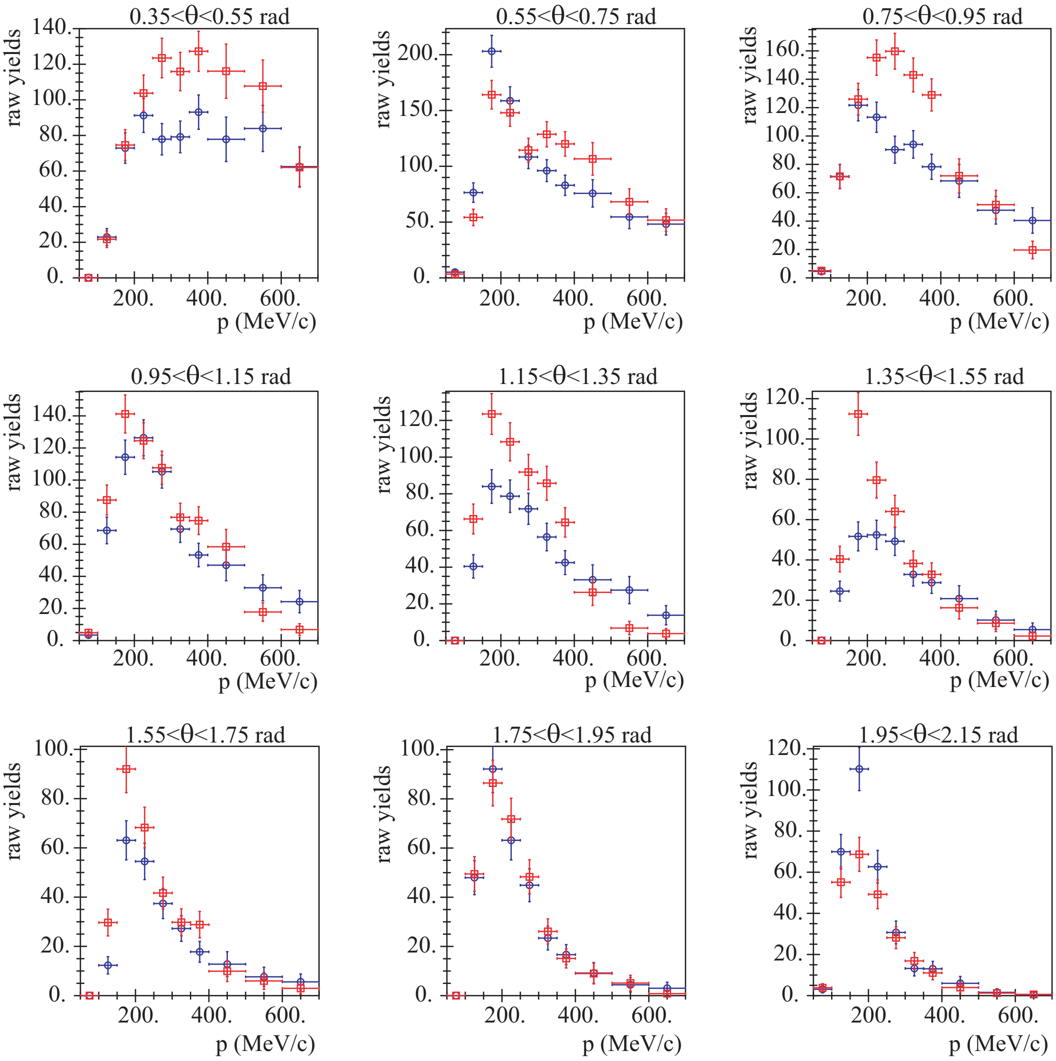

Figure 7.20: *The raw yields as function of total momentum and polar angle for positive (red squares) and negative pions (blue circles) after the analytical cut on dE/dx and the PID purity, PID efficiency correction and the energy loss correction.*

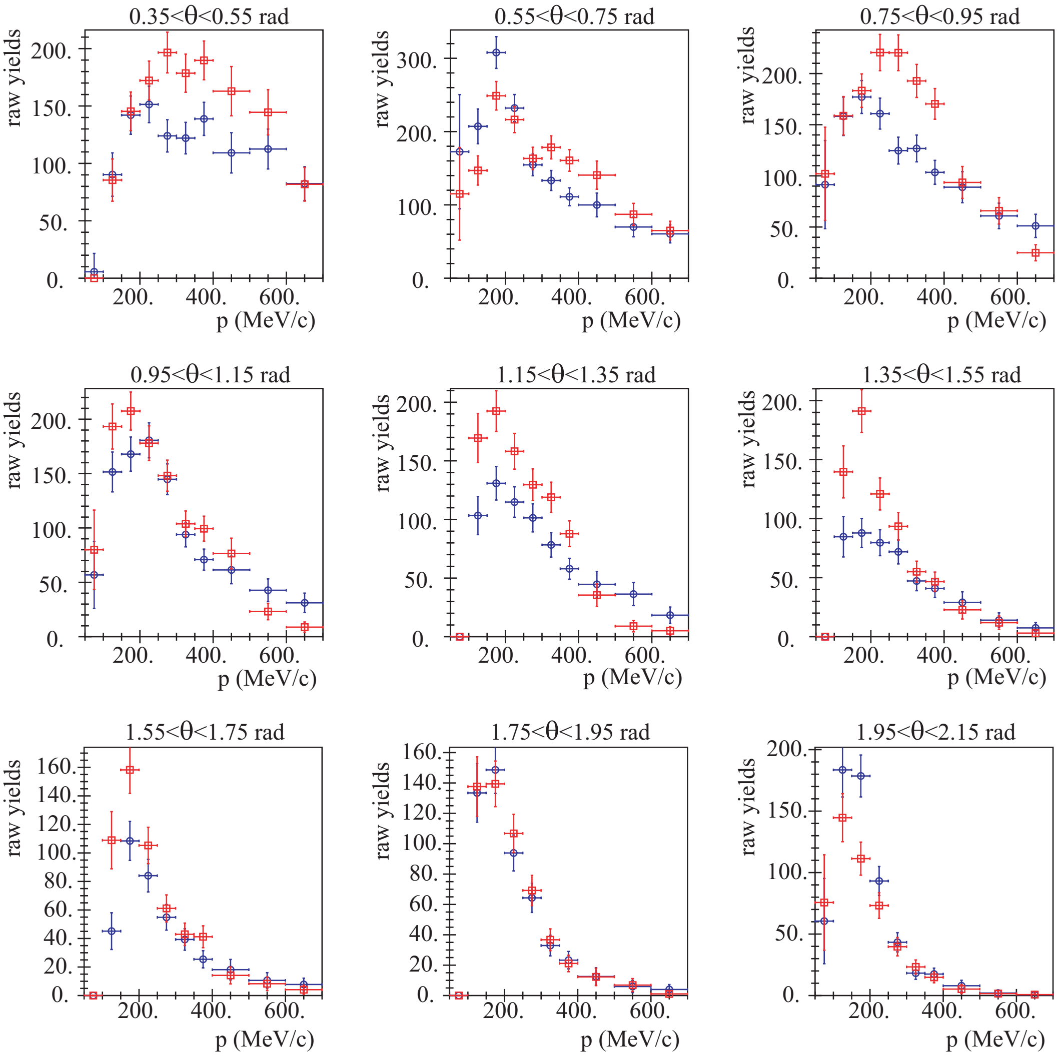

Figure 7.21: *The raw yields as function of total momentum and polar angle for positive (red squares) and negative pions (blue circles) after the analytical cut on dE/dx and the PID purity, PID efficiency correction, the energy loss correction and the total apparatus efficiency correction.*

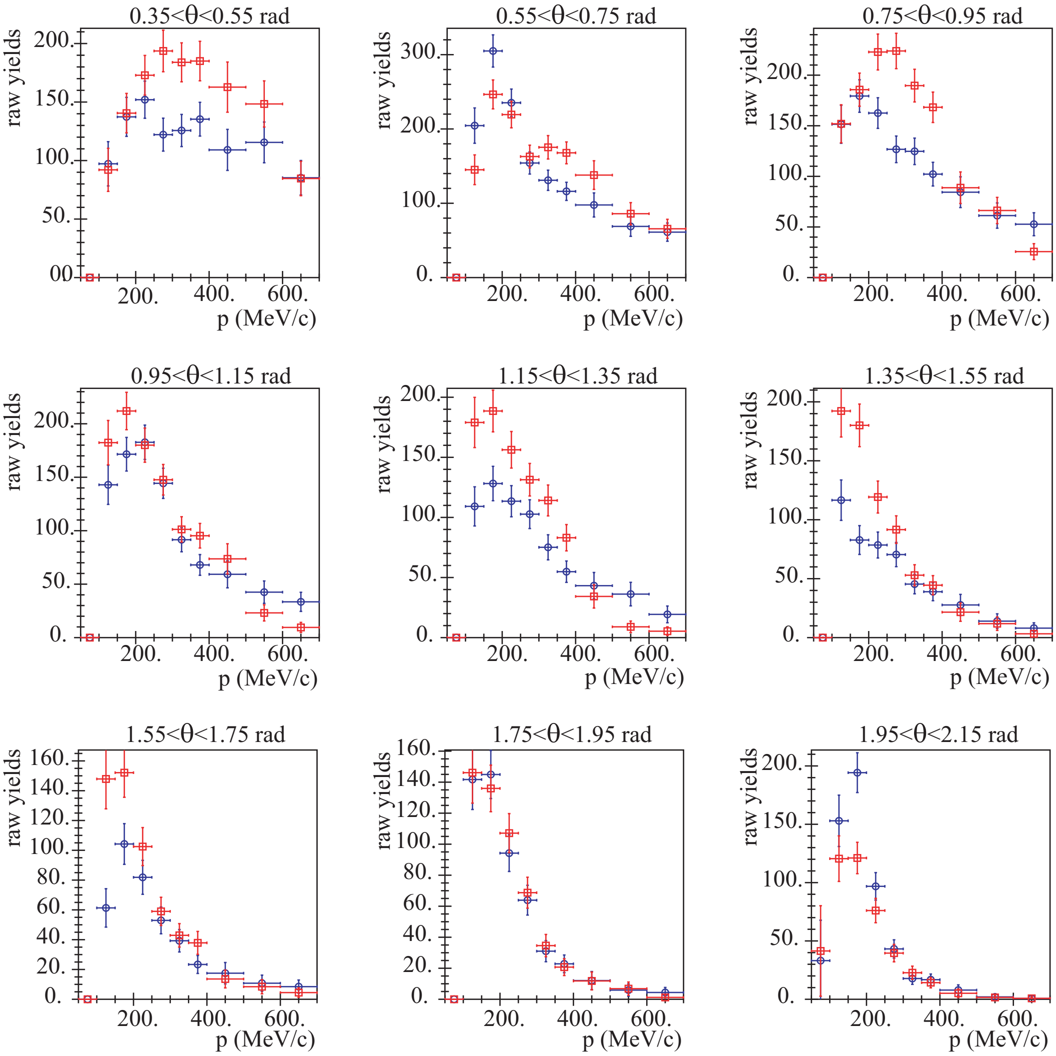

Figure 7.22: *The raw yields as function of total momentum and polar angle for positive (red squares) and negative pions (blue circles) after the analytical cut on dE/dx and the PID purity, PID efficiency correction, the energy loss correction, the total apparatus efficiency correction and with the bin migration corrections*

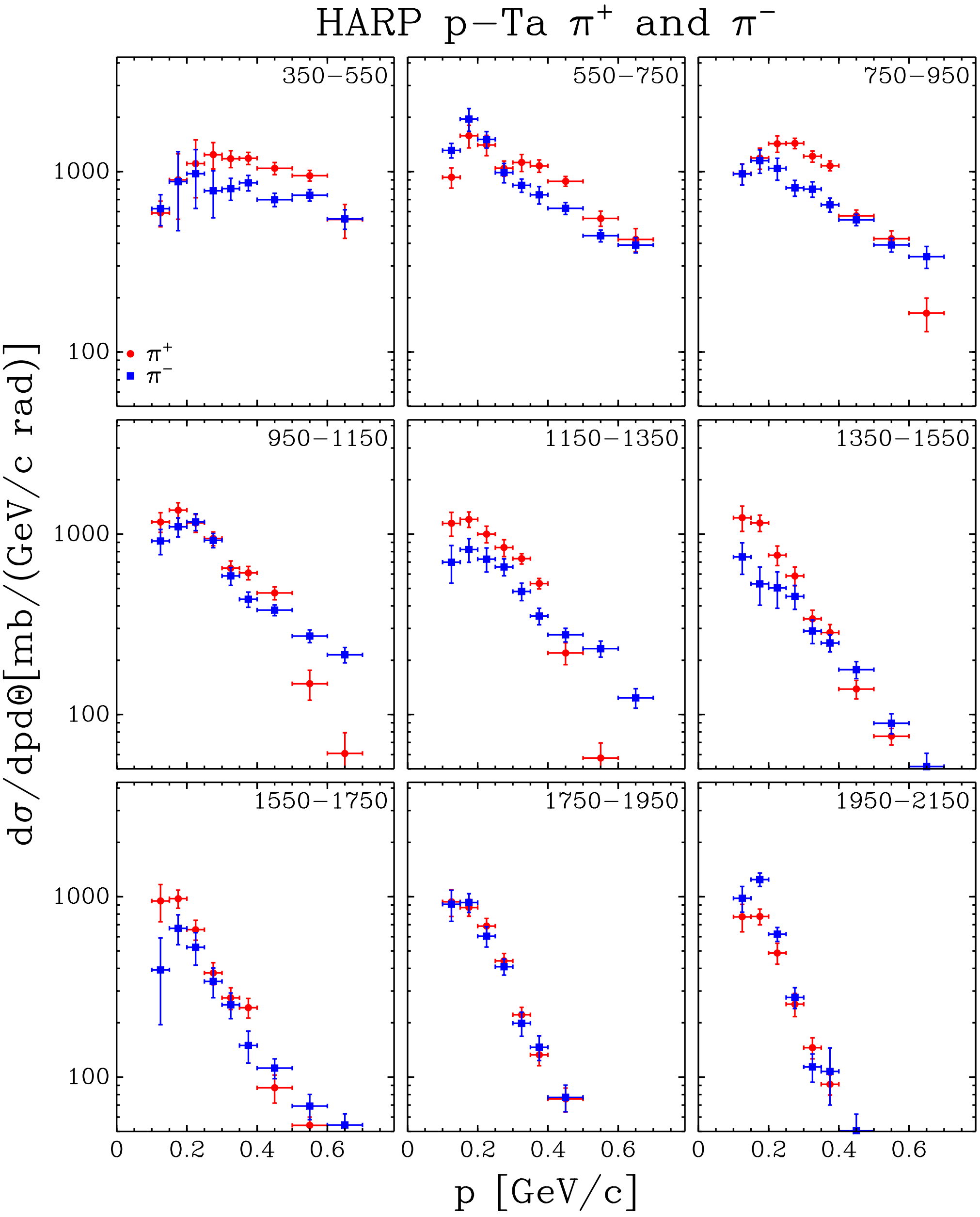

Figure 7.23: *The differential cross section as function of total momentum and polar angle for positive (red circles) and negative pions (blue squares), the error bars represents the statistical errors. The numbers in the insets correspond to the angular bins in mrad.*

7.6 Errors Evaluation

A first error analysis has been performed to evaluate the accuracy of the pion cross-section measurement. The impact of the error sources on the final cross-section measurement has been evaluated, both by analytical error propagation, and by Monte Carlo techniques. Correlation effects among different particle types, and among different (p, θ) bins, have also been taken into account. The main errors entering the measurement of the double differential cross section are listed below.

At first, the statistical uncertainties associated with the track yields measured from the tantalum target setting have been included in the pion production cross-section uncertainty estimates.

Then, several uncertainties associated with the corrections needed to convert the measured track yields to true track yields have been evaluated. The global efficiency includes the track reconstruction efficiency, as well as the correction to the pion and proton yields due to absorption or decay (as explained in section 7.4.3) computed via a Monte Carlo simulation. An uncertainty of 2% for pions has been estimated for this correction, in addition to the uncertainty due to the finite size of the simulated data sample used to compare this correction. Similarly, simulated data (and their associated uncertainties) were used to estimate the correction for the contamination in the sample due to tertiary particles that are not produced in the target, but rather by the decay of secondaries, or by the interaction of secondaries in the spectrometer material. The contribution of tertiary particles is only of 2-3%.

In addition the uncertainties associated with the particle identification of tracks, and with the corrections needed to convert yields of tracks identified as pions into true pion yields, have two sources: the electron-positron subtraction at low momenta and the protons subtraction at high momenta for positive particles. The dominant one is due to the electron subtraction that is about 10% at low momentum and negligible at higher momenta, above 300 MeV/c. The PID migration contribution, mainly for the protons contamination, is about 3-5% as function of the momentum (see section 7.4.1).

Finally, we have evaluated uncertainties associated with the momentum reconstruction performance, and with the corrections needed to convert the measured momenta into true momenta.

Concerning the momentum, biases and resolution effects are taken into account, using cosmic rays, the dE/dx method and the elastic scattering, as explained in sections 5.4 and 6.3.1. It was found that momentum biases do not exceed 5%. A momentum uncertainty is estimated to 10% for momentum below 150 MeV/c and less than 5% for higher momentum, while the angular uncertainty is less than 2%.

Table 7.3 shows the effect of the error sources on the differential cross section in different angle and momentum regions and also the averaged error in angular and momentum bins. The typical error on the double-differential cross-section is about 12.5%. The dominant error contributions arise from PID (5-14% as function of the momentum) and momentum scale (5-10% as function of the momentum). The overall systematic errors is between 6 and 12% as function of the momentum and of the angle, while the statistical error is about 8%.

7.7 Alternative analysis

A complementary analysis have been performed with the aim of checking internal consistency, and checking for possible biases in the respective procedures. This second analysis, called UFO (from UnFOlding), performs a simultaneous unfolding of p, θ and PID, with a correction matrix M^{-1} computed mainly using the Monte Carlo.

The UFO procedure uses an iterative Bayesian technique, described in [150], in order to unfold the measured distribution. The central assumption of the method is that the probability density function in the physical parameter (physical distribution) can be approximated by a histogram with bins of sufficiently small width. A population in the physical distribution of events in a given cell $ij\alpha$ generates a distribution in the measured variables, $M_{ij\alpha i'j'\alpha'}$, where the indices $ij\alpha$ indicate the binning in the physical angular, momentum and PID variables, respectively, and $i'j'\alpha'$ the binning in the measured variables. Thus the observed distribution in the measurements can be represented by a linear superposition of such populations. The task of the unfolding procedure is then redefined as finding the number of events in the physical bins for which the predicted superposition in the measurement space gives the best description of the data. The application of this unfolding method is described in [151].

In order to predict the population of the migration matrix element $M_{ij\alpha i'j'\alpha'}$, the resolution, efficiency and acceptance of the detector are obtained from the Monte Carlo. This is a reasonable approach, since the Monte Carlo simulation describes most of these quantities correctly. Where some deviations from the control samples measured from the data are found, the data are used to introduce small corrections to the Monte Carlo. The results of this alternative analysis are compatible with the results reported in section 7.5 within the quoted systematic errors. The results of the two analysis are compared in fig. 7.24. One observes good agreement between the two sets of spectra. Taking into account the large number of difference between the

Mom. range (MeV/c)	100-300			300-500			500-700			over all bins
Ang. range (rad)	0.35-0.95	0.95-1.55	1.55-2.15	0.35-0.95	0.95-1.55	1.55-2.15	0.35-0.95	0.95-1.55	1.55-2.15	Average error
Absorption	0.9%	1.8%	2.1%	0.5%	0.4%	0.3%	0.3%	0.1%	0.3%	0.6%
Tertiary	3.0%	4.3%	4.8%	2.4%	2.4%	1.4%	2.0%	0.8%	0.6%	3.1%
Target reg. cut	2.8%	0.5%	0.6%	1.7%	0.6%	0.4%	0.0%	0.9%	1.2%	2.2%
Efficiency	1.4%	1.7%	1.2%	1.0%	1.7%	1.9%	1.0%	2.7%	2.8%	1.5%
Electron subtr.	8.9%	2.1%	0.7%	1.1%	0.3%	0.2%	0.0%	0.0%	0.1%	5.7%
Particle ID	4.6%	4.1%	4.0%	1.6%	2.7%	3.7%	4.3%	3.0%	1.3%	3.8%
Mom. Res.	2.0%	1.4%	1.3%	0.5%	1.7%	2.1%	0.1%	0.9%	2.1%	2.3%
Mom. Scale	5.8%	4.2%	3.6%	2.8%	0.9%	4.6%	4.2%	8.5%	10.6%	5.4%
Angle bias	1.0%	0.8%	0.6%	0.1%	1.2%	0.5%	0.7%	1.8%	1.1%	1.4%
Tot. systematic	12.5%	8.2%	7.8%	4.7%	4.6%	6.7%	6.5%	9.6%	11.3%	12.5%
Statistical	4.8%	3.9%	4.8%	3.5%	4.8%	8.6%	3.9%	6.9%	16.1%	8.7%

Table 7.3: *Contributions to the experimental uncertainties. The numbers represent the uncertainty in percent of the cross-section integrated over the angle and momentum region indicated. The last column indicates the average uncertainties over all angle and momentum bins.*

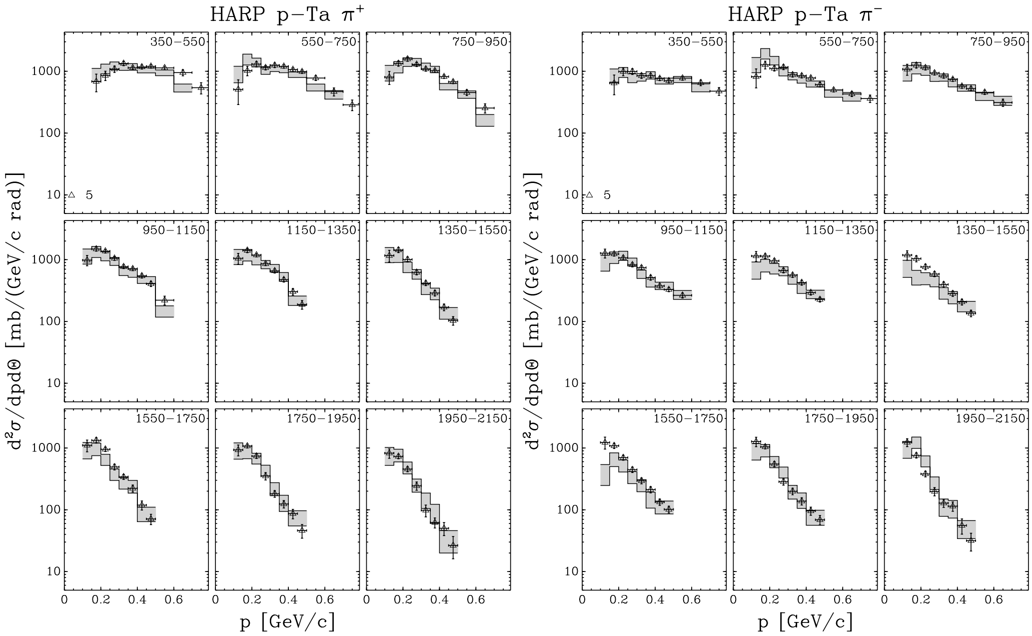

Figure 7.24: *The differential cross section as function of total momentum and polar angle (indicated in mrad) for positive (on the left) and negative pions (on the right). The results of UFO analysis are represented by the black points and the error bars represents the systematic and statistical errors. The results of the analysis described in section 7.4 are shown as shaded bands. The width of the bands represents the statistical and systematic errors.*

two approaches this constitutes an important cross-check of the correctness of the two analysis approaches.

7.8 Results

In the study of the particle production for a Neutrino Factory, the variables affecting the pion production are incident proton beam energy, target material and target geometry (diameter and length). The total proton beam power is only a scaling parameter. It was decided to analyse first a series of settings taken with a range of different beam momenta incident on a tantalum target. This allows to optimize the Neutrino Factory's design in order to achieve the highest number of potentially collected pions of both charge signs per unit of energy. The different settings have been taken within a short period so that in their comparison detector variations are minimized.

Here the measurement of the double differential cross section for $\pi^\pm$ production by protons of 3 GeV/c, 5 GeV/c, 8 GeV/c and 12 GeV/c momentum impinging on a thin Ta target of 5% nuclear interaction length (λ_I) is presented. Fig. 7.25 and 7.26 show the measurements of the double-differential cross-section for the production of positively and negatively charged pions in the laboratory system as function of the momentum and the polar angle for each incident beam momentum. The error bars represent the combined statistical and systematic error. Correlations cannot be shown in the figures. The errors shown are the square roots of the diagonal elements in the covariance matrix. The measurements for the different beam momenta are overlaid in the same figure.

The increase of the pion yield per proton is visible in addition to a change of spectrum towards higher momentum of the secondaries produced by higher momentum beams in the forward direction. Also an asymmetry between π^+ and π^- is observed at relatively small angles with the beam in favour of a higher π^+ rate. At very large angles from the beam the spectra of π^+ and π^- are symmetric within errors. At the higher incoming beam momenta one observes that the number of π^+'s produced is smaller than the number of π^-s in the lowest momentum bin (100 MeV/c - 150 MeV/c). Since this effect is not present at the lower incoming beam momenta and the effect is already visible in the raw spectra one concludes that this effect is significant.

To better visualize the trend of the hardening of the spectrum with incoming beam momentum, the same data integrated over the forward angular range (0.35 rad$< \theta <$1.55 rad) are shown separately for π^+ and π^- in fig. 7.27. It is shown that the pion yield increases nearly linearly with momentum and that in our kinematic coverage the optimum yield is between 5 GeV/c and 8 GeV/c. However, these calculations should be completed with more realistic kinematical cuts in the integration.

Of course this analysis only gives a simplified picture of the results. One should note that the best result can be obtained by using the full information of the double differential cross section and by developing designs optimized specifically for each single beam momentum. Then these optimized designs can be compared.

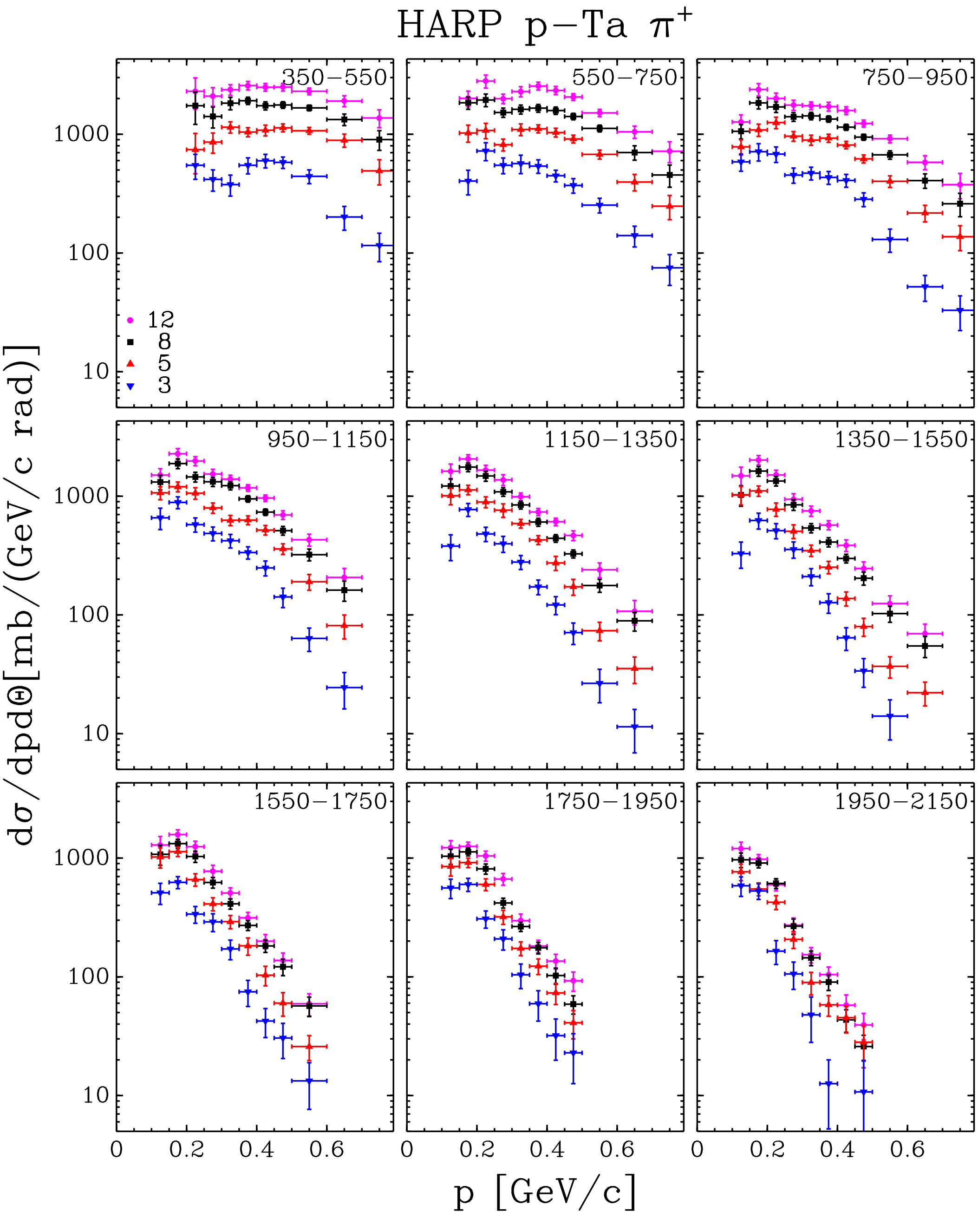

Figure 7.25: *The double differential cross section as function of total momentum and polar angle (indicated in mrad) for positive pions, the error bars represents the statistical and systematic errors. The results are given for all incident beam momenta (blue: 3 GeV/c, red: 5 GeV/c, black: 8 GeV/c, pink: 12 GeV/c).*

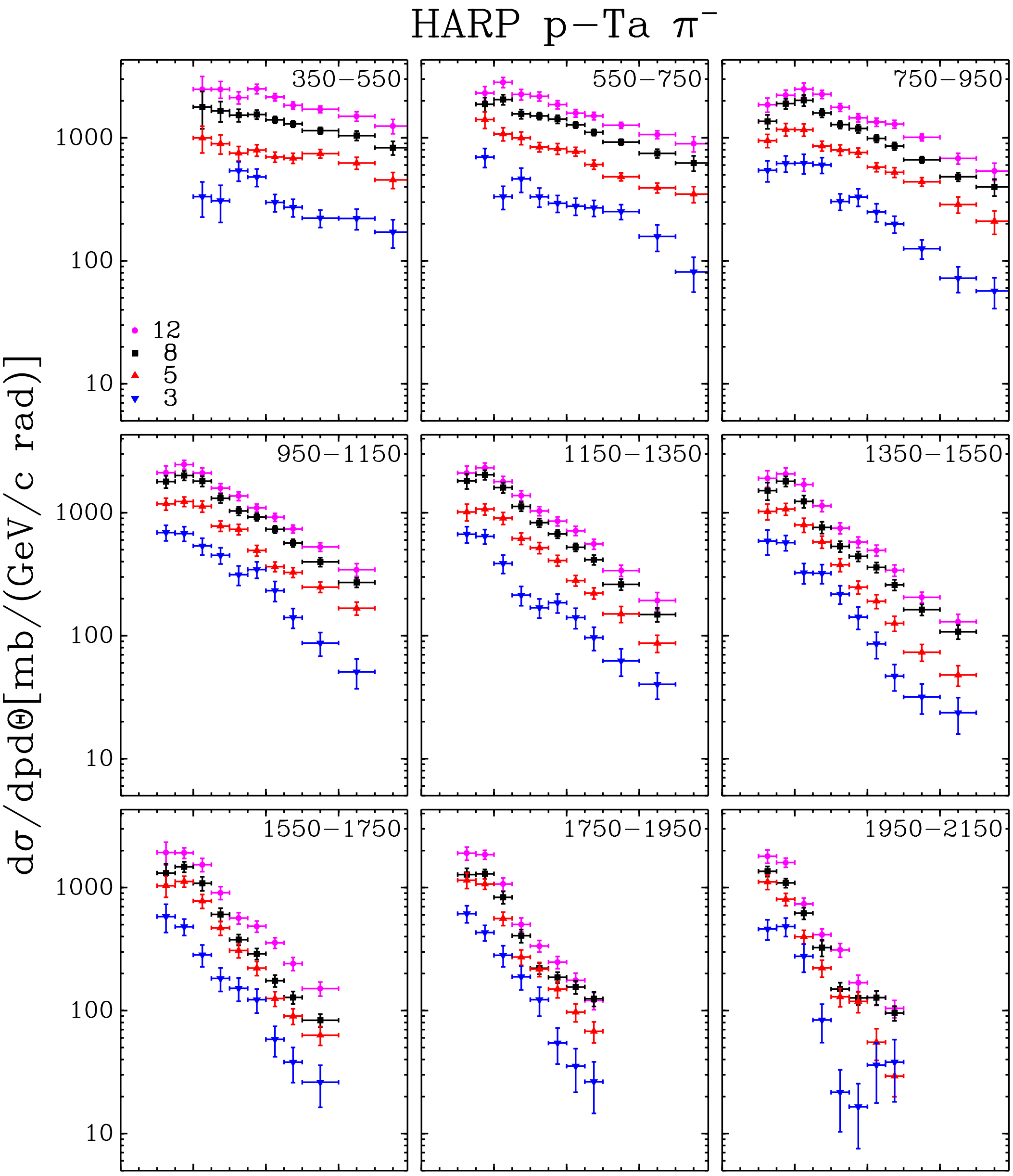

Figure 7.26: *The double differential cross section as function of total momentum and polar angle (indicated in mrad) for negative pions, the error bars represents the statistical and systematic errors. The results are given for all incident beam momenta (blue: 3 GeV/c, red: 5 GeV/c, black: 8 GeV/c, pink: 12 GeV/c).*

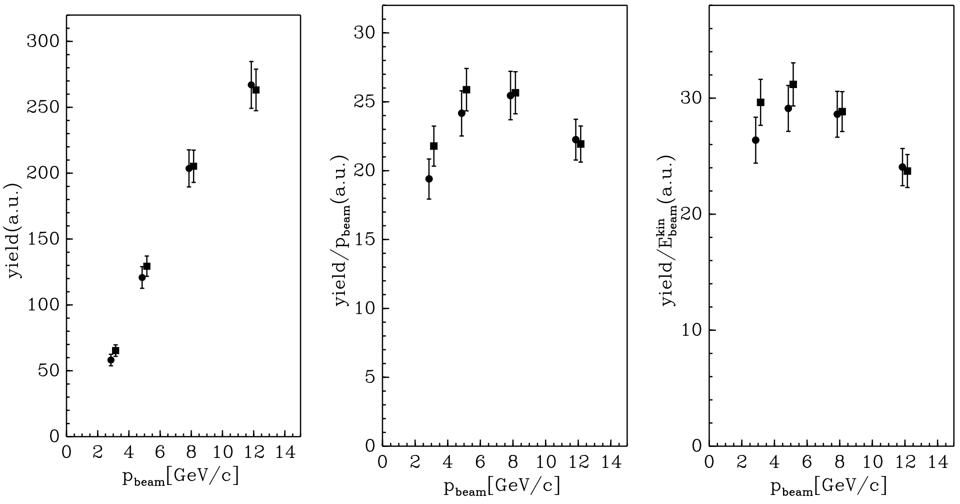

Figure 7.27: *Prediction of the* π^+ *(filled squares) and* π^- *(filled circles) yield integrated over 0.35 rad<* θ *<1.55 rad as a function of incident proton beam momentum for different designs of the neutrino factory focusing stage. Showns are the integrated yields (left), the integrated yields normalized to the total momentum (center) and the integrated yields normalized to the kinetic energy (right). The full error bar shows the overall (systematic and statistical) error.*

7.9 Conclusions

This analysis describes the production of positive and negative pions at large angles (0.35 rad $\leq \theta \leq$ 2.15 rad) with respect to the beam direction for protons of 3 GeV/c, 5 GeV/c, 8 GeV/c and 12 GeV/c impinging on a thin (5% interaction length, 5.6 mm) tantalum target. The secondary pions yield was measured in a large angular and momentum range and double-differential cross-sections were obtained.

The use of a detector such as the HARP TPC for a range of beam momenta makes possible to measure the pion yields as a function of beam momentum with high precision. These data will be used to make predictions for the optimized design of a future Neutrino Factory.

Appendix A

Fit error flag

Four error flags [152] are defined:

-900 is associated to tracks with less than 6 distinguishible points in xy plane. One distinguishes two points in xy plane if they belong to different rows or if they belong to the same row and have a distance larger than 2.4 mm*. As example very forward tracks could have 6 or more points in space, but in the track projection on the xy plane they may not be distinguishible. In particular if the number of distinguishible points is less than 3 no cicle fit can be applied. The request of 6 points allows to perform two indipendent circle fits and to estimate the accuracy of the results.

-800 is associated to tracks crossing less than 3 rows. The radial position of points is discrete, so if a track crosses few rows the circle fit result is strongly biased by this discrete coordinate. The tracks crossing less than 3 rows have an angle with respect to the beam smaller than 4.95^o or a transverse momentum smaller than 3.25 MeV/c.

-700 is associated to tracks with a large transverse momentum. The domain of transverse momentum is limited by the TPC physical dimensions and by the point resolution. The fit cannot give a good estimation of the curvature for the tracks with large radius (used to evaluate the transverse momentum). The maximum radius that the fit can evaluate with a resolution of 4.8 mm (corrispending to 2 sigma of residual distribution) is 9.09 m which corresponds to a maximum transverse momentum of 1.9 GeV/c. This is true for a track that crosses completely the TPC from the 1st row to the 20th row (see fig. A.1). If a

---

[*] This distance is the sigma of a Gaussian fit for the residual distribution in azimuthal direction.

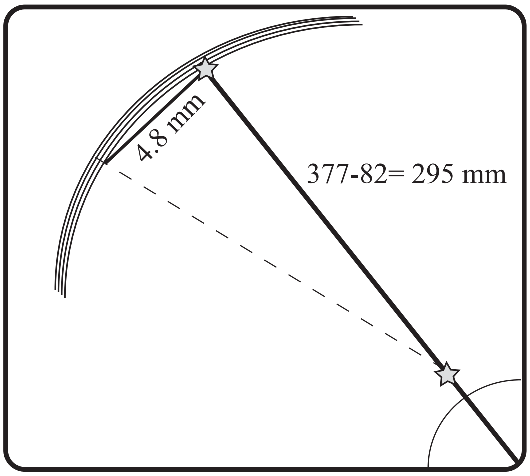

Figure A.1: *The track with maximum radius passes for the two points in the 1st and 20th row and is tangent to the dashed straightline. The distance 4.8 mm is two times the sigma of residuals distribution and it is taken as resolution estimator of our TPC*

track has a smaller length the maximum transverse momentum will be smaller. For example if a track contains only 6 points in consecutive rows (minimum track-length), it has a length of about 178 mm, and the sensitive maximum radius is 0.96 m corresponding to a maximum transverse momentum of 202 MeV/c.

-600 is associated to the tracks that have small radius. In this case the circle fit is affected by the discrete radial distribution of points if the tracks do not cross at least 4 rows: This correspond to a minimum radius of 62 mm and minimum transverse momentum of 13 MeV/c.

The table A.1 summarises the flag definition and it shows the statistics, which are calculated on 54000 events with target Ta thin (5 % λ_I) with a beam line setup at 3 GeV/c.

Error Flag	**Definition**	**All tracks: no cuts**	**Tracks: $\geq$ 12pnts**	**Tracks: $\geq$ 12pnts 0.35< θ <2.09 rad**
0	no error flag associated to the fit	87.8 %	93.5 %	96.55 %
-900	$\leq$ 5 points in xy plane	3.0 %	0.6 %	0.03 %
-800	points lies on too few rows ($\leq$ 3)	3.7 %	1.4 %	0.05 %
-700	too straight line $p_t > 1.9\,GeV/c$	3.1 %	3.1 %	3.28 %
-600	radius too small $p_t < 13\,MeV/c$	2.4 %	1.4 %	0.02 %

Table A.1: *This table summarises the relative population of tracks associated to different error flags. The* 3^{rd} *column gives the statistics for all track candidates found by the pattern reconignition; the* 4^{th} *column gives the statistics for all tracks requiring at least 12 points; and the* 5^{th} *columns gives the statistics requiring also the large angle acceptance (0.35 rad<* θ *<2.09 rad). A sample of 54000 events with target Ta thin (5 %* λ_I*) with a beam line setup at 3 GeV/c was used to evaluate them.*

Appendix B

Helix formulas

Coordinate of circle centre

$$\begin{cases} x_{centre} = a = sign(R) \left(\frac{1}{|\rho|} - d_0 \right) \sin\phi_0 \\ y_{centre} = b = -sign(R) \left(\frac{1}{|\rho|} - d_0 \right) \cos\phi_0 \end{cases} \tag{B.1}$$

Coordinate of impact point

$$\begin{cases} x_{impactpoint} = x_{d_0} = -sign(R)\, d_0\, \sin\phi_0 \\ y_{impactpoint} = y_{d_0} = sign(R)\, d_0\, \cos\phi_0 \\ z_{impactpoint} = z_0 \end{cases} \tag{B.2}$$

Coordinate of a point on the helix

$$\begin{cases} x = a + \frac{1}{|\rho|}\, \cos(\phi) = -sign(R)\, d_0\, \sin\phi_0 + \frac{1}{\rho}\, \sin(\phi_0 + \Delta\psi) \\ y = b + \frac{1}{|\rho|}\, \sin(\phi) = sign(R)\, d_0\, \cos\phi_0 + \frac{1}{\rho}\, \cos(\phi_0 + \Delta\psi) \\ z = z_0 - \tan(\lambda)\, \frac{1}{\rho}\, \Delta\psi \end{cases} \tag{B.3}$$

The momentum in a point on the helix

$$\begin{cases} p_x = p_t \cos(\phi_0 - sign(R)\, \Delta\psi) \\ p_y = p_t \sin(\phi_0 - sign(R)\, \Delta\psi) \\ p_z = p_t \tan(\lambda) \end{cases} \tag{B.4}$$

The meaning of variables:

- $sign(R)$ is the sign of the radius ($R = 1/\rho$) that is positive if the direction associated to the track is clockwise and negative if it is anti-clockwise.
- d_0 is the impact parameter in the xy plane, i.e. the minimum distance between the track and the z-beam axis in xy plane. The sign associate to it indicates if the helix encircles the z-beam axis (positive sign) or not (negative sign).

- ϕ_0 is the emission angle in the xy plane at the impact point, i.e. the angle between the x axis and the oriented tangent (the tangent direction is given by the sign of ρ) to the track at the impact point.
- z_0 is the z coordinate of the impact point.
- $\Delta\psi$ is the angle between the point and the impact point in the plane xy with respect to the centre of track circle; for tracks that turn less than 2π it is positive if the point belongs to the semicircle outgoing the impact point and negative if it belongs to the other semicircle.

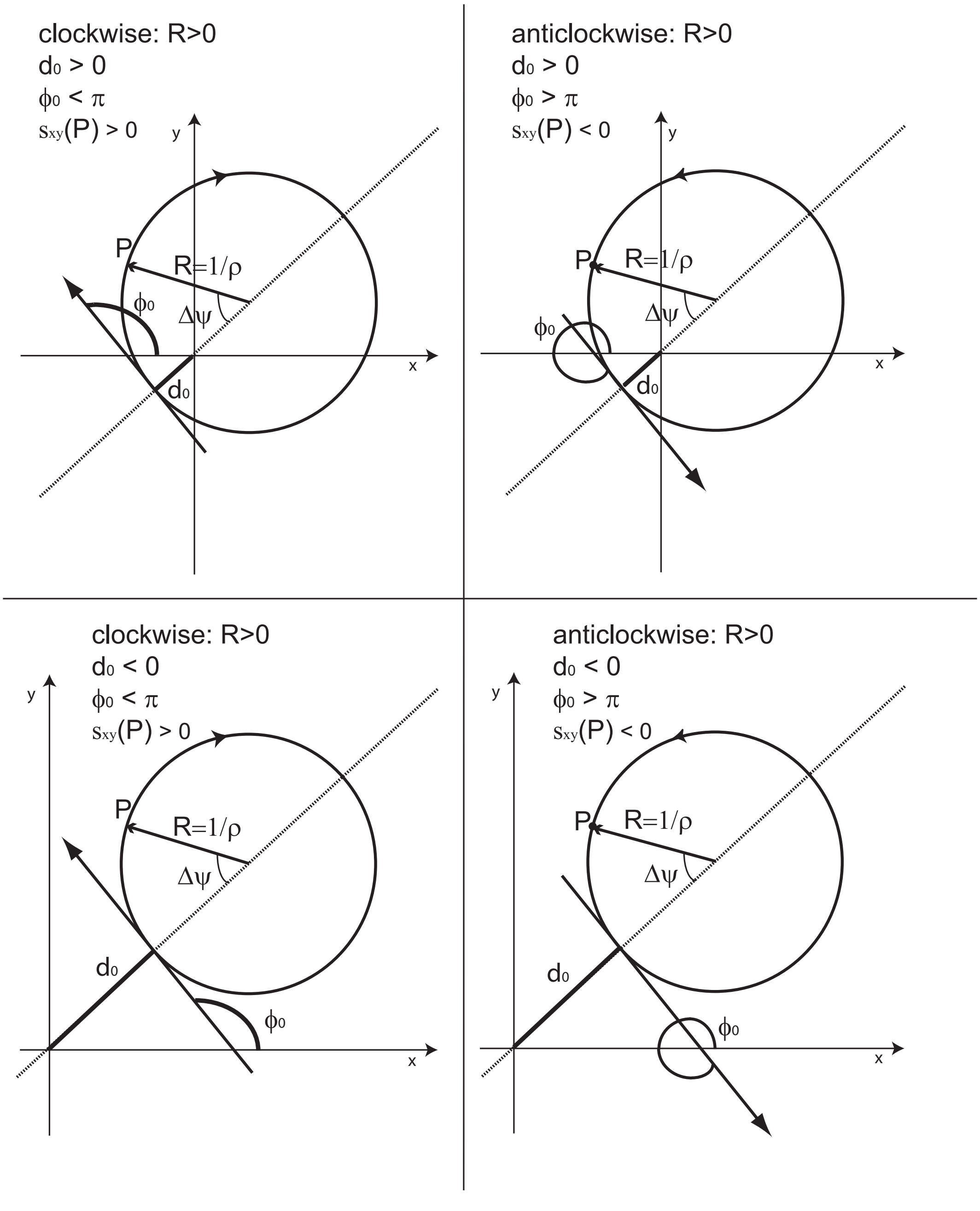

Figure B.1: *Track parameters in xy plane for* $a > 0$ *and* $b > 0$.

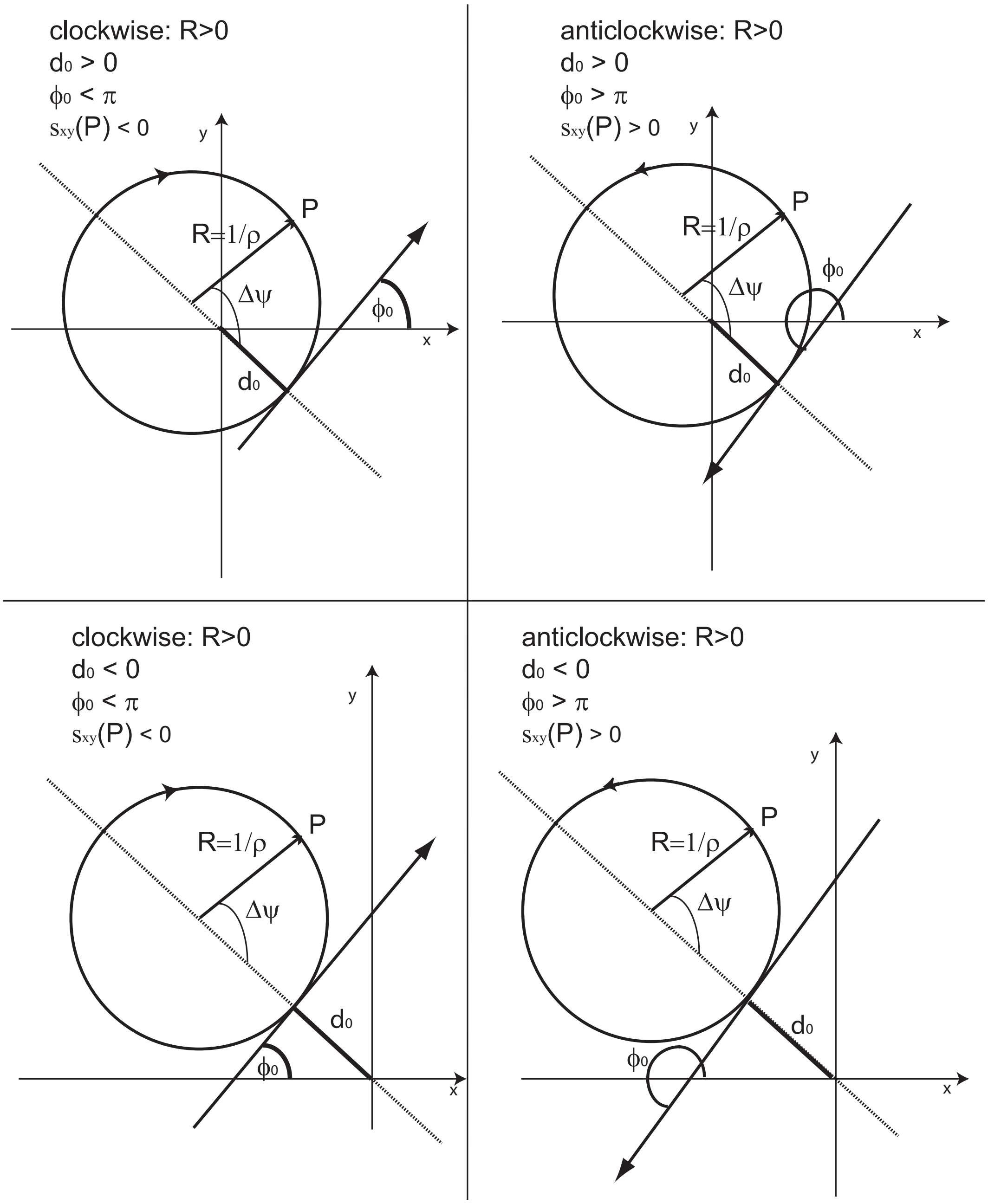

Figure B.2: *Track parameters in xy plane for $a < 0$ and $b > 0$.*

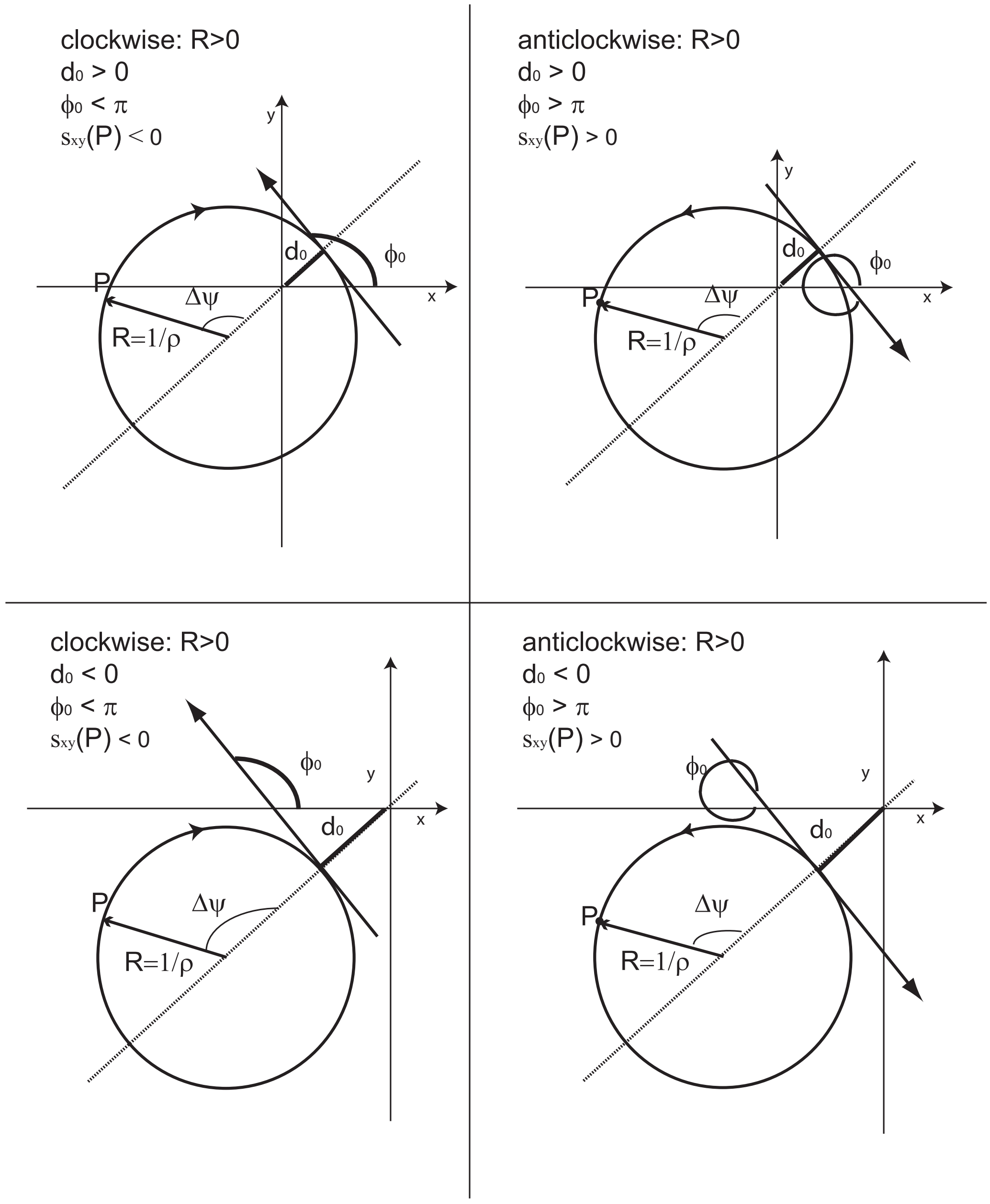

Figure B.3: *Track parameters in xy plane for $a < 0$ and $b < 0$.*

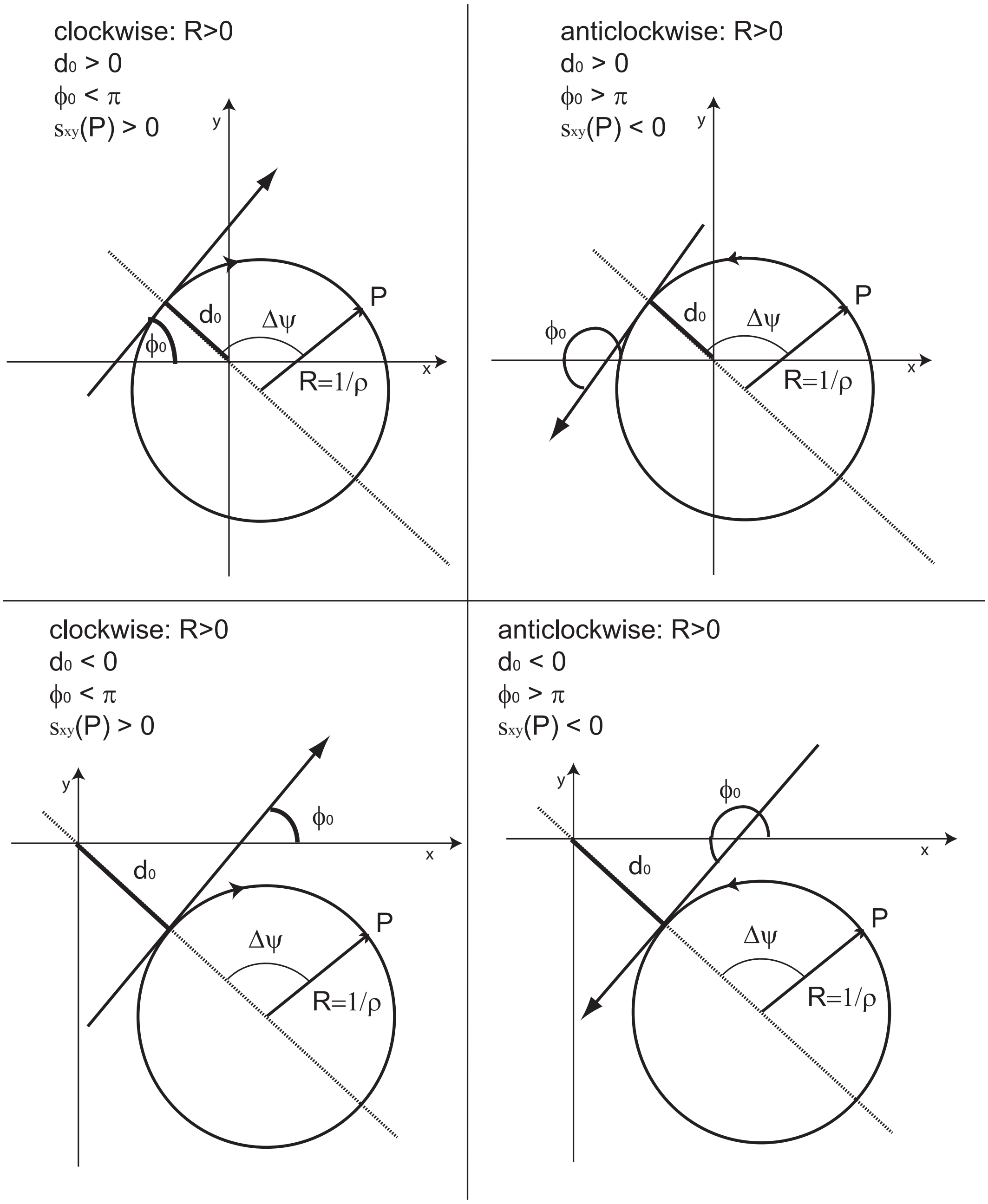

Figure B.4: *Track parameters in xy plane for $a > 0$ and $b < 0$.*

Appendix C

2003 Time Calibration

The cosmic data recorded during 2003 used as trigger a scintillator detector placed along the beam axis (-380 mm < z < 230 mm).

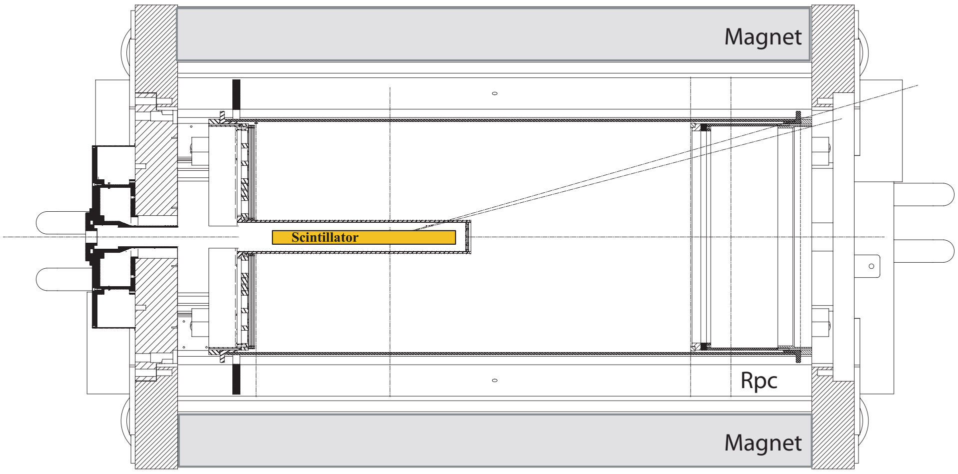

Figure C.1: *Drawing of HARP TPC and the scintillator used as trigger in data recorded during 2003.*

During the data taking of 2003 the tdc_{out} and tdc_{in} values were not stored. The $(tdc_{out} - tdc_{in})$ was measured as 3.62 μs (with a jitter of ±50 ns). The delay between the PMT setup and the system data taking is 3.88 μs with a jitter of ±50 ns. This value is stored in a calibration file dedicated to 2003 data and all measured time bins should be therefore corrected by the following time calibration:

$$time = time_{meas} - 1.6\mu s + \Delta time0 \tag{C.1}$$

where Δtime0 is the measured time of 3.88 μs.

For these data we use the current value of the drift velocity (5.17 cm/μs), taking a conservative 4% error that represents the maximum spread of the drift velocity for the considered settings.

List of Figures

List of Tables

Bibliography

[1] W. Pauli, *Zur lateren und neueren Geschichte des Neutrinos*, in Col- lected Scientific Papers, ed. By R. Kronig and V. F. Weisskopf (Inter- science, New York), volume 2, p.1313 (1964)

[2] J. Chadwick, *Possible Existence of a Neutron*, Nature, p. 312 (1932)

[3] F. Reines et al., Science 124, 103 (1956)

[4] R. Davis et al., *Search for Neutrinos from the Sun*, Phys. Rev. Lett. 20, 1205 (1968)

[5] J. N. Bahcall et al., *Present Status of the Theoretical PRediction for the* ^{36}*Cl Solar-Neutrino Experiment*, Phys. Rev. Lett. 20, 1209 (1968)

[6] Y. Fukuda et al. [Super-K Collaboration], Phys. Rev. Lett. 81, 1562 (1998)

[7] M. H. Ahn et al. [K2K Collaboration], Phys. Rev. Lett. 90, (2003)

[8] E. Aliu et al. [K2K Collaboration], Phys. Rev. Lett. 94, (2005)

[9] Q. R. Ahmad et al. [SNO Collaboration], Phys. Rev. Lett. 89, (2002)

[10] K. Eguchi et al. [Kamland Collaboration],Phys. Rev. Lett. 90, (2003)

[11] B. Aharmim et al. [SNO Collaboration], nucl-ex/0502021

[12] A. Aguilar et al. [LSND Collaboration], Phys. Rev. D64, (2001)

[13] B. Armbruster et al. [KARMEN Collaboration], Phys. Rev. D65, (2002)

[14] ISIS a world centre for condensed matter science with neutrons & muons at the UK Rutherford Appleton Laboratory, http://www.isis.rl.ac.uk/

[15] J. Wolf [KARMEN Collaboration], Prepared for International Europhysics Conference on High- Energy Physics (HEP 2001)

[16] E. Church et al. [MiniBooNE Collaboration], nucl-ex/9706011; LAUR-97-2120, (1997)

[17] D. Decamp et al., *Determination of the number of Light Neutrino Species*, Physics Letters B, 231, 519 (1989)

[18] S. A. Bludman et al., Nucl. Phys. B374, 373 (1992) and Phys. Rev. D45, 1810 (1992)

[19] Fukugita and Yanagida, Phys. Lett. B174, 45 (1986)

[20] V. Tretyak, Y. Zdesenko, *Tables of double beta decay data*, At. Data Nucl. Data Tables 80 (2002)

[21] S.R. Elliott, P. Vogel, *Double Beta Decay*, Ann. Rev. Nucl. Part. Sci. 52 (2002)

[22] E. Nardi et al. *On Higgs and sphaleron effects during the leptogenesis era*, J. High Energy Phys. 01, 068 (2006)

[23] B. Pontecorvo, J.E.T.P. 33, 429 (1957), B. Pontecorvo, J.E.T.P. 34, 172 (1958)

[24] B. Kayser, hep-ph/0104147

[25] : C. Jarlskog, *Commutator of the Quark Mass Matrices in the Standard Electroweak Model and a Measure of Maximal CP Nonconservation*, Phys. Rev. Lett. 55, 1039 (1985)

[26] L. Wolfenstein, Phys. Rev. D17, 2369 (1978); D20, 2634 (1979); S. P. Mikheyev and A. Yu. Smirnov, Yad. Fiz. 42, 1441 (1985) [Sov. J. Nucl. Phys. 42, 913 (1985)]; Nuovo Cimento 9C, 17 (1986).

[27] C. Weinheimer, *Direct neutrino mass experiments: Present and future*, Nucl. Phys. Proc. Suppl. 118, 279 (2003)

[28] V. M. Lobashev et al., *Direct search for neutrino mass and anomaly in the tritium beta-spectrum: Status of 'Troitsk neutrino mass' experiment*, Nucl. Phys. Proc. Suppl. 91, 280 (2001) V. M. Lobashev, proceeding of Neutrino Telescopes 2005, (2005)

[29] KATRIN Coll., hep-ex/0109033.

[30] A. Monfardini et al., arXiv:hep-ex/0509038. *The microcalorimeter arrays for a rhenium experiment (MARE): A next-generation calorimetric neutrino mass experiment*,

[31] For a recent review see: M. Fukugita, *Massive neutrinos in cosmology*, arXiv:hep-ph/0511068.

[32] M.D. Messier *Review of Neutrino Oscillations Experiments*, hep-ex/0606013

[33] M. Apollonio et al., Eur. Phys. J., C 27, 331 (2003)

[34] A. Guglielmi et al., *Measurement of three-family neutrino mixing and search for CP violation*, arXiv:hep-ph/0508034

[35] M.H. Ahn et al. [K2K Collaboration], Phys. Rev. Lett. 90, 21802 (2003)

[36] E. Ables et al. [MINOS Collaboration], *P-875: A Long baseline neutrino oscillation experiment at Fermilab*, Fermilab-proposal-0875; G. S. Tzanakos [MINOS Collaboration], *MINOS status and physics goals*, AIP Conf. Proc. 721, 179 (2004).

[37] The Fermilab NuMI Group, *NumI Facility Technical Design Report*, Fermilab Report NuMI-346, 1998.

[38] OPERA Collaboration, CERN-SPSC-P-318, LNGS-P25-00; H. Pessard [OPERA Collaboration], arXiv:hep-ex/0504033 M. Guler et al. [OPERA Collaboration], *OPERA: An appearance experiment to search for* $\nu_\mu \to \nu_\tau$ *oscillations in the CNGS beam. Experimental proposal*, CERN-SPSC-2000-028.

[39] G. Acquistapace et al., *The CERN neutrino beam to Gran Sasso*, CERN 98-02, INFN/AE-98/05 (1998); CERN-SL/99-034(DI), INFN/AE-99/05 Addendum.

[40] H. W. Atherton et al., *Precise measurements of particle production by 400 GeV/c protons on Beryllium targets*, CERN-80-07

[41] G. Ambrosini et al. [NA56/SPY Collaboration], *Measurement of charged particle production from 450-GeV/c protons on beryllium*, Eur. Phys. J. C 10, 605 (1999)

[42] M.H. Ahn et al. [K2K Collaboration], *Measurement of Neutrino Oscillation by the K2K Experiment* hep-ex/0606032, Submitted to: Phys. Rev. D (2006)

[43] F. Ardellier et al. [Double-CHOOZ Collaboration], arXiv:hep-ex/0405032.

[44] P. Huber et al. *From Double Chooz to Triple Chooz: Neutrino physics at the Chooz reactor complex*, arXiv:hep-ph/0601266.

[45] Y. Itow et al., *The JHF-Kamiokande neutrino project*, arXiv:hep-ex/0106019.

[46] H. Minakata, M. Sonoyama and H. Sugiyama, Phys.Rev.D70:113012,2004; hep-ph/0406073. A. Donini, D. Meloni and S. Rigolin, hep-ph/0506100.

[47] A. Donini, E. Fernandez-Martinez, D. Meloni and S. Rigolin, arXiv:hep-ph/0512038.

[48] D. S. Ayres *et al.* [NOvA Collaboration], *NOvA proposal to build a 30-kiloton off-axis detector to study neutrino oscillations in the Fermilab NuMI beamline*, arXiv:hep-ex/0503053.

[49] P. Zucchelli, *A novel concept for a anti-nu/e / nu/e neutrino factory: The beta beam*, Phys. Lett. B 532, 166 (2002)

[50] J. J. Gomez-Cadenas et al., *Physics potential of very intense conventional neutrino beams*, Proceedings of “Venice 2001, Neutrino telescopes”, vol. 2*, 463-481, arXiv:hep-ph/0105297. A. Blondel et al., *Superbeam studies at CERN*, Nucl. Instrum. Meth. A 503, 173 (2001) M. Mezzetto, J. Phys. G 29, 1771 (2003), [arXiv:hep-ex/0302005].

[51] J. E. Campagne and A. Cazes, *The theta(13) and delta(CP) sensitivities of the SPL-Frejus project revisited*, arXiv:hep-ex/0411062.

[52] S. Gilardoni et al, AIP Conf. Proc. 721, 334 (2004)

[53] A. Blondel et al, CERN-NUFACT-Note-78 (2001)

[54] M.G Catanesi et al., *Proposal to study hadron production for the neutrino factory and for the atmospheric neutrino flux*, CERN-SPSC/99-35, (1999)

[55] M. Mezzetto, *SPL and beta beams to the Frejus*, Nucl. Phys. Proc. Suppl. 149, 179 (2005)

[56] J.E. Campagne, hep-ex/0511005.

[57] M. Apollonio et al., *Oscillation physics with a neutrino factory. ((G)) ((U))*, arXiv:hep-ph/0210192.

[58] A. Cervera et al, Nucl.Phys.B579:17-55,2000, Erratum-ibid.B593:731-732,2001; hep-ph/0002108

[59] J. Burguet-Castell et al., *On the measurement of leptonic CP violation*, Nucl. Phys. B 608, 301 (2001) [arXiv:hep-ph/0103258].

[60] P. Huber and W. Winter; Phys. Rev. D68, 037301(2003); hep/ph-0301257.

[61] A. Blondel et al., *Future neutrino oscillation facilities*, hep-ph/0606111 (2006);

[62] *Internation Scoping Study Interim Report*, ISS/2006/01 (2006), http://www.hep.ph.ic.ac.uk/iss/iss-notes/catalogue.html

[63] S. Ozaki et al., *Feasibility Study-II of a Muon-Based Netrino Source*, ed., BNL-52623 (2001)

[64] A. Heikkinen et al., *Bertini intranuclear cascade implementation in Geant4*, Proc. Computing in High Energy and Nuclear Physics, MOMT008 (2003)

[65] G. Folger et al., *The binary cascade*, Eur. Phys. J. A., vol. 21, pp. 407-417, 2004.

[66] M. Kossov, *Simulation of antiproton-nuclear annihilation at rest*, IEEE NSS-MIC 2004 - pages 1829-1830 (2004)

[67] Dennis Wright, talk at SPENVIS & Geant4 Space Users' Workshop Leuven, Belgium (2005)

[68] J. Ranft, Phys. Rev., D51, 64 (1995); Gran Sasso report INFN/AE-97/45 (1997)

[69] G. Folger,J.P. Wellisch, *String Parton Models in Geant4*, nucl-th/0306007;Geneva CERN, (2003)

[70] V.V. Uzhinskii, JINR-E2-96-192, Dubna (1996)

[71] J.V. Allaby et al., CERN 70-12 (1970)

[72] T. Eichten et al., Nucl. Phys., B44, 333 (1972)

[73] G.Ambrosini et al., Eur Phys. J., C10, 605-627 (1999)

[74] I. Chemakin et al., nucl-ex/9902009

[75] Y. Fisyak et al., FERMILAB-PROPOSAL-P-907

[76] . J. Pasternak et al. *Pion production at low energies* Nucl. Instrum. Methods Phys. Res., A 472, 557-560 (2001)

[77] A. Ferrari, P.R. Sala, The physics of high energy reactions, in: Proceedings of the Workshop on Nuclear Reaction Data and Nuclear Reactors Physics, Design and Safety, (1996)

[78] S.A. Bass et al.Prog. Part. Nucl. Phys. 41, 255 (1998)

[79] N.V. Mokhov, *The MARS Code System User Guide*, Version13(95), Fermilab-FN-628 (1995)

[80] J. Collot, H. G. Kirk and N. V. Mokhov *Pion production models and neutrino factories* Nucl. Instrum. Methods Phys. Res., A 451, 327-330 (2000)

[81] M.G. Catanesi et al. [HARP Collaboration], *Measurement of the production cross-section of positive pions in p–Al collisions at 12.9 GeV/c*, Nucl. Phys. B 732, 1 (2006)

[82] J.R. Sanford and C.L. Wang, *Empirical formulas for particle production in p-Be collisions between 10 and 35 GeV/C*, Brookhaven National Laboratory, AGS internal report, (1967) (*unpublished*)

[83] A. Dell'Acqua et al., GEANT4 Collaboration,

Nucl. Instrum. Meth. A 506, 250 (2003)

[84] M.G. Catanesi et al. [HARP Collaboration], *Measurement of the production cross-section of positive pions in collisions of 8.9 GeV/c protons on beryllium*, paper in preparation (2006)

[85] J. Link, Columbia University, *Pion production by protons on a Be target at 6.4, 12.3 and 17.5 GeV/c*,paper in preparation (2006)

[86] V.D. Barger, et al., PRD63 113011 (2001)

[87] C.R. Prior et al., *Synchrotron-based proton drivers for a neutrino factory*, Proceedings of EPAC (2000)

[88] K. Pretzl et al., Invited talk at the International Symposium on Strangeness and Quark Matter, (1999)

[89] http://www.ansoft.com/products/em/max3d/

[90] R. Veenhof, *Simulation of gaseous detectors*, http://consult.cern.ch/writeup/garfield

[91] OPERA, 3D version, Vector Fields Limited, Oxford, England

[92] J. Baechler et al., *Front-End electronics for the ALICE TPC detector*, CERN-ALI-98-022, 16 Oct 1998.

[93] ALICE Collaboration, *Technical design report of the Time Projection Chamber*, CERN-LHCC-2000-001, 2000.

[94] NA45/CERES Collaboration, Status of the NA45/CERES experiment and plans for 2000, CERN-SPSC-2000-009, 26 Mar 2000.

[95] V. Ammosov et al., *Four-gap glass RPC as a candidate to a large area thin time-of-flight detector*, arXiv:hep-ex/0204022;
V. Ammosov et al. *Comparison of timing properties of glass multigap RPCs with 0.3-mm and 0.6-mm subgap width*, arXiv:hep-ex/0205061.

[96] M. Bogomilov et al., Nucl. Instrum. Methods A508, 152 (2003)

[97] G. Barr et al., Nucl. Instrum. Methods A533, 214 (2004)

[98] J. Altegoer et al. [NOMAD Collaboration], *The NOMAD experiment at the CERN SPS*, Nucl. Instrum. Methods A404, 96 (1998)

[99] A. Cervera, J.J. Gomez-Cadenas and J.A. Hernando, Nucl. Instrum. Methods A534, 180 (2004)

[100] M. Baldo-Ceolin et al., Nucl. Instrum. Methods A532, 548 (2004)

[101] CHORUS Collaboration, Nucl. Instrum. Methods A349, 70 (1994);
CHORUS Collaboration, Nucl. Instrum. Methods A378 221 (1996)

[102] O. Villalobos-Baille et al., *ALICE Technical Design Report of Trigger, Data Acquisition, High Level Trigger, and Control Systerm*, CERN-LHCC-2003-062

[103] G. Barrand et al., Comput. Phys. Commun. 140, 45 (2001)

[104] R. Brun and F. Rademakers, Nucl. Inst. and Meth. A389, 81 (1997)

[105] S.Borghi et al., *Clustering Algorithm*, Harp Memo 03-012

[106] S.Borghi, P. Chimenti, *Experimental study of HARP TPC static distortions*, Harp Memo 05-005

[107] S. Borghi et al. *The HARP TPC fitting algorithm*, HARP Memo 06-002

[108] S. Borghi, *TPC Performance ($\Delta p_t/p_t$, dE/dx)*, HARP Collaboration Meeting, September 2004

[109] S. Borghi et al. *The PID algorithm for the HARP TPC*, HARP Memo in preparation

[110] A. Bagulia, *Energy loss correction*, HARP Collaboration Meeting, June 2005

[111] Private communication Jean-Claude Legrand.

[112] S. Borghi, *Clustering Status*, HARP Collaboration meeting, December 2001.

[113] S. Borghi, *TPC Cluster Algorithm Update*, HARP Collaboration meeting, November 2005.

[114] E. Gatti et al. NIM 163, 83 (1979)

[115] E. Mathieson and J.S. Gordon NIM 227, 277 (1984)

[116] S. Borghi, *TPCino monitoring and analysis*, HARP Collaboration meeting, December 2000

[117] J. Uiterwijk, J. Panman and B. Van de Vyver, Nucl. Instrum. Methods A560 (2006) 317

[118] S. Borghi, *TPC performance: momentum & dE/dx presented*, HARP Collaboration Meeting, November 2003

[119] HARP Collaboration, Status report of the HARP experiment, CERN-SPSC/2002-019

[120] M. Poppe, *TPC Tracking Software*, ALEPH 87-102

[121] J. Knoblock, P. Norton , *TPC Status of Reconstruction*, ALEPH 88-46

[122] Private communication S.Giani

[123] N.I. Chernov, G.A. Ososkov Computer Physics Communications 33, 329 (1984)

[124] S. Borghi, *Residuals study*, HARP Collaboration Meeting, November 2003

[125] S. Eidelman, et al., Review of Particle Physics, Physics Letters B 592, 1 (2004)

[126] http://geant4.web.cern.ch/geant4/geant4.html

[127] R.Veenhof , *Calculations for the HARP TPC read-out*, http://r.home.cern.ch/r/rjd/www/Harp/, (2001)

[128] M.Apollonio et al., *Time calibration and evaluation of the drift velocity*, HARP Memo 05-002

[129] S. Borghi and S. Giani, *Study of TPC distortions*, Harp Memo 04-004

[130] F. James, *Interpretation of the errors on parameters as given by MINUIT*, Supplement to CERN Program Library Long writeup D506. CERN, 1978.

[131] S. Borghi, *Appendix: Hydrogen target*, HARP Memo 05-002 Appendix

[132] W.J. Cody, *Rational chebyshev approximation for the error function*, Math. Comp. 22, 631 (1969)

[133] A. L'Abbate, H *ARP Cryogenic Targets*, Summer Student Report (2002)

[134] Private communication E. Radicioni

[135] Private communication G. Prior

[136] Private comunication J.Burguet, A.Zhemchugov, A.Krasnoperov

[137] G. Vidal Sitjes et al., *The TPC analog signals*, HARP Memo 03-005

[138] HARP Collaboration, *Status report of the HARP experiment*, CERN-SPSC/2003-027

[139] U. Gastaldi and P. Temnikov, *Run by run hot/dead pad map and equalization with beam data. Time and target dependences*, HARP Collaboration meeting, June 2004 and September 2004

[140] L. Howlett-Scotchmer, *Simulation and Correction of Cross Talk in the Harp Time Projection Chamber*, Ph.D. Thesis Sheffield-2004

[141] S. Borghi, *TPC track distortion: review of situation* HARP Collaboration meeting, 7th July 2003

[142] P. Temnikov et al. *pp Elastic Scattering at 3 GeV/c with Liquid* H^2 *Targets in HARP*, HARP Memo 06-003, INFN-LNL(Rep)209(2006)

[143] W. Blum L. Rolandi *Particle Detectionwith Drift Chambers*, Springer-Verlag, 1993

[144] S. Borghi et al., *TPC performance*, HARP Memo 06-001

[145] R.L Gluckstern, Nucl. Instrum. Methods 24, 381 (1963)

[146] S. Borghi *Study of* Δp_t *in the HARP TPC*, HARP Memo 03-016

[147] S. Borghi et al. *Elastic scattering reactions and performance of the HARP TPC*, HARP Memo 05-001

[148] I.Ambats et al., *Systematic study of* $\pi^{\pm}p, K^{\pm}p, pp, \overline{p}p$ *forward elastic scattering from 3 to 6 GeV/c*, Phys.Rev D 9 5, 1179 (1974)

[149] V.Ivanchenko Private comunication

[150] G. D'Agostini, Nucl. Instrum. Meth. A362, 487 (1995)

[151] A. Grossheim, *Particle production yields induced by multi-GeV protons on nuclear targets*, Ph.D. thesis, University of Dortmund, Germany, 2003, CERN-THESIS-2004-010

[152] S. Borghi *Error flags associated to the TPC track helix fit results*, HARP note (2003)